The Dissertation Committee for Daniel Hoyt Eakin Jr. Certifies that this is the approved version of the following dissertation:

An Analysis of Subduction Related Tectonics Offshore Southern and Eastern Taiwan

Committee:

Luc Lavier, Supervisor

Kirk McIntosh, Co-Supervisor

Harm Van Avendonk

Jaime Barnes

Brian Horton

An Analysis of Subduction Related Tectonics Offshore Southern and Eastern Taiwan

by

Daniel Hoyt Eakin Jr., B. S.

Dissertation

Presented to the Faculty of the Graduate School of
The University of Texas at Austin
in Partial Fulfillment
of the Requirements
for the Degree of

Doctor of Philosophy

The University of Texas at Austin
December, 2014

Dedication

For my wife and family.

Acknowledgements

Many people have contributed to this dissertation in many different ways. I am extremely grateful to my advisor for taking me on as a student and involving me in extremely interesting geophysical research in Taiwan. I have benefited and matured as a result of his mentorship, advice, and most importantly his patience while I learned what it is was to be a graduate student. I am very appreciative of the opportunities he afforded me during my time at UT. I would also like to thank Luc Lavier and Harm Van Avendonk, whom I have worked closely with over the past 5 years. I have learned a great deal from all three through our discussions and our travels together. I would like to thank Char-Shine Liu and Chao-Shing Lee for their involvement in the project and the manuscripts that came out of it. I am also grateful to Jaime Barnes and Brian Horton for their insight into this work.

I am forever indebted to Steve Holbrook for taking a chance on me as an undergraduate student and introducing/inspiring me to pursue my newfound passion for marine geology and geophysics. Thank you to my parents and sisters for always encouraging me to excel and work for what was important to me, guiding my growth as a person, and raising me to be who I am today. There are too many friends and colleagues to thank by name, but I would like to mention Philip Guererro for his wonderful work as our Graduate Coordinator and the close friendship we developed during my time here. I also thank my office mates Ryan Lester and Bobby Reece for simultaneously keeping me on track and not letting me work too hard. Finally and most importantly I would like to express my gratitude and love for my beautiful wife Autumn, for enduring 3 years of long distance marriage and never letting me give up on myself. While the culmination of my time at UT was the work within the following dissertation, the highlight was finding my wife. This is for you love.

An Analysis of Subduction Related Tectonics Offshore Southern and Eastern Taiwan

Daniel Hoyt Eakin Jr., PhD
The University of Texas at Austin, 2014

Supervisors: Luc Lavier and Kirk McIntosh

Arc-continent collision is associated with vigorous mountain building and terrane accretion on relatively short (<10 Ma) geologic timescales. It is believed to be an important mechanism for the growth of continents. Taiwan represents one of the few active examples of this process. As such, is the perfect natural laboratory to investigate the nature of the continent ocean boundary and the uncertain behavior of the accretionary prism and extended, transitional rifted margin crust during the collision process. Taiwan also provides a unique opportunity to investigate structures in the backarc, yielding key insights into the still controversial tectonic conditions that were responsible for the unique subduction-collision system observed today. The obliquity of the collision between the North Luzon Arc and the Chinese rifted margin allows for examination of different temporal stages of collision at different locations.

Recently acquired seismic reflection and wide-angle seismic refraction data, offshore Taiwan, document the crustal structure of the incipient mountain belt and of the Philippine Sea Plate in the backarc domain to the east. Geophysical profiles offshore southern Taiwan show evidence for a transition from the subduction of ocean crust to highly extended, transitional continental crust of the northern South China Sea distal margin.

During oceanic subduction, accretion and underplating of thick sedimentary cover sequences create a large 13-15 km thick accretionary prism. Prior to the encroachment of the continental shelf, there is evidence for further underplating of transitional distal margin crust to the base of the prism. These findings support a multi-phase collisional model in which early growth of the mountain belt is driven by structural underplating of the previously sedimentary-only accretionary prism with blocks of transitional crust from the distal rifted margin.

Geophysical profiles offshore eastern Taiwan show evidence for asymmetric crustal thickening, from 12-18 km, along the entire length of the Gagua Ridge suggesting the West Philippine Basin oceanic crust is underthust beneath that of the Huatung Basin. In this interpretation, the Gagua Ridge was the result of a failed subduction initiation event during the early Miocene that may have existed simultaneously and, for a short time, competed with the Manila subduction zone in accommodating convergence between the Eurasia and Philippine Sea plates.

Table of Contents

CHAPTER 3: NEW GEOPHYSICAL CONSTRAINTS ON THE STRUCTURE AND POTENTIAL EVOLUTION OF THE GAGUA RIDGE AND HUATUNG BASIN.... 65

List of Tables

List of Figures

CHAPTER 1: INTRODUCTION AND OVERVIEW

1-1: INTRODUCTION

Mountain belts and orogenesis has been the subject of intense study and debate before plate convergence and collision were determined the driving forces behind their development (Dewey and Bird, 1970). Active coastal mountain belts are usually associated with high levels of seismicity, and therefore present potential earthquake and tsunami hazards. Despite significant advances in our understanding, many fundamental aspects concerning orogenesis and more specifically collisional orogenesis remain unanswered. Examples include the role of the rifted continental margin during collision and how the submarine mountain belt responds to a change in composition from subducting ocean crust to extended continental crust of the rifted margin, both of which can be addressed in Taiwan.

Taiwan is the result of an ongoing, oblique collision between the N-S trending Luzon volcanic arc of the Philippine Sea Plate and the NE-SW trending rifted Chinese continental margin of the Eurasian Plate (Figure 1-1). Convergence is accommodated by the subduction of South China Sea lithosphere in the south along the Manila trench, and by the subduction of Philippine Sea lithosphere along the Ryukyu trench to the northeast. This collision between the N-S trending arc and NE-SW trending passive margin began ~4-7 Ma (Huang et al. 2006), and has since propagated southward at a rate of ~60-95 km/Ma with respect to the Eurasian Plate (Chai 1972; Seno, 1977; Suppe, 1984; Byrne and Liu, 2002 Lee et al., 2006). Because of this geometry, analyzing different spatial locations along the strike of the orogeny can be considered equivalent to viewing the orogen at different temporal stages in the evolution of the mountain belt (Suppe, 1981). This trait distinguishes Taiwan from the few other examples of arc-continent collision and makes it an ideal natural laboratory for investigating how to both the overriding and subducting components are tectonically modified over the course of arc-continent collision.

1-2: GEOLOGIC BACKGROUND

The ongoing Taiwan arc-continent collision represents the final stage of a Wilson Cycle responsible for the opening and present closing of the South China Sea (SCS) (Figure 1-1). Cretaceous-Early Paleogene rifting of the South China continent formed the northern SCS rifted margin and the conjugate margin to the south near Palawan (Lee and Lawver, 1995; Nissen et al., 1995). Continental break-up and seafloor spreading followed to form the SCS during the late Oligocene-middle Miocene (Taylor and Hayes, 1983; Briais et al., 1993).

Beginning in the Oligocene-early Miocene, the South China Sea oceanic crust has subducted eastward beneath the Philippine Sea Plate (PSP) along the Manila trench (Yang et al., 1996; Hall, 2002). Subduction has created a doubly-vergent accretionary prism, the Luzon Trough forearc basin, and Luzon volcanic arc (Figure 1-1). Deep seismicity and global tomography delineates the subducting Eurasian slab to depths of 200-300 km (Kuo et al., 2000; Lallemand et al., 2001).

In the northernmost part of the SCS, ongoing subduction has consumed the SCS ocean crust, resulting in the juxtaposition and collision of the rifted margin with the North Luzon Arc (NLA) (Figure 1-2). Morphological features associated with oceanic subduction far to the south begin to evolve into the earliest stages of a mountain belt just offshore southernmost Taiwan. The Manila accretionary prism thickens to become the Hengchun ridge and its onshore equivalent, the Hengchun Peninsula (Figure 1-2) (Huang et al 1997; Chang et al., 2009). The relatively undeformed Luzon Trough forearc basin sediments in the normal oceanic subduction realm in the south become backthrust over the forearc to form the Huatung Ridge pop-up structure close to Taiwan (Lundberg et al., 1997; Chi et al., 2003; McIntosh et al., 2005; Hirtzel et al., 2009).

Onshore, the Taiwan orogen is divided into 5 morphotectonic units that are separated by major faults and increase in metamorphic grade from west to east (Ernst et al., 1985) (Fig. 1-2, 1-3). The five morphtotectonic units are further distinguished by sedimentary and metamorphic facies. The Coastal Plain, the onshore expression of the flexural foreland basin, consisting of syn-orogenic clastic alluvial sediments shed from the Taiwan mountain belt underlain by Neogene sediments (Figure 1-2, 1-3).

To the east is the Western Foothills foreland fold-and-thrust belt (Figure 1-2, 1-3), separated from the Coastal Plain by the Shingchuang fault. The Western Foothills consist of thrust sheets of pre-orogenic Miocene passive margin sediments and Pleistocene shallow marine detrital material (Ernst et al., 1985, Mouthereau et al., 2002). The Western Foothills are characterized by northwest-verging thrust faults and folds consistent with the northwesterly direction of plate convergence (Mouthereau et al., 2001; Simoes and Avouac, 2006). In northern Taiwan, the Western Foothills are bordered by the Hsuehshan Range and separated by the Chuchih fault (Ernst et al., 1985, Huang et al., 1997; Fisher et al., 2002; Chang et al., 2009). The Hsuehshan Range is a former continental shelf rift basin inverted during collision (Clark et al., 1993; Tillman and Byrne, 1995) consisting of Eocene-Oligocene quartz and carbonate-sandstone, argillites, and shales that from unmetamorphosed in the west, to lower greenschist facies in the east (Clark et al., 1993).

The Lishan fault, a major morphologic and structural boundary, separating the Central Range from the Hsuehshan Range to the west (Figure 1-2, 1-3). The Central Range represents the exhumed metamorphosed core of the Taiwan orogen, and exhibits the greatest elevations (~4km) and erosion rates present on the island. This unit consists of Miocene slates-turbidites in the west (Backbone Range) and Paleozoic-Mesozoic metamorphic rocks in the east (Cheng et al., 2009; Huang et al., 2006; Lee et al., 2006). Source rocks for the Miocene slates-turbidites are deep-marine sediments derived from the Chinese margin that were accreted to the prism and then deformed during further convergence and collision (Lee et al., 2006).

The eastern portion of the Central Range (Tananao Complex) consists of Eocene quartzite-limestone-slates and schists with Paleozoic-Mesozoic metamorphic basement (schists and marbles) thought to represent the deformed sedimentary section and crystalline basement of the underthrust Chinese rifted margin (Figure 1-2, 1-3) (Ho, 1986; Lan et al., 1996, Lee et al., 2006). The easternmost Tananao Complex contains a small distribution of mafic material primarily within the Lichi mélange in southern Taiwan, and the Kenting mélange on the Hengchun Peninsula (Chang et al., 2003).

The Longitudinal Valley separates the Central Range to the west and the Coastal Range volcanic arc complex to the east (Figure 1-2, 1-3) (Angelier et al., 1997). The Longitudinal Valley and thrust fault are the surface expression of a suture zone dipping approximately 55° ESE. The Longitudinal Valley extends northward, eventually intersects the traced location of the Ryukyu trench, and extends southward offshore to align with the South Longitudinal Trough (Lallemand et al., 2001). The Longitudinal fault accommodates ~2-3 cm/yr of shortening with left lateral strike-slip motion of ~1.3 cm/yr (Barrier, 1985; Lee and Angelier, 1993; Angelier et al., 1997; Chang et al., 2009).

The easternmost morphotectonic unit in Taiwan is the Coastal Range (Figure 1-2, 1-3), the accreted segment of the northern Luzon volcanic arc (Chai, 1972; Barrier and Angelier, 1986). It consists of intermediate-composition volcanic rocks, agglomerates, and tuffs (Lundberg et al., 1997) and the Lichi Melange consisting of forearc sediments intermixed with exotic andesitic and ophiolitic blocks (Chang et al., 2009).

East of Taiwan, the Philippine Sea Plate subducts beneath the Eurasian Plate along the Ryukyu trench. The Ryukyu trench extends to the north and east of Taiwan to Japan where its initiation preceded the initiation of arc-continent collision in Taiwan. Along this path, the Ryukyu subduction system is generally divided into 3 segments: Northern, Central, and Southern, separated by the Tokara Strait and the Kerama Gap respectively with decreasing volcanic activity moving south (Shinjo et al., 1999). Subduction of the Philippine Sea Plate generates the Ryukyu arc, Yaeyama Ridge accretioanry prism, and a series of forearc basins (Figure 1-1, 1-2) (Lallemand et al., 1997; Huang et al., 2000). Locally, these features are deformed by the NS trending Gagua Ridge, which is thought to be an ancient fracture zone, transform boundary within the Philippine Sea Plate, or former plate boundary in the past (Deschamps et al., 1998; Font et al., 2000; Hall, 2002). Subduction has also resulted in extension in the form of the Okinawa trough back-arc-basin that extends to northern Taiwan, connecting with the so-called northern Taiwan Volcanic Zone (Shinjo et al., 1999; Nakamura et al., 2003; Lin et al., 2007; Wang et al., 2008; Lin et al., 2009).

1-3: MODELS OF COLLISION FOR TAIWAN

The abundance of studies has prompted various models of mountain building that offer a spectrum of behavior for the converging crust and lithosphere. The studies are often discussed in terms of mutually exclusive hypotheses; each was developed to explain contrasting observations that constrain different elements of the mountain-building process in Taiwan. It may be that aspects of different models are accurate to some capacity, and others may be incorrect.

1-3-1: Wedge Models of Orogen Development

The early and most ubiquitous model of the Taiwan mountain belt characterizes the orogen as being analagous to compressive mountain belts in that it displays large horizontal compressive strain within a deforming crustal wedge overlying a décollement (Suppe 1981). This model, modified from the critical taper of a deforming wedge (Chapple, 1978) is now called the classical-critical wedge model (Figure 1-4) (Davis and Suppe., 1980; Suppe., 1981; Davis et al., 1983; Dahlen et al., 1984). This model describes the mechanics of both fold-and-thrust belts and accretionary wedges as being analogous to a Coulomb wedge that develops in front of a rigid backstop. The shape of the wedge is governed by the brittle strength of the material (Paterson, 1978) and the frictional stress on the décollement (Byerlee, 1978). With continued convergence, the wedge will thicken or propagate into the foreland to maintain its geometry.

Support for this model comes from surface mapping and topographic profiles of Taiwan, as well as, the décollement identified in the foreland fold and thrust belt (Suppe, 1981). The décollement exists at ~6-10 km depth in the foreland and dips at a shallow angle toward the hinterland (Suppe, 1980; Johnson and Segall, 2004). Earthquake hypocenters were used to suggest the position of this main décollement (Carena et al., 2002). Several investigators (Carena et al., 2002; Willett et al 2003; Johnson et al 2005) have attempted to extend the critical wedge model beyond the foreland fold-and-thrust belt, but the presence of a such a shallow décollement in the central part of Taiwan remains highly controversial.

The critical wedge model has been applied to various other mountain belts and accretionary wedges throughout the world and geologic time. Additional studies expanded our knowledge of this model, solving for thermal effects and rheological heterogeneity (Dahlen and Barr, 1989; Willet, 1999) and dynamic processes such as sedimentation, erosion and isostasy (Simpson, 1995; Konstantinovskaia and Malavieille, 2005; Storti and McClay, 2010).

Despite the importance of the so-called thin-skinned critical wedge model in Taiwan, there is significant evidence that suggests simultaneous involvement of the basement along with thin-skin processes in the mountain building process in Taiwan. The majority of the evidence can be found in the Central Range where the Pre-Tertiary basement of the northern Chinese continental margin is exhumed and exposed at the surface (Ho, 1986). Additionally, reactivation of former rift faults has been identified in the foreland beneath thin-skinned structures of the Western Foothills. (Lee et al., 2002; Mouthereau and Lacombe, 2006). Numerous investigations have proposed these thick-skin wedge models, which involve the basement to account for these observations (Figure 1-5).

One approach to thick-skin wedge modeling imposes a deeper mid-crustal décollement (Figure 1-5a) that allows shortening and accretion within the shallow wedge to occur contemporaneously with ductile deformation and metamorphism in the deeper crust (Mouthereau et al 2001; Mouthereau and Lacombe, 2006; Yamato et al., 2009). The presence of a deep décollement at 10-15 km depth is inferred from inversion structures, structural restorations, and seismicity in the foreland of Taiwan (Huang et al., 1993; Mouthereau et al., 2001).

Other thermochronologic and numerical approaches model the development of both the Hsueshan and Central Ranges with an emphasis on underplating (Figure 1-5b) as the driving mechanism for the uplift and exhumation of both the Hsuehshan and Central Ranges (Beyssac et al., 2007; Simoes et al., 2007). These models predict a single décollement that steps-down towards the hinterland. Most of the shortening is absorbed in the foreland that sole into a shallow décollement (Simoes and Avouac, 2006). This shallow décollement steps down into the thick, buoyant continental crust of the subducting Eurasian Plate, shearing portions of the crust and underplating them into the overlying orogenic wedge.

1-3-2: Forearc Detachment Model

The previous wedge models describe how convergence between the Eurasian Plate and the Philippine Sea Plate is accommodated in the shallow wedge and shortening in the incoming rifted SCS rifted margin. However, marine geophysical studies show that shortening is accommodated throughout the forearc (Hirtzel et al., 2009; Lundberg et al., 1997), as the NLA north of Luzon is much wider than the NLA near Taiwan or the accreted Coastal Range for that matter.

These studies indicate that the forearc backstop evolves over the course of the collision and does not act as a simple rigid backstop proposed by critical wedge studies. Instead these data suggest forearc block detachment and subsequent subduction due to frictional coupling to subducting continental lithosphere as a result of the collision process (Figure 1-6). This idea has been explored by analog and numerical modeling studies (Chemenda et al., 2001; Tang et al., 2002; Malavieille and Trullenque, 2007). The studies converge on a model in which the forearc ruptures near a weaker volcanic arc and subducts in the earliest stages of collision. Underthrusting of the forearc induces shortening and rapid thickening at the rear of the accretionary prism that will eventually form the Central Range.

1-3-3 Lithospheric Collision Model

The previous wedge models assume that the development of the Taiwan mountain belt is driven by steady state subduction of the SCS ocean crust and eventually the Chinese continental margin. A lack of seismicity in the upper 30-40 km and absence of a clear Wadati-Benioff zone north of 22.5° N, in the core of the orogeny, are inconsistent with thin-skinned models (Rau and Wu., 1995; Wu et al., 1997; Wu et al., 2004). Thermal modeling supports the previous observation revealing an elevated geothermal gradient beneath the interpreted aseismic Central Range crustal root (Lin, 2000, Song and Ma, 2002). Additionally, recent magnetotelluric data illuminate the Lishan fault to be a conductive feature that penetrates deep into the crust below any thin-processes (Bertrand et al., 2009).

These studies support a model where Taiwan is the result of lithospheric collision between the Eurasian and Philippine plates with the edges of the plates engaged in compressional contact and resulting in thickening towards the core of the orogen (Figure 1-7) (Wu et al., 1997). This model type is based on deep seismicity, tomographic and lithological evidence for the participation of lower crust and upper mantle in the development of the orogen that cannot be explained by thin-skinned models. Most likely, both thin and thick-skinned processes are acting simultaneously, thin-skinned processes limited to the foreland while thick-skin processes are likely more prominent in the hinterland.

1-4: SUBDUCTION INITIATION

A commonality between any of the collisional models is that Taiwan represents the culmination of a complete Wilson Cycle in which the final stage is the consumption of the SCS ocean basin and the collision of the Luzon volcanic arc with the passive

Chinese continental margin. Despite our current understanding of this active boundary, little is known of the Cenozoic plate kinematics and tectonic conditions present in the western Philippines that initiated the active subduction we observe along the Manila trench. This is due in large part to the absence of an undeniable Cenozoic example of a passive or compressional boundary transforming into an active margin and our lack of understanding of the fundamental driving forces for its initiation. Much theoretical and numerical work has focused on both the spontaneous and induced initiation of subduction in a variety of geodynamic environments that reveal a wide-range of fundamental variables that influence the initiation process in different ways.

Spontaneous initiation is related to cycles of opening and closure of Atlantic type ocean basins, i.e. the Wilson Cycle, where rifted oceanic lithosphere ages and increases in density away from the mid-ocean ridge until a lithospheric instability arises and the plate sinks spontaneously into the mantle near the continental margin (Figure 1-8) (Stern and Bloomer 1992). It is difficult to reconcile spontaneous nucleation of subduction with our current understanding of lithospheric strength. Modeling from Cloetingh et al (1989) suggested that by the time oceanic lithosphere adjacent to a continental margin is dense enough to spontaneously subduct, it is too strong to fail. More recently, numerical analysis from Nikolaeva et al., (2010) showed that the stability of a passive margin depends on the strength and thermal properties of the continental lithosphere rather than that of the oceanic lithosphere.

In contrast to spontaneous initiation, induced or forced nucleation (Figure 1-8a-b) requires the rupture of the lithosphere via compressional tectonic forcing and likely represents the driving mechanism of initiation for most modern subduction systems including the Macquarie Ridge complex offshore south of New Zealand since the mid-Miocene (Collot et al., 1995). However, similar to spontaneous nucleation, analyses of available tectonic forces have suggested these may be to weak to overcome homogenous lithospheric strength. McKenzie, (1977) predicted the minimum force required for instability of the oceanic lithosphere to grow and for subduction initiate where ridge push and slab pull forces are resisted by friction on the fault plane and resistance to plate bending. A conclusion from this study is that subduction initiation would be difficult, but not impossible. In a similar study, Mueller and Phillips, (1991) argued that in most cases, the force required to overcome the strength of the lithosphere would be nearly an order of magnitude larger than known ridge push forces, and subduction would be nearly impossible to initiate. Toth and Gurnis (1998) outlined the forces necessary to initiate subduction on a preexisting fault cutting the lithosphere, and suggest a sequence of tectonic events based on numerical modeling and conclude that even with ridge push forces alone, it is still possible to initiate subduction. More recently, Gurnis et al., (2004) modeled catastrophic subduction initiation only when using a small coefficient of friction and speculate that large pore pressure plays a substantial role in reducing rock strength.

Mesozoic and Cenozoic plate reconstructions indicate that changes in relative plate motion across preexisting transform faults and fracture zones can result in the formation of new compressional boundaries (Uyeda and Ben-Avraham, 1972; Hall, 2002). Stern and Bloomer (1992), suggest that both the Eocene Bonin-Mariana and the Jurassic California arcs may have evolved in this manner. Potential examples of this process in its embryonic stages of evolution include the Mussau Trench and Macquarie Ridge complex south of New Zealand along the Pacific-Australian plate boundary (Figure 1-8b). Collot et al. (1995) interpreted the Puysegur Ridge as a strike-slip plate boundary that has recently undergone oblique convergence, due to the migration of the Pacific-Australian pole of rotation. The transpressional fault is evolving into an embryonic subduction zone further north.

1-5: DISSERTATION OUTLINE

The wide range of models for the evolution of Taiwan demonstrates the uncertain behavior of the subduction/collisional related terranes prior and during arc-continent collision. Ultimately, the goal of this dissertation is to apply crustal-scale geophysical methods to:

- Ascertain the crustal-scale structure and composition of the northern SCS in order to illuminate the likely position of the continent ocean boundary (COB) subducting along the Manila trench
- Document compressional deformation and structure of the Gagua Ridge and Huatung Basin east of Taiwan and develop a chronologic model of their mutual development with regards to the initiation of subduciton along the Manila trench
- Investigate accretion processes and morphology of the Manila accretionary prism offshore southern Taiwan

Results of these analyses will constrain a previously understudied phase of the arc-continent collision cycle and provide insight into the validity of the various evolutionary models developed to explain the Taiwan arc continent collision as well as the initial tectonic conditions that may have existed prior to the onset of subduction along the Manila trench.

The dissertation is organized into chapters consisting of published or publication ready manuscripts that address these goals.

Chapter 2: Crustal-scale seismic profiles across the Manila subduction zone: the transition from intra-oceanic subduction to incipient collision (Eakin et al., 2013 Journal of Geophysical Research).

In chapter 2, I discuss travel-time tomographic velocity models and coincident seismic reflection images from the 2009 TAIGER (Taiwan Integrated Geodynamics Research) marine acquisition program. These profiles delineate the crustal architecture and features of the northern SCS continent-ocean transition (COB) and Manila accretionary prism south of Taiwan. These data also track the significantly stretched continental crust of the distal margin far south into the ocean basin rather than oceanic crust as previously interpreted. The velocity models and seismic images reveal the stretched continental crust is as thin as ~12 km, potential volcanic bodies, and syn-rift strata. Farther south, reflection images identify normal oceanic crust and a linear NE-SW trending bathymetric high that is likely associated with the COB.

Shallow high velocities (5.0-6.5 km/sec) in the Manila prism are evidence for initial phases of structural underplating of stretched continental crust into the prism via inherited structural weaknesses from the rifting of the Chinese margin. Farther south, a second velocity model shows the accretionary prism to be composed of low velocity (2.5-4.0 km/sec) material, diagnostic of a primarily sedimentary composition. These observations suggest that until recently ocean crust had been subducting here and that structural underplating begins at some point between. The models also indicate that the forearc backstop may be steeply dipping to near vertical contrary to previous geometries assumed by other studies.

Chapter 3: New geophysical constraints on the structure and potential evolution of the Gagua Ridge and Huatung Basin (Eakin et al, (in revision) Geochemistry, Geophysics, Geosystems).

Chapter 3 uses a suite of new and previously published travel-time tomography models and coincident seismic reflection images to illuminate the shallow basement morphology and crustal structure of the Huatung Basin and Gagua Ridge. The velocity models indicate significant crustal thickening associated with the Gagua Ridge, to 12-18 km along its entire length. Most importantly, the two central velocity models also show a significant asymmetry in the crustal thickening suggesting a failed underthrusting episode of the West Philippine Basin oceanic crust beneath the oceanic crust of the Huatung Basin. In this scenario, the present day Gagua Ridge represents a snapshot of a failed subduction initiation preserved in the geologic record. Additionally, the velocity models show evidence for normal (5-7 km) oceanic crustal thicknesses in the Huatung Basin and West Philippine Basin.

Chapter 4: Along Strike Variability of Prism architecture in the Intra-Oceanic Subduction Domain Offshore Southern Taiwan (Eakin et al., in prep Tectonophysics).

Chapter 4 uses a series of ~trench perpendicular seismic reflection profiles from the TAIGER program in the pre-collision setting of Taiwan offshore northern Luzon. These profiles provide high-resolution ~dip oriented cross-sections of the subducting SCS oceanic crust and overriding Manila accretionary prism. The seismic reflection images reveal the majority of the sediments comprising the subduction trench are accreted directly to the toe of the prism while the deepest units are underthrust beneath the lower slope. A deep zone of reflectivity in the rear of the prism along the southernmost transects suggests thickening of the prism is primarily accomplished by underplating of previously underthrust material.

The northern transects illuminate the development of a disparate lower slope and upper slope domains. The taper of the lower slope is nearly horizontal that is shown to be the result of a subducting topographic high in the basement that causes local compression and taper adjustment in the frontal slope of the prism.

1-7 SUMMARY

This dissertation discusses the evolution of subduction related structures associated with the Taiwan arc-continent collision. In doing so, I seek to address outstanding issues regarding the early behavior of the Manila accretionary prism with the addition of buoyant, stretched continental crust in to the subduction system. Chapter 2 identifies the transition zone between thick, highly stretched continental crust and oceanic crust actively subducting along the Manila trench well into the south offshore southern Taiwan. The stretched continental crust actively subducts along the Manila trench subduction zone, where there is evidence for the earliest growth of the mountain belt driven by structural underplating of this crust. Chapter 3 documents the deformation in the frontal part of the Manila accretionary prism offshore northwest Luzon and provides compelling evidence for underplating of underthrust sedimentary units derived from the subducting SCS crust. Chapter 4 focuses on the enigmatic Gagua Ridge and Huatung Basin to the south and east Taiwan and argues that this feature is the result of the failed underthrusting of the West Philippine Basin ocean crust beneath the ocean crust of the Huatung Basin. This chapter concludes with arguments that this feature previously existed as a transpressional boundary and a location of failed subduction event that was active just prior or coevally with the initiation of subduction along the Manila trench in the early-Miocene. The findings in this dissertation ultimately suggest a link between the Wilson Cycle of ocean basin rifting/subduction and the resulting mountain belt of Taiwan and regional compressional features preserved in the bathymetry.

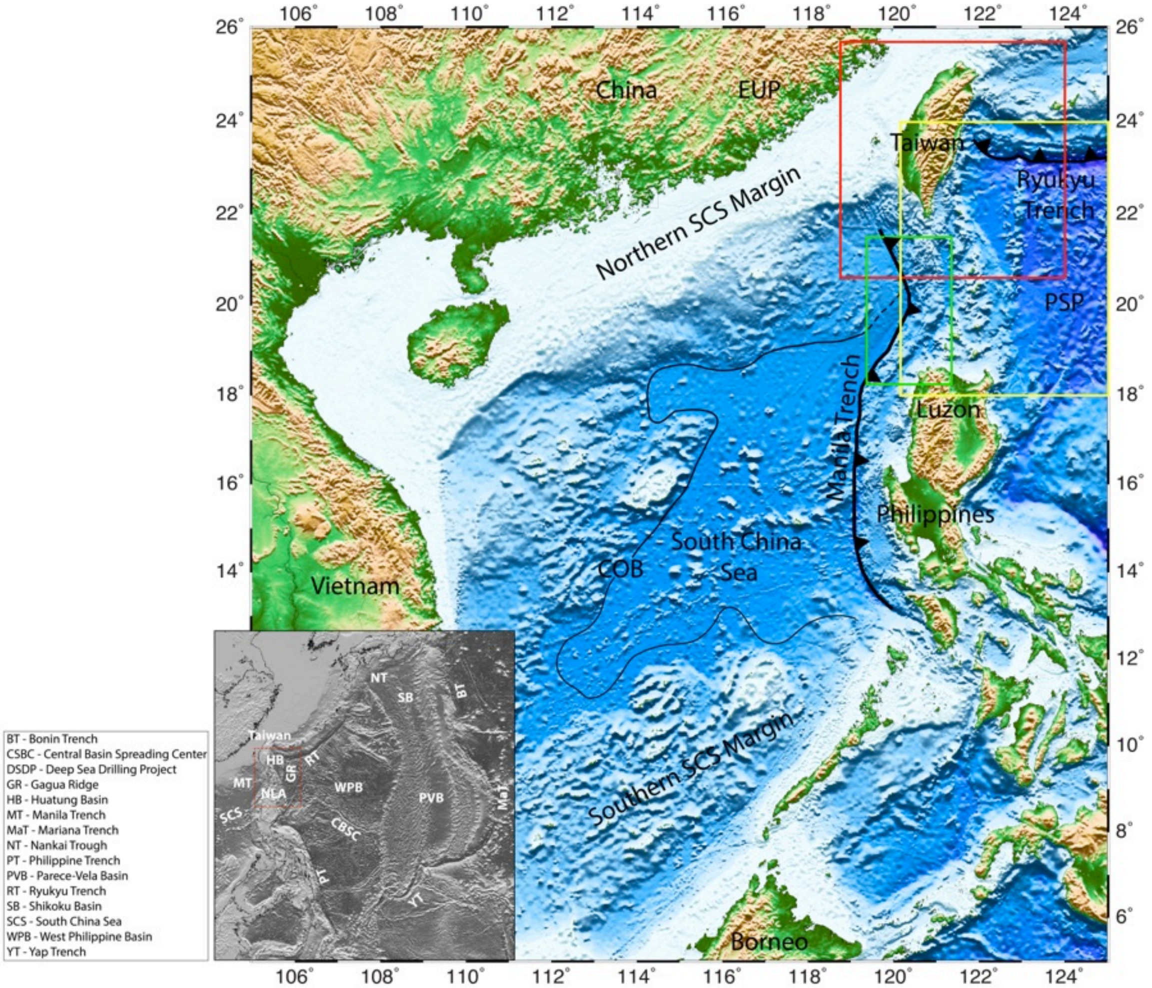

Figure 1-1. Regional map of the South China Sea marginal basin, Southeast Asia, and the northern Philippines. Major tectonic features are labeled including the Eurasia Plate (EUP), Philippine Sea Plate (PSP), northern and southern SCS rifted margins, Manila trench, and Ryukyu trench. Red, yellow, and green boxes are locations of Figures 1-2, 2-1, 3-1, and 4-1 respectively. Black and white inset highlights the location of the SCS marginal basin relative to major structures and geography of the greater PSP plate.

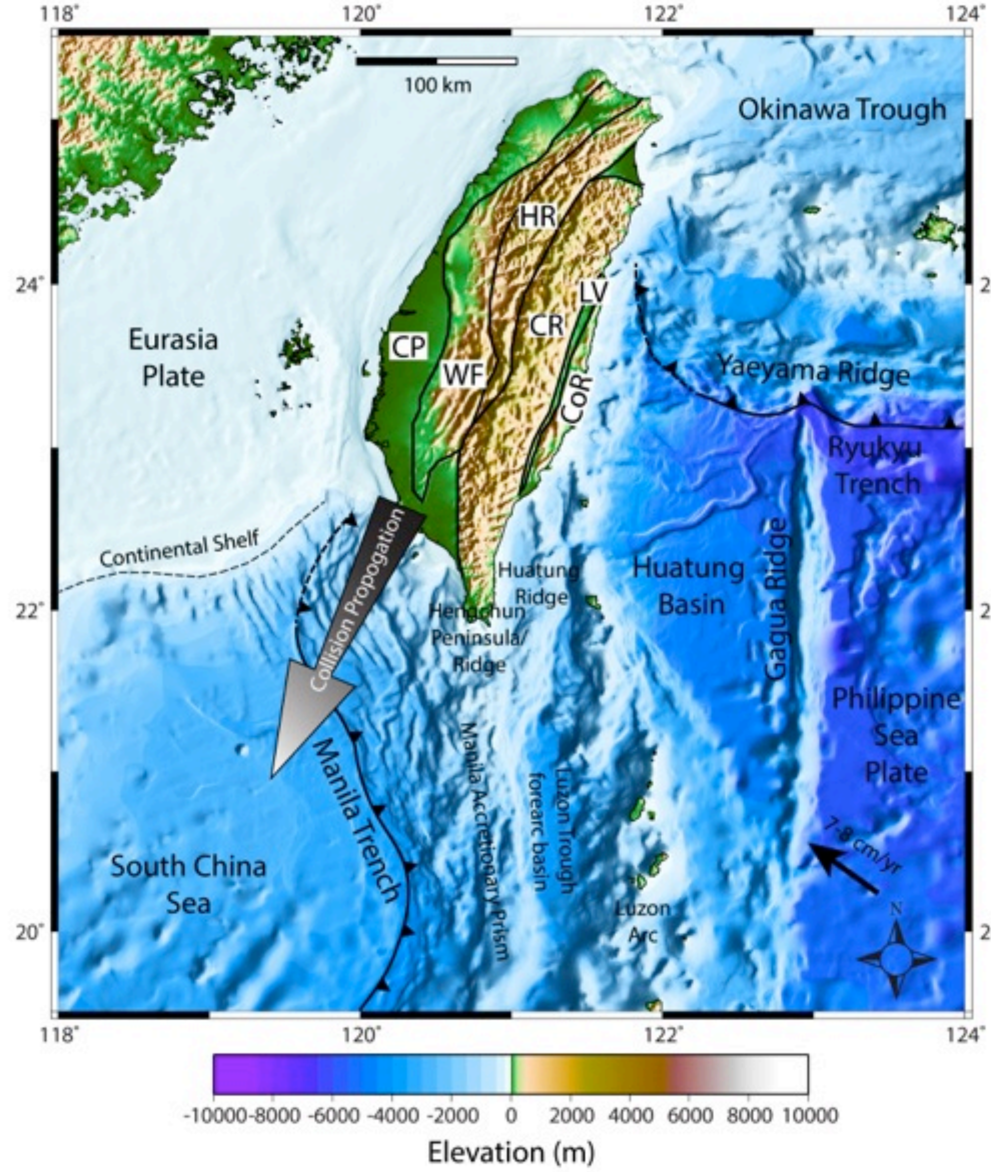

Figure 1-2. Elevation map of the Taiwan arc-continent collision and northern SCS. Taiwan consists of five tectonostratigraphic terranes: CP – Coastal Plain foreland basin; WF – Western Foothills fold-and-thrust belt; HR – Hsuehshan Range inverted rift basin; CR – Central Range metamorphic hinterland; CoR – Coastal Range accreted arc complex; LV – Longitudinal Valley. Plate convergence is NW-SE at 7-8 cm/yr, but the collision propagates to the south due to the obliquity between the NE-SW trending passive Chinese continental margin and the ~N-S trending NLA.

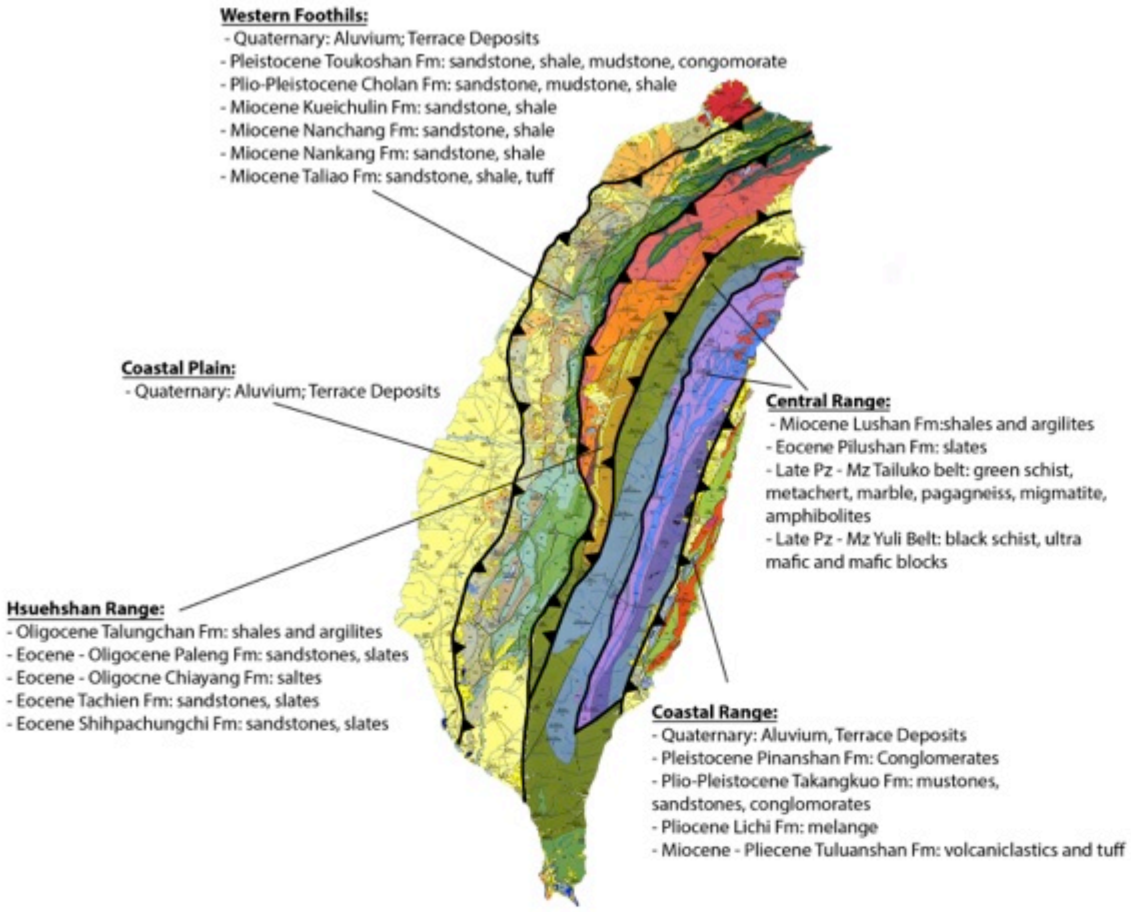

Figure 1-3. Geologic map of Taiwan (modified from Ho, 1988).

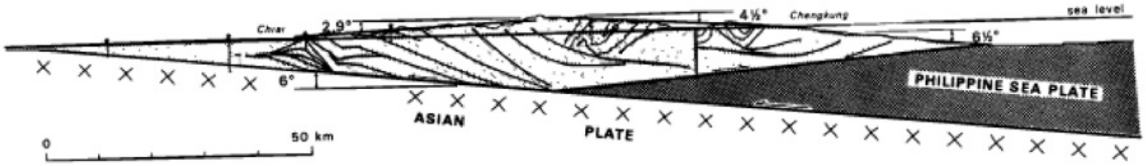

Figure 1-4. Thin-skin critical wedge model (from Davis et al., 1983). In this model, the northern SCS continental margin of the EUP subducts beneath the NLA of the PSP. The NLA acts as a backstop, off-scraping incoming sediments derived from the passive Chinese continental margin into a deforming, doubly-vergent wedge. The shallow dipping décollement decouples the deforming wedge from the subducting crust below.

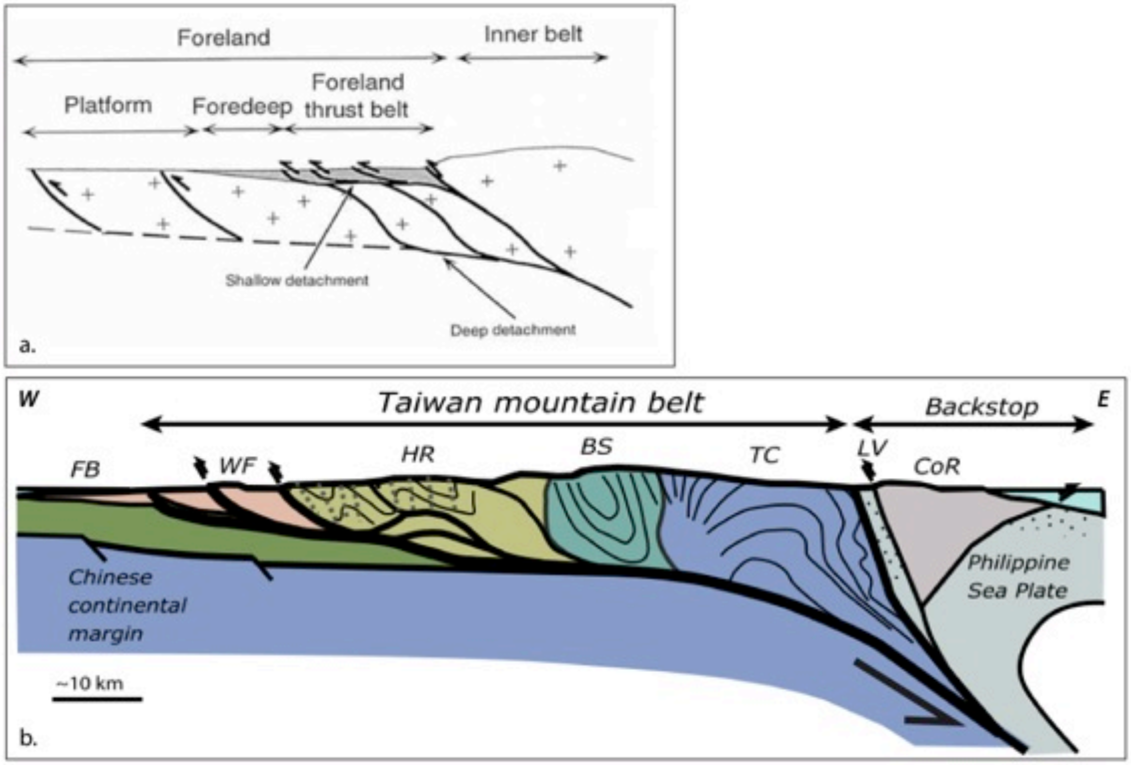

Figure 1-5. Examples of thick-skin wedge models that utilize a) both shallow and deep décollements (from Lacombe and Mouthereau, 2002) or b) a single décollement that steps down into the subducting crust, thickening the overriding wedge in the hinterland by underplating (from Simoes et al., 2007).

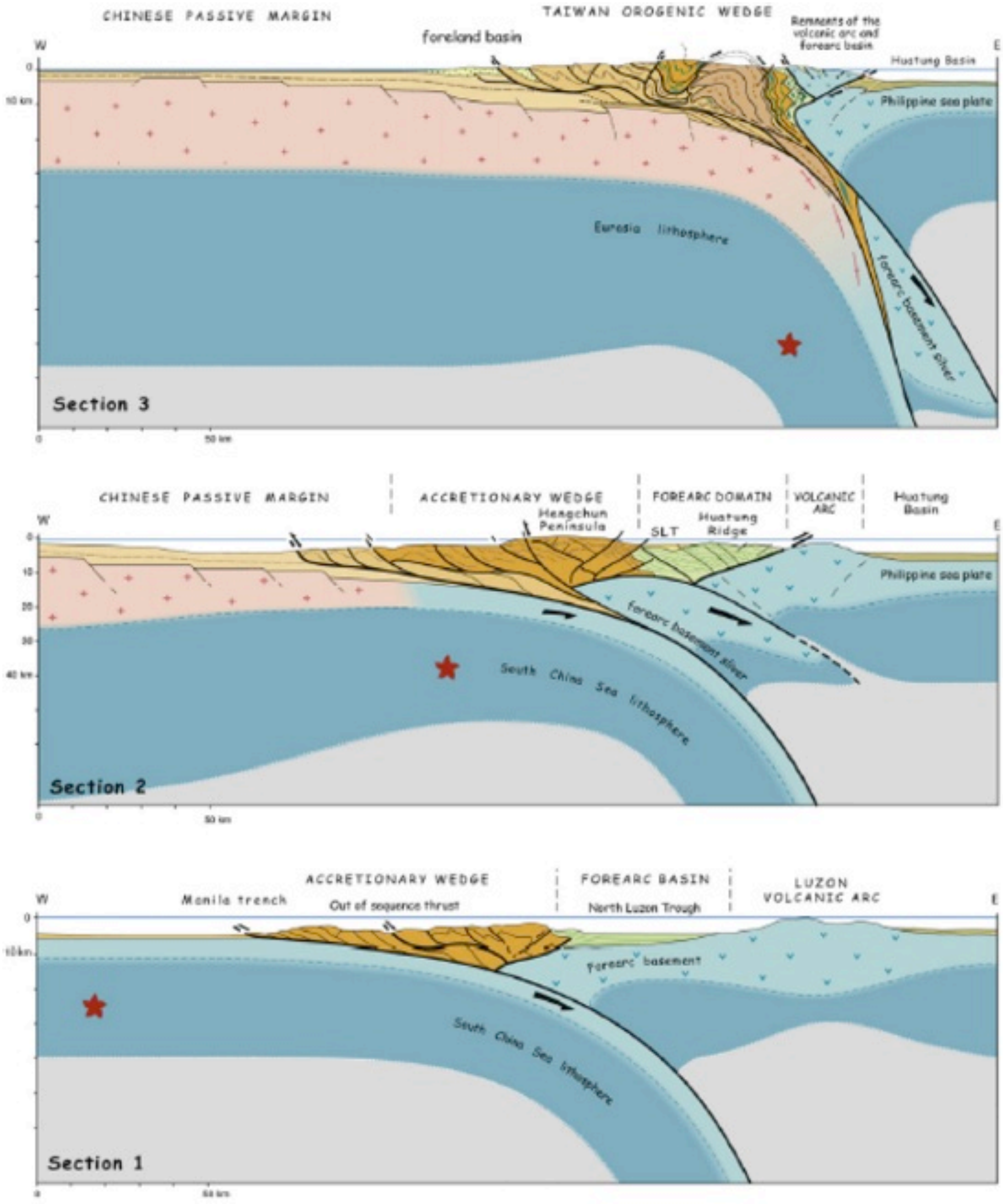

Figure 1-6. Forearc subduction model adaptation of the critical wedge models (from Malavieille and Trullenque, 2009). During subduciton of the SCS lithosphere (lower panel), the forearc block shortens in the incipient stages of collision and increasing deformation of the mountain belt (middle panel) and eventually decoupling from the NLA and subducting with the downgoing EUP (top panel).

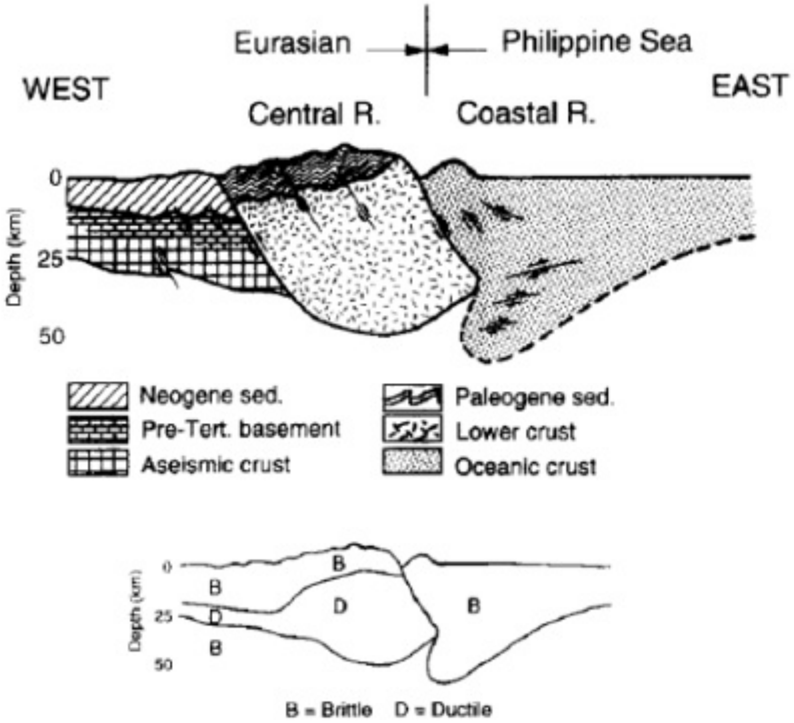

Figure 1-7. Lithospheric-scale collision model (from Wu et al., 1997). The entire crust and lithosphere of the continental margin and volcanic arc thicken during the collision. Neither the EUP or the PSP is subducting, instead a ductile crustal root has developed beneath the Central Range.

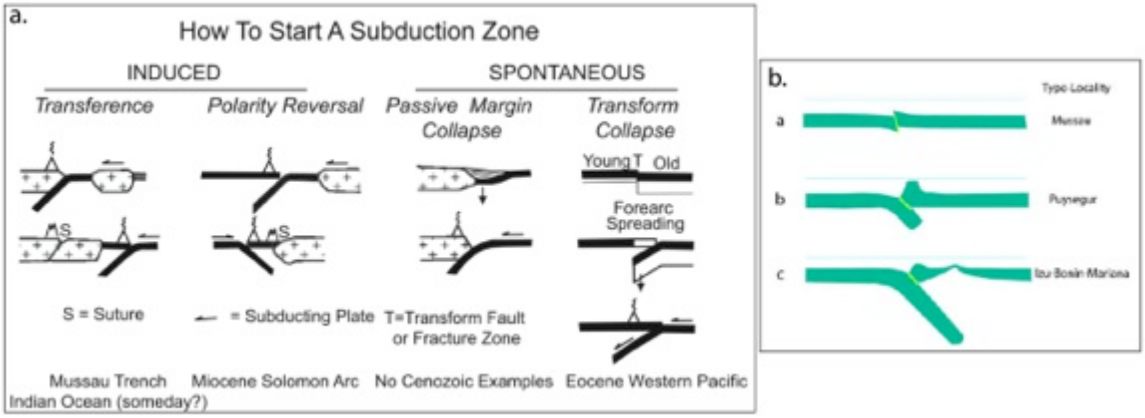

Figure 1-8. a) General classes, and subclasses of the theories about how subduction zones form (from Stern, 2004). b) Three phases of induced subduction initiation shown schematically, with type locality (from Gurnis et al., 2004).

CHAPTER 2: CRUSTAL-SCALE SEISMIC PROFILES ACROSS THE MANILA SUBDUCTION ZONE: THE TRANSITION FROM INRA-OCEANIC SUBDUCTION TO INCIPIENT COLLISION.[1]

2-1: INTRODUCTION

Arc-continent collisions play an important but poorly understood role in the growth and tectonic evolution of continental margins. It is an environment associated with vigorous mountain building and terrane accretion on relatively short geologic timescales. One of the few examples of active arc-continent collision is in progress in the Taiwan area. Much of the previous work conducted in Taiwan has been focused on uplift and erosion onshore (Suppe, 1987; Wu et al 1997) and post-orogenic collapse (Teng et al 2000, 1996). Due to the obliquity of the Chinese margin with respect to the Luzon arc, and the angle of plate motion of the Philippine Sea Plate (PSP) with respect to the Eurasian Plate (EUP), the resulting arc-continent collision is time transgressive. Because of this, significant efforts have also been made in the northern South China Sea (SCS) and Bashi Strait south of Taiwan to understand the incipient collision. Ludwig (1969) and Taylor and Hayes (1983) analyzed seismic refraction data from transects west of Luzon that show the crust of the subducting South China Sea to be thin (5-6 km thick). Briais et al (1993) compiled magnetic anomaly data sets to interpret timing of seafloor spreading in the northern SCS. Their work indicated that the continent-ocean-boundary (COB) intersects the Manila trench at ~19° N (Figure 2-1) and suggests that seafloor spreading

---

[1] Eakin, D. H., K. D. McIntosh, H. J. A. Van Avendonk, L. Lavier, R. Lester, C.-S. Liu, and C.-S. Lee (2014), Crustal-scale seismic profiles across the Manila subduction zone: The transition from intraoceanic subduction to incipient collision, Journal of Geophysical Research: Solid Earth, 119, 1-17.
Co-Author Contributions:
Kirk McIntosh: Research Advisor. Guidance of tectonic concepts and acted as primary editor of manuscript.
Harm Van Avendonk: Guidance of tomographic modeling concepts and edited of manuscript.
Luc Lavier: Academic supervisor. Guidance of geodynamic concepts and edited manuscript.
Ryan Lester: Guidance of multi-channel seismic reflection processing techniques during research phase.
Char-Shine Liu: Edited manuscript.
Chao-Shing Lee: Edited manuscript.

initiated at ~28-32 Ma. Wang et al (2006) constructed a seismic velocity model across the Chinese margin into the northern SCS ocean basin in which they interpret a broad (> 200 km) continent-ocean transition zone (COT) that is composed of extended continental crust with a thickness of 11-15 km as far south as 19° N. More recently, reflection profiles from McIntosh et al (2013) have identified zones of thinned continental crust to the south of 20° N. Conversely, Hsu et al (2004) mapped E-W trending magnetic lineations offshore southwestern Taiwan interpreting that the northern SCS is composed entirely of ocean crust to 21.5° N.

Several geophysical studies south of Taiwan have examined the structure of the Manila subduction zone and incipient collision. Liu et al (2004) and Lin et al (2008) used multi-channel seismic reflection (MCS) data characterize the Manila accretionary prism and Chinese rifted margin offshore southwest Taiwan. McIntosh et al (2005) used wide-angle seismic data to construct several tomographic transects that illuminate the deep crustal processes of the collision in southernmost Taiwan including apparent forearc detachment and subduction. Chi et al (2003) used MCS and gravity data to study the deeper structural geometry and kinematics of the Manilla accretionary prism. A key result of that work was the observation of a free-air gravity anomaly high in the rear of the accretionary prism at 20.9° N, requiring a significant component of high-density material interpreted to be derived from the forearc. In contrast, gravity modeling on a parallel transect to the south at 20.2° N did not require this high-density material and is consistent with a deforming wedge composed only of sedimentary material.

Despite the successes of various geophysical studies, there is still great uncertainty about the incipient collision zone offshore southern Taiwan due to the lack of crustal-scale information. To understand the collision from its incipient to mature stages, it is imperative to answer fundamental questions such as: Does the crustal structure of the northern SCS suggest a continental or oceanic affinity? Is thinned continental crust actively subducting along the Manila trench? If subduction of rifted continental material is occurring to the north, do the deformation patterns in the Manila accretionary prism change as well? Is there an underlying structural process that is responsible for the appearance of the lower to upper slope transition zone and sudden volumetric increase in the accretionary prism offshore southern Taiwan?

In this paper we describe results of 2 marine wide-angle ocean-bottom seismometer (OBS) transects and their coincident MCS data that show the crust subducting along the Manila trench between 20.5° N and 21.5° N, more than 200 km southeast of the continental shelf, to be composed of hyper-extended continental material from the rifted Chinese margin. The extended upper crust appears to be structurally underplated to the base of the accretionary prism during subduction along the northernmost OBS/MCS transect. In contrast, MCS reflection data from a third transect at 19° N shows crust of typical oceanic thickness subducting along the Manila trench.

2-2: GEOLOGIC AND TECTONIC SETTING

Taiwan is the result of oblique collision of the N-S trending Luzon volcanic arc of the Philippine Sea plate (PSP) and the NE-SW trending passive Chinese continental margin of the Eurasian plate (EUP). Taiwan is situated in the northernmost SCS that was the result of late Cretaceous-Early Paleogene rifting of the south China continent followed by N-S seafloor spreading during the Oligocene-Miocene (Taylor and Hayes 1983; Briais et al 1993; Lee and Lawver 1995; Nissen et al 1995). Here the PSP moves northwest and overrides the EUP at a rate of 7-8 cm/yr (Ranken et al 1984; Seno et al 1993; Yu et al 1999; Yu and Kuo 2001). Due to the obliquity of convergence, many authors interpret that the collision that initiated 4-7 Ma propagates south with respect to the continental margin (Huang et al 1997, 2006; Lee et al 2006).

The onshore geology of Taiwan has been well studied and is often discussed in terms of its five-tectonistratigraphic units (Figure 2-1). These units are distributed parallel to the length of Taiwan, separated by major faults, and increase in metamorphic grade from west to east (Ernst et al 1985). The spatial relationships of the mapped onshore geology suggest a genetic link with the offshore incipient collision domain and have motivated the development of many evolutionary models of Taiwan (Suppe 1981; Rau and Wu, 1995; Chemenda et al 1997; Mouthereau et al 2002; Byrne et al 2002). Despite our understanding, sources of high-pressure low-temperature lithologies with blocks of passive margin metamorphic and igneous basement, such as the Tananao Complex exposed in the southern Central Range (Simoes et al 2007; Beyssac et al 2008) are still ambiguous. Our goal is to use the data acquired during the Taiwan Geodynamic Research (TAIGER) Project to understand the evolution of the accretionary prism as it progressed from subduction to collision and improve ideas about how each tectonic component may have been assembled in the incipient phase of the arc-continent collision.

2-3: TAIGER EXPERIMENT

The marine TAIGER experiment took place March through July 2009, and included the acquisition of 12 transects with coincident MCS and OBS data over the course of three legs (MGL0905, 06, 08). In this paper we describe the results from two east-west MCS and coincident wide-angle transects that extend across the Manila subduction zone south of Taiwan (Figure 2-1). The MCS transects (lines 25A and 23 from here forward) were acquired during leg 1 (MGL0905), with the coincident wide-angle transects (lines T1 and T2 from here forward) acquired during leg 3 (MGL0908). Air-gun source firing and MCS acquisition were performed with the R/V Marcus G. Langseth. The seismic source array was composed of 4 sub-arrays consisting of 9 Bolt air guns each with a total volume of 6600 in3 towed at a depth of 8 m. Wide-angle and MCS reflection data were recorded separately to obtain shot spacing for ideal acquisition of both datasets. The nominal airgun source interval was 50 m for MCS data acquisition and 120 m for wide-angle acquisition. The increased shot spacing for wide-angle acquisition is based on the timing of the predicted previous shot noise and attempts to place noise at far offsets in the OBS record so as not to interfere with usable signal. MCS data were recorded on a 6 km seismic streamer consisting of 486 channels with 12.5 m spacing. Taiwanese vessels deployed and recovered 18 OBSs of the National Taiwan Ocean University (NTOU) along line T1 over a distance of 178 km, and 29 OBSs along T2 made up of 18 NTOU instruments and 11 instruments of the U.S. OBS instrument pool (OBSIP) over ~480 km. The key objectives for the analysis of these data are 1) Determine the velocity structure of the subducting SCS crust, and 2) Identify differences in morphology and crustal structure of the accretionary prism and North Luzon Arc to better understand the south to north transition from subduction to collision.

2-3-1: OBS Data

OBS spacing varied from ~10-15 km along both T1 and T2, and data were collected continuously during air-gun shooting. Both NTOU and OBSIP instruments recorded three geophone channels and a hydrophone. Sample interval was 4 ms for NTOU instruments and 5 ms for OBSIP instruments. Initial OBS data processing included instrument relocation and SEGY-header corrections. Levels of processing varied depending on data quality and typically included band-pass frequency filtering and gain, such as amplitude gain with distance, and automatic gain control (AGC). Due to structural complexities present along these transects, several instruments required additional processing steps including spectral balancing to equalize frequency content as needed to increase signal to noise ratio and first arrival picking confidence in the far offsets. Data along line T1 and T2 provide excellent constraints on the velocity structure of the subducting South China Sea crust, accretionary prism and forearc crust, however, T1 does not represent a complete cross-subduction transect as the Luzon arc is not covered. The first arrivals of T1 OBS data can be clearly seen at offsets up to 75 km (Figure 2-2a-b, e-f) and in some cases as far as 100 km (Figure 2-2c-d). Similarly, first arrivals of much of the T2 OBS data can be clearly seen at offsets up to ~65 km (Figure 2-3a-f). Despite advanced processing steps, the data quality from OBS's 17-22 positioned on the accretionary prism along T2 were poor, containing little signal past 20 km offset (Figure 2-3c-d). Poor data quality may be indicative of insufficient instrument coupling with the seafloor, complicated geological structures such as near vertical faults, or the presence of fluids in the shallow sediment preventing adequate signal penetration. Interestingly, despite average arrival offsets of ~65 km and a maximum of 100 km west of the trench, no clear velocity evidence of a refracted arrival from the Moho (Pn) is indicated on any record from line T1 or T2 that samples the EUP (Figure 2-2a-d; 3c-f) that may be due to a steep gradient in the upper mantle or low signal to noise ratio at long offset. Furthermore, the apparent velocity of the first arrivals is lower than what may be expected (~6.5-6.7 km/sec). The EUP crust here is dipping to the east into the Manila trench and therefore the apparent velocity observed here is likely greater than the true velocity, but still far less than expected for Pn.

2-4: METHODS

2.4.1 MCS Data Processing

Preliminary MCS processing took place aboard the R/V Langseth. Standard processing techniques were used including trace editing, sorting into common midpoint gathers, normal moveout velocity analysis and correction, stack, band-pass filtering, and f-k time migration. Subsequently, all MCS data shown here were subjected to a series of multiple attenuation techniques to improve crustal imaging including surface related multiple attenuation, Radon transform multiple attenuation, muting, and offset weighted stacking (see Lester and McIntosh 2012).

2-4-2: Tomography

The velocity structure of the Manila subduction zone is constrained with wide-angle travel times from 18 OBS receiver gathers along T1, and 30 OBS receiver gathers along T2 (Figure 2-1). To develop a velocity model that fits our OBS data we used a regularized travel-time inversion method similar to that implemented by Van Avendonk et al (2004). In short, we created a starting velocity model and alternated between ray tracing and linear inversions of the updated travel time residuals to reduce $\chi 2$, defined by travel-time misfits weighted by pick uncertainties ranging between 40 ms and 200 ms for these data (Figure 2-2 and 2-3). Iterations of raytracing and inversion are completed when a satisfactory fit between observed and calculated arrival times within the tolerance of pick uncertainties.

Both T1 and T2 extend across complicated structures including the Manila accretionary prism and Luzon forearc basin while T2 extends further east crossing the N.

Luzon arc. The tomography code coupled with the simplified starting models allow us to model first-arrival refraction travel-times without adding bias that may result from parameterization of a layer-based model. T1 spans 271 km in the horizontal direction and 30 km in the vertical direction, and contains 271 x 90 = 24,390 grid nodes. Grid spacing is 1 km in the horizontal direction, and 0.3 km in the vertical direction. The initial velocity model was constructed from a gradational 1-D velocity function hung from the seafloor bathymetry. 9,455 first-arrival picks (Figure 2) 14 iterations of travel-time tomography were performed to update the model, reducing $\chi 2$ from 180 in the initial model to .95 in the final velocity model. The final velocity model has an RMS misfit of 75 ms.

T2 spans 510 km in the horizontal direction and 30 km in the vertical direction, and contains 510 km x 30 = 15,300 grid points, although only 360 km of the transect is shown here. Grid spacing is 1 km in the horizontal direction and 0.3 km in the vertical direction. The initial velocity model was constructed in an identical manner as T1. 12,223 first-arrival picks (Figure 2-3) 13 iterations of travel-time tomography were performed to update the model, reducing $\chi 2$ from 160 in the initial model to .95 in the final velocity model. The final model has an RMS misfit of 75 ms.

2-4-3: Tomography Resolution Testing

The quality of our seismic data is quite variable especially along line T2 resulting in uneven ray coverage of our seismic velocity model. Ray coverage can be quantified with the derivative weight sum (DWS). DWS provides a useful measure of ray density at each model parameter in the final inversion (Thurber and Eberhart-Phillips 1999). In the profiles of T1 and T2, the DWS is higher in the crust than the upper mantle (Figure 2-2 -

2-4) due to the greater sampling and smaller uncertainties in the crustal refractions and at near offsets close to each instrument.

To better express the ability of the inversion to constrain seismic structure we used a procedure similar to that described in Van Avendonk et al (2004) using the resolution matrix, which is derived from the generalized inverse. We first assume that the series of linearized inversions have converged to a stable model solution. We then calculate the resolution matrix from the generalized inverse matrix. It is expected that where the models are well covered with overlapping raypaths, the resolution matrix will approach the identity matrix, so the velocity image is not distorted. In the regions where ray coverage is poor, the off diagonal elements of the resolution matrix average the seismic velocity structure over large distances in the inversion. Resolution is still poor with high ray coverage if raypaths have the same direction. After calculating the resolution matrix for each velocity model, we then slide an elliptical window of fixed dimensions over the resolution matrix to see how well the object of this size is imaged (Van Avendonk et al 2004).

Resolution testing investigates how well our data can resolve model features of 6 km wide by 3 km high, and 12 km wide by 6 km high. Resolution values are scaled between 0.00 and 1.00 to indicate whether the features are poorly or well resolved and we consider a value of 0.5 an adequate resolution. In the first test (Figure 2-5a, 2-5c) the larger averaging window shows that structures of 12 km (horizontal) X 6 km (vertical) are very well resolved (> 0.5) throughout the entire crust (3-15 km) and upper mantle (~15-25 km) along T1. Resolution of the deeper prism structure is limited in the center of T2 (190-220 km) due to poor data quality.

The second test (Figure -25b, 2-5d) shows that seismic velocity anomalies of 6 km (horizontal) by 3 km (vertical) are resolved quite well in the upper 10 km throughout both model spaces although lateral variations in the seismic velocity of the upper crust are better resolved along T2. The lower crust (> 10 km) shows adequate resolution at this scale with low resolution in the upper mantle (> 15 km). We can therefore assume that our final velocity models are good representations of the seismic velocity structure of the Manila subduction zone along both T1 and T2 on these length scales.

2-5: ANALYSIS AND RESULTS

2-5-1: MCS Line 15

Geological and geophysical data offshore western Luzon show that subduction has occurred along the Manila trench south of 18° N since the early Miocene (Lewis and Hayes 1983). West of Luzon, the Manila accretionary prism has been built from deformed sedimentary material accreted from the subducting SCS oceanic crust (Figure 2-1). Line 15 provides data to help describe the tectonic environment of subduction and the nature of the subducting SCS crust at this latitude for comparison with lines 25A and 23.

The pre-stack time migrated (PSTM) segment of line 15 shows the basement of the SCS and overlying post-rift sedimentary strata outboard of the Manila accretionary prism (Figure 2-6). Residual multiple energy still exists between 10 and 11 sec two-way-travel time (TWTT), however, this is much later than the arrival time of the Moho reflection and does not affect our imaging of it. The top of basement reflection is consistently smooth in character with a strong, high amplitude Moho reflection observed at 2 seconds TWTT below top of basement, suggesting a crustal thickness of ~6 km thick, which is typical for ocean crust (White et al 1992). The Moho clearly follows the bending of the subducting crust at it approaches the trench and is only obscured when residual multiple energy from the accretionary prism cuts across it. Outboard of the trench, normal faults are observed in the post-rift sedimentary cover that extend from the seafloor to the upper crust and increase in frequency approaching the trench. Several east-dipping reflectors observed in the basement appear to penetrate the Moho. Spreading rates in the SCS from 32-17 Ma were intermediate with full rates of 50mm/yr and 37 mm/yr from 27-16 Ma (Briais et al 1993). It is possible these are reactivated faults inherited from oceanic rifting, new faulting related to bending of SCS ocean crust as it enters the Manila trench, or a combination of both, similar to those observed in other convergent margins (Ranero et al 2003; Kopp et al 2004).

Westward of CDP 21000 a basement high protrudes through the pre-rift sedimentary cover to be exposed at the seafloor. From the bathymetry we can see this feature is actually part of a larger linear structure trending NE-SW (Figure 2-1). Similar features observed elsewhere in the SCS have been speculated to be part of a zone of volcanism near the COB (Hu et al 2009; Wang et al 2006) or and exposed peridotite ridge associated with the COB (Franke et al., 2011). Lacking reliable velocity constraints or direct samples, the origin of this feature remains enigmatic.

The post-rift sedimentary cover sequence is only slightly deformed on the flank of the ridge feature. A high amplitude sedimentary reflection at CDP 23000, ~6 sec TWTT, is observed to thin eastward and pinch out at ~CDP 11000. Assuming the thicker strata below this high amplitude reflection between CDP 20000-22000 are the oldest, it is likely that the oldest oceanic crust lies below, with crust becoming younger to the SE where the units thin and eventually pinch out.

2-5-2: MCS Line 25A

Between Taiwan and Luzon the Manila accretionary prism trends ~N-S (Figure 1). To the east of the prism, the North Luzon Trough (NLT) forearc basin deforms as the result of continuing convergence and uplift of the growing accretionary prism. Line 25A shows crust of the SCS subducting into the Manila trench, sediment deformation front, the deforming accretionary prism, top of subducting EUP slab reflection within the prism, and the deforming NLT (Figure 2-7a-e). West of the trench, we image 1-1.5 s TWTT post-rift sedimentary strata below the seafloor, intermittent weakly reflective packages capped by high amplitude reflections that we interpret to be pre or syn-rift sediments, and 3.5 s TWTT thick crust. Strong reflectivity within the post-rift sediments and a clear unconformity with the surrounding strata below the seafloor between CDP 63000-64250 marks the extent of a (~7 km wide) relict channel incised and then filled with sediment (Figure 2-7c). Between CDP 59000 and 64000 between 5-6 sec TWTT, the post-rift sedimentary sequence caps two weakly reflective packages that we interpret as syn-rift or possible pre-rift sediments below a high amplitude breakup unconformity (Figure 2-7c). McIntosh et al (2013) observed weakly reflective sedimentary packages interpreted to be syn-rift strata near to the north with a similar high amplitude breakup unconformity.

At CDP 62000, the post-rift sediments directly overlie the top of basement reflection. The top of basement reflection here is rugose and highly diffractive, disrupting the overlying sedimentary sequence (Figure 2-7c). This structure is similar to other examples of possible post-rift basaltic volcanic bodies in the SCS (Clift et al 2001; Lester et al 2013). Elsewhere in the seismic section, the top of basement exhibits highly variable topography with several alternating highs and lows that we interpret to be the expression of faulted blocks of upper crust whose fault traces are out of the plane with respect to the orientation of this transect (Figure 2-7a). Based on evidence from marine-magnetic studies of oceanic crust to the south that indicate that spreading in this area was ~N-S, so the E-W orientation of the transect places it perpendicular to the spreading direction, i.e., a strike line, and therefore limiting the resolution of rift structures including fault planes. Additionally, observations of faulted-rotated blocks of upper crust that correspond with variable basement topography are similar to observations along a ~N-S (parallel to dip of rifting) MCS line to the northwest (McIntosh et al 2013), and a NE-SW, trench perpendicular MCS to the north of transect T2 (Lester et al 2013). The water-bottom multiples have been sufficiently attenuated allowing for sparse imaging of the Moho between 8-8.5 sec TWTT and 3-3.5 sec TWTT below top of basement.

In the area of the trench, post-rift strata are deformed into a series of highly reflective folds and imbricate thrusts that sole into a detachment near the top of the basement. Further east, a large topographic break in the prism separates the reflective folded strata from the less reflective upper slope of the prism (Figure 2-7d). Beneath the topographic break we observe sporadic, steeply dipping eastward reflections that may represent evidence of a large out-of-sequence thrust (OOST). This fault may dissect the entire prism and soles into a zone of high amplitude reflections. Motion history of this fault is difficult to determine as both the reflections signaling its presence are intermittent and marker reflectivity within the prism that would be used to identify this motion are deformed beyond our ability to image them.

The reflective characteristics within the prism are intriguing, showing a high amplitude double reflection that may be evidence for structural underplating related to the imbricate thrusting above, reflectivity within the subducting crust, or more likely a pocket of underthrust, post-rift sediment. This point is illustrated by observing the geometry of the frontal thrust in Figure 2-7. Just below its position, a topographic low in the faulted basement is in filled with post-rift sediment. As convergence continues, the sediment above the frontal thrust will be deformed and accreted at the next imbricate thrust in the series while the next thrust will likely break at a high structural level, potentially bypassing the sediment below ~ 6 sec. This pocket of sediment may continue to subduct with the basement and could produce a similar double reflection as observed beneath the prism.

To the east, the uplifting arc-ward flank of the accretionary prism deforms the forearc basin strata of the NLT (Figure 2-7e). Deformation of the NLT strata indicates uplift of the accretionary prism that will most likely result in the eastward backthrusting and formation of the Huatung Ridge compressional structure (Figure 2-1) similar to that documented by Hirtzel et al (2009). The deeper structure of the forearc backstop is obscured by residual multiple-energy, however we are able to constrain the crustal structure in the coincident tomographic model described below.

2-5-3: Line T1 Model Description, Observations, and Interpretation

The tomographic travel time inversion of T1 produced a velocity model that has for the first time defined some of the critical features across the Manila subduction system. The result (Figure 2-8a-b) shows the velocity model and OBS locations, a simplified tectonic interpretation and labels for the main tectonic elements with a 20-km-wide swath of seismicity overlain.

A swarm of seismicity extends from near the seafloor to depths approaching 40 km at model range 100 km (Figure 2-8c). Fault motion solutions do not exist for these events; however, they seem to occur in a narrow time window between September and October 2006. Both the timing and location with respect to the trench correlate well with the magnitude Mw=7.0 Pingtung earthquake in November of the same year and we speculate the two swarms may be related. Seismicity from Pingtung extends to depths of

~50 km with focal mechanisms from Wu et al (2009) suggesting largely normal faulting associated with bending of the lithosphere. It is likely that this seismicity in Figure 2-8c and a similar package in Figure 2-10c are also related to bending related stresses on the subducting SCS slab.

The green dashed line labeled M in Figure 2-8b shows the approximate position of the Eurasian plate Moho that is well constrained only in the model range ~50-110 km, but is consistent with previous estimates of transitional crust thickness (Nissen et al 1995; Qiu et al 2001; Wang et al 2006; Yan et al 2001). We estimate the position of the basal décollement from the coincident MCS profiles and the velocity model with a dashed white line labeled D. West of the accretionary prism the frontal thrust quickly cuts through the sedimentary section to the surface from the 5 km/sec contour which we infer to be near the top of crystalline crust. East of 180 km the subducting slab is not resolved with the OBS data. However, sparse earthquake hypocenters define a broad region of events beneath the prism that may be the result of subduction related seismicity in the upper mantle or within the slab near the plate interface. Furthermore, our interpretation of the plate boundary in the model space is consistent with deeper seismicity likely associated with the Benioff zone to a depth of 120 km (Figure 2-8c).

Notably, the accretionary prism here appears to be composed entirely of relatively low velocity (3.0-4.5 km/sec) sedimentary material. Aside from the sedimentary composition of the prism, the most striking result from this model is the abrupt velocity change (see 5 and 6 km /sec contours) near 210 km. The abrupt vertical velocity contours in our model suggest that the western edge of the forearc is steeply dipping.. Previous studies of the forearc crust backstop interpret this feature to dip trenchward (e.g. Suppe, 1981; Lewis and Hayes 1984, Chi et al 2003; Malavieille and Trullenque 2009) beneath a doubly-vergent accretionary prism. However, the asymmetric geometry of the prism at this latitude agrees well with analogue modeling of accretionary prism development and deformation against a steeply dipping backstop (Rossetti et al 2002; Byrne 1993). A similar steeply dipping forearc backstop has been observed along the southern end of the Ryukyu trench forearc region (Font et al 2001).

2-5-4: MCS Line 23

Line 23 shows crust of the northern SCS and overlying sedimentary sequence subducting into the Manila trench, a lower slope characterized by imbricate thrust sheets, and highly diffractive upper slope (Figure 2-9a-c). West of the trench a thick, 2 s TWTT, highly reflective, post rift sedimentary sequence is imaged. The post rift sediments cap an intermittent, weakly reflective package that we interpret to be similar to the syn-rift or pre-rift sedimentary strata that overlay 3 s TWTT thick crust (Figure 2-9b). The post rift sediments are separated from the pre-syn-rift sediments by a high amplitude reflection that we interpret to be the break up unconformity.

A similar topographically irregular basement reflection to that observed along line 25A to the south is also observed here. Multiple suppression techniques were particularly successful outboard of the trench and allow for the imaging of deep crustal structure. We observe a high amplitude reflection extending from CDP 0-13800 at ~9 s TWTT as the Moho reflection (Figure 2-9b). Shallower in the section a strong continuous reflection in the mid-crust at ~8 s TWTT between CDP 0-8700 is observed beneath the interpreted syn-rift sedimentary packages. This reflection deepens to the east and eventually approaches the Moho reflection at CDP 8700. Both the Moho reflection and lower crustal reflection become weak near the trench and are not imaged further east beneath the accretionary prism.

While the structures and bathymetry observed in the prism along Line 25A are somewhat homogeneous, the prism along line 23 is separated into two distinct units based on the reflectivity character. The lower slope domain extends from the Manila trench (CDP 10000) to a sharp change in bathymetry at the prism upper slope (CDP 21000) (Figure 2-9c). At the deformation front, the frontal thrust cuts the post-rift strata at a steep angle near CDP 10000, and likely soles into a detachment surface near the basement-sediment interface and possibly along the syn-rift-post-rift unconformity (Figure 2-9C).

Eastward, between CDP 18000-21000, near the lower-upper slope domain transition, several westward verging listric thrust faults are imaged that penetrate up to or near the seafloor and likely sole into the basal décollement. Between this zone of faulting and the thrust ramp (CDP 10000-18000), the post-rift sediments are relatively undeformed suggesting this package is moving as a cohesively over the basal detachment surface. While this disparity between the geometry of the frontal thrust and zone of deformation to the east may seem anomalous, this behavior may be controlled by active sedimentation in the trench derived from the continental margin and growing mountain belt to the north. Analogue modeling from Simpson (2010) shows that if sedimentation occurs in the trench, deformation tends to be concentrated behind the zone of sedimentation. Deformation is also sporadic within the zone of active sedimentation on widely spaced thrusts that develop relatively little displacement, similar to what we observe along the frontal thrust in Figure 2-9.

Any evidence of the basal detachment surface eastward of CDP 18000 is interrupted by residual multiple energy and poor signal to noise ratio, however, we believe it is likely that the detachment surface continues at the same structural level above the top of basement. The reflection image shows only the very shallow sedimentary features of the upper slope of the accretionary prism but little of the deeper prism structure. This may be due to several factors including poor signal penetration through a hard seafloor, or the presence of steeply dipping thrust faults and structures not imaged by our acquisition geometry. Another reason, based on the observation of extremely low seismic velocities (1.5-1.8 km/sec) in the upper 2 km of the prism in the coincident tomographic model suggests that the shallow sediment in the upper slope may be fluid saturated and therefore inhibits the ability of the acoustic energy to penetrate the prism.

Although we do not image thrust faults in the upper slope, the bathymetry and progressive steepening of thrusts we do image in the lower slope suggest fault planes may progressively steepen and rotate into orientations we cannot resolve in the MCS reflection data. We do not observe evidence of an OOST in the data, however we do observe several breaks in the topography between the lower and upper slope domains that may be the expressions of such faults reaching the surface.

Unfortunately, the MCS data do not constrain the structural limits of the forearc backstop due to steeply dipping, complex structures resulting from the uplift and backthrusting of prism and forearc basin toward the arc. Instead, we must rely on the boundary inferred by coincident tomographic modeling that places the limit of the forearc east of the arcward flank of the accretionary prism.

2-5-5: Line T2 Model Description, Observations, and Interpretation

The T2 tomographic model (Figure 2-10a-c) is presented in the same manner as T1. West of the accretionary prism (model distance 0-100 km) a thick package (3-4 km) of low velocity material (1.8-4.5 km/sec) overlies the top of basement, here indicated with seismic velocity of ≥ 5 km/sec. A green dashed line labeled M shows the approximate position of Eurasian plate Moho that is well constrained between 40-130 km model distance, and is again consistent with estimates of transitional crustal thickness (9-15 km) (Nissen et al 1995; Qiu et al 2001; Wang et al 2006; Yan et al 2001). As noted by others, some of the lower crust is high velocity (>7 km/sec) and may be associated with magmatic underplating during the Eocene rifting of the SCS (Pin et al 2001), pre-existing mafic lower crust (Nissen et al 1995), serpentinized upper mantle (Wang et al 2006), or post rift magmatism (Franke 2012).

We estimate the position of the basal décollement with the white dashed line labeled D using the coincident MCS reflection profile of line 23. This estimate quickly becomes uncertain due to the lack of resolution of both the OBS and MCS reflection data beneath the prism. Normally, the subducting slab is positioned ~80 km below the active volcanic arc, however, seismicity between 200-230 km and 20 km depth in Figure 2-10 suggest the position of the slab here to be between 30-40 km beneath the NLA. The subduction of thicker and more buoyant hyper-extended continental crust may also explain cessation of volcanism in the NLA at this latitude. Again, our interpretation is consistent with deeper seismicity associated with the Benioff zone to a depth of 120 km (Figure 2-10c).

For a typical subduction profile, the top of the subducting crust is expected to steadily deepen arcward beneath the prism similar to that observed along the top of the EUP (5 km/sec velocity contour) at model distance 70-150 km along T1 (Figure 2-8b). However, along T2, the top of the EUP initially deepens to the east at model distance 100 km, but then we observe high velocities at a shallower depth between 130-180 km model distance, 12-15 km depth, corresponding with the transition from the lower slope to upper slope domain of the accretionary prism. We interpret these high seismic velocities to be likely evidence of crustal material structurally underplated from the subducting thinned-continental crust and accreted to the prism. Addition of structurally underplated material may account for much of the dramatic increase in the volume of the prism observed when comparing T1 and T2.

Between 180-220 km, the resolved portion of the tomographic model shallows due to poor data quality. Despite this reduction, the model still illuminates important structures within the forearc and arc domains. The top of forearc crust is clearly resolved to a depth of ~10 km (model distance 220 km) where it abruptly steepens out of the well resolved model space. This observation may suggest a structurally blunt shape of the forearc backstop consistent with that observed at the forearc backstop along T1 to the south. Furthermore, seismicity in the bottom panel of Figure 2-10 supports the interpretation of a steeply dipping limit of the forearc backstop, with a concentrated band of events coincident with the apparent westward limit of the forearc crust in the velocity model.

The structure of the NLA over model distance 250-300 km is complicated by a sudden westward shift in the trend of the arc that can be observed in the bathymetry where T2 bisects it (Figure 2-1). It is unclear why this sudden step occurs, although it may from a late-stage change in the dip of the EUP plate possibly as a function of composition or age of subducting crust. East of the NLA, the crust of the Huatung Basin thins to 6-8 km indicative of normal oceanic crust in this area.

2-6: DISCUSSION

2-6-1: Velocity Structure of SCS Crust and Likely Location of COB

One of the debates in the northern SCS is the distribution of continental vs. transitional vs. oceanic crust and the location of the COB (Figure 2-1). Although this debate reflects processes related to rifting, the potential subduction of rifted continental material is likely to have profound consequences on the structural evolution of the accretionary prism and collision to the north. Specifically, the subduction of extended to hyper-extended continental crust with weaknesses such as faulting and mid-crustal shear zones in the upper and middle crust inherited from the rifting phase is expected to behave very differently than oceanic crust. It is possible that the weakened crust is subducted to 10-15 km depth but then underplated into the overriding accretionary prism as suggested by McIntosh et al (2013). Evidence of thinned continental crust in the northern SCS was discussed earlier with tomographic evidence from this study (Figure 2-8 and 2-10) at latitude 20.5° (T1) and 21.5° (T2) where the thickness of the subducting crust is 10-15 km. A detailed examination of crustal velocities (Figure 2-11) shows that the velocity models compare very well with the velocity structure of transitional crust of the southern Chinese margin (Nissen et al 1995; Yan et al 2001; Wang et al 2006), but are incompatible with the layer 2/layer 3 structure of typical ocean crust (White et al 1992) or thick ocean crust (Mutter and Mutter 1993).

Coincident MCS reflection data provide several additional pieces of evidence to support this interpretation: 1) Highly faulted upper crust capped by an intermittent weakly reflective syn-rift sedimentary package separated from the overlaying post-rift strata by a break-up unconformity (Figures 2-7 and 2-9) similar to that identified by McIntosh et al (2013). 2) A high amplitude Moho reflection observed along both lines 25A (Figure 2-7: CDP 61000-75000) and 23 (Figure 2-9: CDP 0-13700) at 3-4 sec two-way travel time below the top of crust that is consistent with the 10-14 km thicknesses constrained by the coincident tomographic models. We also observe a fairly continuous reflection in the mid-crust along line 23 (Figure 2-9: CDP 0-8700) beneath what appear to be fault blocks. We interpret this reflection to be a mid-crustal detachment between the upper and lower crust similar to structures observed in other hyper-extended continental margins such as Iberia (e.g. Sutra and Manatschal 2012). The strike orientation of the MCS line is not appropriate to image fault planes of crustal blocks, however evidence from nearby MCS profiles suggest that faults bounding these rotated blocks sole into this mid-crustal detachment (McIntosh et al 2013; Lester et al 2013).

With evidence of extended to hyper-extended continental crust extending as far south as 20.5° N, the question still remains, where is the location of the COB and geophysical evidence of oceanic crust in the SCS? Line 15 images the transition from rifted continental crust to ocean crust in the SCS (Figure 2-6), the most striking being a strong Moho reflection at 2 sec TWTT, or ~6 km below top of basement, suggesting a typical thickness for ocean crust (White et al 1992). This reflection begins at CDP 1900 and can be traced southeast across much of the profile and well beneath the accretionary prism.

The origin of the large basement structure imaged on the west end of this line remains unclear. Several geophysical studies have observed similar features throughout the SCS, interpreting them to be a zone of increased volcanism near the COB (Zhu et al 2012; Hu et al 2009; Wang et al 2006). With its likely proximity to the COB, and no reliable velocity constraints or direct sampling that would clarify the origin of this structure, we speculate that the large basement structure may be an exposed peridotite ridge similar to the interpretation from Franke et al (2011) north of Palawan, and those observed within the transition zones of other hyper-extended continental margins (Shillington et al 2006; Sutra and Manatschal 2012; Whitmarsh et al 2001; Boillot and Froitzheim 2001).

Although we do not image a direct transition from hyper-extended continental crust to purely oceanic crust, our result favors a position of the COB similar to Briais et al (1993) (dashed yellow line in Figure 2-1). From the bathymetry, the basement high is observed to be part of a series of linear features trending NE-SW while Figure 6 shows the crust to the southeast of this structure to be likely oceanic in origin. If we assume this structure represents the COB, separating extended to hyper-extended continental crust to the northwest from oceanic crust to the southeast and project its trend northeast, we see that it intersects the Manila trench just to the south of line T1 (Figure 2-1). This suggests the COB has only recently subducted at T1 and in turn that the extended to hyper-extended continental crust has only recently started to subduct there. The recent addition of hyper-extended continental crust into the subduction system may explain the lack of basement underplating and purely sedimentary nature of the prism along T1.

If T1 marks the approximate seaward limit of hyper-extended continental crust in the SCS, as much as ~100 km of this material has potentially subducted at the position of transect T2. Continuous subduction of hyper-extended continental crust may result in the structural underplating of mid-upper crustal blocks into the prism similar to the collision model of McIntosh et al (2013). We submit that the high velocities (5.0-6.5 km/sec) observed in the accretionary prism in T2 (Figure 2-10) are indicative of the first phases of structural underplating of mid-upper crustal blocks from the subducting EUP plate in agreement with this model.

2-6-2: Accretionary Prism Structure

The Manila trench accretionary prism is the dominant tectonic feature offshore southern Taiwan due to its dramatic structural variability and its tectonic role in the evolving arc-continent collision to the north. Between Luzon and Taiwan, the prism increases in width from ~80 km at 20.5° N to over 135 km just offshore Taiwan (Figure 2-1). This increase in width and elevation is accompanied by a significant change in morphology and the development of two distinct structural domains; the lower slope, consisting of west-verging folded strata and thrusts, and the extremely deformed and non-reflective upper slope domain (Reed et al 1992) (see Figure 2-9).

Although much of the structural variation reflects the rapid vertical growth of the accretionary prism due to the addition and incorporation of thick passive margin sequences and orogenic sediments from the north and the presence of steeply dipping backstop, the fact that a much larger volume of accretionary material now rests on the subducting, hyper-extended continental crust may have profound effect on the style of accretion. Specifically, rather than passively subducting the thinned continental crust, the huge mass of the sedimentary prism sitting above the subducting plate may promote underplating of rifted blocks of upper crust material along detachment surfaces or shear zones inherited from the previous rifting phase of the continental margin. Evidence for one of these surfaces is shown in Figure 2-9. Observations of similar lower crustal shear zones facilitating the tectonic emplacement of subducting material has been observed beneath Vancouver Island from 15-30 km depth (Calvert et al 2003). While the evolution of these lower crustal shear zones may differ, the manner in which they are utilized to tectonically emplace material into the overlying plate may be analogous.

If these observations of a mid-crustal shear zone are true, what becomes of the weakened, buoyant upper crust during subduction? The seismic velocities of the accretionary prism along T2 reveal a possible mechanism and explanation. The velocity model shows an increase in seismic velocities at a shallow level of 10-15 km within the prism near the transition from the lower-slope to upper-slope domain (Figure 2-10: model distance 130-180 km). While it is expected that seismic velocities in the prism would increase somewhat due to compaction, dewatering processes, cementation, continued sedimentary accretion and even low-grade metamorphism, we observe velocities greater than 6.0 km/sec at shallow structural level, which are far greater than any sedimentary velocities observed to the south along T1 or in other accretionary prisms (Westbrook et al 1988; Fowler et al 1998; Christeson et al 1999).

It is possible that the high velocities observed represent accreted and/or underplated ophiolitic material or oceanic crust similar to observations in Sumatra by Singh et al 2008. However, given the likely position of the COB and the nature of the hyper-extended continental margin currently subducting north of T1, it is highly unlikely that such a large volume of oceanic crust would accrete rather than continue to subduct. Additionally, the dimensions of the high velocity anomaly (~5 km vertical X 10 km horizontal) would be anomalously large for a structural high such as a seamount in the SCS.

Alternatively, we interpret the high velocity material to be evidence of the initiation of structural underplating of blocks of hyper-extended upper crust into the accretionary prism. Earlier, we discussed what might be expected from a cross section through a normal subduction profile. We observe an initial eastward steepening of the top of subducting basement at model distance 110 km, followed by an abrupt shoaling of high velocities between 130-180 km model distance (Figure 2-10). Lester et al (2013) observes a similar high velocity anomaly (>6.0 km/sec) in same position and depth within the prism on a NNE-SSW line that crosses T2 (Figure 2-1). Tomographic modeling along T1 to the south shows a ~15 km thick, highly developed sedimentary prism with no evidence of high velocity material. Additional tomographic modeling from McIntosh et al (2013) to the north of T2 (Figure 2-1) shows the uplifted Hengchun peninsula to be cored by a large volume high velocity (>6.0 km/sec) material. This south to north progression and development of this high velocity anomaly suggests this is an evolutionary process involving structural underplating of rifted continental basement. Structural underplating of this nature may contribute to the significant volume increase observed in the prism and provide an explanation for high-pressure low-temperature lithologies of apparent continental in origin such as the Tananao Complex exposed in the southern Central Range (Simoes et al 2007; Beyssac et al 2008; Malavieille 2010).

We can only speculate the significance of imbricate thrusting given the lack deeper resolution the MCS images. The thrusts along transect T2 seem to be blind with minimal offset that may or may not interact with the basement. Although the role of the imbricate thrusts remains enigmatic at this stage of tectonic underplating due to lack of MCS data resolution, it is possible that thrust faulting becomes more important later in the evolution of this process.

2-6-3: Forearc Backstop Geometry and Implications

Previous shallow geophysical studies of the NLA forearc have assumed a seaward-dipping backstop without sufficient crustal scale data to support this claim. Although the presence and potential role of the forearc in the evolving arc-continent collision have been modeled and discussed in terms of deformation in the forarc basin (Lundberg et al., 1997; Hirtzel et al 2009), and even detachment and subduction of the forearc as modeled by Chemenda et al (1997) and Malavieille et al (2002), its role prior to the onset of collision may be of equivalent importance. Our models provide constraints that will modify the previous ideas concerning the architecture and orientation of the forarc block prior to collision. Specifically, rather than a gentle trench dipping wedge as assumed by most investigators, we observe evidence of a steeply dipping forearc backstop.

Although MCS reflection data acquired along T1 and T2 in this study were insufficient to image forearc basement at depth due to signal attenuation and multiple contamination, coincident tomographic models provide detailed insight of the of the deeper velocity structure of the forearc crust. We interpret the steeply dipping 5 km/sec velocity contour extending to a depth of 15 km in T1 (Figure 2-8) and an abrupt steepening of the 5 km/sec velocity contour along T2 as evidence for the near vertical nature of the forearc backstop (Figure 2-10). This boundary is not defined below 10 km along T2 except for a concentration of seismicity, which suggests a steep boundary at depth. These observations are consistent with tomographic modeling of an E-W onshore offshore wide-angle transect from McIntosh et al (2013) (Figure 2-1) that shows the trench-ward limit of the forearc block bound to the west by a similar near vertical concentration of seismicity. Similarly, a tomographic model of an E-W onshore offshore transect by Cheng, (2009) using P-and S-wave travel times from local earthquakes shows the trench-ward limit of the forearc block to be steeply dipping in the vicinity of Hengchun Peninsula.

Implications of such a steeply dipping backstop are significant as this parameter defines the flow trajectories of accreted material as well as the states of stress in the hinterland and foreland of the deforming prism. A number of authors have proposed that the structure of the Manila accretionary prism near Taiwan is analogous of a double-wedge, consisting of a pro-wedge that verges and deforms to the west and a retro-wedge that verges and deforms to the east over a trench dipping forearc backstop (Suppe, 1981; Davies et al 1983). The velocity model from transect T2 and its coincident MCS reflection data (Figure 2-9 and 2-10) seem to agree with this interpretation. However, farther south along transect T1, the prism structure becomes highly asymmetric and coincident MCS reflection data (Figure 2-7) show dominantly westward verging structures with little evidence of retro-wedge behavior. Our observations of a steep forearc backstop and a dominantly west-verging prism agree with experimental results from Rossetti et al., (2002) that measure the effects of convergence rate and backstop dip angle on the evolution of deforming wedges. Their results indicate that a decrease of the convergence velocity and/or an increase of the backstop dip angle can effect a change from prevalent hinterland–to foreland-vergent deformation, similar to the architecture we observe in the MCS along transect T1. As stated previously, further north, the accretionary prism seems to conform to the double-wedge geometry. This may be due to increased uplift with the involvement of thinned continental crust, a volumetric increase of the prism resulting from the accretion of terrigenous sediments she from the continental margin and Taiwan orogen to the north, or a change from a steep backstop configuration to a lower angle configuration promoting backthrusting in the hinterland.

Additionally, this result may have alternative significance regarding the flow trajectory of accreted/underplated materials in the prism. That is, steeply-dipping backstop geometries promote extreme particle motion through the prism, allowing structurally underplated crustal material to be accreted and buried, exposing it to hi-pressure-low-temperature metamorphic conditions, before quickly returning it to the surface similar to the analogue and thermo-mechanical modeling of Fuller et al (2006) and Malavieille (2010). Moreover, if the steeply dipping backstop is prevalent further north, it may be a key component in the process controlling the trajectory and exhumation of high velocity material beneath the Hengchun Peninsula identified by McIntosh et al 2013.

2.7 CONCLUSIONS

MCS reflection imaging of the Moho along Line 15 (19° N), indicate the subducting crust to be ~6 km thick, typical oceanic crust. A linear, NE-SW trending basement high, likely associated with the COB, can be projected NE into the Manila trench to intersect transect T1, suggesting that until recently oceanic crust was subducting there.

Our model across T1 (~20.5° N), along with coincident MCS reflection profile 25A, indicates that 10-12 km thick, hyper-extended continental crust has recently begun to subduct along the Manila trench at this location. Low seismic velocities (2.5-4.0 km/sec) are diagnostic of a primarily sedimentary composition of the prism and provide further evidence that until recently oceanic subduction may have been occurring here.

Our model across T2 (~21.5° N), along with coincident MCS profile 23, suggest as much as ~100 km of 10-15 km thick, hyper-extended continental crust have subducted at this location. A high amplitude mid-crustal reflection is observed beneath faulted basement blocks outboard of the trench that we interpret to be a relic detachment surface from previous rifting. Unusually shallow high velocities (5.0-6.5 km/sec) in the prism in our model are evidence for initial phases of structural underplating of EUP basement to the base of the prism via inherited weaknesses from the rifting of the Chinese margin.

Our models across the NLA forearc, along with seismicity data, indicates that the forearc backstop may be steeply dipping, and near vertical contrary to the seaward dipping backstop geometries previously assumed in other studies.

Our set of transects support a model of collision where prior to true arc-continent collision blocks of hyper-extended continental crust of the rifted Chinese margin are subducted and underplated into the accretionary prism along pre-existing detachment surfaces. Prior to collisional uplift, continued convergence and buoyancy forces are likely the main components in the exhumation, although erosion may have an underappreciated role in expediting and focusing exhumation after the prism is uplifted above sea level.

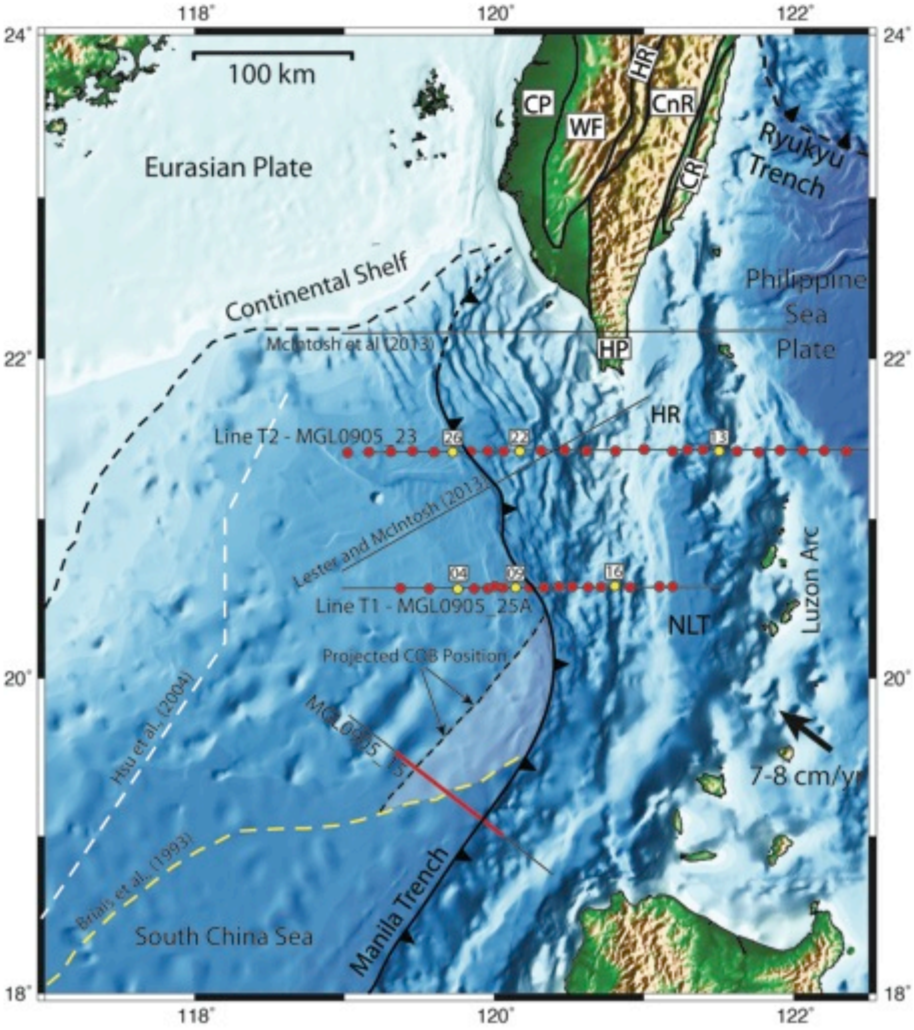

Figure 2-1. Regional bathymetry and elevation of Taiwan and major tectonic features. Major morphotectonic units of Taiwan are shown: CP - Coastal Plain; WF – Western Foothills; HR – Hsueshan Range; CnR – Central Range; CR – Coastal Range. MCS reflection data from this study (black lines) were acquired along MGL0905_15, MGL0905_25A, and MGL0905_23. Wide-angle OBS data (red-yellow circles) were acquired along transects T1 and T2. White and yellow dashed lines show approximate location of interpreted COB from Hsu et al., (2004) and Briais et al., (1993). Thin black lines denote position of other MCS and wide-angle transects from Lester and McIntosh (2013) and McIntosh et al (2013) referred to in this paper. White transparent zone shows our updated interpretation of oceanic crust and COB (black dashed line). NLT = North Luzon Trough; HR = Huatung Ridge; HP = Hengchun Peninsula.

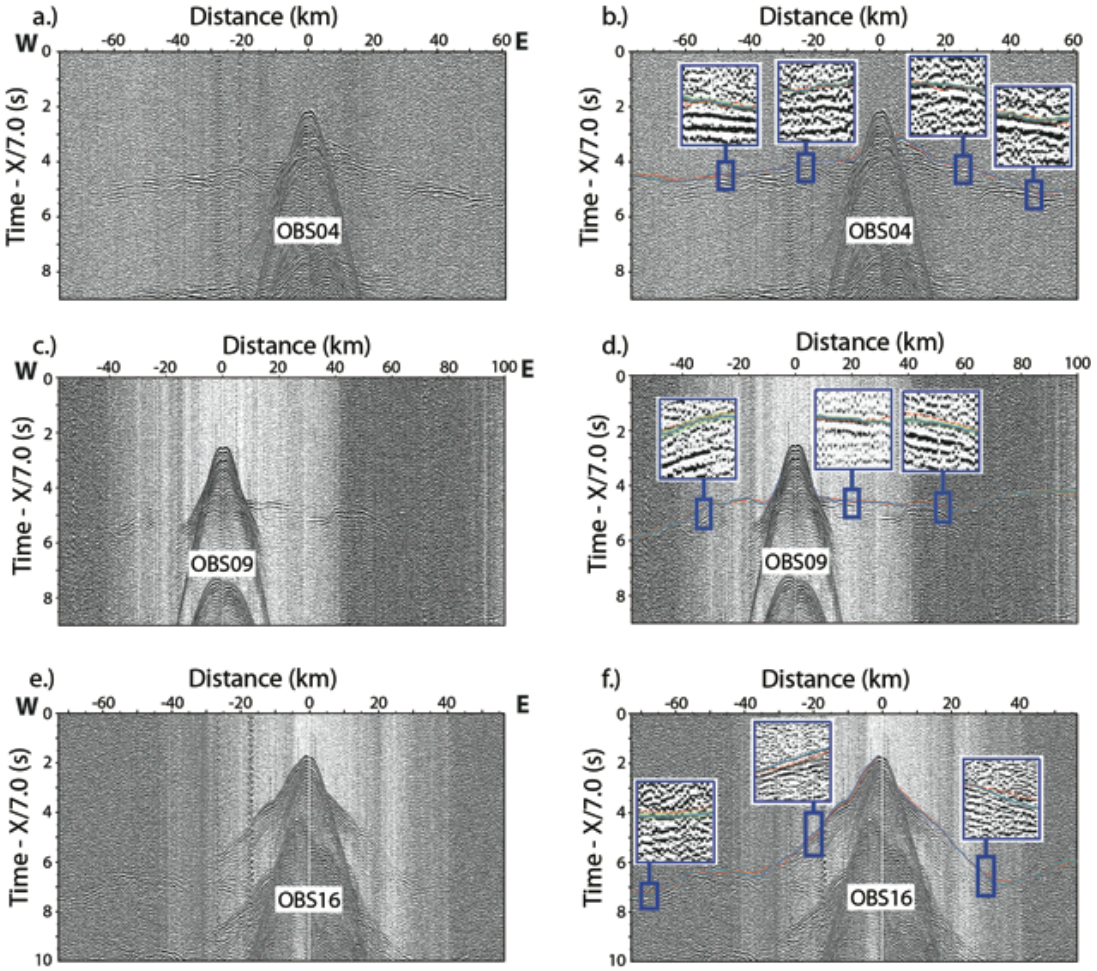

Figure 2-2. Example OBS records from the western (OBS04), central (OBS09), and eastern (OBS16) parts of transect T1 (MGL0905_25A). OBS locations are marked in Figure 1. Left and right panels show data with minimal processing (bandpass filter, spectral balancing) which was sufficient to resolve first arrival refractions to offsets greater than 40 km. Left panels a., c., and e. show uninterpreted records, while the right panels b., d., and f. show picked first arrivals (solid blue line), pick uncertainties (green window), and calculated first arrivals (red dashed lines).

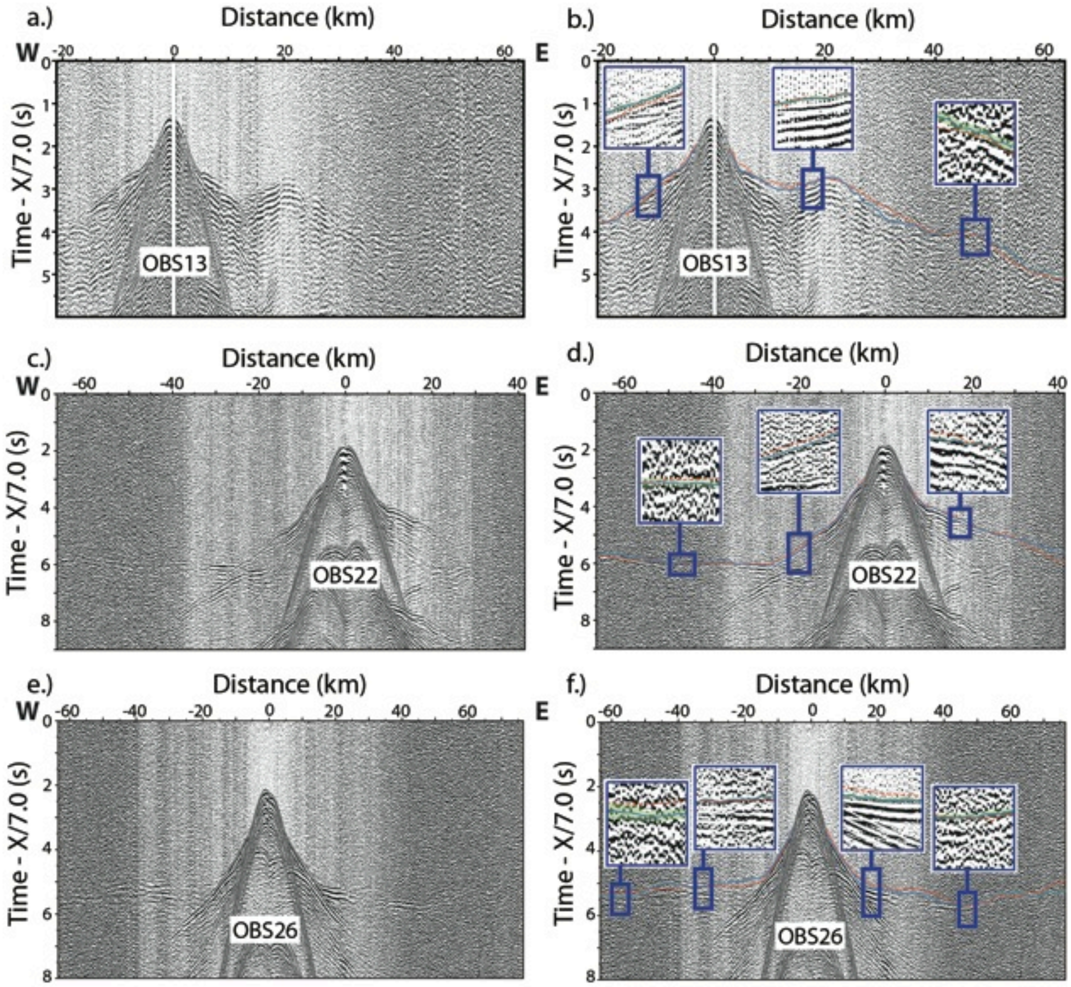

Figure 2-3. Example OBS records from the eastern (OBS13), central (OBS22), and western parts of transect T2 (MGL0905_23). OBS locations are marked in Figure 1. Left and right panels are with minimal processing (bandpass filter, spectral balancing) which was sufficient to resolve first arrival refractions to offsets greater than 40 km. Left panels a., c., and e. show un-picked records, while the right panels b., d., and f. show picked first arrivals (solid blue line), pick uncertainties (green window), and calculated first arrivals (red dashed lines).

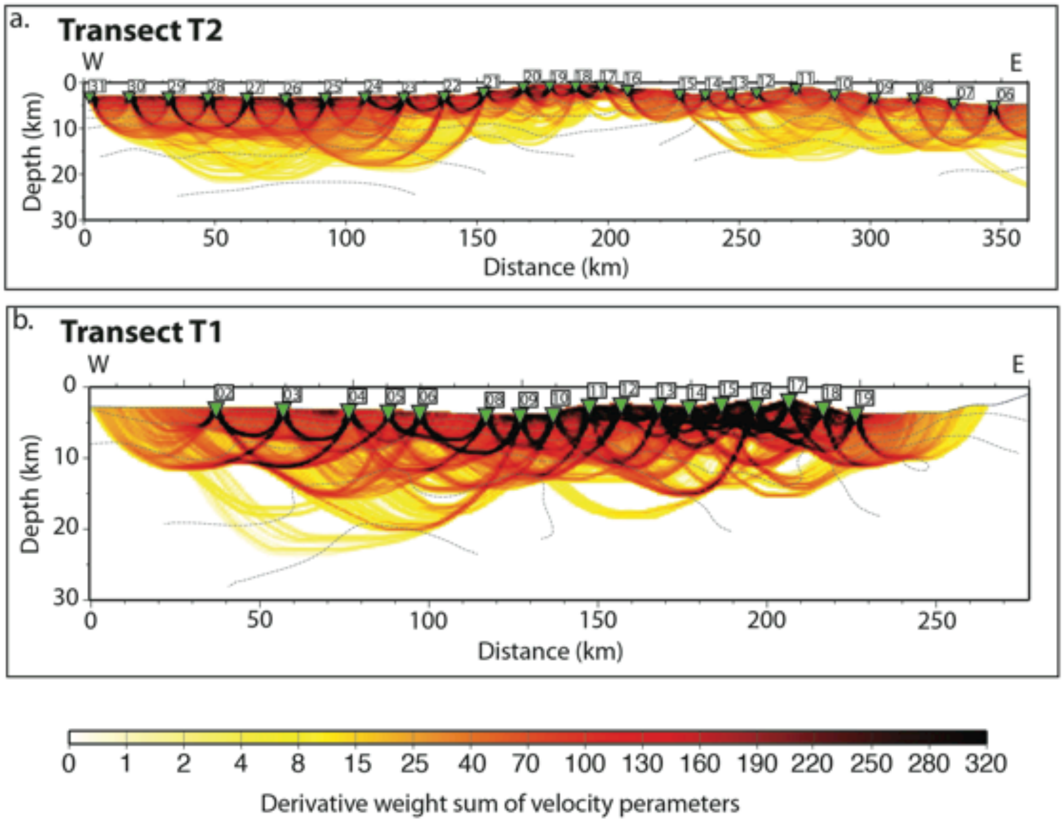

Figure 2-4. Derivative weight sum (DWS) of transect T1 (lower) and T2 (upper) show ray coverage throughout the model spaces. Ray coverage is very good in the shallow crust between OBS locations but shows significant variation at depth due to variable data quality.

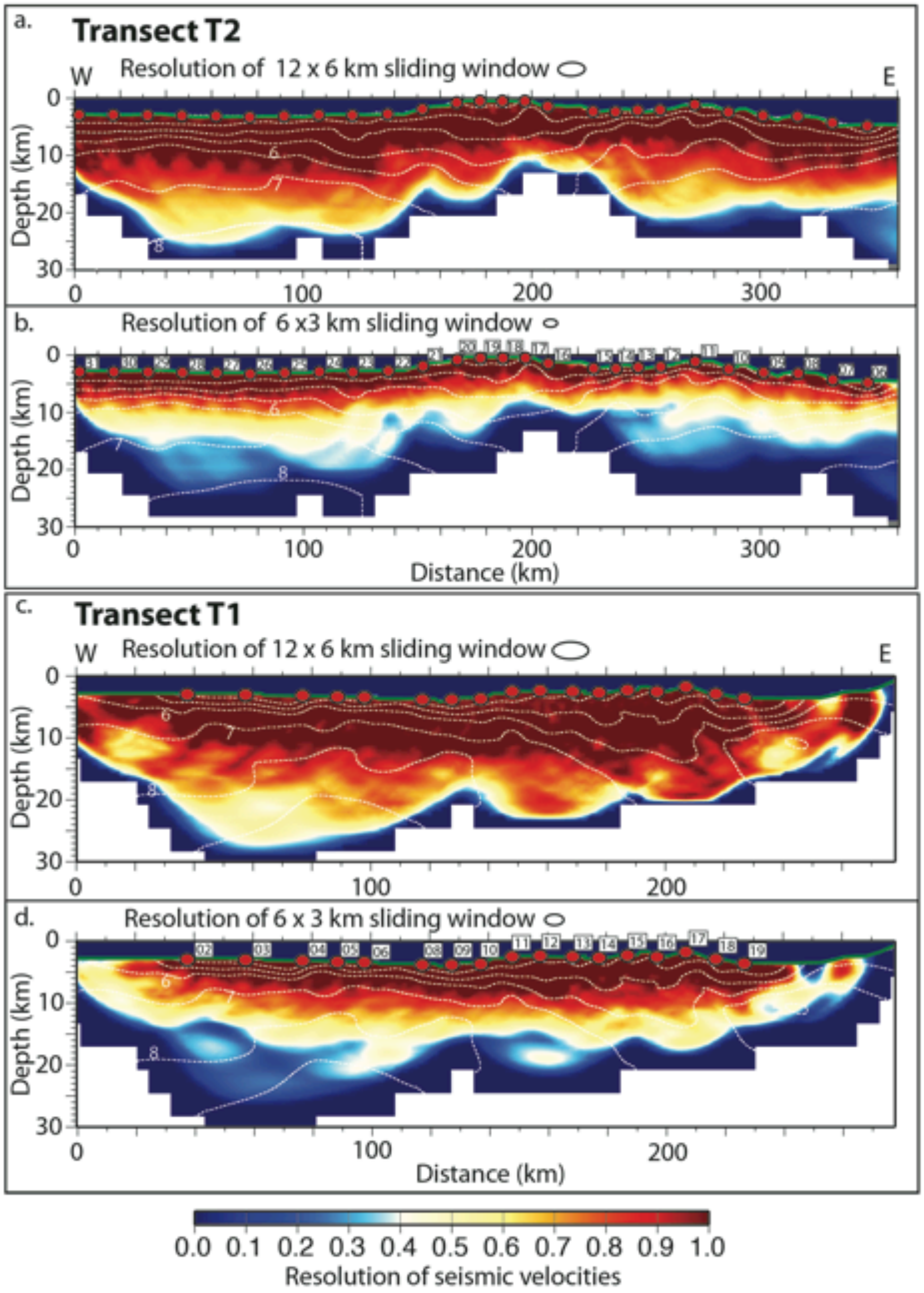

Figure 2-5. Resolution matrix for first-arrival tomography models T1 (bottom) and T2 (top). Regions with resolution values of >0.5 are considered well-resolved. This test shows that features in the crust are well resolved. Outside OBS locations, resolution suffers, although large-wavelength features are still resolved.

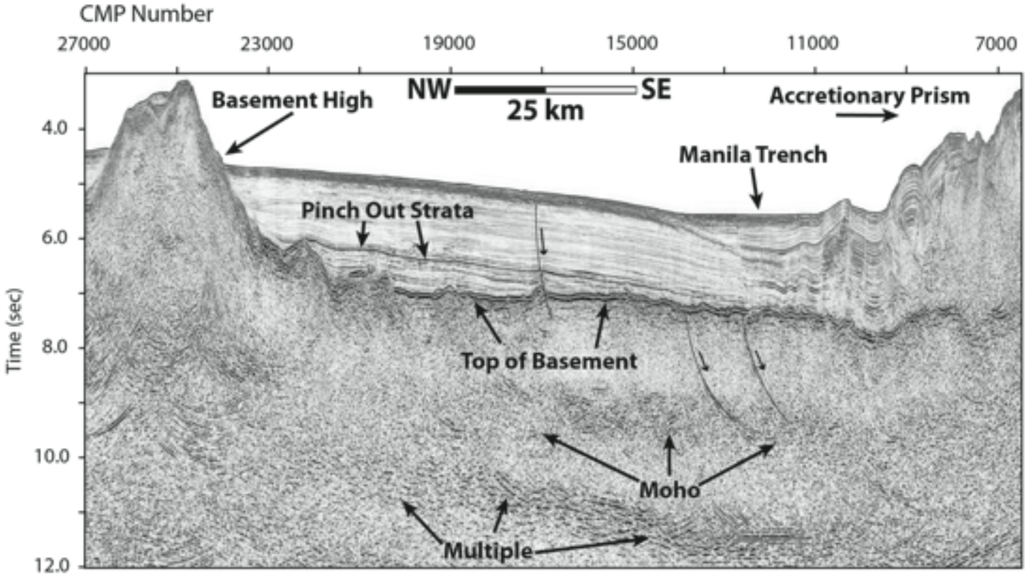

Figure 2-6. Pre-stack time migrated data from MGL0905_15 image sediment and crustal structures along the incoming, oceanic SCS crust. Bending faults are highlighted along with main tectonic structures.

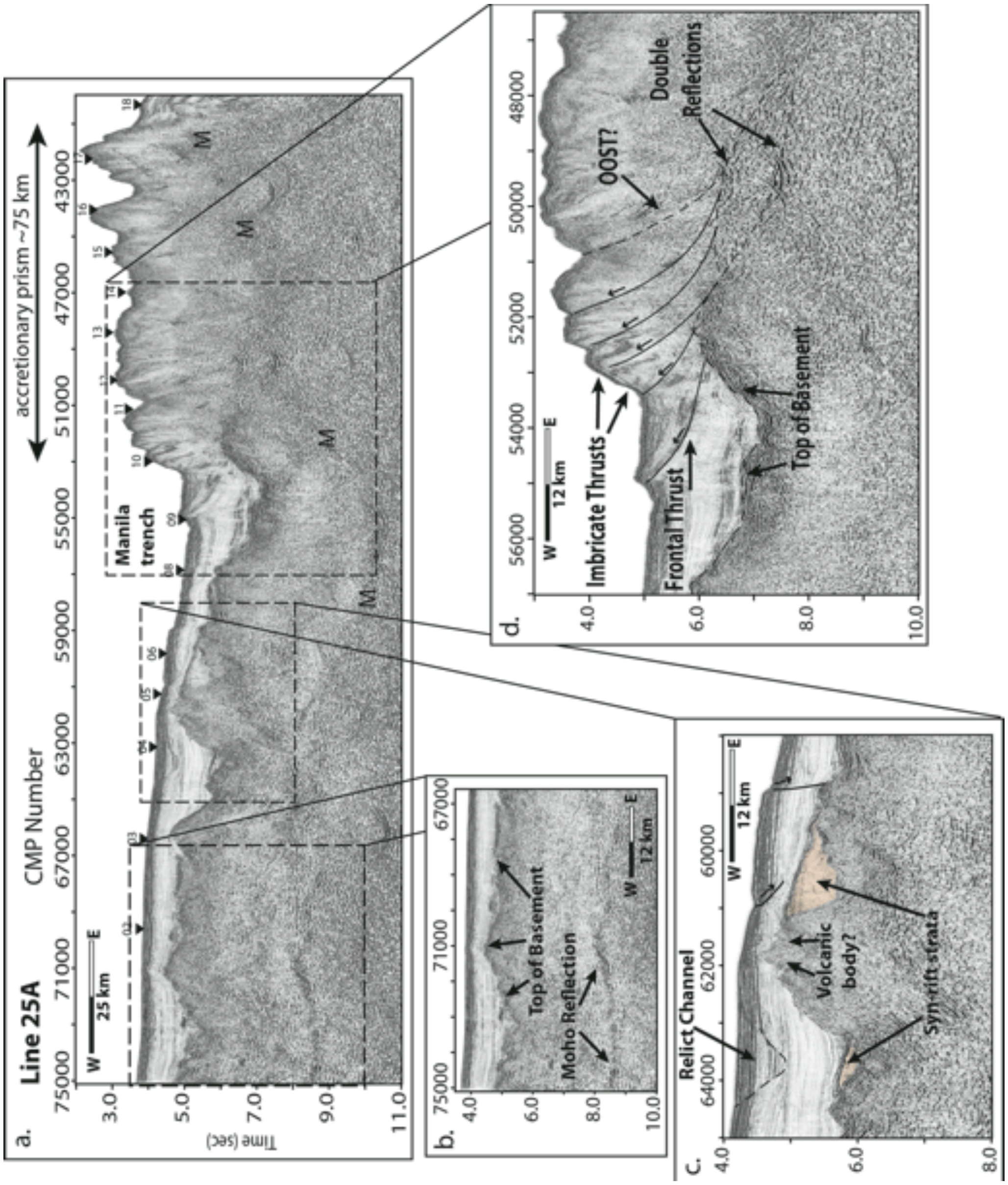
a.
Line 25A
CMP Number
accretionary prism ~75 km
Manila trench
Time (sec)
W 25 km E
M
b.
Top of Basement
Moho Reflection
W 12 km E
c.
Relict Channel
Volcanic body?
Syn-rift strata
W 12 km E
d.
OOST?
Double Reflections
Imbricate Thrusts
Frontal Thrust
Top of Basement
W 12 km E

Figure 2-7

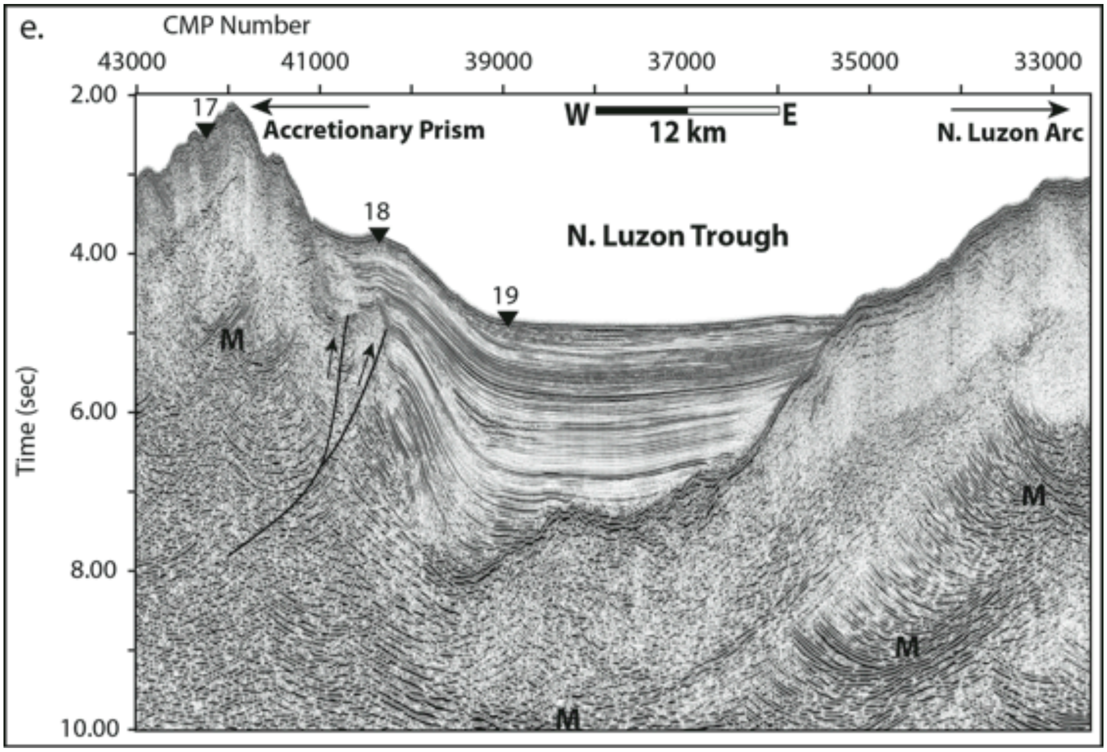

Figure 2-7. Pre-stack time migrated data from MGL0905_25A (SCS crust and accretionary prism: a-d; forearc basin: e). Panels b-d show the incoming hyper-extended continental crust of the SCS, intermittent Moho reflection at ~8.5 sec TWTT, syn-rift and post-rift sedimentary structures, and structures within the rapidly growing accretionary prism. Panel e. shows early-stage thrusting and deformation structures within the N. Luzon Trough forearc basin. OBS positions are marked by black triangles and labeled 2-19; M = water bottom multiple reflection.

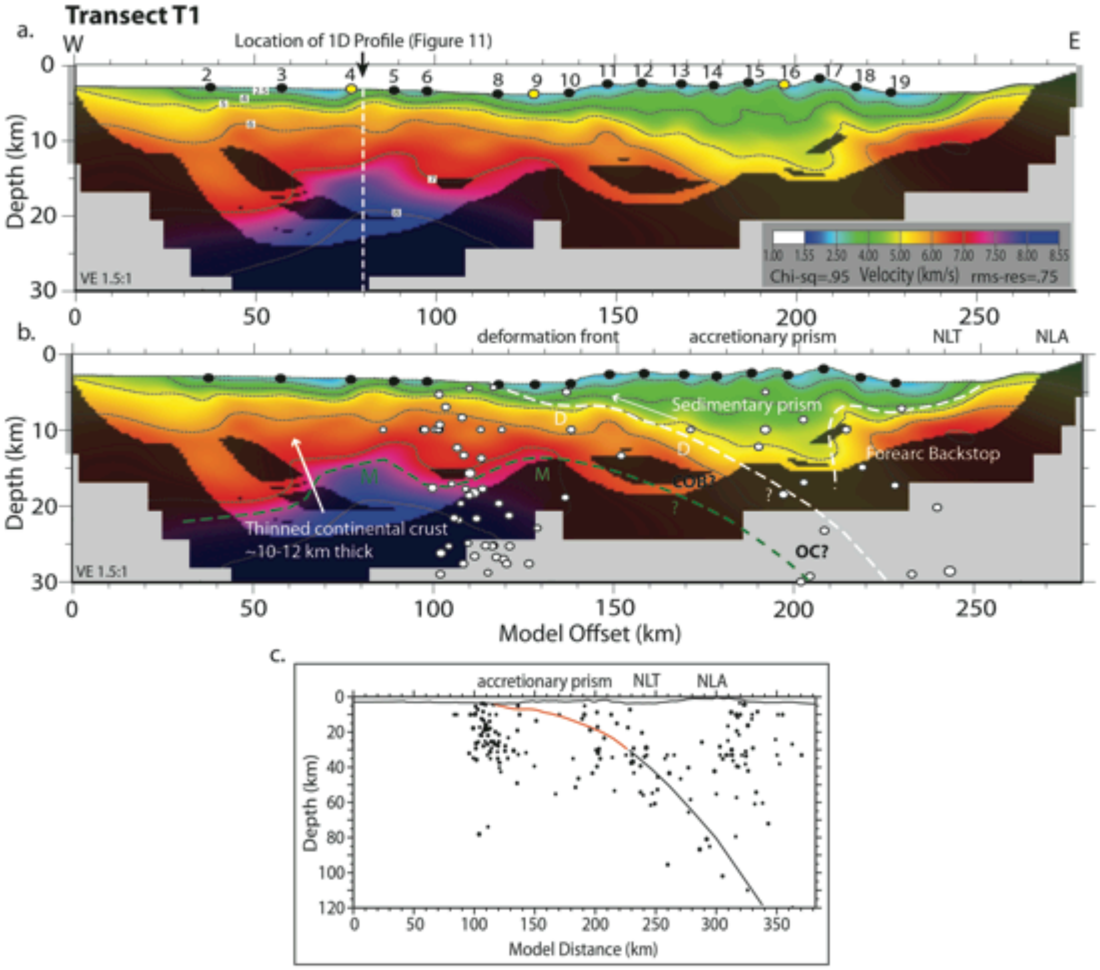

Figure 2-8. Tomographic model of Line T1 transect with seismicity across the Manila subduction zone. a.) Tomographic velocity model and instrument locations. Instruments highlighted in yellow are those shown in Figure 2. The curving edges of the colored model show the limits of the rays traced during the inversion. b.) First-order interpretation of the model, using additional constraints from MCS reflection data, and surface morphology including seismicity from the IRIS database (20 km swath width). The basal detachment between the accretionary prism and subducting thinned-continental crust is labeled D, and the base of the crust is labeled M. Vertical dashed white line denotes position of 1-D velocity profile shown in Figure 11. NLA = North Luzon arc; NLT = North Luzon Trough. c.) Seismicity from the IRIS database along the tomographic model showing consistency between picked plate boundary fault (red corresponds to dash in B) and the deeper seismicity of the Benioff zone.

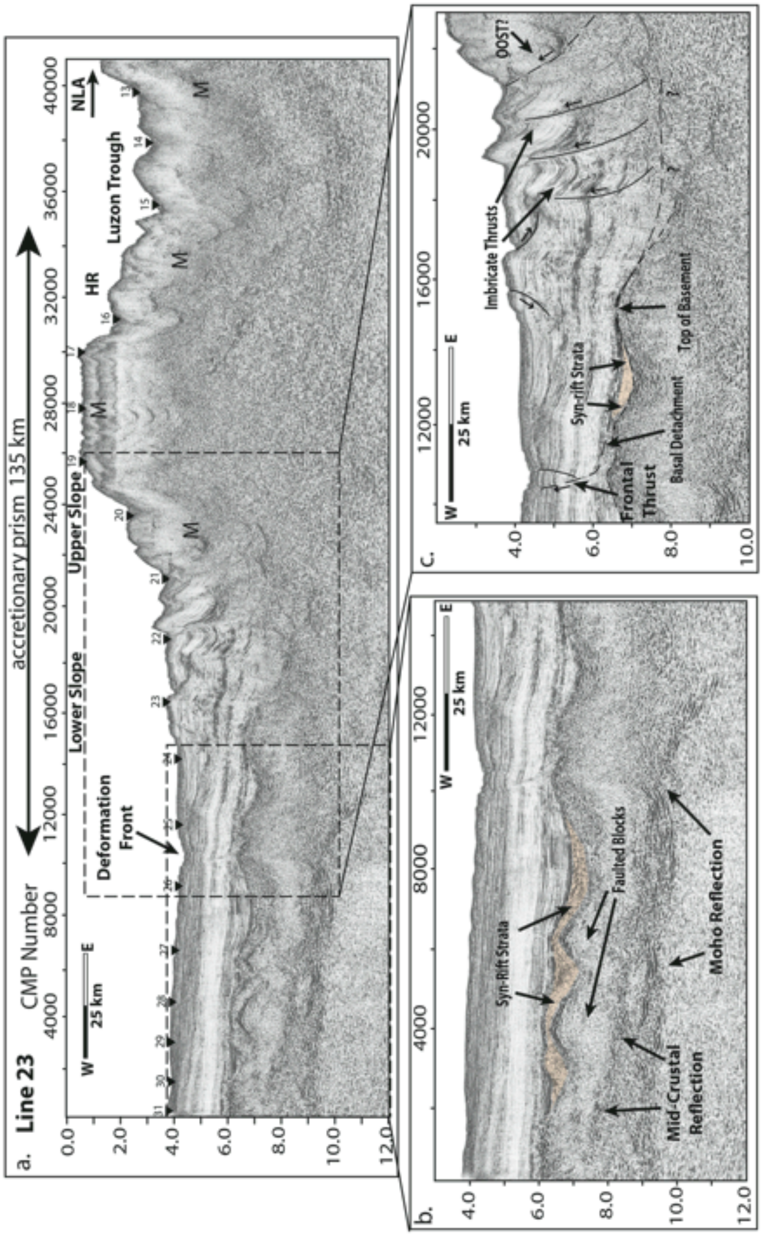

Figure 2-9. Pre-stack time migrated data from MGL0905_23 from the incoming hyper-extended continental crust across the Hengchun peninsula into the deforming N. Luzon trough. OBS positions are marked with triangles and labeled. Multiple reflections re marked with M. Boxes in the upper panel mark the portions of MGL0905_23 included in the lower panels, including: a.) the incoming hyper-extended continental crust, Moho reflection at ~9.0 sec TWTT, syn-rift and post-rift strata, and mid-crustal detachment, and b.) lower slope structures of the accretionary prism.

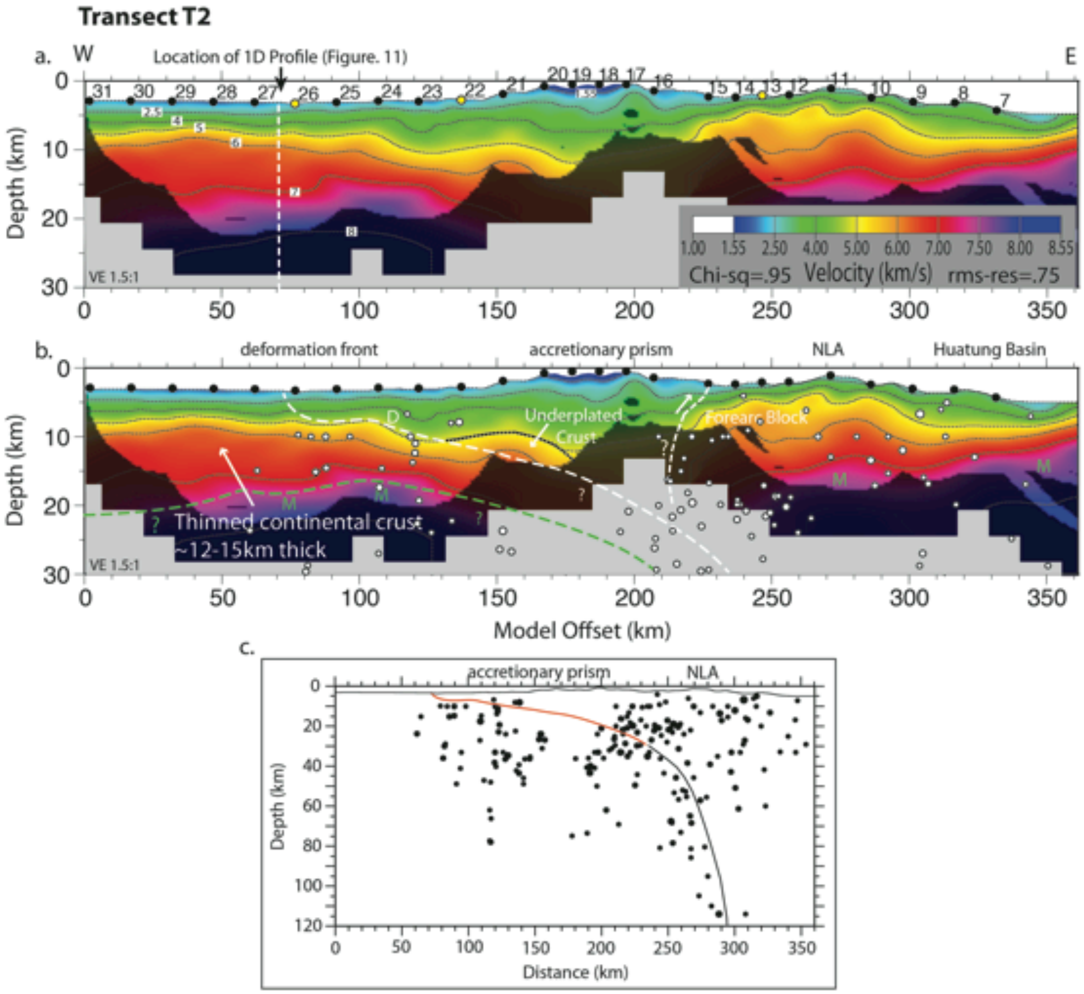

Figure 2-10. First-arrival tomography model of Line T2 transect. This figure is organized in panels identical to Figure 8. Instruments highlighted in yellow are those shown in Figure 3. NLA = North Luzon arc.

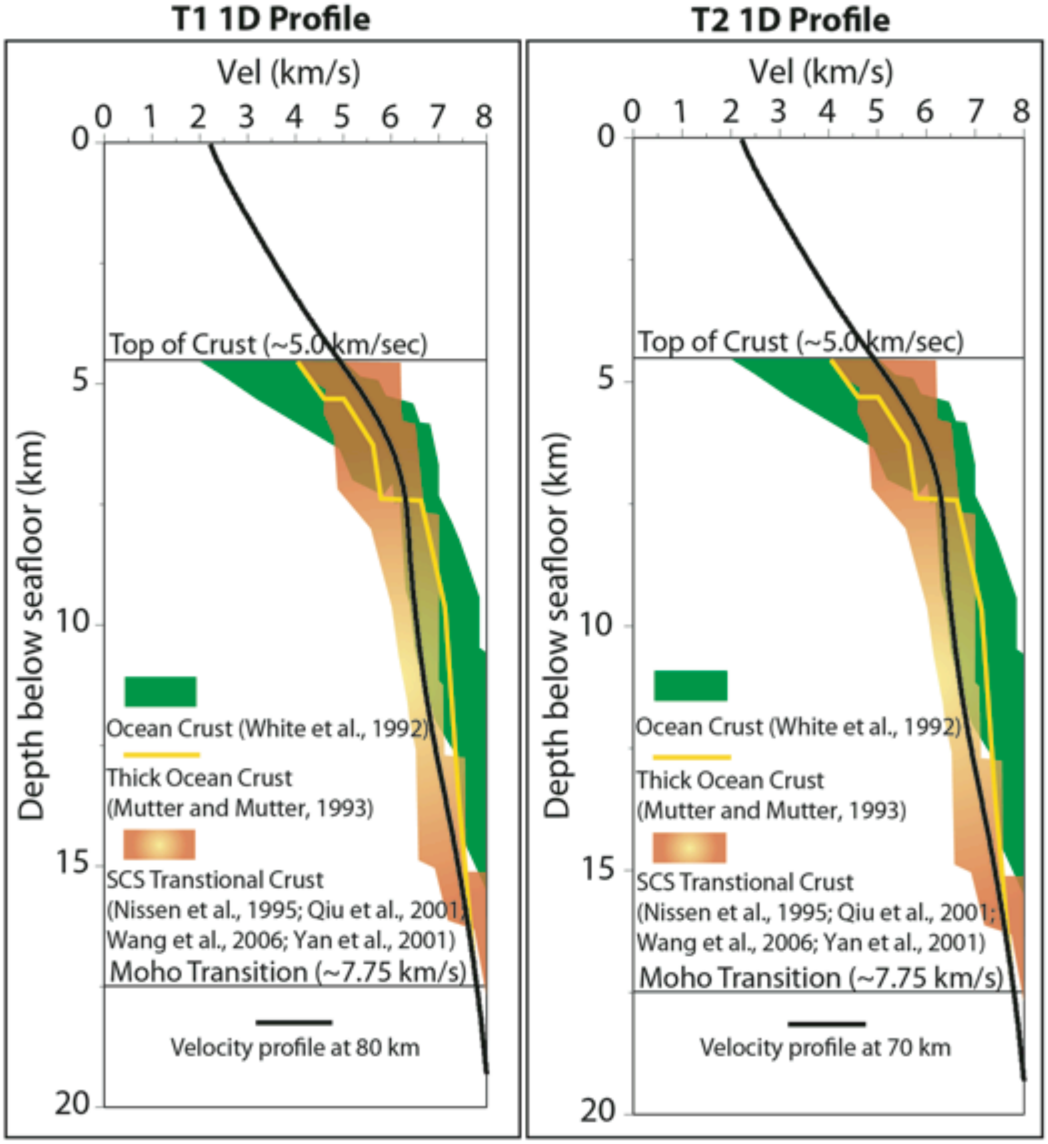

Figure 2-11. 1D velocity profiles show the structure of the SCS crust along transect T1 (a: model distance 80 km) and T2 (b: model distance 70 km) are consistent with velocity structure of SCS transitional crust of (Nissen et al., 1995; Qiu et al., 2001; Wang et al., 2006; Yan et al., 2001) that contains hyper-extended continental crust. The velocity structure is also incompatible with the faster, two-layer velocity structure of typical ocean crust (White et al., 1992) and thick ocean crust (Mutter and Mutter, 1993).

CHAPTER 3: NEW GEOPHYSICAL CONSTRAINTS ON THE STRUCTURE AND POTENTIAL EVOLUTION OF THE GAGUA RIDGE AND HUATUNG BASIN

3-1: INTRODUCTION

Subduction initiation is a fundamental phase of the plate tectonic cycle, yet the mechanisms that might trigger it remain unclear. Based on our current understanding of driving and resistive forces and of lithospheric strength, theoretical studies (Cloetingh et al., 1989; McKenzie, 1977; Mueller and Phillips, 1991; Stern and Bloomer, 1992; Toth and Gurnis, 1998) conclude that it is very difficult, but not impossible to initiate a new subduction zone in a passive margin or transform setting. In addition, there is little evidence of subduction initiation in the geological record, because the leading edge of the downgoing plate is immediately lost and subsequent deformation and volcanism often overprint the structure of the overriding plate. It is therefore important to identify examples of subduction initiation in an early stage, such as the Macquarie Ridge Complex and Puysegur trench at the Australian-Pacific plate boundary (Collot et al., 1995; Massell et al., 1999). The Gagua Ridge and associated trough on the Philippine Sea plate southeast of Taiwan may represent an additional example of early subduction, but in this case failed to fully develop as a convergent plate boundary.

The Gagua Ridge (GR) is a continuous bathymetric high that extends north over 300 km from the island of Luzon to intersect the Ryukyu subduction zone east of Taiwan. The N-S ridge separates the West Philippine Basin (WPB) to the east from the Huatung Basin (HB) to the west. Early interpretations of GR include a trench break of an inactive subduction zone (Karig and Wageman, 1975), the remnants of an extinct spreading center (Bowin et al., 1978), and an uplifted sliver of oceanic crust (Morzowski et al., 1982).

Hilde and Lee (1984) interpreted GR as an intra-oceanic fracture zone. Deschamps et al., (1998) expanded on this idea relating the structure to an intra-oceanic fracture zone uplifted during a compressional episode during a plate reorganization in the mid-Eocene. More recently, Deschamps et al. (2000) conclude that GR may have acted as an important transpressional plate boundary between the Eocene Philippine Sea Plate (PSP) and Cretaceous HB ocean crust. A similar hypothesis is suggested by Sibuet et al. (2002), however, in their scenario GR acted as a plate boundary between the independently formed Eocene PSP and the 'old' Taiwan Sea Plate.

Despite extensive analysis of the various geophysical studies conducted in this area, the origin and tectonic significance of GR has remained controversial. This is in part due to our lack of understanding of the complex evolution and interaction of the Philippine Sea Plate (PSP) and South China margin in Mesozoic and Cenozoic times. Additionally, deeply penetrating geophysical data that may provide crustal scale structural information of this feature have not been available until now.

In this paper, we describe results of four marine wide-angle ocean-bottom seismometer (OBS) transects and their coincident multichannel seismic (MCS) reflection profiles that cross the GR. The resultant seismic images indicate crustal thickening on the order of ~12-18 km beneath the GR, between 20.5° N and 23° N. The asymmetric velocity structure of GR suggests that the oceanic crust of the West Philippine Basin (WPB) underthrusts the oceanic crust of the HB to the west and may represent a rare example of a failed subduction attempt preserved in the geologic record.

3-2: TECTONIC BACKGROUND

3-2-1 Philippine Sea Plate

The Philippine Sea Plate (PSP) is a major plate that separates the Pacific, Australian, and Eurasian plates. It is bounded on all sides by active subduction zones that separate it from an oceanic ridge system, and it lacks an accreting boundary (Hall et al., 1995). The greater PSP is composed of three large sub-basins (Figure 3-1) that include the Shikoku Basin (SB; ~25-15 Ma), the Parece Vela Basin (PVB; ~30-17 Ma), the West Philippine Sea Basin (WPB; ~56-35 Ma) (Rangin and Pubellier, 1990), and the smaller Mariana Basin (~6 Ma) (Hussong and Uyeda, 1981) and Huatung Basin (Hilde and Lee, 1984). Presently, the PSP is moving N308° at a rate of 7-8 cm/yr relative to the Eurasian plate near Taiwan (Ranken et al., 1984; Seno et al., 1993; Yu et al., 1999; Yu and Kuo, 2001) and subducts northward along the Ryukyu trench, which constitutes the northwest boundary of the PSP. Several seismic refraction experiments (Murauchi et al., 1968; Henry et al., 1975; Hayes et al., 1978; Louden, 1980; Langseth and Mrozowski, 1980) have confirmed that the WPB is floored by ocean crust (6-8 km thick). Hilde and Lee, (1984) analyzed magnetic lineations and bathymetric structures of the WPB to show that it was likely formed from the Central Basin Spreading Center (CBSC) in two distinct spreading phases, one from ~60 Ma – 45 Ma, and one from ~45 Ma – 30 Ma. Ar/Ar dated gabbro samples recovered by deep-sea drilling (DSDP) site 293 (Ozima et al., 1977) in the WPB produced an age of ~42 Ma in reasonable agreement with ages derived from Hilde and Lee (1984).

3.2.2 Huatung Basin and Gagua Ridge

The HB is located on the western edge of the PSP and is bounded by the Ryukyu subduction zone, GR, the northern Luzon volcanic arc (NLA), and eastern Taiwan

(Figure 3-1). The dimensions of the basin are small, ~150 km in width by ~250 km in length. Thick sedimentary units (~4 km; Van Avendonk et al., Deep crustal structure of an arc-continent collision: Constraints from seismic travel times in central Taiwan and the Philippine Sea, submitted to Journal of Geophysical Research Solid Earth, 2014) in the basin are derived primarily from the uplift and erosion of the Taiwan mountain belt and have become ponded within the basin due to the presence of the GR bounding to the east. No deep-sea drilling exists within the basin, and as a result, most of the previous interpretations concerning the age of the seafloor are based on marine magnetic anomaly data. Early work from Hilde and Lee (1984) identified several E-W trending magnetic anomalies, interpreted as anomalies 19 to 16 in the northern part of HB, and indicating an age for the seafloor between 44 and 36 Ma. This interpretation was based on the correlation of these magnetic anomalies in the HB to anomalies in the later phase of WPB seafloor spreading during the Eocene. More recently, Ar/Ar dating of gabbros collected from several basement highs in the southern HB were dated as Early Cretaceous in age, between 115 and 125 Ma, leading to the hypothesis that the basin could be a trapped piece of Cretaceous Proto-South China Sea, or perhaps a piece Mesozoic New Guinea Basin oceanic crust (Deschamps et al., 2000; Hall, 2002). Conversely, Sibuet et al. (2002), using updated marine magnetic anomaly and gravity anomaly data collected offshore southern and southeastern Taiwan, suggest an alternate age and origin for the HB. These authors support the interpretation that the HB is part of a separate plate, the 'old' Taiwan Sea Plate, formed 51 to 15 Ma, the majority of which has already subducted beneath the Ryukyu trench to the north. More recently, Kuo et al. (2009) estimated that the age of the HB is close to the age of the PVB (~15-30 Ma) of the eastern PSP based on the similarity of Rayleigh wave seismic velocities between the two basins.

Several geophysical studies have examined the morphology, seismic velocity structure, and seismicity in the lithosphere of the basin and their relation to the ongoing Taiwan arc continent collision occurring along the west margin of the basin. Schnürle et al. (1998) analyzed seismic reflection data exploring the potential for E-W structural control on the Taitung Canyon within the Huatung Basin. These authors found that in most cases, the canyon followed a depression in the oceanic basement and identify the existence of local WSW-ENE strike-slip seismicity in the vicinity. However, such faults are not well expressed in seismic reflection data, and they do not outcrop in bathymetry data. More recently, Lallemand et al. (2013) examined the interaction of the PSP and EUP using a combination of a new 3D velocity model, earthquake relocations, and MCS reflection data in an effort to reconcile the observed deformation style with the distribution of seismicity. The authors argue for NW-SE shortening of the northern, subducted portion of the HB between 23.3° N and 24.3°N through folding and slicing of the ocean crust corresponding with two concentrated clusters of seismicity at or near the subduction interface. Despite this new evidence, it is unclear whether the deformation observed by these authors corresponds to an existent structural fabric within the HB that has been reactivated or if the deformation is limited to the region proximal to the collision. Additionally, the deformation identified is interpreted on the already subducted portion of the HB and therefore difficult to confirm.

The GR, is a linear, ~300 km long, 25-30 km wide, N-S trending bathymetric high to the south and east of Taiwan that rises 2 to 4 km above the surrounding seafloor (Deschamps et al., 1998). The ridge extends north from the eastern flank of the NLA (on Luzon Island) and isolates the HB from the WPB (Figure 3-1). The ridge is continuous to the north and has been shown to subduct beneath the Ryukyu trench, forming a reentrant scar into the Yaeyama ridge accretionary prism (Lallemand and Liu, 1997; Dominguez et al., 1998).

Past interpretations concerning the origin and tectonic significance of GR are speculative, because they are largely based on indirect observation from geophysical studies of the adjacent ocean basins. Recent studies agree that GR likely represents a zone of earlier compressional and strike-slip deformation. However several investigations (Deschamps et al., 2000; Sibuet et al., 2002) suggest that the GR may have acted as an important plate boundary rather than an intra-oceanic fracture zone between what would have been a separate HB plate from the younger Eocene age WPB to the east. Because great uncertainty remains regarding the age of the ocean crust in the HB, it is difficult to establish the role of GR in the regional tectonic history. Below we describe a detailed geophysical study of the GR that provides fundamental constraints on the crustal scale structure of the ridge and surrounding ocean crust that can then be used to analyze the true nature of this boundary and its importance in the development of the PSP.

3-3: GEOPHYSICAL DATA AND PROCESSING

3-3-1: TAIGER Experiment

MCS reflection and wide-angle refraction data were acquired in the vicinity of GR as part of the 2009 TAIGER (Taiwan Integrated Geodynamics Research) program, designed to study the evolution and geodynamics of the Taiwan arc-continent collision and surrounding region. We present subsets of wide-angle OBS transects T1B, T2 (Eakin et al., 2014), T4A (McIntosh et al., 2013), and T5 (Van Avendonk et al., Deep crustal structure of an arc-continent collision: Constraints from seismic travel times in central Taiwan and the Philippine Sea, submitted to Journal of Geophysical Research Solid

Earth, 2014) and MCS reflection profiles, MGL0905_17 and MGL0906_14 and MGL0906_30N from this program acquired offshore south and east of Taiwan (Figure 3-1). These data constrain the crustal structure of the HB ocean crust, GR, and WPB. MCS reflection data were acquired with the seismic vessel R/V Marcus Langseth using a 468 channel, 6 km streamer and a source array consisting of 36 air guns with a total volume of ~6600 in3 towed at a depth of 9 m. Source spacing was 50 m for MCS data acquisition with hydrophone spacing of 12.5 m resulting in nominal common midpoint (CMP) spacing of 6.25m. MCS data were recorded for 15 sec with a 2 ms sample rate. Wide-angle data were acquired using the same seismic source, and recorded on OBS instruments from National Taiwan Ocean University (NTOU) and U.S. OBS instrument pool (OBSIP). Lines T5 and T4A also recorded seismic arrivals with instruments on land; however, the model and data subsets presented in this paper show only the marine portions of these transects. Shot spacing for wide-wide angle acquisition was 150 m with instrument spacing of 12-15 km for lines T5, T4, and T2, and 10 km for line T1B. Sample interval was 4 ms for NTOU instruments and 5 ms for the OBSIP instruments.

3-3-2: MCS Data

Data processing was performed using the Paradigm Focus software. MCS data processing included advanced multiple attenuation techniques to improve deeper crustal imaging, as outlined by Lester and McIntosh, (2012) and Eakin et al. (2014), including gap deconvolution, 2D surface-related multiple attenuation (SRME), radon de-multiple filtering, offset-weighting, and time-variant bandpass filtering. The final pre-stack time migrated images provide high-resolution constraints on the sedimentary and crustal structure across the HB, GR, and WPB ocean crust.

3.3.3: OBS Data

OBS data quality are generally of fair quality in the vicinity of GR, however additional processing steps were applied to improve signal to noise ratio and increase picking confidence at longer offsets. The processing steps for the near-to-middle offsets (0-40km) varied between instruments depending on data quality but typically included band-pass frequency filtering, automatic gain control (AGC), or gain with offset. Additional processing steps were applied including gap deconvolution and spectral balancing to equalize frequency content as needed to increase signal-to-noise ratio for picking first arriving wide-angle refractions.

In Figure 3-2, OBS records from two instruments along transect T1B show wide-angle seismic refractions from sediments, crust and uppermost mantle, along with calculated first arrivals, picked first arrivals, and travel-time uncertainties. These data are representative for the other transects, and they can be used to constrain the velocity structure associated with the NLA, GR, and the WPB. Similar OBS data records from transect T2 were presented by (Eakin et al., 2014), from T4A in (McIntosh et al., 2013), and T5 in (Van Avendonk et al., Deep crustal structure of an arc-continent collision: Constraints from seismic travel times in central Taiwan and the Philippine Sea, submitted to Journal of Geophysical Research Solid Earth, 2014).

3-4: METHODS

3-4-1: Tomography and Resolution Testing

All of the seismic velocity models presented in this paper were created by inverting the travel times of first arriving refractions that were recorded on OBSs, using the regularized inversion method of Van Avendonk et al. (2004). First, a simple starting seismic velocity model is created, composed of a water layer above a subsurface layer.

Here we assume the seismic velocity increases with depth beneath the seafloor. Iterative steps of ray tracing and linearized inversion with smoothness constraints are then performed to reduce travel-time misfits until a satisfactory fit between calculated and observed arrival times is achieved within the tolerance level of the pick uncertainties.

While the inversion procedure that led to each velocity model shown in this manuscript was nearly identical, the velocity model for line T1B has not been presented previously, and details of the modeling process and resolution testing will be given here. T1B (Figure 3-3a,b) spans 207 km in the horizontal and 30 km in the vertical direction, and contains 414 x 91 = 37,674 grid nodes. Grid spacing is 0.5 km in the horizontal direction, and 0.3 km in the vertical direction. 3,467 first arrival picks and 15 iterations of travel-time tomography were performed to update the model, reducing $\chi 2$ from 160 in the initial model to 0.95 in the final model iteration. The final velocity model has an RMS misfit of 86 ms.

The resolution and reliability of the final velocity models can be assessed using the derivative weight sum (DWS) and a display of the resolution matrix. DWS provides a measure of the ray density at each model parameter in the final inversion (Thurber and Eberhart-Phillips, 1999). Along profile T1B, DWS is much higher in the upper ~10 km between 0-80 km (Figure 3-3a) due to the greater sampling and smaller uncertainties in the first arrivals at the near offset of each instrument.

The resolution of the final velocity models can be further assessed by computing the resolution matrix (van Avendonk et al., 2004), which can be used to test how well model features of specific dimensions are resolved in the inversions. Figure 3-3b demonstrates that 6 km horizontal by 3 km vertical and 12 km horizontal by 6 km vertical elliptical velocity anomalies in the crust are well resolved from model distance 0 km – 100 km and adequately resolved at shallow depths (0 km – 5 km). Upper mantle velocities are well resolved between 20 km and 80 km. Resolution is poorer at depth at model distance 80 km – 140 km where we lack coverage with crossing ray paths. This resolution analysis indicates that the crustal thickness and upper mantle structure beneath the GR and northern Luzon Arc crust to the west is well resolved. Similar tests were performed for each wide-angle transect shown in Figure 3-7. More details of the outcome of tomographic modeling and resolution testing for T2, T4A, and T5 can be found in (Eakin et al., 2014; McIntosh et al., 2013; and Van Avendonk et al., Deep crustal structure of an arc-continent collision: Constraints from seismic travel times in central Taiwan and the Philippine Sea, submitted to Journal of Geophysical Research Solid Earth, 2014).

3-5: ANALYSIS AND RESULTS

The TAIGER OBS and MCS data shown in the following sections provide new, high-resolution constraints on the structure of the oceanic crust offshore southeast Taiwan. The tomographic velocity models and coincident pre-stack time-migrated images cross the HB and the GR and yield for the first time, first-order constraints of the crustal structure, basement morphology, and sedimentary cover associated with the GR as well as the adjacent HB and WPB. In the following sections, we will first describe the MCS reflection profiles and discuss the tomographic velocity models.

3-5-1: MCS Line MGL0906_17

Between 22° N and 23° N, the HB achieves its maximum width of ~150 km. To the west of the basin at this latitude, the remnant NLA is in the incipient stages of collision with the Chinese passive margin. Line 17 provides important constraints on the structure and thickness of HB ocean crust and deformation associated with the GR

(Figure 3-4a). In the majority of the HB (CMP 6000-18000), 1.5-2.0 sec TWTT, or 1.5-2 km thick, sediments overlay a high amplitude basement reflection assuming a sedimentary velocity between 2-3 km/sec. The sedimentary section generally thickens westward and reflectivity is relatively continuous until the base of the steep slope section. There is a slight wavy pattern in the shallow sedimentary section up to the seafloor, from CMP 13500 west to the flank of the NLA similar to structures observed by McIntosh et al. (2005). These features do not seem to extend deep in to the section and are likely due to gravity sliding from the arc flank toward in the HB.

Intermittent Moho reflections can be traced across much of the profile (Figure 3-4b: CMP 7500-16000), at ~2 sec TWTT below the top of basement, or 5-7 km assuming an average velocity of 6 km/sec. The top of basement is relatively smooth in the central part of the profile and is bound by two large, symmetric troughs, ~18-20 km in width located at CMP 11000 to the west, and CMP 20594 (Figure 3-4b-c) to the east, approximately 50 km apart. Interestingly, the spatial distribution of these structures roughly coincide with previously published magnetic data (Deschamps et al., 2000) that show an established pattern of N-S trending fracture zones spaced ~50 km apart. The overlying, collision-derived sedimentary (~1.5-2.0 sec TWTT thick or 1.5-3.0 km assuming a sedimentary velocity of 2.0-3.k km/sec) cover infilling the troughs is undeformed, requiring that the basement deformation pre-dated sedimentation associated with the Taiwan arc-continent collision, and likely occurred in a deep ocean environment with extremely low sedimentation rates. The seafloor above the easternmost trough is dominated by the Taitung Canyon system indicating that it is structurally controlled at this location (Figure 3-4c). Between CMP 19000 and 25000, the top of the basement shoals very near the seafloor. Within this interval, the top of basement is deformed into a series of alternating ridges and troughs, and the sedimentary cover thins from an average of ~1 s TWTT to less than 0.5 s TWTT near the eastern flank of GR. Unfortunately, the crustal heterogeneity obscures possible deeper Moho reflections.

The GR (Figure 3-4c: CMP 26000-29000) rises ~2.8-3.0 s TWTT, or ~2.1-2.8 km from the surrounding seafloor assuming a water velocity of 1.5 km/s, and consists of a main promontory and a secondary promontory on the western flank. The slope of the ridge is slightly asymmetric, with the eastern flank at a steeper angle than the western flank. The ridge itself lacks significant internal reflectivity and appears to exhibit similar seismic characteristics as the surrounding ocean crust. Potential deep Moho reflections are obscured by strong residual multiple energy that we were unable to remove due to its steeply dipping nature. A sedimentary basin, ~1 s TWTT, or 1-1.5 km assuming 2-3 km/s sedimentary velocity, has developed on the east side of the GR (Figure 3-4c: CMP 29000-30900). Layered sediments on either side of GR onlap onto its flanks and show no evidence of tectonic deformation.

Line 17 terminates 12 km east of GR and as a result does not constrain the ocean crust of the WPB. At this position, the top of the WPB oceanic basement is observed at ~9 s TWTT, or ~7.5 km depth, assuming a water velocity of 1.5 km/sec and sedimentary velocity of 2.5 km/s. Edge effects from the migration acting on the low fold areas at the end of the profile limit the resolution of the deeper structure in this area. However, two strong, linear, westward dipping reflectors (CMP 30500: 9 sec TWTT) extend from the edge of the profile several km west beneath the flank of GR. These reflections may represent a continuation of the top of WPB ocean crust and evidence for partial underthrusting beneath the GR and HB oceanic crust.

3-5-2: MCS Line MGL0906_14

Line 14 extends SE from the eastern flank of the NLA at 23° N, across the arc slope and HB, and bisects the GR near 22° N (Figure 3-1). The eastern end of Line 14 crosses Line 17 before continuing SE providing an interesting opportunity to analyze the spatial continuity and distribution of similar basement structures in the HB. Similar to Line 17, sedimentary thickness increases to the west approaching the NLA as the basement deepens away from GR. Sedimentary thickness for the majority of the basin (CMP 6000-16000) is on the order of 1.5-2.0 sec TWTT, or ~1.5-3.0 km thick, assuming a sedimentary velocity between 2.0-3.0 km/sec (Figure 3-5a). A wavy pattern similar to that of Line 17 is observed in the shallow sedimentary section east of CMP 6000, to CMP 16500 where the Taitung Canyon is observed at the seafloor (Figure 3-5b). The wavy structures soles into a high amplitude reflector that may represent a local detachment facilitating gravity sliding in to the HB. Arc-ward of CMP 5000, there is a large scarp at the seafloor and reflections show large folds with wavelengths >4 km (Figure 3-5a). This area may mark the limit of collision related deformation similar to that observed by McIntosh et al. (2005).

Intermittent Moho reflections are visible throughout much of the western part of the profile at 1.5-2.0 sec TWTT, or 4-6 km depth (Figure 3-5b). Further interpretation of Moho becomes difficult in the eastern end of the profile, possibly due to increasing deformation approaching GR. The basement is fairly smooth between CMP 12000-16000, but is bounded on either side by abrupt structural breaks in the basement. West of CMP 12000, we image the same graben-like trough observed on Line 17 (Figure 3-5b). It is unclear whether the arc-ward flank of this depression represents a previously active footwall or simply the seaward extent of the NLA edifice in the HB. Because the overlying sedimentary cover is undeformed, it is likely that the deformation and faulting are pre-collisional, related to the seafloor-spreading episode that formed the HB.

The seafloor expression of the Taitung Canyon marks the transition from the relatively smooth basement to the west to the rugged, apparently deformed basement to the east. Here (CMP 17000-25000) the basement consists of a series of sharp ridges and troughs that shoal and eventually emerge at the seafloor to the west of GR (Figure 3-5c). Sporadic reflectivity in the basement may be a further indication of faulting and extensive deformation, making it extremely difficult to identify Moho consistently. Despite the evidence for deformation in the underlying basement, the overlying sedimentary cover is relatively undisturbed within the troughs only show slight folding near the sediment basement interface that decreases rapidly near the seafloor.

The GR rises ~4.5 sec TWTT, or ~3.5 km from the surrounding seafloor on line 14 (Figure 3-5c). The shape of the ridge is slightly asymmetric in cross section, where the western flank has a steeper angle than the eastern flank. The upper 2.5-3.0 sec TWTT of the ridge lacks significant coherent reflectivity and appears to exhibit similar seismic characteristics as the surrounding ocean crust. Deeper reflectivity including evidence for Moho reflections are obscured by strong residual multiples. Sediment-filled troughs bound the GR to the east and west. Sediments within the troughs onlap the ridge unconformably similar to line 17 and show little evidence for significant deformation, indicating GR has been relatively stable tectonically since its formation. A high-amplitude reflection extends to the west from the base of the easternmost trough bounding GR. We interpret this reflection to be the top of WPB ocean crust and evidence for underthrusting beneath the GR, however the reflection is quickly obscured by residual multiple energy.

3-5-3: MCS Line MGL0906_30N

Line 30N extends NE from the eastern flank of the NLA and terminates in the middle of the HB near 22.5° N (Figure 3-1). This profile exhibits quite different basement structure than the profiles to the north and it also provides new information on the nature of the regional, bench-like feature that dominates the southwest margin of the Huatung Basin. The majority of the HB imaged here (Figure 3-6a: CMP 500-11000) consists of ~1.0-2.0 sec TWTT, or ~1.0-3.0 km thick sedimentary section, assuming sedimentary velocities between 2-3 km/sec. In general, the overlying sedimentary cover is far more deformed than the previous MCS reflection transects. Between CMP 500 and 7200 minor faulting of the lower units is commonly observed, however no faults are seen to reach the seafloor (Figure 3-6b).

Intermittent Moho reflections are visible throughout the profile (Figure 3-6b: CMP 500-5000; Figure 3-5d: CMP 6000-8750) at ~2 sec below the top of the basement, or 5-7 km thick assuming an average crustal velocity between 5-7 km/sec, in agreement with observations from line 17 and 14. The top of the oceanic basement is quite smooth and regular in stark contrast with the large amounts of basement deformation that can be identified in lines 17 and 14 to the north. None of the graben-like troughs identified on those reflection profiles to the north, specifically the trough closest to the NLA, are observed here.

We observe the sudden emergence of a prominent, bathymetric bench protruding from the NLA slope at the west end of the profile (Figure 3-5c). Interestingly, the emergence of this structure is coincident with the appearance of a major regional bathymetric high that widens to fill the basin south of 22° N as the deeper basin itself narrows (Figure 3-3-1). The seismic character of this structure is unusual. Shallow in the section between CMP 14300-15000 at 5-5.75 sec TWTT, the structure is composed of semi-coherent, layered strata that are easily differentiated from the arc basement reflection. Subtle reflectivity in the upper sedimentary unit outlines the flanks of what appears to be a submarine canyon approximately 5 km wide by ~1 km deep. Seaward of CMP 14300, the coherent layer is underlain by a lens of material (Figure 3-6c: CMP 13000-14300 at 5.75-6.75 TWTT) with poor internal reflectivity and floored by a high amplitude reflection that clearly separate it from the arc-basement below. This lower unit reaches its maximum thickness near CMP 13600 where it forms small pinnacle or platform. Additional MCS reflection lines (not shown here) cross the structural high as it broadens to the south and show a similar structural trend. Farther south the underlying layer increases in volume and it becomes increasingly difficult to differentiate it from the arc basement below. Fortunately, both tomographic models T1B and T2 (discussed later) cross the same bathymetric feature to the south after it has widened to fill the majority of the basin and provide important velocity information of the structure. Based on the velocity structure and observations derived from this analysis, we are confident this underlying layer is likely related to the arc, but separate from the arc basement. This point will be discussed in further detail in the Discussion section.

3-5-4: OBS Derived Velocity Model Description, Observations, and Interpretation

The tomographic travel time inversions of T1B, T2, T4A, and T5 have for the first time defined the crustal structure across the HB and GR bathymetric feature. The resulting velocity models (Figure 3-7a-e) show the OBS locations, a simplified tectonic interpretation, and labels for the main tectonic elements. The green dashed lines labeled M in Figure 3-7b-e denote the approximate location of the HB and WPB Moho that are well constrained in all of the models shown. Because line T4A is coincident with MCS line 17, we infer that the 5 km/sec contour is close to the top of crystalline crust.

3-5-5: Line T1 Model Description, Observations, and Interpretation

The southernmost line T1 (Figure 3-7c) crosses the GR near its intersection with the NLA and provides important velocity constraints for the regional, bench-like feature that dominates the southwest margin of the Huatung Basin. East of the GR (model distance 115-155 km), low velocity material (3.0-4.5 km/sec) marks a small trough that is also visible in the satellite-derived gravity data (Sandwell et al., 2013) forming a large negative anomaly highlighted in the associated gravity profile (Figure 3-7b, c). Most notably, the velocity structure beneath the GR indicates a doubling of the crust, to about 12-15 km thick. West of GR, the thickness of the HB is consistent (5-7 km) with other profiles to the north and then shows a rapid thickening to >15 km toward the NLA (model distance 40-100 km), however the resolution westward quickly degrades due to lack of crossing ray paths.

The basement west of the GR (denoted by the 5km/sec contour) is covered by ~3-4 km of low-velocity (2.5-4.0 km/sec) sedimentary material. This thick package correlates with the regional bathymetric platform described along line MGL0906_30N (Figure 3-1, 3-6c) that extends into the HB from the eastern flank of the NLA. The obvious disparity in the velocity structure when compared to the underlying basement is further evidence that this feature is likely unrelated to the arc basement. The bench spans the entire HB at the location of this transect and becomes narrower to the north, eventually pinching out at ~22° N. While the bench of low-velocity material represents a structural high in the bathymetry, the feature is associated with a large negative gravity anomaly on the eastern flank of the NLA that is continuous along the westernmost HB south of ~22.4° N until it intersects the gravity high produced by the GR. (Figure 3-7b, c). This observation is significant when considering the potential relationship this feature has to the NLA to the west that will be discussed in further detail in the Discussion section.

3-5-6: Line T2 Model Description, Observations, and Interpretation

Line T2 extends E-W and crosses the HB and GR at ~21.5° N. Here, the NLA trends ~NW and GR ~N with the HB filling the area in between (Figure 3-1). This profile has quite different basement structure than T1B to the south and also provides additional coverage of the bench-like bathymetric feature as well as a crustal scale definition of the GR. Analysis of the tomographic model (Figure 3-7d) (model distance 300-390 km) confirms the thin (5-7 km) oceanic nature of the HB, east of the NLA, estimated from the position of Moho observed in the MCS reflection profiles discussed previously. The crust thickens to the west approaching the NLA and the overlying low velocity (2.5-3.0 km/sec) sedimentary cover thickens from 0-2 km at model distance 380 km at to upwards of 5-6 km near the NLA as a result. A key observation is that the thickest low-velocity material seems to correspond to the same bathymetric bench identified along T1B to the south. The low seismic velocities of this bench are intriguing and are associated with the same linear negative gravity anomaly trending NW-SE on the eastern flank of the NLA as T1B (Figure 3-7b). While a first-order interpretation of the bathymetry might suggest that the bench is an eastward continuation of the NLA basement, the negative gravity anomaly correlates with the thickest low-velocity zone observed in the velocity model (Figure 3-7c: model distance 320-340 km) suggesting it is unrelated to the higher velocity arc basement below. The tectonic significance of such a continuous bathymetric feature is intriguing and will be discussed further in the Discussion section.

The most striking observation along line T2 concerns the velocity structure of the GR and immediate surrounding area. Directly east of the ridge (model distance 410-450 km) a deep basin of low velocity (2.5-3.0 km/sec) sedimentary material covers the deepening oceanic basement of the WPB similar to that observed to the south along line T1B (Figure 3-7c). The GR is composed of high velocity material (5-6.5 km/sec) and is actually the surface expression of a thicker root on the order of 15-18 km total thickness. Unlike line T1, the thickening appears to be asymmetrically distributed beneath the bathymetric expression of the ridge suggesting the ocean crust of the WPB may be partially underthrust beneath the ocean crust of the HB. Directly west of the ridge (model distance 380-400 km), the basement of the HB shoals to very near the seafloor. This shallowing of the oceanic basement is consistent with a large positive gravity anomaly (Figure 3-7b) that dominates the southern part of the HB.

3-5-7: Line T4A Model Description, Observations, and Interpretation

Line T4A, located at ~22.8° N, extends E-W from the eastern flank of the NLA across the HB and GR into the WPB (Figure 3-7e). Here, the HB reaches its maximum width (~135-140 km) and the entire crustal velocity structure is constrained along with the GR and WPB ocean crust. The basement-controlled Taitung Canyon is clearly visible at model distance 310 km, as a slightly thicker zone (~3.0 km) of low velocities (2.5 km/sec) relative to the surrounding 1.5-2 km sedimentary cover. The oceanic crustal thickness is variable throughout the HB with areas as thin as ~5 km and as thick as ~7-8 km, but overall consistent with estimates derived from Moho reflections in the MCS reflection profiles and previous wide-angle transects. The thin zones in the ocean crust seem to correlate with the position of potential N-S trending fracture zones, described earlier and identified in previous magnetic studies (Hilde and Lee, 1984; Deschamps et al., 2000; Sibuet et al., 2002).

The HB oceanic crust shoals from ~3-4 km below the seafloor, to >~2 km as it approaches the GR. Similar to line T2, the most striking feature of line T4A is the velocity structure of the GR itself. The ridge consists of a thickened high velocity material (5-6.5 km/sec) to a total of 12-15 km. Most interestingly, the velocity structure beneath the ridge exhibits the same asymmetry observed to the south along line T2 to the south, again indicating underthrusting of the WPB beneath the HB and suggesting that this tectonic process responsible was likely active along the entire ridge.

East of the GR, the T4A velocity model extends 80 km into the WPB. Here, the velocity structure indicates an average oceanic crustal thickness of 5-7 km. Between 355 km and 390 km, we observe a clear deepening of the WPB oceanic basement as it approaches GR from the east. This sudden deepening forms a trough filled with low velocity (2.0-4.0 km/sec) material confirmed by the coincident reflection profile, line 17 (Figure 3-4), and consistent with the linear negative gravity anomaly parallel to the eastern flank of GR and in the associated gravity profile (Figure 3-7b and 3-7e).

3-5-8 Line T5 Model Description, Observations, and Interpretation

Line T5, the northernmost wide-angle transect shown in this study, extends SE across the Ryukyu accretionary prism, crosses GR at 123°E, and terminates in the Ryukyu trench to the east (Van Avendonk et al., Deep crustal structure of an arc-continent collision: Constraints from seismic travel times in central Taiwan and the Philippine Sea, submitted to Journal of Geophysical Research Solid Earth, 2014) (Figure 3-1, 3-7f). Here, the PSP subducts beneath the Ryukyu accretionary prism and the top of the basement now resides at ~ 10 km depth. As a result, the GR also actively underthrusts the Ryukyu prism, deforming the prism as it does so, and leaving a clear reentrant scar in the bathymetry (Schnürle et al., 1998).

Since the PSP has underthrust the toe of the Ryukyu prism along transect T5, the deeper crustal velocity structure here is not very well constrained (Van Avendonk et al., Deep crustal structure of an arc-continent collision: Constraints from seismic travel times in central Taiwan and the Philippine Sea, submitted to Journal of Geophysical Research Solid Earth, 2014). Nonetheless, some important observations concerning the evolution of GR and the surrounding area can still be made. Throughout the profile (Figure 3-7f), a thick package (6-8 km) of low velocity (2.5-4.0 km/sec) sedimentary material, the Ryukyu accretionary prism, overlies the PSP basement (5 km/sec contour). To the west of GR (model distance 200-260 km) the velocity structure confirms the presence of normal ocean crust (5-7 km) in the HB in agreement with observations from wide-angle and MCS data discussed previously. The top of the basement here deepens slightly from ~9 km to 12-13 km as it approaches GR. To the east of GR (model distance 315-370 km) the velocity structure also suggests relatively thin crust (~5 km) in the WPB, also in agreement with previously discussed geophysical data. The ocean crust here also deepens slightly as it approaches GR.

Because GR is buried here and adjacent crust is partially thrust beneath the Ryukyu prism, it is not clear whether the same asymmetric velocity structure observed on lines T4A and T2 farther south also exists here. However, the velocity structure does indicate evidence for at least doubling of the crust to about 15-18 km similar to the velocity structure of the ridge farther south.

3-6: DISCUSSION

Based on the data presented herein, we interpret GR to have formed as a result of a failed subduction initiation event. It is likely that this event preceded the ongoing arc-continent collision in Taiwan. Here, we will discuss the observations from our geophysical data and other geophysical studies and the implications toward the likely age distribution of the HB. We then discuss possible mechanisms responsible for the formation of GR and propose a hypothetical scenario for its development.

3-6-1: Huatung Basin Structure

The HB is an important tectonic feature offshore southern Taiwan in spite of its relatively small area. The relationship of the HB to the adjacent SCS, WPB, and plate reconstruction of the greater western Pacific remains speculative, because its age and crustal affinity have not yet been adequately determined. As noted in the Geological Background section, early studies, primarily based on magnetic anomaly data (Hilde and Lee, 1984; Deschamps et al., 1998), suggest that the oceanic crust within the basin is Eocene in age, and genetically related to oceanic crust of the WPB on the opposite side of the Gagua Ridge. However, dredged gabbros (Figure 3-1: RD 19 and RD 20) from the southern HB appear to indicate that the crust of the HB was generated in the early Cretaceous and trapped by the northward migration of the PSP (Deschamps et al., 2000). The correlation of the limited magnetic anomalies with a magnetic model yield solutions that are inherently non-unique. Conversely, gabbro samples dated from dredging must also be scrutinized due to the possibility that those samples may represent rafted material from an older oceanic domain to the south displaced by previous strike-slip motion of GR. Evidence for Upper Cretaceous to Eocene volcanic rocks in Luzon and the eastern Philippines is well known (Karig, 1983).

The series of tomographic velocity models presented in this paper provide comprehensive coverage of the crustal structure here (Figure 3-7). The seismic velocities strongly indicate that the majority of the basin consists of oceanic crust on the order of 5-7 km thick, consistent with McIntosh et al. (2005) and an important revision of the ~10-

12 km estimates postulated by previous studies (Yang and Wang, 1998; Deschamps et al., 2000). Additionally, our tomographic models are substantiated further by MCS reflection profiles 17, 14, and 30N, (Figures 3-4 – 3-6) that show intermittent Moho reflections at 1.5-2.0 sec TWTT below the top of basement. Furthermore, gravity modeling from an E-W transect across the basin from Li et al. (2007) requires ocean crust of average thickness (~5-6 km) to satisfy the observed gravity anomaly.

3-6-2: Deepening of the Huatung Basin Crust Towards the NLA

MCS lines 17, 14, and 30N (Figures 3-4 – 3-6) as well as tomographic models T2 and T4A (Figure 3-7d and 3-7e) show a deepening of the top of the HB oceanic basement westward toward the NLA. Given the proximity to subduction and collisional zones acting on western and northern boundaries of the basin it is difficult to determine if they are associated with this observed deepening. One possibility may be that the western margin of the basin is loaded by deep crustal bodies emplaced during volcano building along the NLA similar to the process described by Watts et al. (1985). Another possibility (Bahlburg and Furlong, 1996; Smith et al., 2002; Waltham et al., 2008) is that the arc volcanism itself produces significant near-surface loads leading to the flexure of the western part of the basin. Alternatively, the deepening of the ocean crust could also simply be the result of the uplift of the GR in the eastern part of the basin, such that the uplift creates the illusion of a deepening of the basement to the west. In light of the data presented here, we propose that the observed deepening of the HB to the west is likely the result of a combination of flexural loading by the NLA complemented by the strike-slip/compressional deformation in the eastern part of the basin leading to uplift of the GR.

3-6-3: Huatung Basin Shallow Basement Structure and Deformation

We observe a shift in the style of basement deformation in the HB MCS reflection data, from a series of highly deformed ridges and troughs in the east near GR (Figure 3-4a-c and 3-5a-c), to smooth, relatively undeformed basement and potential relict extensional features similar to graben in the west-central part of the basin (Figures 3-4a-b, 3-5a-b, and 3-6). The shift is coincidental with the emergence of the oceanic basement at seafloor near GR and may be evidence of the poly-phase tectonic history of HB. The less deformed, western-central portion of the basin may represent the original seafloor architecture. The significance of the N-S trending troughs (Figure 3-4c and 3-5c) bounding the smooth ocean crust is ambiguous, however one possibility may be that these structures are related to fracture zones or transforms that accommodated N-S seafloor spreading that produced the ocean crust here. The preserved portions of smooth oceanic basement are on the order of ~50-60 km wide and are similar to the width of crustal segments between fracture zones associated with slow spreading ridges (Schouten et al., 1985). This idea has circumstantial support because spreading rates used by many investigators in magnetic reconstructions of the HB, are in the low (10-20 mm/yr: Sibuet et al., 2002) to medium (25-30 mm/yr: Deschamps et al., 2000) range for ocean crust production. The more deformed ridges and troughs in the eastern part of the basin may represent a later stage compressional episode related to the underthrusting of the WPB oceanic crust and subsequent uplift of the GR. The linearity of the ridges and troughs associated with the deformation may also indicate that these features may have started as fracture zones or transforms that were reactivated and/or deformed during the later stage transpression associated with the GR.

3-6-4: Bench in the Huatung Basin

South of ~22.5° N, HB decreases from its maximum width of ~150 km to less than 75 km near 21° N. This change in width is accompanied by the appearance of a peculiar bathymetric high that increases in width away from the NLA to the south until it comprises the entirety of the basin (Figure 3-1). Many authors have investigated the abrupt emergence of this feature, associating its emergence with the NLA and changes in subduction processes along the Manila trench father west. Yang et al. (1996) propose that the subduction of an aseismic ridge segment of the SCS coupled with a clockwise rotation of the overriding PSP created a wide zone of volcanism of the NLA south of 21°N. Others propose a flattening of the SCS slab resulting from the introduction of buoyant material, i.e. continental crust, into the Manila trench north of 20°N, also resulting in a wide zone of volcanism at the surface (Bautista et al., 2001). While it is difficult speculate on the tectonic process responsible for the emplacement of this structure, the data presented here provide important constraints on its seismic character and velocity structure. Line 30N images the initial emergence of this structure near 22°N and shows that it can be divided in a lower, poorly reflective zone, and an upper highly reflective sedimentary unit that provides the distinctive seafloor morphology (Figure 3-6c). Although the lower unit is internally, poorly reflective, a strong reflector can be traced along its base that we believe represents the arc basement contact. This lower unit provides a platform that has allowed for the accumulation of the upper sedimentary unit. Tomographic modeling from lines T1B and T2 cross the structure to the south where it has grown laterally to fill the HB. Interestingly, both models (Figure 3-7c: 50-90 km; Figure 3-7d: 300-340 km) show that the comparable structure is composed of relatively lower seismic velocity material (3-4 km/sec) than would be expected for arc basement. Based on these data, it is clear that the bench does not represent the edge of the arc-basement as the bathymetry might lead one to believe. Instead, this structure may represent a large clastic wedge of pyroclastic and epiclastic debris erupted and deposited on the flank of the NLA similar to the submarine debris and transport processes outlined by Fisher (1984).

3-6-5: Age of the Huatung Basin

The data presented in this manuscript do not provide direct insight into the potential age of the HB apart from some lower bounds. The age of the HB oceanic crust must be greater than the onset of arc-continent collision to the northwest (4-6 Ma). Secondly, the NLA is built on the western boundary of the HB and therefore should be younger than the basin itself. Radiometric dating of volcanic rocks of the accreted NLA in the northern Coastal Range show a maximum age of ~16 Ma (Yang et al., 1995) and thus a more reasonable lower bound for the HB age.

Several other investigations have proposed upper age limits for HB based on magnetic anomaly data and correlation in basement depths that generally cluster within the mid-late Eocene: ~40 Ma (Hilde and Lee, 1984); 51 Ma (Sibuet et al., 2002) with the exception of Early Cretaceous ages derived from the dredged gabbro samples (Deschamps et al., 2000 (130 Ma)). It is difficult to consider paleomagnetic a robust constraint due to the non-uniqueness of solutions for such a small basin. Similarly, while the Ar/Ar dating techniques from Deschamps et al. (2000) are likely sound, the samples were taken from basement highs far to the south near the GR and extrapolated for the entirety of the basin. Considering that it is likely that the GR originally formed as a transform fault, it is possible the samples represent exotic Early Cretaceous material from farther south emplaced by strike-slip faulting. In situ data from elsewhere in the basin is needed to add credibility to this claim.

Recently, Kuo et al. (2009) analyzed interstation phase velocities between OBS stations off the eastern coast of Taiwan and found that in the short period range, the phase velocities were comparable to those characterizing the 15-30 Ma Parece-Vela Basin. These authors also noted that the HB is 500-1000 m shallower than the Eocene age WPB, despite claims that the HB is much older. Deschamps et al. (2000) attribute this depth mismatch to thermal rejuvenation via heat produced from Manila subduction zone and NLA. However, Kuo et al. (2009) calculated the heat flux necessary to buoyantly raise a portion of Cretaceous crust in an area equivalent to HB to its present observed depth. They conclude that to raise the seafloor by the hypothesized 1.3 km, a plume restricted spatially to the HB and comparable to the Hawaiian plume, the strongest in the world in terms of buoyancy flux (Sleep, 1990) would be required. With no evidence of a deep mantle plume in this region, it is difficult to support thermal rejuvenation as a mechanism to explain such a shallow depth for early Cretaceous crust in the HB. Instead, the geometry of the interacting WPB and HB oceanic crust in our velocity models combined with recent geophysical studies tend to support a younger (~20-50 Ma) origin for the HB.

The absolute age distribution of the HB will remain unknown until significant efforts are made to sample the in situ ocean crust. In the following section, we will discuss the significance of the shallow and crustal velocity structure of the GR and comment on the potential understanding these observations may impart to the evolution of the ridge itself.

3-6-6: Gagua Ridge Structure and Development

Our velocity models (Figure 3-7), for the first time, provide important fundamental details about the velocity structure of the GR that also shed light on the interaction of the WPB and HB oceanic lithospheres. The models show that GR is comprised of ~12-18 km of high velocity (5.0-6.5 km/sec) material, similar to the velocity of the surrounding ocean crust. Most importantly, the two velocity models that cross the central part of the ridge (T2: Figure 3-7d and T4A: Figure 3-7e) show a significant asymmetry in the crustal thickening indicating that the ocean crust of the WPB has been partially underthrust to the west beneath the ocean crust of the HB. In this scenario, GR represents the surface deformation associated with incipient subduction that failed to progress towards a full-fledged subduction system. The velocity models also show the shoaling of the HB ocean crust to the west of GR that is likely the result of deformation resulting from the underthrusting of the WPB ocean crust. The MCS reflection profiles presented here show that dipping reflectors from the top of the WPB basement clearly extend beneath the ridge on lines 17 and 14 (Figure 3-4c and 3-5c). The flexure of the WPB oceanic crust forms a deep sedimentary trough that is continuous along the length of GR in free-air gravity data (Figure 3-4c, 3-5c, and 3-7b) and is also visible in the velocity models as a depression of low velocity material (2.5-4.0 km/sec) to the east of GR (Figure 3-7). Previous studies (Deschamps et al., 1998; Li et al., 2007) observe an asymmetric gravity profile associated with the GR and corresponding sedimentary trench that are very similar to type examples of gravity profiles acquired across active subduction systems. We observe a similar asymmetry in the gravity profiles coincident to transects T1B, T2, and T4A (Figure 3-7c, 3-7d and 3-7e).

The geodynamic environment where subduction initiation occurs, as well as, the age and presence of structural heterogeneities within the lithosphere are important in the subsequent evolution of a subduction system. Specifically, they control the success or failure of the system to nucleate into a self-sustaining subduction zone. Discussing the GR in these terms is difficult considering the lack of critical information about the tectonic components involved in its formation, i.e. the are of HB, the WPB, and absolute

PSP motion in the Cenozoic. Mesozoic and Cenozoic plate reconstructions indicate that changes in relative plate motion across preexisting transform faults and fracture zones can result in the formation of new convergent boundaries via induced subduction initiation (Uyeda and Ben-Avraham, 1972). Stern and Bloomer (1992) suggest that both the Eocene Bonin-Mariana and the Jurassic California arcs may have evolved in this manner, as well as, the ongoing subduction initiation along the northern segment of the Macquarie Ridge Complex south of New Zealand (Collot et al., 1995; Massell et al., 1999). The transpressional component of these systems may be a requirement for intra-oceanic underthrusting considering what we know about lithospheric strength. Mueller and Phillips (1991) argued that in most cases, the force required to overcome the strength of the lithosphere would need to be an order of magnitude larger than known ridge push forces, and subduction would be nearly impossible to initiate. More recently, Toth and Gurnis (1998) outlined the forces necessary to initiate subduction on a preexisting fault cutting the lithosphere. In contrast, these authors conclude that even with ridge push forces alone, it is still possible to initiate subduction and initiation along transform boundaries.

There are two previously published hypotheses regarding the initial geometry of the boundary that evolved into what is now the GR, and both are tied to the supposed age of the HB. In the first, the GR existed as a relict intra-oceanic fracture zone from the early stage of seafloor spreading of the WPB (Hilde and Lee, 1984; Deschamps et al., 1998). In the second, the GR existed as an important plate boundary separating the Eocene oceanic crust of the WPB from the exotic Early Cretaceous crust of the HB (Deschamps et al., 2000). Plate tectonic reconstructions from Hall (2002) require a large portion of the motion between the PSP and EUP to be accommodated by large, N-S strike-slip faults in the Cenozoic. Although both scenarios are adequate environments for a subduction initiation event to occur, it is difficult to reconcile the geometry of the underthrusting observed in our velocity models with the proposed Cretaceous age of the HB oceanic crust. Hypothetically, if two oceanic plates of largely differing age (>30 Ma difference) were juxtaposed via a heterogeneity in the crust (strike-slip fault or fracture zone) and compressional stress is imposed on the system, one would expect the older dense lithosphere to sink into the mantle as the younger, more buoyant lithosphere overrides it. While this scenario is an obvious over simplification, recent numerical modeling by Gurnis et al. (2004) analyzed subduction initiation at a fracture zone separating oceanic lithosphere of 10 Myr and 40 Myr. They found that during the initial phases of convergence (the time span we are interested in), deformation concentrates in the younger plate near the original fracture zone and large amounts of uplift are recorded as the older, denser oceanic lithosphere underthrusts. As the region becomes weaker, deformation localizes in the younger plate near the original fracture zone. Our velocity models (Figure 3-7d and 3-7e) indicate the Eocene oceanic crust of the WPB has been partially underthrust beneath the oceanic crust of the HB. The corresponding MCS reflection profiles (Figure 3-4 and 3-5) show large amounts of deformation in the basement to the west of the GR, although it is unclear whether it is associated with compression related to failed subduction or earlier transform/fracture zone activity. If the HB were early Cretaceous, this observation is contradictory to our knowledge of plate density and subductability. It is unlikely the much older (>60 Ma) plate would overthrust and deform so readily. Based on the geometry of the underthrusting in our velocity models, the deformation observed in the accompanying MCS reflection images, and recent geophysical work discussed above, it seems more likely that the age of the HB is young (20-40 Ma; Kuo et al., 2009). If this assessment of the HB age is correct, then it is possible to propose a hypothetical yet reasonable timeframe for the transpressional event and subsequent underthrusting that formed the GR.

3-6-7: Gagua Ridge: An Example of Failed Subduction Initiation in the Miocene?

Based on the observations and references discussed above, we interpret that the early Eocene (~50 Ma) WPB ocean crust has been underthrust beneath presumably younger (~20-40 Ma) oceanic crust of the HB. The HB ocean crust would, in this case, represent the second phase rifting of the WPB, as identified by Hilde and Lee (1984), and the GR, an intra-oceanic fracture zone similar to that suggested by Deschamps et al. (l998). Initial deformation at the fracture zone may have resulted from same the clockwise rotation of the WPB identified by Deschamps et al. (1998) between 50-40 Ma. However, based on the oldest volcanics associated with the NLA (Yang et al., 1996) and evidence for a possibly younger HB age (Kuo et al., 2009), the primary phase of deformation and subsequent failed underthrusting responsible for the emplacement of the GR may have extended throughout the Oligocene and into the early Miocene. Interestingly, this timeframe roughly corresponds with the onset of ~N-S seafloor spreading in the SCS in the mid-Oligocene (Taylor and Hayes, 1983; Briais et al., 1993; Lee and Lawver, 1995; Nissen et al., 1995). Additionally, Hall (1995; 2002) suggests that the PSP has been translating N-NW throughout the Cenozoic relative to the EUP and the motion of which was likely accommodated by large N-S strike-slip faults on its western boundary. It is this transpressional plate motion that may have been the driving component for the subsequent tectonic provinces and relict seafloor topography of the GR we observe today. In this scenario, during the Oligocene both the eastern bounding transform fracture zone (proto-GR), and the western strike-slip plate boundary (proto-Manila trench) separating the newly formed SCS ocean crust from the HB ocean crust may have deformed coevally. It is possible that a slight change in the PSP plate vector in the earliest Miocene to a more oblique angle introduced a transpressive component into the system instigating a competition between the two strike-slip boundaries to initiate subduction. For unknown reasons, the transient subduction episode that uplifted the GR was short lived. The newly formed SCS ocean crust coupled with the proximity of the SCS spreading center to a transpressional plate boundary likely provided a weaker, more easily deformed mechanical boundary to exploit such as the inner corner of the ridge transform intersection as suggested by (Casey and Dewey, 1984). When subduction initiated along the Manila trench, the strain and deformation occuring along the GR was abandoned and transferred to the new active boundary.

Regardless of the timing validity of our scenario, it is apparent that the GR is the result of a transient underthrusting episode that was abandoned. GR is unique in this way and potentially represents an important, relict part of the subduction initiation process rarely preserved in the geologic record. A potential analogue to the process that formed the GR is ongoing in the Macquarie Ridge complex south of New Zealand along the Pacific-Australian plate boundary. This boundary is dominated by linear 1500 km long, 4-5 km bathymetric peaks, including the Puysegur Ridge, roughly the same dimensions as GR. Collot et al. (1995) interpreted the Puysegur Ridge as a strike-slip plate boundary that has recently undergone oblique convergence, due to the migration of the Pacific-Australian pole of rotation. The transpressional fault is evolving into an embryonic subduction zone further north. Despite the similarities to the GR, the process of subduction initiation is in inherently unique, with a variety of tectonic environments and variables specific to each example that cannot be explained by a single hypothesis. For these reasons it is important to locate and document not only existing examples of subduction initiation, but also relict evidence of where this process may have failed in order to better understand the full range of variables important for the evolution of subduction zones.

3.7 CONCLUSIONS

Our set of wide-angle transects (Figure 3-7) indicate that there is 12-18 km of crustal thickening associated with the GR. The central transects T2 and T4A clearly indicate an asymmetry associated with the crustal thickening that likely represents the failed underthrusting of the WPB oceanic crust beneath that of the HB. The observed underthrusting likely initiated along an intra-oceanic fracture zone of the WPB that underwent a period of strike-slip deformation throughout the Eocene-Oligocene followed by a short lived compression in the early Miocene. The underthrusting was subsequently abandoned potentially in favor of the Manila subduction system further west later in the Miocene.

Our MCS reflection data along with wide-angle velocity models indicate that the oceanic crust of the HB is thin to normal ocean crustal thickness, on the order of 5-7 km. The crust is relatively undeformed in the west-central part of the basin and highly deformed into a series of ridges and troughs near the GR. The deformation observed within the HB basement is likely older than the onset of arc volcanism associated with the NLA (>16 Ma). Furthermore, the geometry of the underthrusting of the WPB and HB oceanic crust agrees with a young age for the basin (~20-40 Ma) and is consistent with recent geophysical studies (Kuo et al., 2007; Li et al., 2009). The Cretaceous ages determined by Deschamps et al., (2000) likely represent rafted material from another oceanic domain farther south, emplaced by strike-slip faulting during the evolution of the GR and its probable predecessor transform boundary.

MCS reflection data show the bathymetric bench in the HB to be a separate unit from the NLA basement consisting of a shallow layered sedimentary unit underlain by material seismically similar to the basement. A strong reflector at the base of the unit separates it from the arc-basement below. Additionally, the low velocity (3.0-4.0 km/sec) nature of the bench derived from wide-angle velocity models relative to the high velocity (5.0+ km/sec) basement below support this interpretation. Instead, it is likely the bench represents a large accumulation of volcaniclastic and epiclastic debris related to the volcanic activity along the NLA. It is still unclear how or why such an accumulation of volcaniclastic debris was deposited. Further geophysical study and sampling are necessary to provide clues to its origin and depositional history.

The absolute age distribution of the Huatung Basin and timing of the formation of the Gagua Ridge remain unknown. Drilling and accurate dating of sites within the basin as well as along the ridge axis are required to accurately determine the absolute age and style of deformation. Furthermore, detailed seismicity, magnetic, and gravity studies are necessary to confirm the location of intra-basin fracture zones, faults, and the extent of the NLA at all structural levels. Finally, 3D geodynamic modeling is also necessary to accurately represent the evolution of this complex tectonic environment.

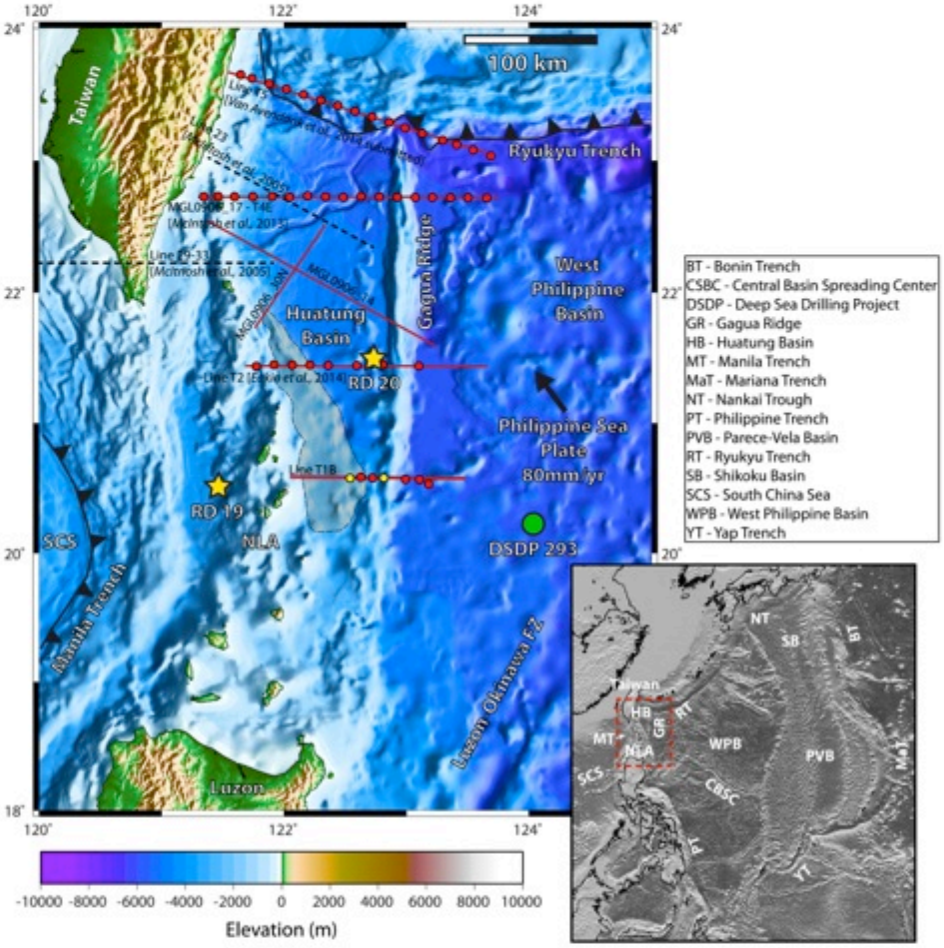

Figure 3-1. Shaded relief map (lower right), and regional bathymetric and elevation map showing the major tectonic elements offshore south and east of Taiwan. MCS reflection data from this study (red lines) were acquired along MGL0906_17, MGL0906_14, and MGL0906_30N. Wide-angle OBS data (red-yellow circles) were acquired along transects T1B, T2, T4A and T5. Black dashed lines denote position of other MCS and wide-angle transects from McIntosh et al., (2005) referred to in this study. Yellow stars (RD 19 and RD20) denote locations of dredge samples from Deschamps et al., (2000). Green circle (DSDP 293) denotes the position of Deep Sea Drilling Site 293 (Hilde and Lee, 1984). Orange transparent zone outlines the bathymetric structure in the Huatung Basin described in this manuscript.

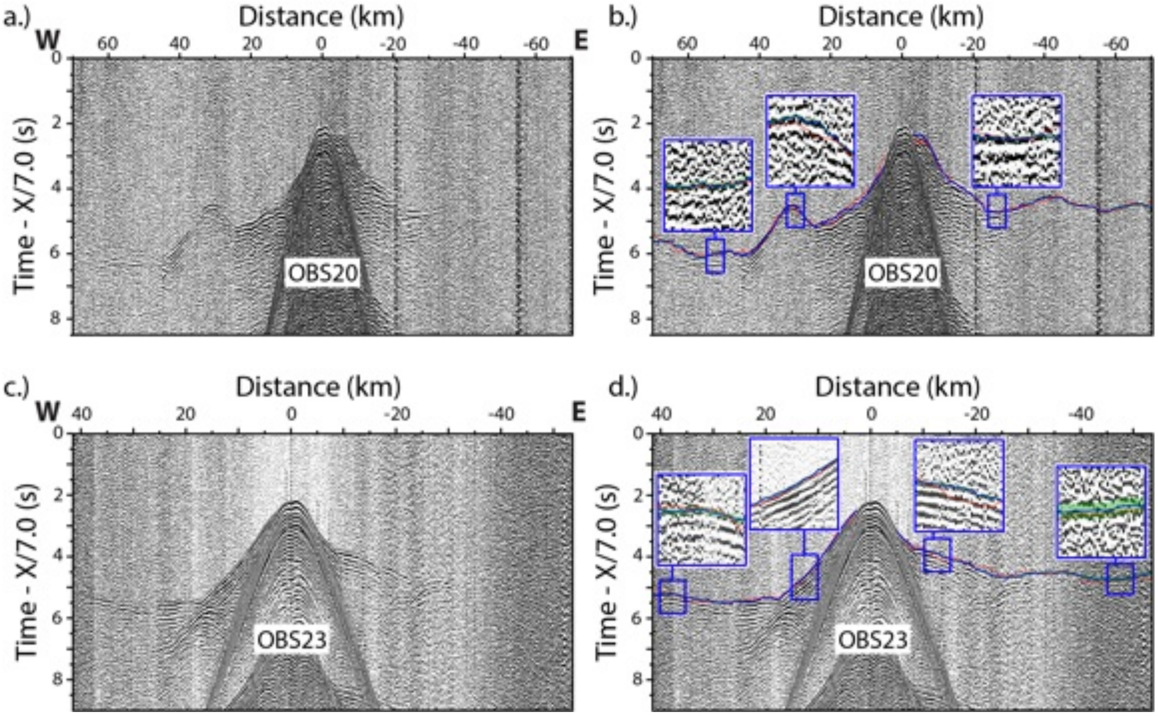

Figure 3-2. Example OBS records from the western (OBS 20) and central (OBS 23) parts of transect T1B. OBS locations are marked in Figure 3-3-1a. Left and right panels show data with minimal processing (bandpass filter, spectral balancing) which was sufficient to resolve first arrival refractions to offsets greater than 50 km. Left panels a. and c., show uninterpreted records, while the right panels b. and d. show picked first arrivals (solid blue line), Pick uncertainties (green window), and calculated first arrivals (dashed red line).

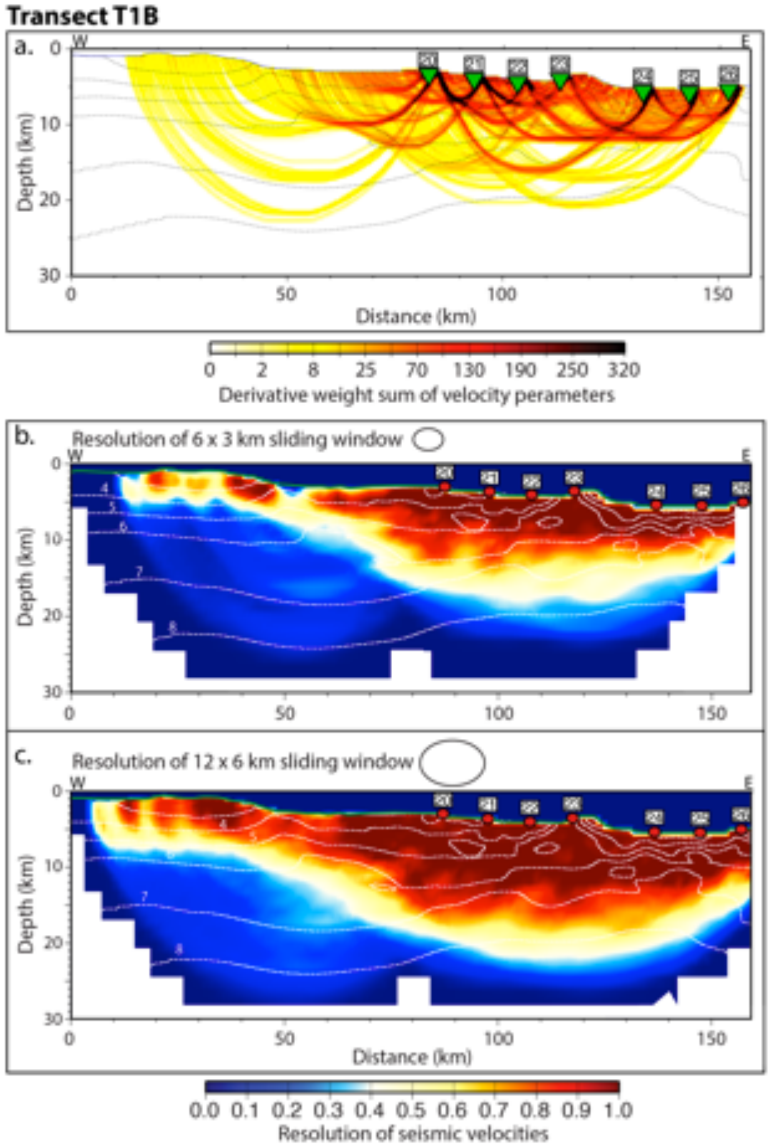

Figure 3-3. a) Derivative weight sum (DWS) of transect T1B shows the ray coverage throughout the model space. Ray coverage is very good in the shallow crust between OBS locations but shows significant variation at depth and to the west due to variable data quality and non crossing raypaths. b-c) Resolution matrix for first-arrival tomography model T1B. Regionals with resolution values of >0.5 are considered well resolved. This test shows that features in the crust are well resolved. Outside OBS locations, resolution suffers, although large wavelength features are still resolved.

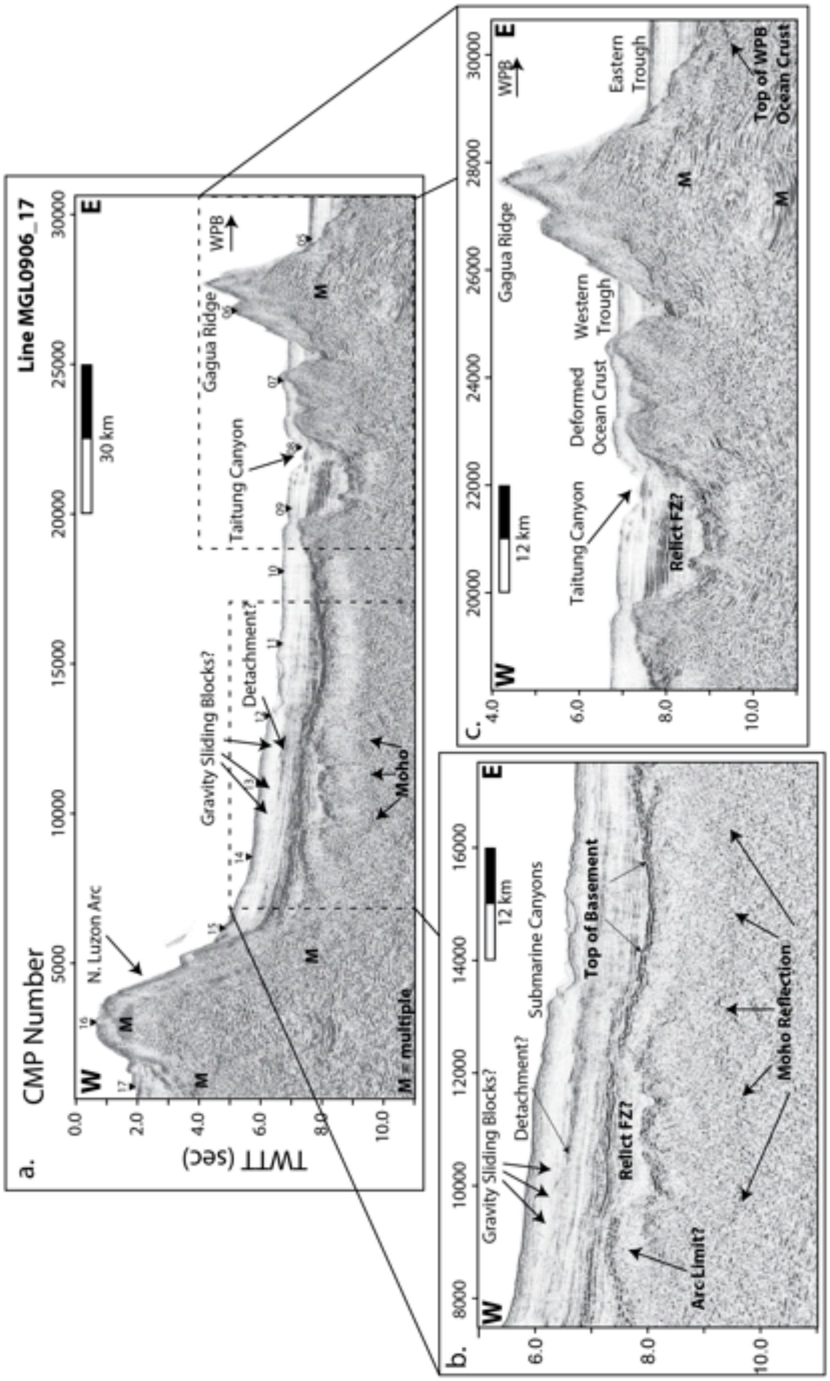
a.
CMP Number
Line MGL0906_17
W
E
0
5000
10000
15000
20000
25000
30000
TWTT (sec)
0.0
2.0
4.0
6.0
8.0
10.0
N. Luzon Arc
M
M = multiple
Gravity Sliding Blocks?
Detachment?
Moho
Taitung Canyon
Gagua Ridge
WPB
30 km
17
16
15
14
13
12
11
10
09
08
07
06
05
b.
8000
10000
12000
14000
16000
Submarine Canyons
Top of Basement
Relict FZ?
Arc Limit?
Moho Reflection
12 km
c.
Deformed Ocean Crust
Western Trough
Eastern Trough
Top of WPB Ocean Crust

Figure 3-4.

Figure 3-4. a) Pre-stack time migrated data from MGL0906_17 coincident with T4A (North Luzon Arc: a; Huatung Basin: b; Gagua Ridge: c). b) The oceanic crust of the Huatung Basin, intermittent Moho reflections and post-collisional sedimentary overburden. c) The deformation associated with the Gagua Ridge bathymetric feature, top of the underthrust West Philippine Basin ocean crust, marginal basins on either side of the structure, and position of the structurally controlled Taitung Canyon. OBS positions from coincident wide-angle transect T2 are marked by black triangles and labeled 05-17; M = water bottom multiple reflection.

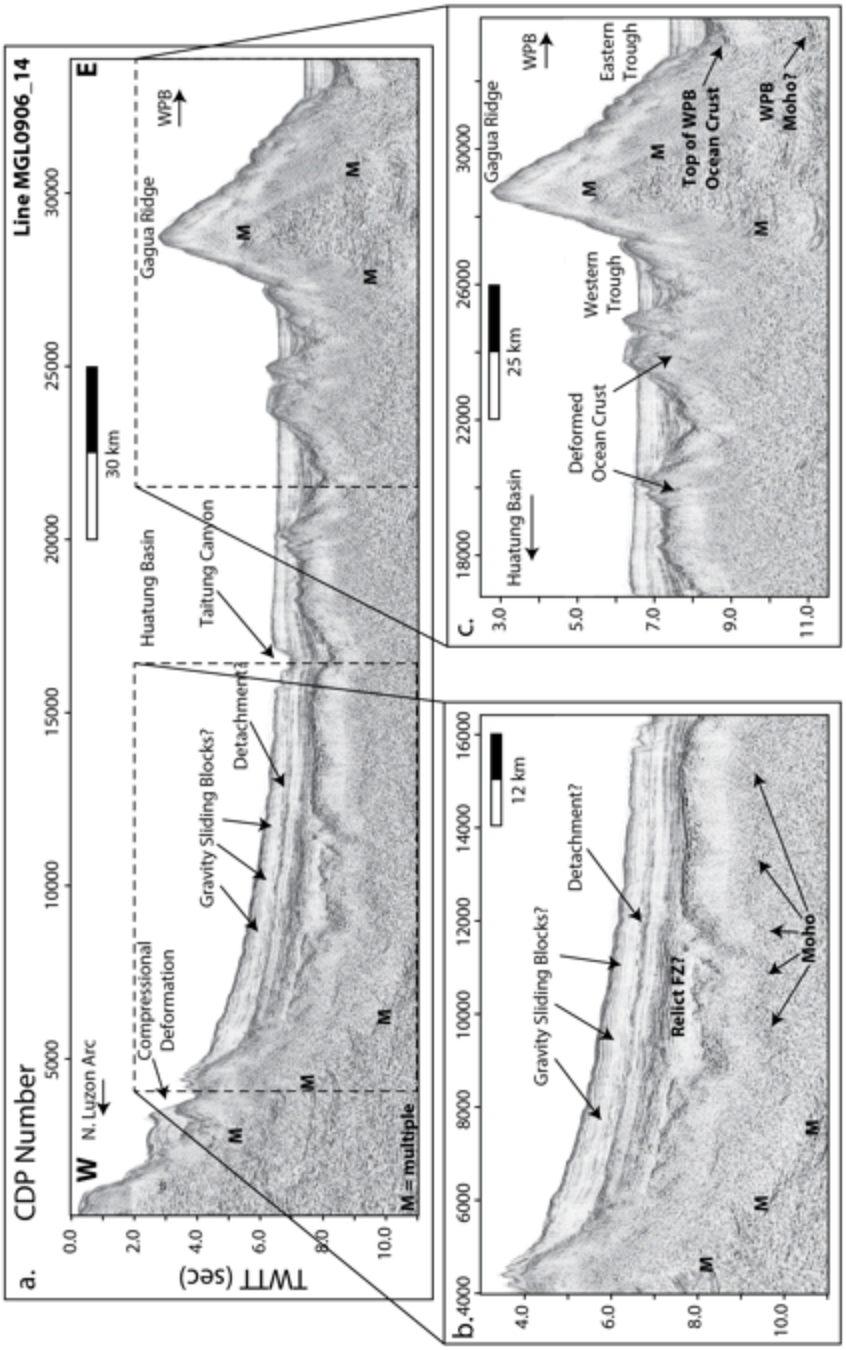
a.
CDP Number
Line MGL0906_14
W
E
N. Luzon Arc
Compressional Deformation
Gravity Sliding Blocks?
Detachment?
Huatung Basin
Taitung Canyon
Gagua Ridge
WPB
30 km
M
M = multiple
TWTT (sec)
0.0
2.0
4.0
6.0
8.0
10.0
5000
10000
15000
20000
25000
30000
b.
Gravity Sliding Blocks?
Detachment?
Relict FZ?
Moho
12 km
4.0
6.0
8.0
10.0
4000
6000
8000
10000
12000
14000
16000
c.
Huatung Basin
Deformed Ocean Crust
Western Trough
Gagua Ridge
Eastern Trough
Top of WPB Ocean Crust
WPB Moho?
WPB
25 km
3.0
5.0
7.0
9.0
11.0
18000
22000
26000
30000

Figure 3-5.

Figure 3-5. a) Pre-stack time migrated data from MGL0906_14 (North Luzon Arc a; Huatung Basin b-c; Gagua Ridge b-c). b) The oceanic crust of the Huatung Basin, intermittent Moho reflections, and post-collisional sedimentary overburden. c) Basement deformation associated with the Gagua Ridge bathymetric feature, marginal troughs on either side of the ridge, top of the underthrust West Philippine Basin ocean crust and potential associated Moho reflection. M = water bottom multiple reflection.

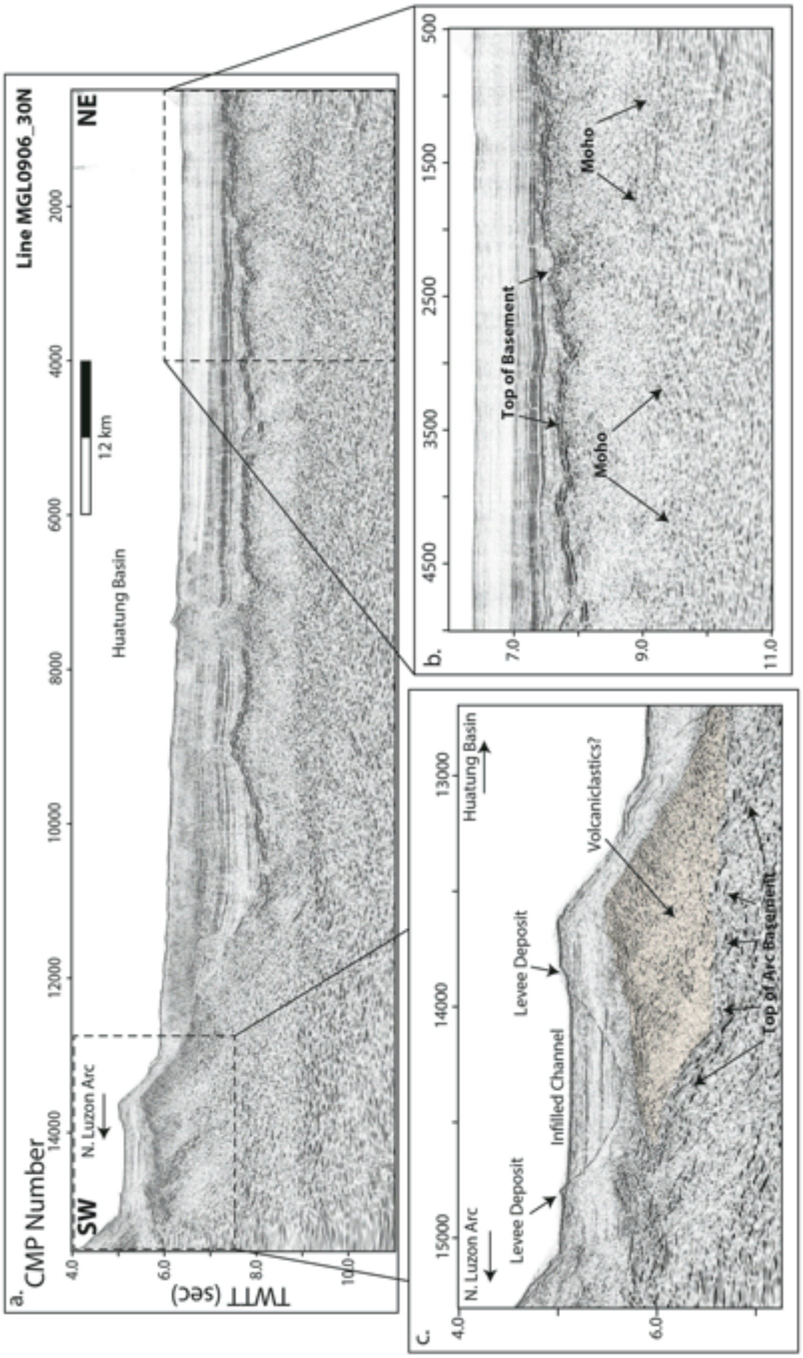
a.
CMP Number
Line MGL0906_30N
SW
NE
N. Luzon Arc
Huatung Basin
12 km
TWTT (sec)
4.0
6.0
8.0
10.0
2000
4000
6000
8000
10000
12000
14000
b.
Top of Basement
Moho
Moho
500
1500
2500
3500
4500
7.0
9.0
11.0
c.
N. Luzon Arc
Huatung Basin
Levee Deposit
Infilled Channel
Levee Deposit
Volcaniclastics?
Top of Arc Basement
15000
14000
13000
4.0
6.0

Figure 3-6.

Figure 3-6. a) Pre-stack time migrated data from MGL0906_30N from the eastern flank of the North Luzon Arc into the Huatung Basin. Panel b shows the structure of the Huatung Basin ocean crust including intermittent Moho reflections, and the overlying post-collisional sedimentary cover. c) Zoom of the bench-like bathymetric structure located near the slope break of the North Luzon Arc. The structure is composed of an upper sedimentary layer and a basal layer that is seismically similar but separate from the arc basement that may represent volcaniclastic and epiclastic debris. An in-filled channel and associated levy deposits are highlighted in the upper sedimentary section.

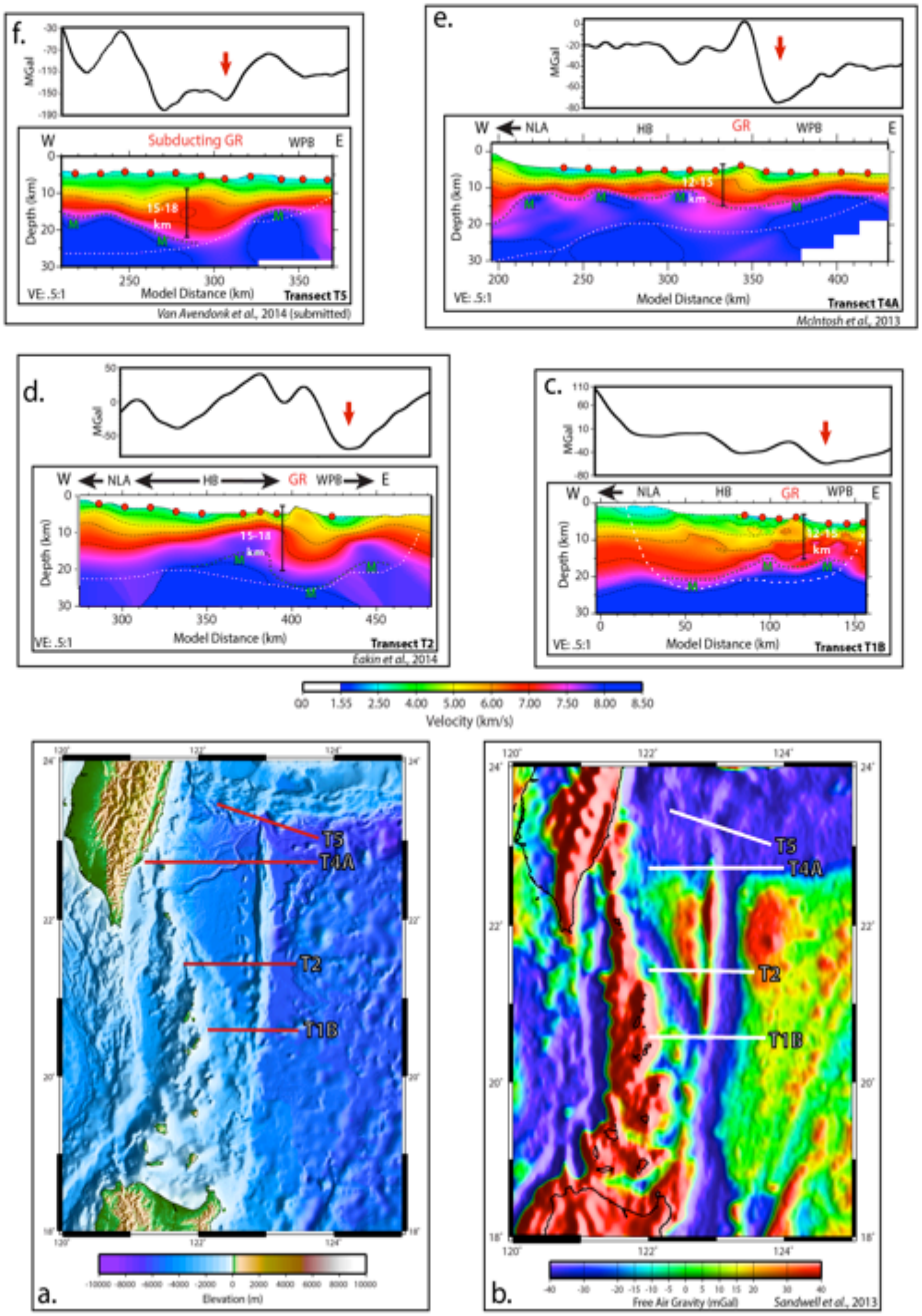f.
MGal
Subducting GR
WPB
W
E
Depth (km)
15-18 km
M
Model Distance (km)
VE: .5:1
Transect T5
Van Avendonk et al., 2014 (submitted)
e.
MGal
W
NLA
HB
GR
WPB
E
12-15 km
Depth (km)
Model Distance (km)
VE: .5:1
Transect T4A
McIntosh et al., 2013
d.
MGal
NLA
HB
GR
WPB
15-18 km
Model Distance (km)
VE: .5:1
Transect T2
Eakin et al., 2014
c.
MGal
NLA
HB
GR
WPB
12-15 km
Model Distance (km)
VE: .5:1
Transect T1B
Velocity (km/s)
0.0
1.55
2.50
4.00
5.00
6.00
7.00
7.50
8.00
8.50
T5
T4A
T2
T1B
120°
122°
124°
24°
22°
20°
18°
Elevation (m)
a.
Free Air Gravity (mGal)
b.
Sandwell et al., 2013

Figure 3-7.

Figure 3-7. a-b) Regional bathymetry and elevation map and equivalent area satellite derived marine gravity map showing the locations of wide angle transects T1B, T2 (Eakin et al., 2013) T4A (McIntosh et al., 2013), T5 (Van Avendonk et al., 2014, Deep crustal structure of an arc-continent collision: Constraints from seismic travel times in central Taiwan and the Philippine Sea, submitted to Journal of Geophysical Research Solid Earth) and associated gravity profiles. c-f) First-arrival tomographic models of transects of c) T1B, d) T2, e) T4A, and f) T5, across the Huatung Basin and Gagua Ridge. All transects are annotated identically and show the velocity model, instrument locations, and the white dashed line marks the limit of good model resolution. Major bathymetric features including the Huautng Basin, Gagua Ridge, West Philippine Basin, and N. Luzon Arc are labeled. The green dashed line and M in the models marks the approximate location of the base of the crust, using additional constrains from seismic reflection profiles. The panel above each model shows an equivalent gravity profile extracted from the same dataset used to create the satellite derived marine gravity map (Sandwell et al., 2013). Red arrow marks the location negative-positive anomaly associated with the Gagua Ridge referred to in the manuscript.

CHAPTER 4: ALONG STRIKE VARIABILITY OF PRISM ARCHITECTURE IN THE INTRA-OCEANIC SUBDUCTION DOMAIN OFFSHORE SOUTHERN TAIWAN.

4-1: INTRODUCTION

Accretionary prisms occur between a trench and associated volcanic arc in a subduction system. In both intra-oceanic and ocean-continent subduction, sediments deposited on the ocean floor are offscraped, accreted and stacked in the accretionary prism (e.g., Karig and Sharman, 1975). In the instance of arc-continent collision, this process can be further complicated by the presence of thick passive continental margin sedimentary sequences (Karig et al., 1987; Teng, 1990) and variable lower plate topography resulting from a change in the composition of the subducting crust from oceanic, to highly faulted extended continental crust. Yet there are few examples of active margins where a transition occurs between subduction of ocean crust and subduction of extended continental crust along the strike (subduction-to-incipient collision) in the present day to inform evolutionary models of an accretionary prism-to-collisional mountain belt.

This problem is particularly pertinent in Taiwan, where there has been much debate over the time-transgressive evolution of the Manila accretionary prism from an intra-oceanic prism to a collisional mountain belt. Huang et al., (2006) noted the Central Range is morphologically contiguous with the Hengchun peninsula and offshore Hengchun Ridge that extends hundreds of kilometers to the south. Recent onshore-offshore tomographic modeling shows the Hengchun Peninsula and southern Central Range (McIntosh et al., 2013) to be comprised of >20 km of high velocity (>5 km/sec) material indicative of basement underplating of extended to hyper-extended continental crust. This underplating is thought to be facilitated by rift-related faulting and detachments developed during the Paleogene rifting of the Chinese continental margin. Additional wide-angle tomographic models from Lester et al., (2013) and Eakin et al., (2013) documented the early stages of this underplating process in the submarine Hengchun ridge, some 50 km offshore southern Taiwan. Together, these models argue that Taiwan is the result of a multi-stage collision in which, thinned continental crust, between 12-15 km thick, is subducted and structurally underplated to the prism prior to the encroachment of the continental shelf (Lester et al., 2013). Eakin et al., (2013) also present an additional wide-angle tomographic profile T1 near 20.6° N that constrains the velocity structure of the Manila accretionary prism and forearc backstop. This result is consistent with previous work from gravity modeling from Chi et al., (2003) that shows the majority of the prism is low velocity (2.5-4.0 km/sec) indicating primarily sedimentary composition and suggesting that until recently, ocean crust was subducting at this location. Perhaps the most intriguing result from this study is the thickness of the prism, reaching a maximum thickness of ~15 km near what appears to be a near vertical forearc backstop.

Although the fundamental mechanisms of sedimentary underplating and accretion are well documented (Karig and Sharmin, 1975; Silver et al., 1985; Meneghini et al., 2009), how these mechanisms operate to construct the unusually large pre-collisional Manila accretionary prism has not been documented. For instance, how does a larger sediment supply affect accretion processes within the prism? What is the proportion of frontal accretion vs. underplating? How does this proportion vary from S-N? We investigate these questions with multi-channel seismic (MCS) reflection data that reveal the sedimentary structures and deformation of the intra-oceanic Manila accretionary prism prior to the subduction of the rifted Chinese continental margin crust. These data reveal a thick sedimentary section (~ 2.0 km – 3.0 km assuming a seismic velocity between 2.0-3.0 km/sec) on the subducting Eurasia plate (EUP) and a well-developed trench wedge. The data show both an increase in the width of the prism as well as a significant change in the seaward slope taper from south to north. These data also show a clear pattern of frontal accretion of the majority of the incoming sedimentary sequence, while a significant volume is bypassed and underthrust beneath the prism. Lines 15 and 17 also highlight a large volume of discontinuous, west and east dipping reflectivity deeper within the prism may indicate that the majority of the uplift of the prism is accomplished by underplating of previously underthrust sedimentary material. Continued increase in the dimensions of the prism along the northern lines 23 and 22 support a model of accretionary prism development where thickening near the toe is accomplished by the frontal accretion and continued deformation of trench wedge sediments and the majority of the uplift is accomplished by underplating of underthust sedimentary material.

4-2: GEOLOGIC BACKGROUND

The arc-continent collision in Taiwan is the final stage in the life of the South China Sea (SCS) marginal basin that began with the rifting of South China in the late Cretaceous forming the southern Chinese continental margin and conjugate margin farther south (Ru and Pigott, 1986). Continental rifting eventually led to break-up and sea-floor spreading in the SCS in the Oligocene – mid-Miocene constrained by magnetic anomaly correlation and seismic reflection studies (Taylor and Hayes, 1983; Briais et al., 1993; Nissen et al., 1995; Barckhausen et al., 2014). Oceanic crust of the SCS likely began subducting east beneath the PSP starting in the earliest Miocene (Yang et al., 1995; Hall, 2002). The consumption of the SCS oceanic crust formed the Manila accretionary prism and NLA that acts as a backstop to the deforming prism (Figure 1).

Due to the obliquity of the convergence between the NLA and passive Chinese margin, the Taiwan arc-continent collision initiated in central-northern Taiwan ~4-7 Ma (Huang et al., 2006) and actively propagates southward at a rate of 60-90 km/Myr (Byrne and Liu, 2002; Lee et al., 2006; Suppe, 1984). Previous investigators have exploited this time-transgressive geometry interpreting different spatial transects across Taiwan as representations of different temporal stages of collision evolution. In northern Taiwan, post-collisional processes have waned while active collision is believed to be occurring in the south central portion of the island, and incipient collisional process operate immediately offshore to the south (Huang et al., 2000). Further south, offshore northern Luzon likely represents the pre-collisional, intra-oceanic subduction conditions of the SCS and Manila trench subduction system (Byrne and Liu, 2002).

Numerous geophysical studies have focused on the Manila trench and accretionary prism south of Taiwan. North of 20° N, the Manila accretionary prism grows significantly (Figure 4-1), likely due to incipient collisional processes initiated by the introduction of the rifted continental margin crust near ~20.5°N and proximity to sediment sources of the Chinese margin and Taiwan mountain belt (Huang et al., 2006). In this area, several studies (Davis et al., 1983; Liu et al., 1997) describe the accretionary wedge as a doubly-vergent prism, with a lower slope domain consisting of imbricate folds and thrusts, and an upper slope domain characterized by a lack of seismic reflectivity and an increase in the bathymetric slope from the thrust fault ridges of the lower slope. Lin et al., (2009) infer that this bathymetric change may be controlled by the presence of one or more out-of-sequence thrusts (OOSTs) while others (Reed et al., 1992) infer that thickening was accomplished via passive duplex undeplating. Liu et al (2004) and Lin et al (2008) used multi-channel seismic reflection (MCS) data and swath bathymetry offshore southwest Taiwan to show that the pre-deformational architecture and morphology of the rifted continental margin exerts strong controls on the structural style of the lower, frontal part of the accretionary prism. Ku et al., (2009) used MCS reflection images to study the deformation of the trench fill sediments and crustal structures in the incipient collision realm of the Bashi Strait.

Shortening of the accretionary prism is also accommodated by deformation in the rear of the wedge (Lundberg et al., 1997) and of the forearc basin (Cheng, 2008; Malavieille et al., 2002; McIntosh et al., 2005). Chi et al., (2003) used MCS and shipboard gravity to study the deeper structure of the Manila accretionary prism. A key result of their work was the presence of a free-air gravity high at the rear of the prism at 20.9° N, requiring a significant component of high-density material. In contrast, a second transect to the south near 20.2° N did not express the same free-air gravity high and is consistent with an accretionary prism composed entirely of sedimentary material.

Despite the successes of the various geophysical studies presented above, none of these investigations clearly image the key structural components in the interior of the prism in the intra-oceanic subduction domain. This is extremely significant, as the structures developed here are likely similar to those modified by basement underplating of rifted continental crust to the north as shown by McIntosh et al. (2013). Our goal is to use selected MCS transects to document the early evolution of the sedimentary accretionary prism to improve the understanding of the accretion and underplating processes in the Manila trench prior to the subduction of the distal margin crust. The key objectives of this analysis are 1) Identify the primary modes of deformation and growth in the accretionary prism, and 2) Identify differences in morphology to document characteristics of the south to north evolution of the prism. Documenting this first stage of accretionary prism development will help complete the picture of the entire evolutionary process of arc-continent collision.

4-3: DATA AND PROCESSING

MCS reflection profiles included in this manuscript (lines 15, 17, 22, and 23 from here forward) were acquired over the course of two of the three legs of the 2009 marine TAIGER experiment. Each transect is approximately trench perpendicular and constrains the structures associated with the subducting SCS crust and overriding accretionary prism of the Manila subduction system (Figure 4-1). MCS acquisition and source firing was performed with the R/V Marcus G. Langseth with a source array that consisted of 36 air-guns with a total volume of 6600 in3 towed at a depth of 8 m. Nominal source interval was 50 m and recorded on a 6 km, 468 channel streamer with a channel spacing of 12.5 m. Data were recorded for 15 sec at a 2 ms sample rate.

4-3-1: MCS data processing

MCS data were processed through pre-stack time migration following standard techniques including trace editing, sorting into common mid-point (CMP) gathers, normal-moveout (NMO) velocity analysis and correction, stack, band-pass filtering and f-k migration. Additionally, all data were subject to advanced multiple attenuation techniques including surface-related multiple (SRME) attenuation and Radon transform multiple attenuation designed to improve resolution of important structures within the deeper portions of the accretionary prism (see additional description in Lester and McIntosh, 2012). Prior to the application of Radon, the data were re-sorted to 12.5 m CMP effectively increasing the number of traces from ~60 traces per CMP to ~120 traces per CMP in an effort to increase the signal to noise ratio. Following the multiple removal applications, muting and offset weighted stacking were applied to reduce residual multiple energy and enhance deeper reflectivity following pre-stack time migration.

4-4: STRUCTURE OF THE INTRA-OCEANIC MANILA ACCRETIONARY PRISM

The MCS data provide new, high-resolution constraints on the sedimentary structures and deformational processes of the Manila accretionary prism offshore northern Luzon. Our results yield new insights into the nature of accretionary processes at the toe, lower-slope, and upper slope domains along the strike of the Manila accretionary prism. The MCS reflection profiles will be described from south to north. Lines 17 and 15 show similar morphology and structure in the south whereas lines 23 and 22 share similar characteristics farther north.

4-4-1: MCS Reflection Line 15

Line 15 extends southeast from the SCS basin and crosses the Manila subduction zone near 20°N (Figure 4-1, 4-2a-c). Here the Manila Trench accretionary prism maintains an average width of ~50 km. West of the trench, we image ~1.8-2.7 km thick sediments (assuming seismic velocities between 2.0-3.0 km/sec) on top of the incoming oceanic basement (Figure 2a). Seaward of the frontal thrust (CMP 9370-7651), a well-developed trench wedge is imaged that is composed of horizontal strata (Figure 4-2b-c). On average, the trench wedge is ~22 km wide and ~1.0 sec TWTT thick, or ~1.0-1.5 km (assuming a seismic velocity of 2.0-3.0 km/sec). Between CMP 9447-9849, the upper ~1.5 sec TWTT of the sedimentary section are deformed by east and west dipping thrusts that sole into a sub-horizontal reflector interpreted near 7.0 sec TWTT and form a popup structure at the seafloor. The sedimentary section below this reflection is thinly bedded and less reflective. (Figure 4-2b-c). East of this initial deformation, a high amplitude reflection separates the faulted sedimentary section from the lower unit below and separates sediments that will be accreted at the toe from those bypassed with the subducting ocean crust. Based on these observations, we infer that this reflector likely represents the basal décollement. The lower interval is ~0.75-1.0 km in thickness and continues to the east beneath the frontal thrust zone, maintaining its thickness as it does so. East of CMP 10653, the reflectivity within this interval increases and the position of the reflector becomes difficult to interpret.

Near CMP 10251, we observe an increase in slope associated with east dipping frontal thrusts and west dipping backthrusts bounding a lightly folded package of trench wedge sediment (Figure 4-2b-c). The east dipping thrusts extend from the seafloor to a depth of ~7.0 sec TWTT, where we infer that they likely sole into the location of the décollement interpreted above. It appears that initial thickening of the prism is accomplished by the frontal accretion and continued deformation of primarily trench wedge sediment while a large thickness (0.75-1.0 km) are bypassed and allowed to underthrust with the subducting oceanic basement.

The taper of the prism slope is consistent between the frontal thrust zone and the highest elevations of the prism and therefore does not distinguish a separate upper slope domain (Figure 3a). Figure 3b-c shows a segment of the prism east of that shown in Figure 2b-c. Within this interval, the prism reaches its maximum thickness (~8-10 km). Apart from a small wedge of slightly deformed layered strata near the seafloor at CMP 11615 and very fine scale shallow bedding near the seafloor, the shallow section of the upper slope is largely incoherent suggesting perhaps the original bedding is largely dismembered at this state of advanced deformation (Figure 4-3b-c). Shallow in the section, we observe an intermittent, high-amplitude low-frequency reflector between CMP 12019 and the eastern end of the zoomed profile at 3.0-3.5sec TWTT that mimics the seafloor topography (Figure 4-3b-d) and most likely represents evidence for fluid accumulation or bottom simulating reflector (BSR). Water-bottom multiple reflection attenuation techniques were very successful in this part of the prism and reveal a large zone of semi-coherent reflectivity below ~5.0 sec TWTT (Figure 4-3b). Within this zone we observe both west and east dipping reflections, segments where the reflectivity appears horizontal, and both anitformal and synformal reflectivity. These intermittent reflectors appear at different depths and may indicate multiple levels of deformation (Figure 4-3c). Near the seafloor, intermittent, east-dipping reflectivity may be an indication of widely spaced thrusts. The majority these faults appear to sole out ~2.0-2.5 sec TWTT below the seafloor, near the top of the zone of deep reflectivity. East of CMP 11615 the faults potentially extend deeper than 5.0 sec TWTT. These observations suggest that much of the volume increase is accomplished by thickening of the underthrust sedimentary interval, however due to the complex nature of the reflectivity a unique interpretation is difficult, therefore we offer several alternate explanations in the discussion.

The rear of the prism represents the highest seafloor topography and is characterized by east dipping reflective fabric on the arcward slope (Figure 4-4a-c). A high-amplitude low frequency reflector, ~0.5 sec TWTT from the seafloor, can be traced from the west end of the profile, down the prism slope to near the forearc basin. The shallow strata above this horizon are very finely bedded and locally deformed and folded and likely represent recent sedimentation above the older deformed prism strata. The high amplitude-low frequency horizon is offset near CMP 13029 and most notably near CMP 13331 where we interpret a large thrust faults that extend from the seafloor to near the forearc basement before the residual seafloor multiple obscures further interpretation. Additional evidence for uplift in this area is shown by the eastward tilting of the forearc basin strata near CMP 14241 (Figure 4-4b-c).

4-4-2: MCS Reflection Line 17

Line 17 extends E-W near 20°N from the SCS basin and crosses the Manila subduction zone and line 15 at an oblique angle (Figure 4-1, 4-5a). As a result, the morphology observed along this transect is very similar. West of the trench, we image ~2.0-3.0 km of horizontal sediments (assuming seismic velocities between 2.0-3.0 km/sec) on top of the incoming oceanic basement (Figure 4-5a). Seaward of the frontal thrust (CMP 7035), the data show a well-developed trench wedge that is composed of flat lying strata (Figure 4-5b-c), ~28 km wide (oblique transect) and a maximum of ~1.0 sec TWTT thick, or ~1.0-1.5 km assuming a seismic velocity of 2.0-3.0 km/sec. The trench wedge strata are lightly deformed with minor extensional faulting (Figure 4-5b-c). Between CMP 6433-7035 we observe both east and west dipping thrust faults that sole into a sub-horizontal reflector near 7.0 sec TWTT similar to that observed along line 15 and likely representing the basal décollement. These faults bound an uplifted and slightly deformed package of strata into the popup structure. East of CMP 6231 this pattern is repeated upslope where we clearly observe east dipping thrusts and oppositely dipping backthrusts bounding packages of uplifted trench sediment. The east dipping thrusts sole into the same sub-horizontal décollement observed near the toe in the lower sedimentary unit above the basement. The lower sedimentary section is ~0.75-1.0 km in thickness, and less reflective than the overlying trench wedge strata. The underthrust interval maintains its thickness beneath the frontal thrust zone (CMP 5025-6231) with little evidence of deformation from the east dipping thrusts (Figure 4-5b-c).

Similar to line 15, the taper of the prism slope is constant between the frontal thrust zone and the highest elevations of the prism (Figure 4-6a), with only limited convex curvature. Figure 4-6c-d shows a segment of the prism to the east of that shown in Figure 4-5b-c. The shallow section (CMP 4623-3417; 1.5-2.0 sec TWTT) consists of fault bound packages of layered sedimentary strata that appear to have been accreted in a similar manner to those observed in the frontal thrust zone and coherently uplifted to their present position. Steep, east dipping reflectivity highlight the paths of thrust faults that can be traced to ~5.5 sec TWTT. Water-bottom multiple reflection attenuation techniques were again very successful and reveal a zone of semi-coherent reflectivity below ~5.0 sec TWTT that is very similar to that observed along line 15 (Figure 4-3b-c). Within this zone we again observe both west and east dipping reflections, as well as segments where the reflectivity appears horizontal, and others appearing to ‘roll-over’ forming antiformal structures (Figure 4-6b). The relatively undeformed nature of the shallow section of the prism may indicate that these strata were passively uplifted to their current position by underplating from below, possibly in the form of a duplex or series of duplexes. Therefore, we offer similar interpretations to line 15 in the discussion to explain the nature of the deeper reflectivity (Figure 4-6b-c).

The rear of the prism is highly reflective, showing evidence for folding and continued deformation along steeply dipping thrusts (Figure 4-7a-c). A high-amplitude reflection dominates much of the shallow section with ~0.5 sec TWTT of thinly bedded sedimentary sediments draped over much of the prism slope. The high amplitude reflection is segmented between CMP 1809-2211 and folded between CMP 1407-1809, further indicating the presence of steeply dipping thrusts (Figure 4-7b-c). The sediments in the westernmost forearc basin are deformed possible by an east dipping thrust indicating continuing deformation and uplift in the rear of the prism. Unfortunately, interpretation below ~5.0 sec TWTT is compromised due to the presence of residual multiple energy, however steeply dipping reflective fabric supports the interpretation of steeply dipping structures (Figure 4-7b-c).

4-4-3: MCS Reflection Line 23

Line 23 extends NW-SE and crosses the Manila prism ~50 km north of lines 15 and 17 (Figure 4-1, 4-8a). Over this interval, the prism increases in width to ~70 km compared to ~50 km along the southern transects. West of the trench, ~2.5 sec TWTT, or ~2.5-3.75 km of flat-lying sediments (assuming seismic velocities between 2.0-3.0 km/sec) cover the incoming oceanic basement (Figure 4-8a). Seaward of the frontal thrust, pervasive normal faulting cuts the entire sedimentary section (Figure 8a) that are likely related to plate bending as the SCS ocean crust enters the Manila trench. Notably, we observe a basement high seaward of the trench near CMP 4000 that is completely buried by the overlying sedimentary sequence. This variability in basement topography continues beneath the frontal thrust zone and lower slope (Figure 4-8b-c). Interestingly, in contrast to the MCS profiles described previously, the dimensions of the trench wedge decrease here to an average width of ~15 km and ~0.75-1.0 sec TWTT thick, or ~1.0-1.25 km assuming a seismic velocity of 2.5 km/sec (Figure 4-8a). A similar observation was made by Ku and Hsu (2007) and may be an early indication of a seaward migration of the prism.

The frontal thrust zone is characterized by east dipping thrust faulting and anticlinal folding (Figure 4-8b-c). Interestingly, the frontal thrust cuts nearly the entire trench wedge package and appears to sole into a sub-horizontal décollement near 7.0 sec TWTT. The décollement is likely stratigraphically controlled, however its exact location is difficult to interpret.

Between CMP 6600-7400 (Figure 4-8b-c) a topographic high emerges from the prism slope that is coincident with local high in the basement topography. The shallow section of the uplifted area is composed of layered sedimentary strata similar to that in the trench wedge that has been lightly deformed and uplifted primarily by east dipping thrusts and west dipping backthrusts. Within this same CMP interval, between 6.0 and 7.0 sec TWTT, the section is characterized by closely spaced, oppositely dipping reflectivity with evidence of sub-horizontal reflectivity between. The significance of the complex reflectivity may indicate a complex series of folding and faulting at depth (Figure 8c). We propose that the subducting basement topography is responsible for the intensified deformation and local uplift at the seafloor.

East of the local uplift, the surface taper of the prism slope becomes horizontal between CMP 7000-8400. The shallow section within this CMP interval (~4.5-5.5 sec TWTT) is composed of layered strata similar to that observed in the trench wedge that is deformed by a dense network of minor faulting. Linear, east-dipping reflectivity supports the interpretation of larger thrust faults that likely sole into a décollement interpreted near 7.0 sec TWTT. East of CMP 7000, the nature of the décollement is difficult to interpret. Faint reflectivity between CMP 7200-7800 near 7.0 sec TWTT may indicate a structural or stratigraphic boundary, however this zone becomes diffuse farther east making further interpretation speculative. The dense network of faulting in the shallow section may be to blame for the lack of deeper coherent reflectivity below, as a significant portion of the seismic energy may have been attenuated at shallow depths. Although it is poorly defined, we tentatively suggest that the décollement surface continues to the east at a similar depth (~6.5-7.0 sec TWTT) as the décollement we interpret in the frontal thrust zone.

Unlike lines 15 and 17 to the south, the prism along line 23 has developed a distinct upper slope domain that is delineated from the lower slope by an increase in the surface slope to the crest of the prism (Figure 4-9a-c). Reflectivity within the prism at this location is largely discontinuous apart from a zone of thinly bedded sedimentary drape at the seafloor and a small, perched basin near CMP 9000. Topographic highs on the upper slope may signal the presence of widely spaced thrust faults, however evidence for fault plane reflectors is limited to the upper ~2.0 sec TWTT. This is due to the presence of strong residual multiple energy that limits our ability to interpret potential structures below ~6.0 sec TWTT. Therefore, we can only speculate on the potential for thickening of the prism from below although we would expect similar structures to those observed along lines 15 and 17 to the south.

The morphology of the arcward slope of the prism is very similar to that observed on lines 15 and 17 to the south (Figure 4-10a-c). The majority of the prism slope is draped with ~0.25 sec TWTT, or 250-375 m, of thinly bedded sediments separated from the heterogeneous, and presumably older prism strata below by a high amplitude reflective zone (Figure 4-10b-c). Large folding deforms the reflective zone, most notably between CMP 10200-10800. This large wavelength folding is likely accomplished by high angle thrust faults that radiate from a location near the forearc backstop (Figure 10c). Deeper interpretation of potential structures including the subducting SCS slab is obscured by strong residual multiple energy below 5.0 sec TWTT. Near CMP 11200, an east dipping thrust uplifts and deforms the sedimentary strata of the forearc basin. The fault likely extends to the sediment basement interface and suggests the rear of the prism is actively uplifting and deforming.

4-4-4: MCS Reflection Line 22

Line 22 extends ~E-W south of 20° N and is the northernmost transect discussed in this paper. While the entire transect extends eastward across the Manila accretinary prism and NLA, we only show a subset from the entire profile that crosses the accretionary prism (Figure 4-11a). The prism width at this latitude is ~90 km, compared to ~70 km along line 23, and ~50 km along the southern transects 15 and 17, again, indicating lateral growth of the prism. West of the trench, ~2.0 sec TWTT, or ~2.0-3.0 km of flat-lying sediments (assuming seismic velocities between 2.0-3.0 km/sec) cover the incoming oceanic basement (Figure 4-11a). Pervasive faulting is clearly observed in the sediments below the trench wedge. Only a handful of these faults slightly offset the trench wedge strata (Figure 4-11a). Similar to line 23, the trench wedge is ~15 km in width, ~1.0-1.5 km maximum thickness, and separated from the sedimentary section below by a series of high amplitude reflectors that dip towards the frontal thrust zone.

The frontal thrust zone shows a series of east dipping thrusts and anticlinal folding of the (CMP 13800-13000) followed by the development of landward verging backthrusting east of CMP 13200 (Figure 4-11b-c). The frontal thrust clearly cuts and deforms the trench wedge strata, however, unlike line 23, the curvature of the faults suggest a shallow basal décollement at or near the base of the trench wedge strata. If true, the entire lower interval (~1.5 km) is bypassed with the subducting oceanic crust and underthrust beneath the prism. The seismic character of the lower strata is less reflective than the trench wedge strata.

Between CMP 11600-12600, the seafloor is locally uplifted into a topographic high similar to that observed along line 23. The majority of the uplift appears to be achieved by a large, east dipping thrust that extends from the seafloor near CMP 12600 and becomes sub-horizontal near ~7.0 sec TWTT, possibly indicating the presence of a décollement at this depth. This inferred décollement is present at a similar structural depth to that observed near the frontal thrust zone to the west. We interpret that the décollement continues east at a similar stratigraphic level (Figure 4-11c). The shallow section of the topographic high is composed of accreted trench wedge strata that have been lightly deformed by larger east dipping thrust and smaller west dipping backthrusts.

East of CMP 11800, the prism slope surface exhibits the same horizontal taper angle observed along line 23. Between CMP 11400-19000, west-dipping reflectivity is observed between 4.5-5.5 sec TWTT, which may be an indication of fault plane reflectivity (Figure 4-11b-c). It is possible these reflectors represent a series of backthrusts branching off of a larger, east dipping thrust. Interestingly, east of CMP 11400, deeper reflectivity indicates the presence of buried, east dipping fault planes. The nature of the décollement within this interval is difficult to determine. Based on its position in the frontal thrust zone, it is likely that the décollement continues east at a similar structural depth (~7.0 sec TWTT) to that observed in the frontal thrust zone.

The upper slope is delineated from the lower slope by an increase in the taper angle to the crest of the prism (Figure 4-12a-c). Similar to line 23, reflectivity within the prism is largely discontinuous apart from a zone of thinly layered strata draped at the seafloor. In the upper 2.0 sec TWTT of the section, east dipping reflectivity is associated with topographic changes at the seafloor and may indicate the presence of fault planes at depth (Figure 4-12b-c). The dip of the interpreted reflectivity increases to the east, consistent with observations on line 23 to the south. Interpretation of these fault planes in the deeper section is difficult due to the presence of residual seafloor multiple and migration artifacts. However, based on evidence for similar east dipping reflectivity on line 23 to the south, we interpret that the upper slope here is deformed and uplifted in a similar manner (Figure 4-12b-c).

The morphology of the arcward slope of the prism is different from the previous transects. The rear of the prism appears to be uplifted >1.0 sec TWTT, or ~1.5 km in elevation when compared with line 23 to the south (Figure 4-13a-c). Additionally, the well developed strata of the North Luzon trough forearc basin that are present on all transects to the south are missing and the flank of the NLA is juxtaposed against the rear of the prism (Figure 13b-c). The thinly bedded draped strata are limited to the highest elevations (CMP 8000-8800) where the taper is low. The upper 1.0-1.5 sec TWTT of this same CMP interval shows prominent, steeply east dipping reflectivity that we interpreted to be evidence of fault plane reflections. The shallow draped strata are disturbed above several of these faults indicating that faulting reaches the seafloor. Strong residual multiple energy dominates much of the deeper section below ~4.0 sec TWTT making deeper interpretation of fault traces difficult. However, it is likely that these faults are deeply seated and localize near the prism interface with the forearc backstop.

4-5: DISCUSSION

4-5-1: Variability in behavior of the frontal thrust zone and lower slope

The frontal thrust zone in all transects (Figures 4-2, 4-5, 4-8, and 4-11) show variations in the style of thrusting, however all transects exhibit frontal accretion of the upper 1.5-2.0 km of incoming sediment and underthrusting of the remaining bottom ~0.75-1.5 km of sediments. Both MCS lines 15 and 17 (Figures 4-2 and 4-5) show popup structures and uplifting wedges of sediments into the lower slope similar to those observed in the Aleutian (Davis and Von Huene, 1987), Oregon, and Nankai accretionary prisms (Lallemand et al., 1994). These authors used these popup structures to determine the "internal" and "basal effective" coefficient of friction at the toe of these prisms. Primary east dipping thrusts sole into a sub-horizontal reflection that we interpret to represent a décollement near 7.0 sec TWTT (Figure 2b-c; 5b-c). Based on its parallelism with the strata above and below, the décollement is clearly stratigraphically controlled, however it is not associated with a strong, distinctive reflector in the sedimentary sequence in front of the accretionary complex. Lewis and Hayes, (1984) speculated that trench turbidites are the preferentially accreted whereas pelagic or hemipelagic sediments are preferentially bypassed and subducted. Below the interpreted décollement, the reflectivity of the strata is low, potentially indicating a compositional change and/or the presence of high pore fluid pressures. The low reflectivity decreases within this interval as it continues beneath the frontal thrust zone. The loss in reflective character may be due to the intersection with a thrust fault that acts as a conduit for pore water (Cloos, 1984), and so the loss in brightness might be from dewatering of the sequence through pathways provided by the faulting. Alternatively, fluid escape may occur as a result of hydrofracturing through a system of dilatant fractures parallel and perpendicular to the décollement as proposed by Meneghini et al., (2009).

Initial thickening of the prism along line 23 and line 22 is accomplished by primarily east dipping imbricate thrusts that deform the upper section of the incoming strata into a series of anticlinal folds (Figure 4-8 and 4-11). The development of conjugate backthrusting occurrs after initial faulting as a result of continued compression. The position of the interpreted décollement changes in the frontal thrust zone from a position within the strata below the trench wedge along line 23 to a position corresponding with the base of the trench wedge on line 22 to the north. Although a change in the position of the décollement is not unusual over such a short distance, we submit that local variations in the topography of the subducting oceanic basement, observed along both line 23 and 22 (Figure 4-8b-c; 4-11b-c) alter the behavior of the décollement in a way similar to a subducting basement asperity as modeled by Lallemand et al., (1994). Similar topographical morphologies are observed in several other accretionary prisms as a result of seamount subduction including Tonga (Ballance et al., 1989). In these examples, the subducting basement topography cause prism-ward compression/shortening, local uplift of the prism above the basement topography and obstruction or partial obstruction the basal décollement propagation. The décollement is then forced up-section and a new décollement forms near the top of the basement topography. The explanation for the sudden jump of the active décollement to the base of the trench wedge observed along line 22 is unclear (Figure 4-11). It is likely that the boundary between the trench wedge sediments and underlying sedimentary section represents a weaker mechanical boundary that is easier to exploit.

The subduction of variable basement topography may cause local uplift near CMP 7000 on line 23 (Figure 4-8b-c) and CMP 12200 on line 22 (Figure 4-11b-c), and may explain the horizontal taper of the prism slope to the west of the observed uplift. Park et al., (1999) observe similar uplift and low taper geometry of the landward part of the wedge associated with seamount subduction. In their model, as the seamount subducts, the prism uplifts landward and subsides seaward. These combine to form a thickened prism with low taper and a local high at the location of the seamount. As the seamount continues to subduct, strong compression is expected within the landward, thickened part of the prism. We observe strong evidence of both east and west dipping thrust faulting east of the interpreted subducting basement topography along lines 23 and 22 (Figure 4-8 and 4-11) in agreement with this model.

4-5-2: Models for Accretionary Prism Growth

While it has recently been shown that the subduction of the extended continental margin crust of the northern SCS margin is an important phase in the evolution of the Manila accretionary prism and subsequent arc-continent collision (McIntosh et al., 2013; Lester et al., 2013; Eakin et al., 2013), our data highlight a number of previously unrecorded fundamental observations of prism structures in the intra-oceanic subduction domain offshore northern Luzon. For instance, the topographic slope of the prism changes dramatically from south to north from a fairly consistent taper along lines 15 (Figure 4-2a) and 17 (Figure 4-5a), to the development of distinct lower slope and upper slope domains along lines 23 (Figure 4-8a) and 22 (Figure 4-11a). Over this same interval, the width of the prism nearly doubles from an average of ~50 km along the southernmost line 15, to more than 90 km along the northernmost line 23 (Figure 4-1). One of the surprising features of our data is deeper prism reflectivity associated with the highest elevations of the prism along lines 15 (Figure 4-3b-d) and 17 (Figure 4-7b-d). Unfortunately, our data do not unambiguously constrain the structures responsible for the observed reflectivity. However, we can gain insight into its nature by considering our interpretation of the deeper reflectivity within the prism and the mechanisms by which a wedge thickens to achieve critical taper.

If we have imaged a large volume of structurally thickened material in the rear of the prism, then it may be possible that frontal accretion is the dominant mode of deformation and continued growth of the prism is accomplished by large thrusts and perhaps OOSTs that uplift and deform material previously accreted at the toe of the prism. A simplified model of this process is shown in Figure 4-14a-b where the prism growth is driven by frontal accretion of the entire incoming sedimentary section by a series of imbricate thrust faults or imbricate fan of thrusts that sole into a central décollement located at the top of the basement (Figure 4-14a). With continued convergence, OOSTs may develop as a mechanism to structurally thicken the wedge and maintain critical taper (Figure 4-14b). Reed et al., (1992) suggested significant shortening in the central part of the prism is accomplished with out-of-sequence thrusting in the Manila prism father north near 22°N, though its development may have been in response to significant shortening occurring in the forearc domain. Evidence of east-dipping faults is observed in the upper 2.0 sec TWTT of the arcward parts of the prism in all reflection profiles (Figures 4-3, -6, -9, and -12). Large imbricate thrusts and OOSTs could act as conduits for dewatering occurring as a result of continuing compaction deep within the prism. The high-amplitude low-frequency reflections observed in the shallow section on Figure 3b-c may therefore represent accumulations of dewatered fluids that have migrated along permeable fault planes similar to observations associated with the "bottom-simulating-reflector" in the Makran accretionary prism (Minshull and White, 1989). However, it is difficult to determine the magnitude of slip and the depth of penetration of the observed fault planes given the variability of the resolution in the reflection profiles and therefore difficult to determine if the observed thicknesses of the prism (8-10 km) can be achieved by frontal accretion alone and continued thickening via OOSTs.

Alternative to prism growth via complete frontal accretion, our interpretations support a model where the deeper zone of reflectivity represents a large accumulation of underplated material. A simplified model of this process is shown in Figure 4-14b-c where the upper ~2.0 km of the incoming sedimentary section including the trench wedge are accreted by imbricated thrusts that sole into a shallow décollement within the sedimentary section, while the remaining ~1.0 km of sediment below the décollement are underthrust and subsequently underplated. Underplating requires the décollement to "step-down" to a deeper structural level, so that material below the original décollement is uplifted above the new décollement (Figure 4-14b). Unfortunately, we do not constrain the location of this "step-down" in our reflection profiles, however we would infer that its location as being coincident with the appearance of the deeper zone of reflectivity along lines 17 and 15 (Figure 4-3 and 4-6). Within the context of this model, the deeper zone of east and west dipping reflectivity we observe along lines 15 and 17 (Figure 4-3 and 4-6) may represent thrust ramps of a passive duplex, while intermittent horizontal reflectivity may represent portions of the former shallow décollement surface preserved in the underplated unit. Underplating may also explain the passive uplift of relatively undeformed accreted material observed in the highest elevations of the prism along line 17 and would not preclude thrust faulting in the overlying decoupled accreted section with continued convergence.. A subaerial analog of this proposed system is a passive roof duplex structure in the central Foothills, Rocky Mountain thrust belt identified by Couzens-Schultz and Wiltschko (1999).

We believe the underplating is a plausible mechanism to explain the large volume of deeper reflectivity along lines 15 and 17, as well as the continued growth of the prism to the north along lines 23 and 22. Between 0.75 km and 1.0 km of sedimentary material underthrust at the toe of the prism along all transects (Figure 4-2b-c; 4-5b-c). Coupled with convergence rates of ~70 km/Myr (Seno, 1977) along the Manila trench at this latitude, a volume of underplated sediments on the order of what we interpret along lines 15 and 17 can be emplaced over relatively short timescales, growing a thick prism quickly. Tomographic modeling from Eakin et al., (2013) shows the prism thickness to be between ~13-15 km near 20.5°N in support of this hypothesis.

4-6: CONCLUSIONS

The new MCS reflection images for lines 15, 17, 23, and 22 provide constraints on the internal structure of the accretionary prism in the intra-oceanic subduction domain offshore northern Luzon. Our data reveal both an increase in width of the prism and development of disparate lower and upper slope domains from south to north. We image local uplift and low taper of the prism slope along lines 23 and 22. The structures and deformation are similar to those associated with the subduction of a basement asperity similar to that modeled by Lallemand et al., (1994) and observed by Park et al., (1999).

This may be a significant observation as the prism develops a distinct lower slope and upper slope in response to the subducting topography. This zonation of the prism appears to be a local phenomenon when compared with lines 15 and 17 to the south, and previously published MCS reflection profiles to the north (Eakin et al., 2014) that show the prism lacking these two domains.

In the south, a zone of complex, deep reflectivity occupies a large volume of the rear of the Manila accretionary prism along MCS profiles 15 and 17. Evidence of steeply dipping fault planes may indicate the presence of large thrust faults, however the deeper nature of these faults is difficult to interpret and we cannot speculate whether the deeper reflectivity is a result of faulting alone. Alternatively, we propose a model where the zone of deeper reflectivity is associated with a large volume of underplated material derived from sedimentary units underthrust at the prism toe and deformed into passive duplex or series of duplexes. Similar reflectivity cannot be constrained in the rear of the prism along lines 23 and 22, however the prism does show continued deformation and an increase in elevation consistent with thickening at depth. These results support a model of a deforming critical wedge that increases its taper via underplating by basal duplex. The results support previously published tomographic models north of the profiles shown here that indicate prism thicknesses > 13 km and provide a mechanism to build such a large wedge over a short geologic time. Together, the data presented here illuminate a previously unrecorded phase of prism growth prior to the transition from oceanic subduction to the subduction of transitional continental crust of the SCS distal margin and provides a snapshot of the structures that are likely modified farther north by subsequent basement underplating.

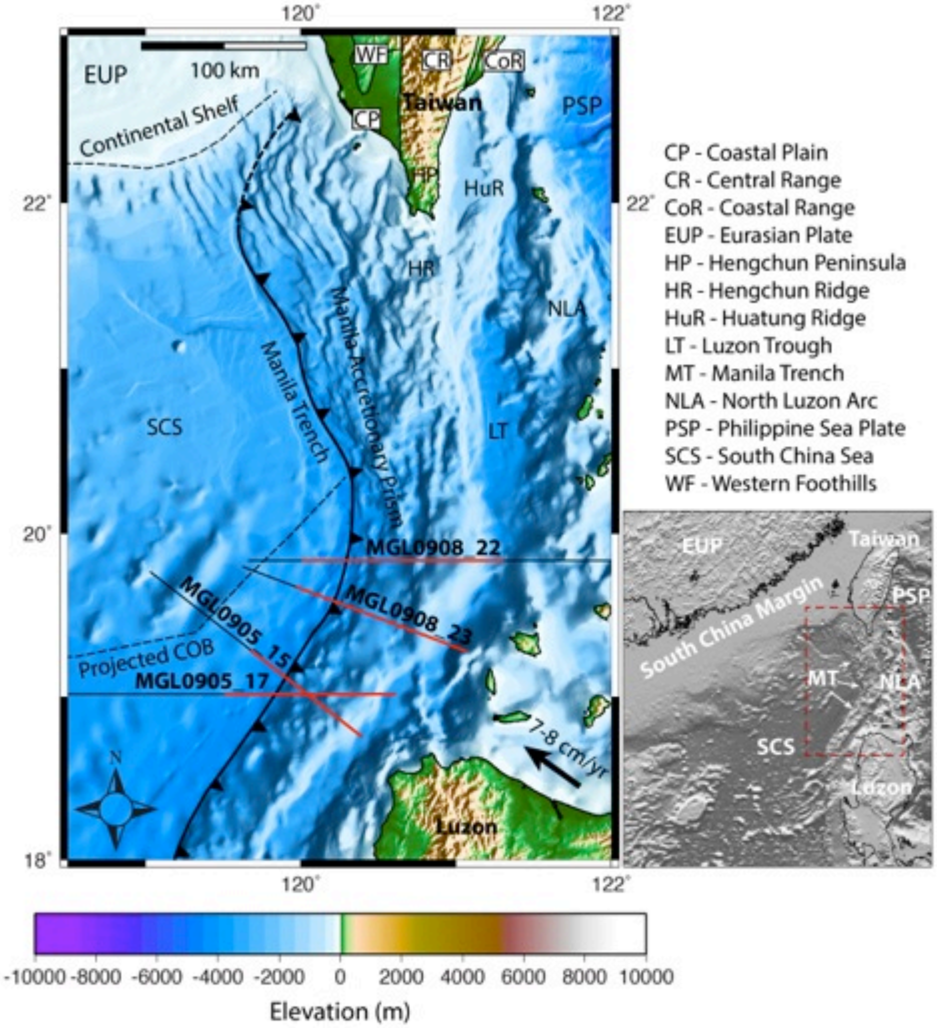

Figure 4-1. Shaded relief map (lower right), and regional bathymetric and elevation map showing the major tectonic elements offshore south and east of Taiwan. MCS reflection data from this study (black-red lines) were acquired along MGL0905_15, MGL0905_17, MGL0908_23, and MGL908_22. Black dashed lines denote the positions of the Chinese continental margin and continent-ocean boundary interpreted by Eakin et al., 2013. (COB = continent-ocean boundary).

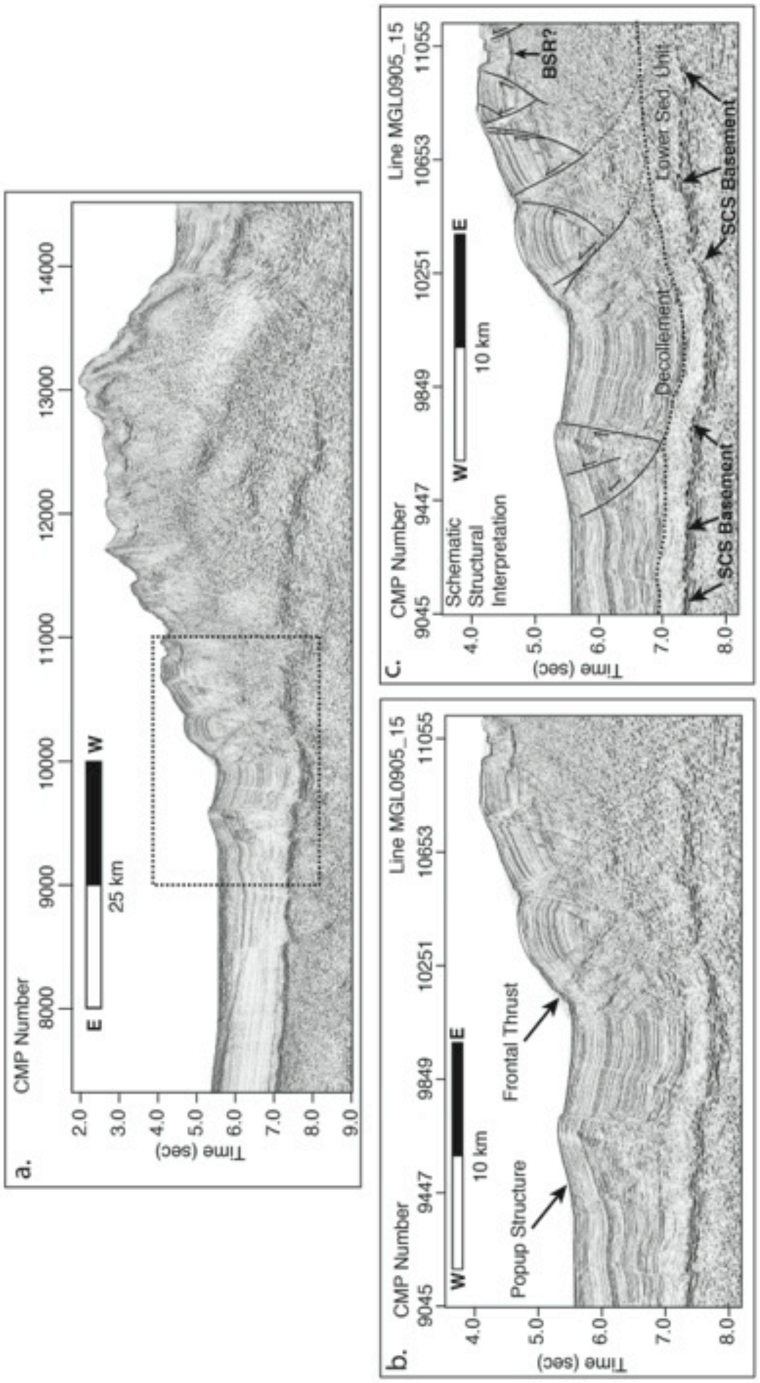
a.
CMP Number
8000
9000
10000
11000
12000
13000
14000
Time (sec)
2.0
3.0
4.0
5.0
6.0
7.0
8.0
9.0
E
W
25 km
b.
CMP Number
9045
9447
9849
10251
10653
11055
Line MGL0905_15
Time (sec)
4.0
5.0
6.0
7.0
8.0
W
E
10 km
Popup Structure
Frontal Thrust
c.
CMP Number
9045
9447
9849
10251
10653
11055
Line MGL0905_15
Time (sec)
4.0
5.0
6.0
7.0
8.0
W
E
10 km
Schematic Structural Interpretation
Decollement
Lower Sed. Unit
SCS Basement
SCS Basement
BSR?

Figure 4-2.

Figure 4-2. a) Time-migrated seismic reflection section of Line 15 (a) with outline of zoomed uninterpreted (b) and interpreted (c). Line 15 shows the subducting SCS oceanic basement and sedimentary cover sequence, the Manila accretionary prism, and Luzon Trough forearc basin. b-c) Uninterpreted and interpreted zooms of the frontal thrust zone showing bi-vergent thrusting that develops a popup structure seaward of the trench and sole into an interpreted basal dècollement within the sedimentary section. Sediments above the dècollement are accreted and deformed by seaward verging thrusts and conjugate backtrhusts while those sediments below are subducted. BSR = bottom-simulating-reflector.

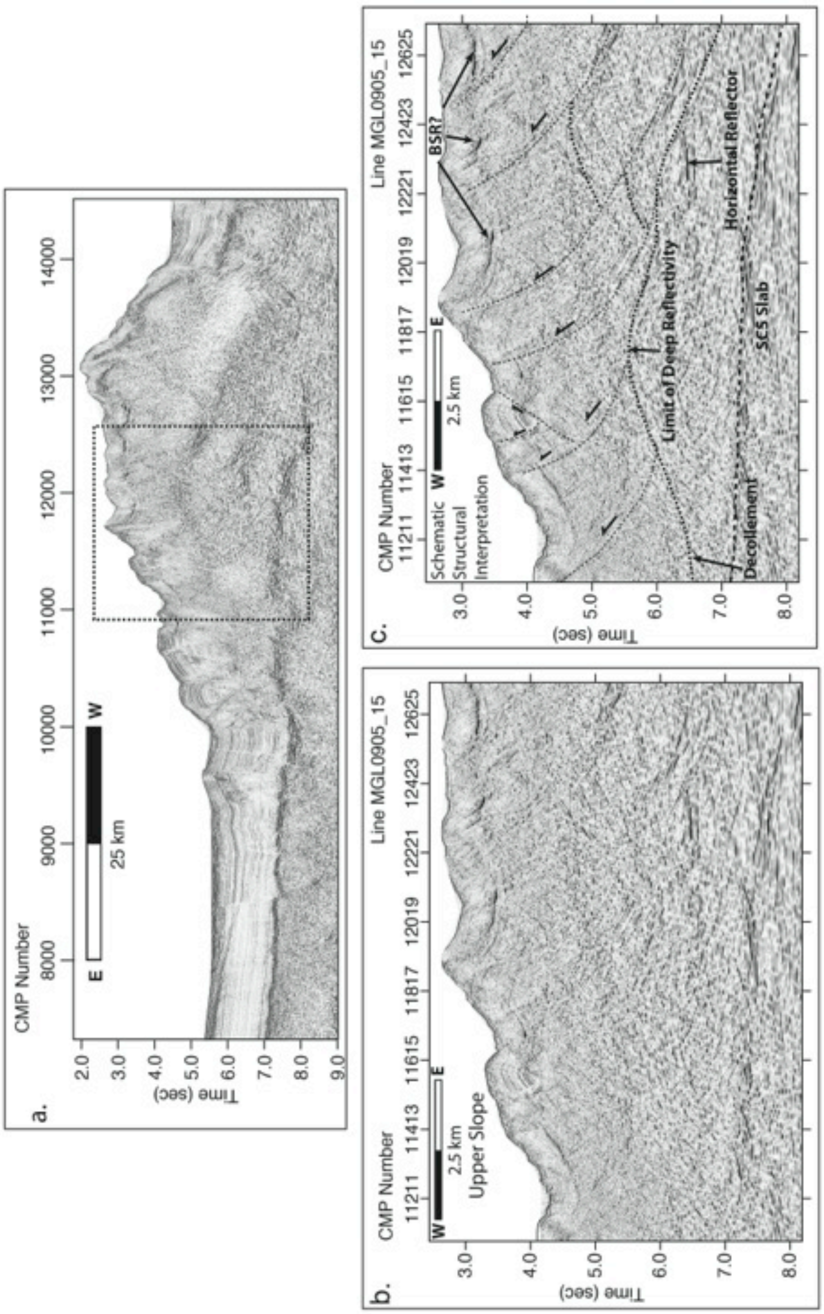
a.
CMP Number
8000
9000
10000
11000
12000
13000
14000
E
W
25 km
Time (sec)
2.0
3.0
4.0
5.0
6.0
7.0
8.0
9.0
b.
CMP Number
11211
11413
11615
11817
12019
12221
12423
12625
Line MGL0905_15
W
E
2.5 km
Upper Slope
Time (sec)
3.0
4.0
5.0
6.0
7.0
8.0
c.
CMP Number
11211
11413
11615
11817
12019
12221
12423
12625
Line MGL0905_15
Schematic Structural Interpretation
W
E
2.5 km
BSR?
Limit of Deep Reflectivity
Horizontal Reflector
Decollement
SCS Slab
Time (sec)
3.0
4.0
5.0
6.0
7.0
8.0

Figure 4-3.

Figure 4-3. a) Time-migrated seismic reflection section of Line 15 (a) with outline of zoomed uninterpreted (b) and interpreted (c). b-c) Uninterpreted and interpreted zooms of the central part of prism showing evidence for thrusting in the shallow section and a large area below composed of discontinuous, bi-vergent reflectivity that extends to the top of subducting basement. The position of the dècollement is inferred from the position interpreted in Figure 2. Intermittent high-amplitude low-frequency near 3.0 sec TWTT may indicate the presence of a bottom-simulating-reflector.

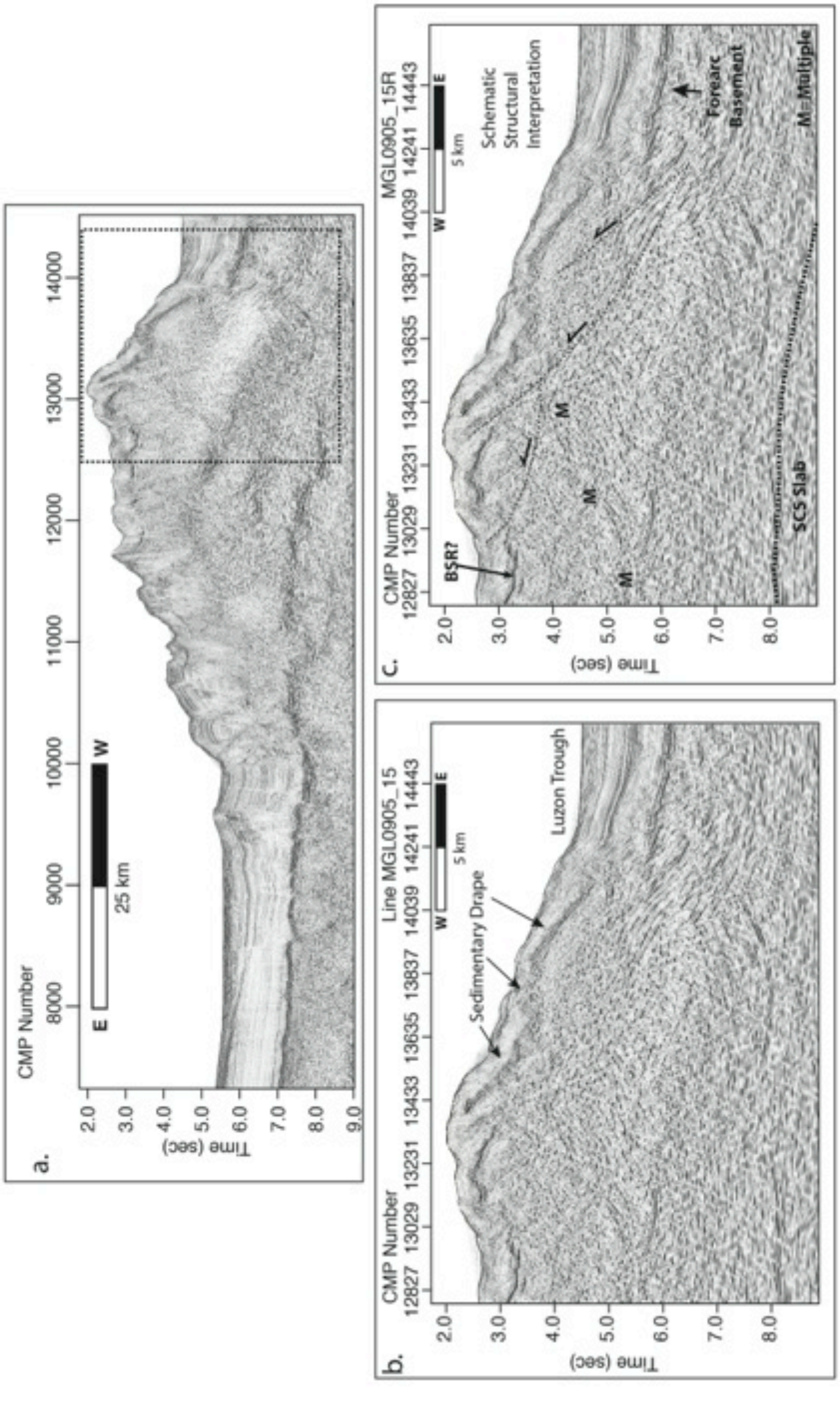
a.
CMP Number
8000
9000
10000
11000
12000
13000
14000
Time (sec)
2.0
3.0
4.0
5.0
6.0
7.0
8.0
9.0
E
W
25 km
b.
CMP Number
12827 13029 13231 13433 13635 13837 14039 14241 14443
Line MGL0905_15
Sedimentary Drape
Luzon Trough
W
E
5 km
Time (sec)
2.0
3.0
4.0
5.0
6.0
7.0
8.0
c.
CMP Number
12827 13029 13231 13433 13635 13837 14039 14241 14443
MGL0905_15R
Schematic Structural Interpretation
W
E
5 km
BSR?
M
M
M
Forearc Basement
SCS Slab
M=Multiple
Time (sec)
2.0
3.0
4.0
5.0
6.0
7.0
8.0

Figure 4-4.

Figure 4-4. a) Time-migrated seismic reflection section of Line 15 (a) with outline of zoomed uninterpreted (b) and interpreted (c). b-c) Uninterpreted and interpreted zooms of the rear of the prism showing evidence for large, steeply dipping faults. A thin layer of lightly bedded sedimentary material is separated by the older prism strata by a continuous high-amplitude refelction. This boundary is deformed and offset by large steeply dipping thrust faults.

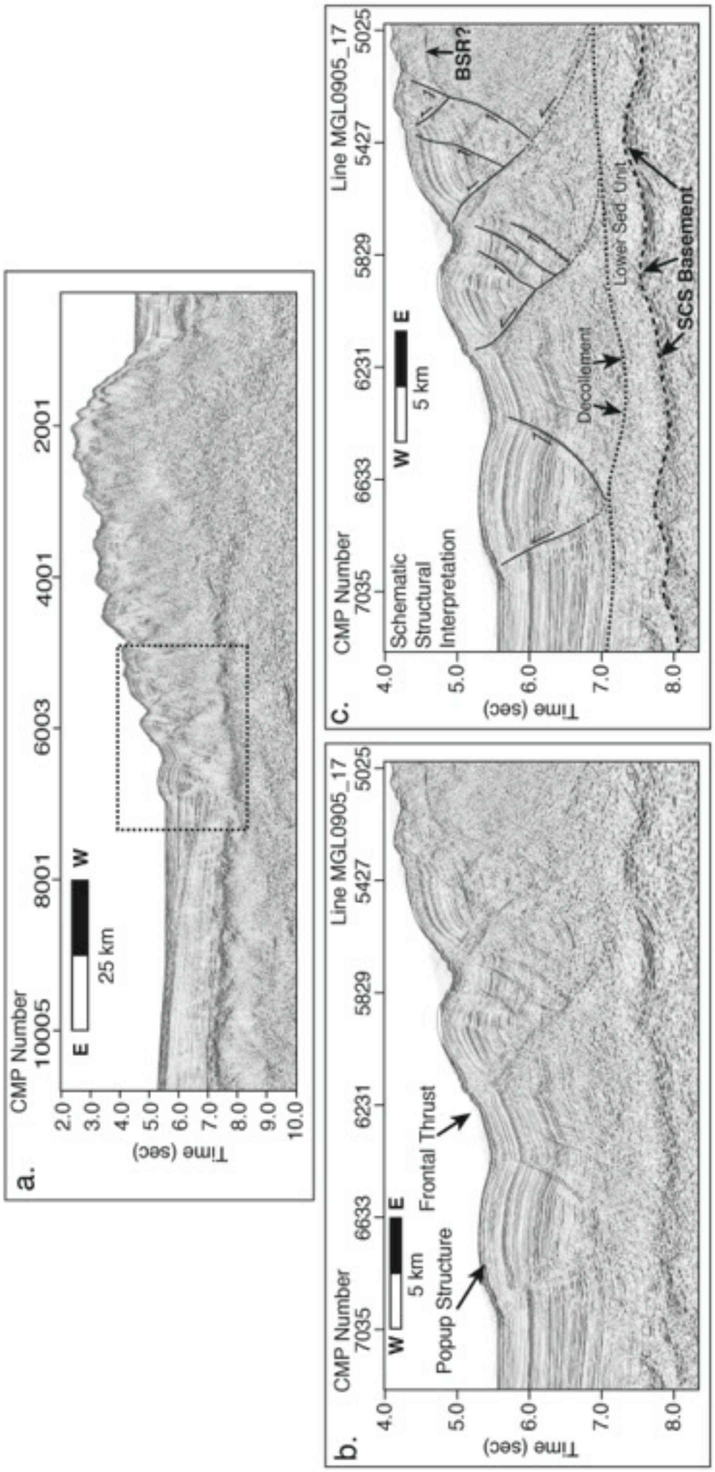
a.
CMP Number
10005
8001
6003
4001
2001
E
W
25 km
Time (sec)
2.0
3.0
4.0
5.0
6.0
7.0
8.0
9.0
10.0
b.
CMP Number
7035
6633
6231
5829
5427
Line MGL0905_17
5025
W
E
5 km
Popup Structure
Frontal Thrust
Time (sec)
4.0
5.0
6.0
7.0
8.0
c.
CMP Number
7035
6633
6231
5829
5427
Line MGL0905_17
5025
W
E
5 km
Schematic
Structural
Interpretation
Decollement
Lower Sed. Unit
SCS Basement
BSR?
Time (sec)
4.0
5.0
6.0
7.0
8.0

Figure 4-5.

Figure 4-5. a) Time-migrated seismic reflection section of Line 17 (a) with outline of zoomed uninterpreted (b) and interpreted (c). b-c) Uninterpreted and interpreted zooms of the frontal thrust zone showing bi-vergent thrusting that develops a popup structure seaward of the trench and sole into an interpreted basal dècollement within the sedimentary section. Sediments above the dècollement are accreted and deformed by seaward verging thrusts and conjugate backtrhusts while those sediments below are subducted. BSR = bottom-simulating-reflector.

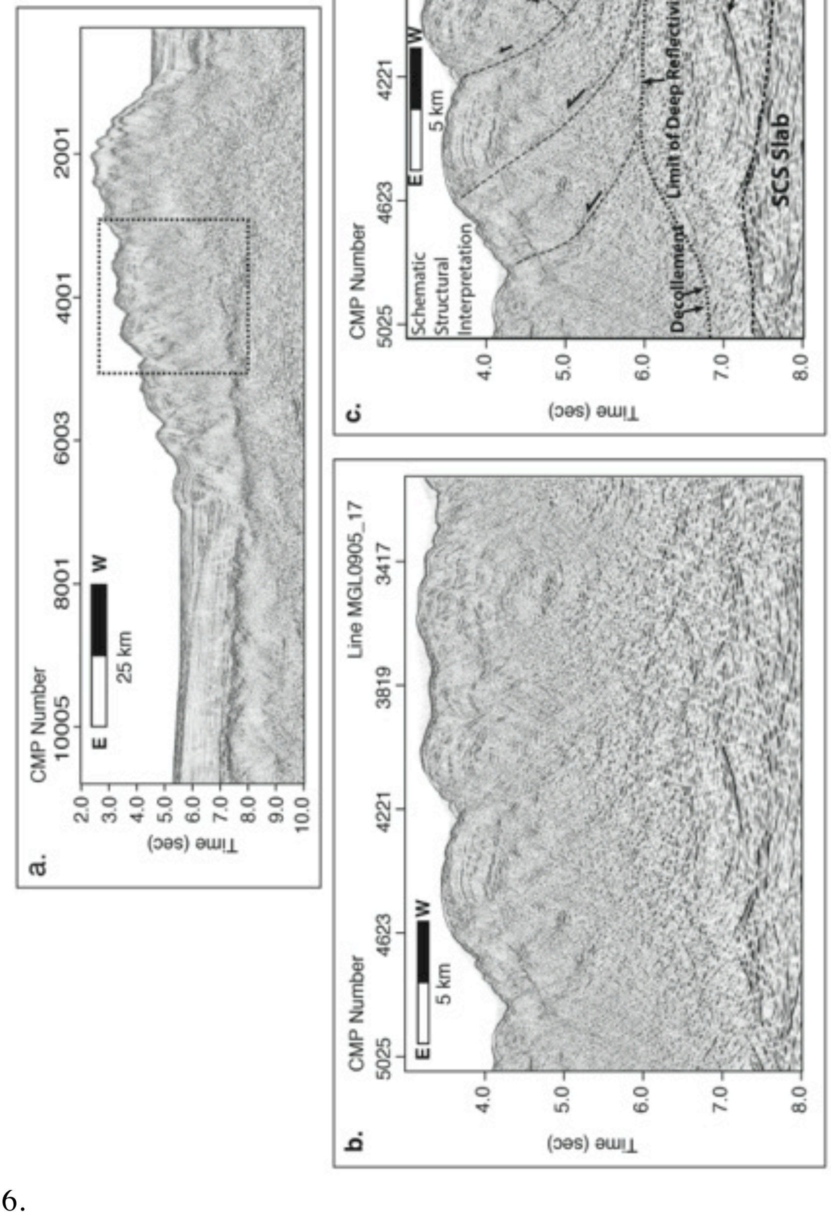
a.
CMP Number
10005
8001
6003
4001
2001
E
W
25 km
Time (sec)
2.0
3.0
4.0
5.0
6.0
7.0
8.0
9.0
10.0
b.
CMP Number
Line MGL0905_17
5025
4623
4221
3819
3417
E
W
5 km
Time (sec)
4.0
5.0
6.0
7.0
8.0
c.
CMP Number
Line MGL0905_17
5025
4623
4221
3819
3417
E
W
5 km
Schematic
Structural
Interpretation
Decollement
Limit of Deep Reflectivity
SCS Slab
East/West
Dipping
Reflectors
Time (sec)
4.0
5.0
6.0
7.0
8.0

Figure 4-6.

Figure 4-6. a) Time-migrated seismic reflection section of Line 17 (a) with outline of zoomed uninterpreted (b) and interpreted (c). b-c) Uninterpreted and interpreted zooms of the central part of prism showing evidence for thrusting in the shallow section and a large area below composed of discontinuous, bi-vergent reflectivity that extends to the top of subducting basement. The shallow section is composed of deformed, layered strata similar to packages accreted at the toe of the prism on Figure 5. The position of the dècollement is inferred from the position interpreted in Figure 2.

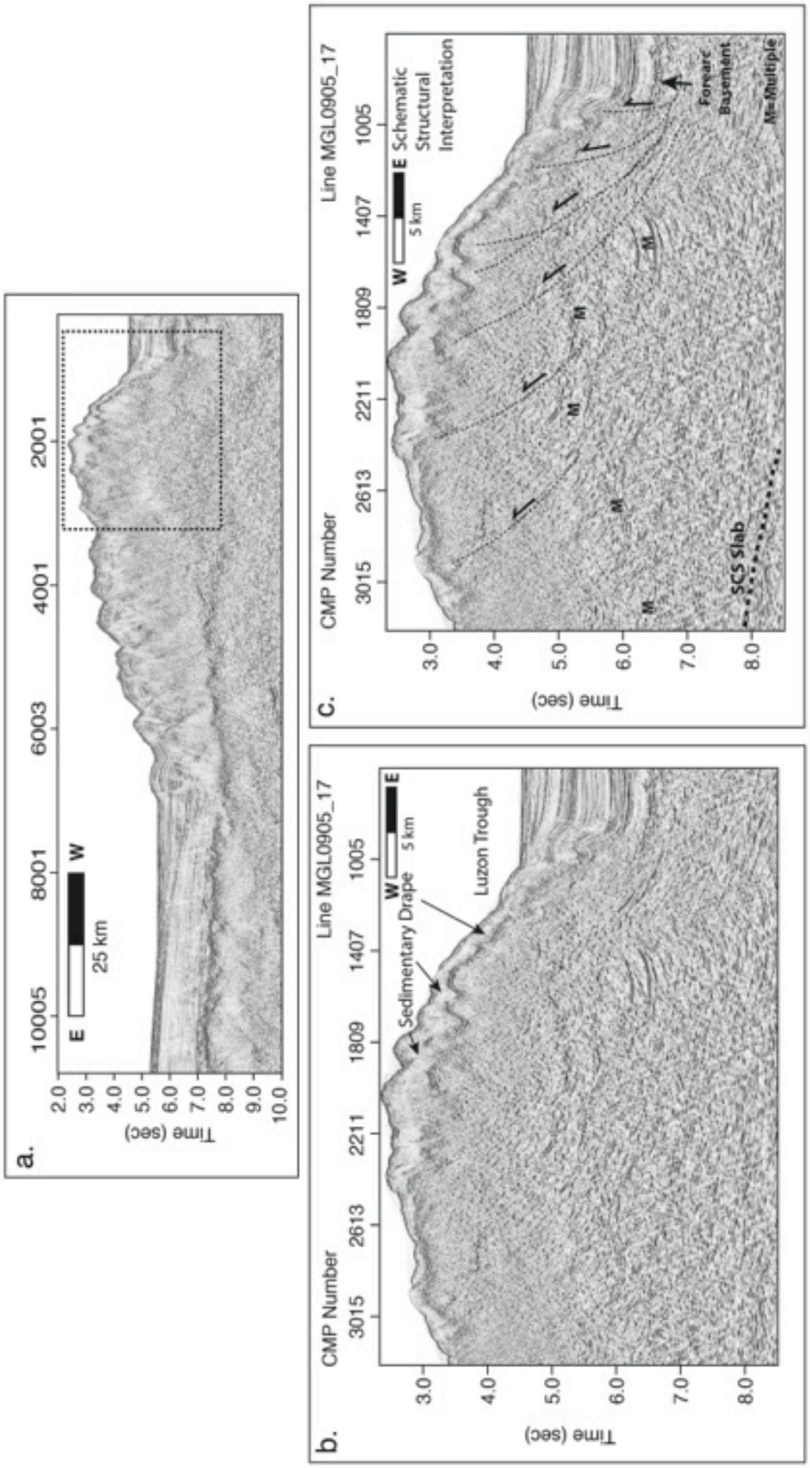
a.
Time (sec)
2.0
3.0
4.0
5.0
6.0
7.0
8.0
9.0
10.0
10005
8001
6003
4001
2001
E
W
25 km
b.
CMP Number
Line MGL0905_17
3015
2613
2211
1809
1407
1005
Sedimentary Drape
Luzon Trough
W
E
5 km
c.
Schematic Structural Interpretation
M
Forearc Basement
M=Multiple
SCS Slab

Figure 4-7.

Figure 4-7. a) Time-migrated seismic reflection section of Line 17 (a) with outline of zoomed uninterpreted (b) and interpreted (c). b-c) Uninterpreted and interpreted zooms of the rear of the prism showing evidence for large, steeply dipping faults. A thin layer of lightly bedded sedimentary material is separated by the older prism strata by a continuous high-amplitude refelction. This boundary is deformed and offset by large steeply dipping thrust faults. The forearc basin strata near the arcward slope of the prism are folded and faulted indicating active deformation and uplift of the rear of the prism or shortening in the forearc.

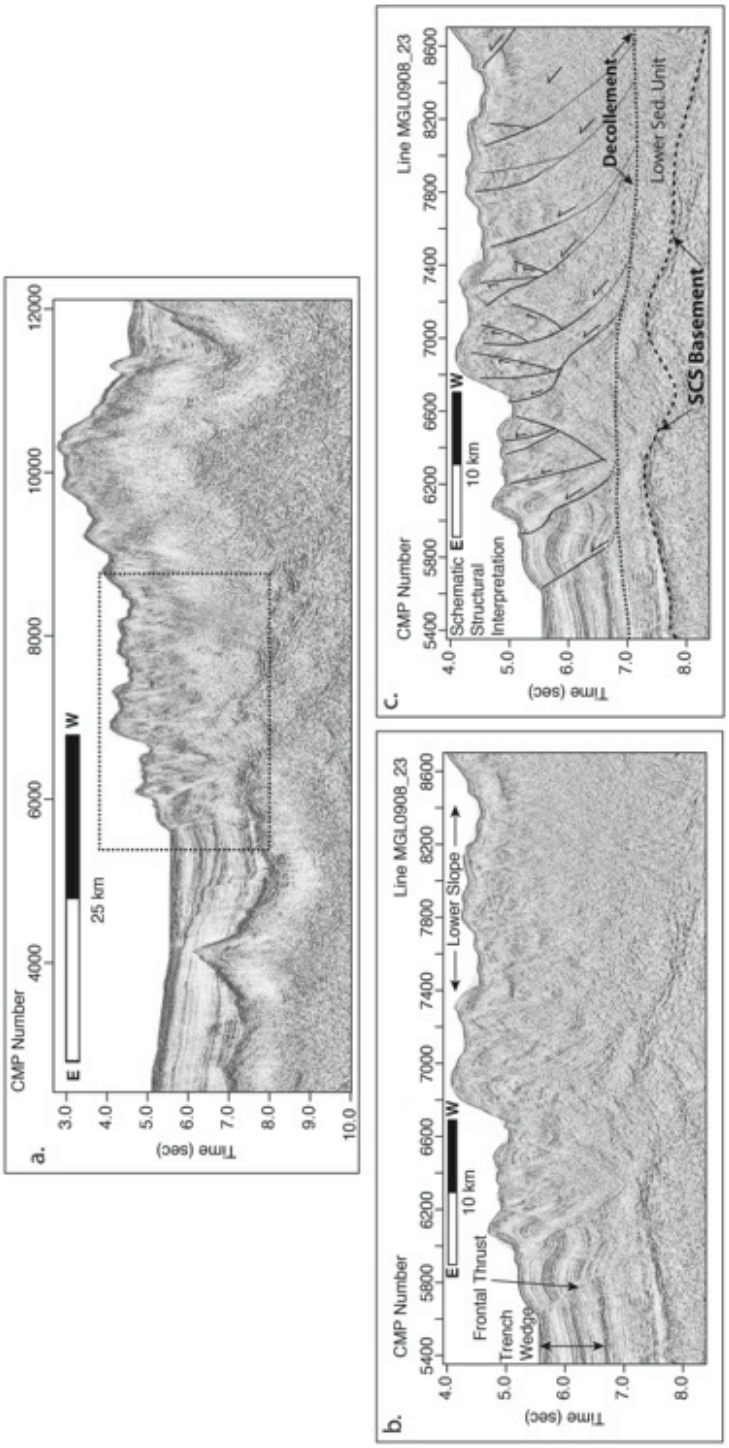
a.
CMP Number
4000
6000
8000
10000
12000
E
W
25 km
Time (sec)
3.0
4.0
5.0
6.0
7.0
8.0
9.0
10.0
b.
CMP Number
5400
5800
6200
6600
7000
7400
7800
8200
8600
Line MGL0908_23
Lower Slope
E
W
10 km
Trench Wedge
Frontal Thrust
Time (sec)
4.0
5.0
6.0
7.0
8.0
c.
CMP Number
5400
5800
6200
6600
7000
7400
7800
8200
8600
Line MGL0908_23
Schematic Structural Interpretation
E
W
10 km
Decollement
Lower Sed. Unit
SCS Basement
Time (sec)
4.0
5.0
6.0
7.0
8.0

Figure 4-8.

Figure 4-8. Time-migrated seismic reflection section of Line 23 (a) with outline of zoomed uninterpreted (b) and interpreted (c). b-c) Uninterpreted and interpreted zooms showing fault bend folding and a seaward dipping frontal thrust that soles into the sediemtn basement interface. A basement high near CMP 7000 is associated with local uplift at the seafloor. The uplifted strata are deformed by seaward verging thrusts and conjugate backtrhusts. West of CMP 7000 the prism slope taper is low and deformed by a series of landward verging thrusts that sole into a dècollement interpreted near the sediment basement interface.

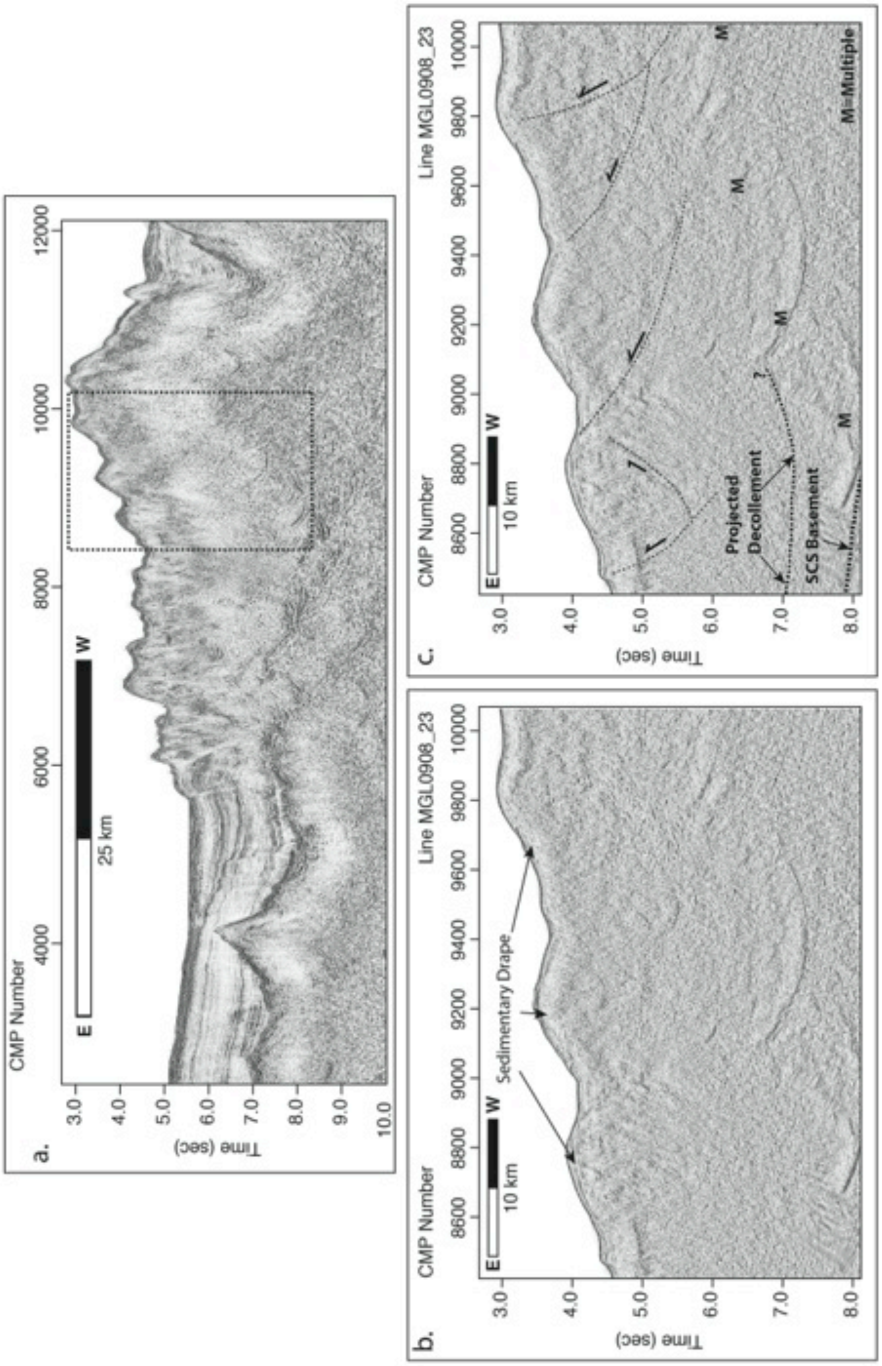
a.
b.
c.
CMP Number
Time (sec)
3.0
4.0
5.0
6.0
7.0
8.0
9.0
10.0
4000
6000
8000
10000
12000
8600
8800
9000
9200
9400
9600
9800
10000
E
W
25 km
10 km
Line MGL0908_23
Sedimentary Drape
Projected Decollement
SCS Basement
?
M
M=Multiple

Figure 4-9.

Figure 4-9. a) Time-migrated seismic reflection section of Line 23 (a) with outline of zoomed uninterpreted (b) and interpreted (c). A large seamount is observed searwad of the frontal thrust near CMP 4000. b-c) Uninterpreted and interpreted zooms of the central part of prism showing evidence for thrusting associated with local topography at the seafloor. A thinly layered sedimentary section is draped over much of the prism slope. Deeper interpretation of prism structure is obscured by strong multiple energy. The position of the dècollement is inferred from the position interpreted in Figure 8.

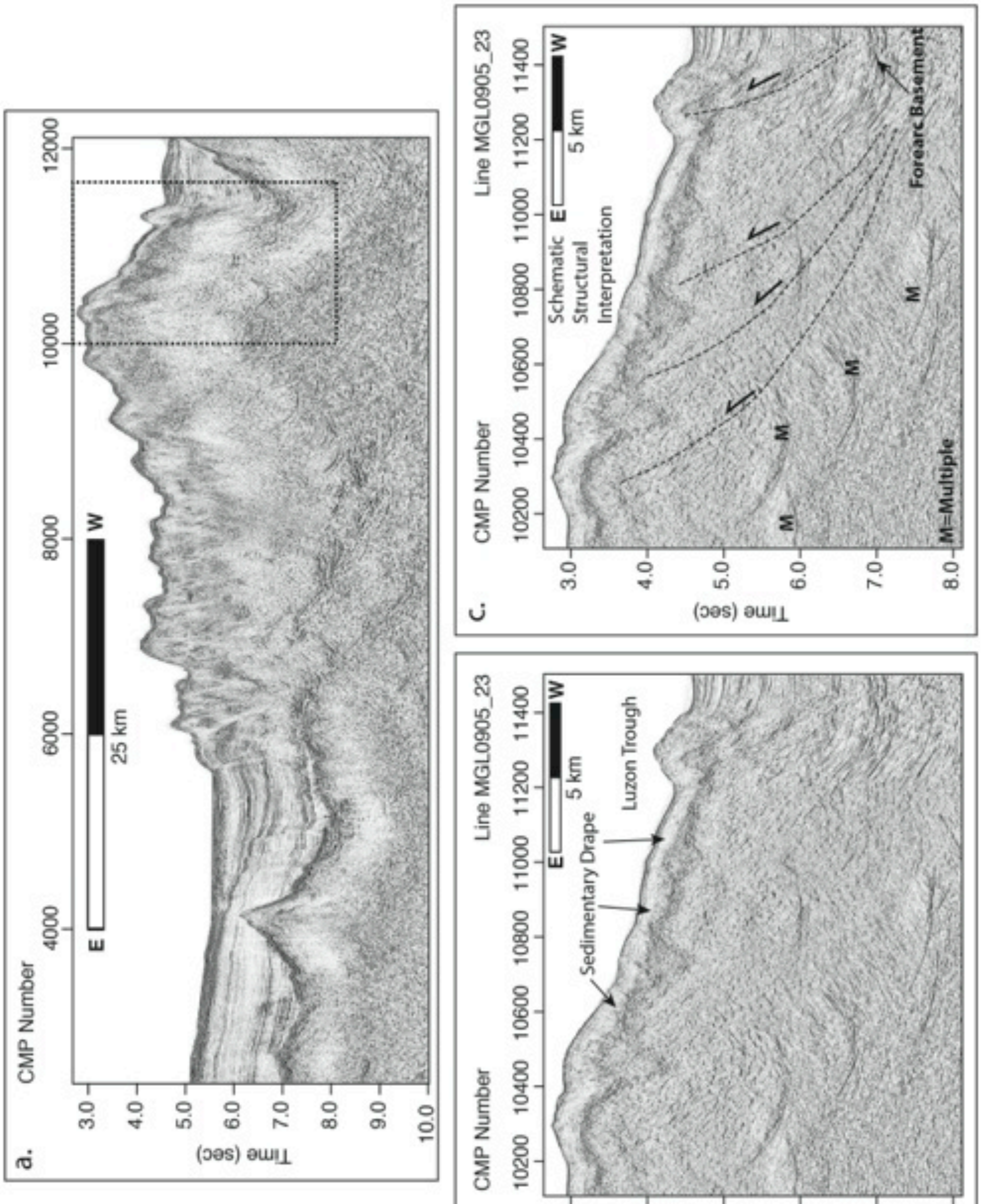
a.
CMP Number
4000
6000
8000
10000
12000
Time (sec)
3.0
4.0
5.0
6.0
7.0
8.0
9.0
10.0
E
W
25 km
b.
CMP Number
10200
10400
10600
10800
11000
11200
11400
Line MGL0905_23
E
W
5 km
Sedimentary Drape
Luzon Trough
Time (sec)
3.0
4.0
5.0
6.0
7.0
8.0
c.
CMP Number
10200
10400
10600
10800
11000
11200
11400
Line MGL0905_23
E
W
5 km
Schematic
Structural
Interpretation
Forearc Basement
M
M
M
M
M=Multiple
Time (sec)
3.0
4.0
5.0
6.0
7.0
8.0

Figure 4-10.

Figure 4-10. a) Time-migrated seismic reflection section of Line 23 (a) with outline of zoomed uninterpreted (b) and interpreted (c). b-c) Uninterpreted and interpreted zooms of the rear of the prism showing evidence for large, steeply dipping faults. A thin layer of lightly bedded sedimentary material is separated by the older prism strata by a continuous high-amplitude reflection. This boundary is deformed and offset by large steeply dipping thrust faults. The forearc basin strata near the arcward slope of the prism are folded and uplifted by a steeply dipping thrust indicating shortening in the forearc.

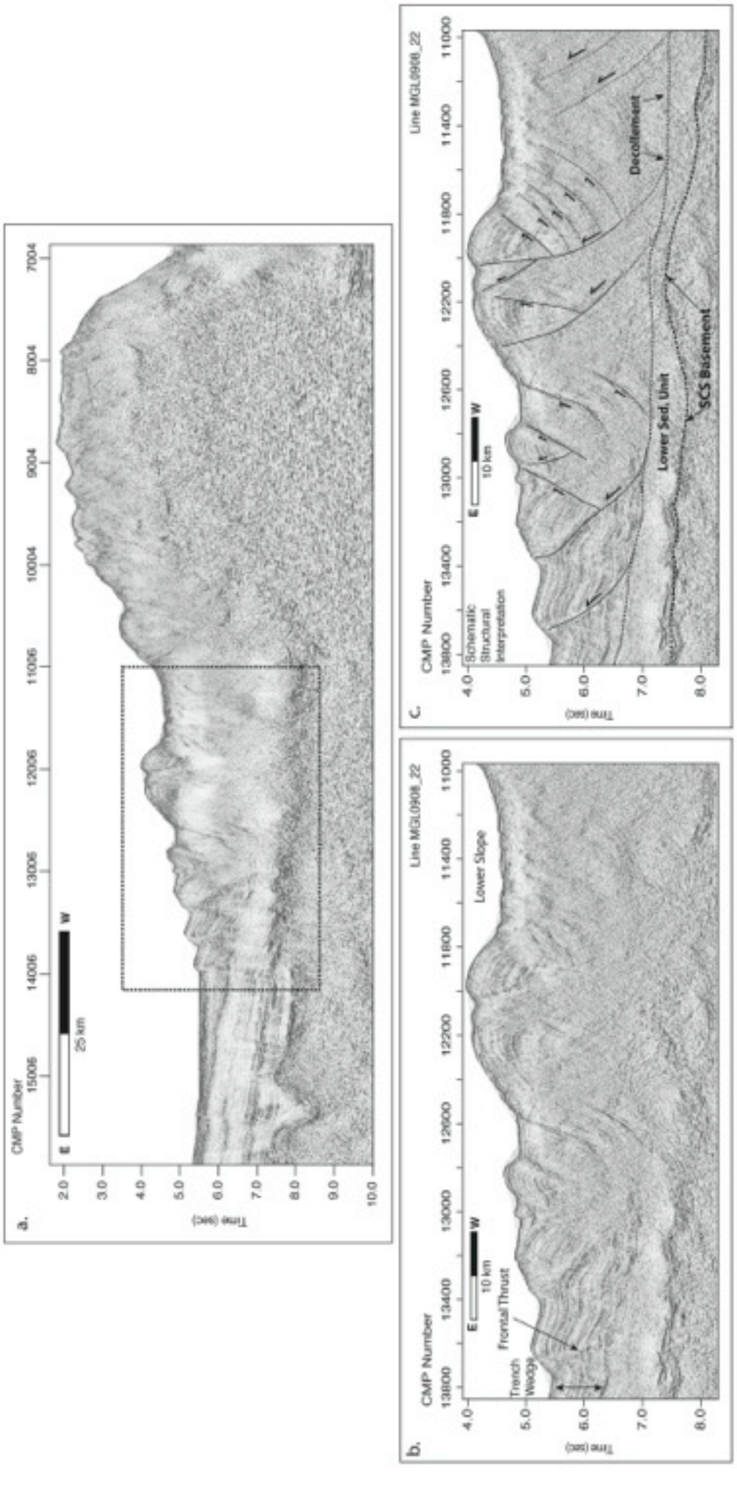
a.
CMP Number
15006
14006
13006
12006
11006
10004
9004
8004
7004
E
W
25 km
Time (sec)
2.0
3.0
4.0
5.0
6.0
7.0
8.0
9.0
10.0
b.
CMP Number
13800
13400
13000
12600
12200
11800
11400
11000
Line MGL0908_22
E
W
10 km
Trench Wedge
Frontal Thrust
Lower Slope
Time (sec)
4.0
5.0
6.0
7.0
8.0
c.
CMP Number
13800
13400
13000
12600
12200
11800
11400
11000
Line MGL0908_22
Schematic Structural Interpretation
E
W
10 km
Decollement
Lower Sed. Unit
SCS Basement
Time (sec)
4.0
5.0
6.0
7.0
8.0

Figure 4-11.

Figure 4-11. Time-migrated seismic reflection section of Line 22 (a) with outline of zoomed uninterpreted (b) and interpreted (c). b-c) Uninterpreted and interpreted zooms showing fault bend folding and a seaward dipping frontal thrust that soles into base of the trench wedge sediments. The remainder of the sedimentary section continues to subduct. A basement high similar to that observed along line 23 near CMP 12200 is associated with local uplift at the seafloor. The uplifted strata are deformed by seaward verging thrusts and conjugate backtrhusts. West of 11800 the low taper zone is deformed by lanward verging backthrusts in the east, and seaward verging thrusts in the west.

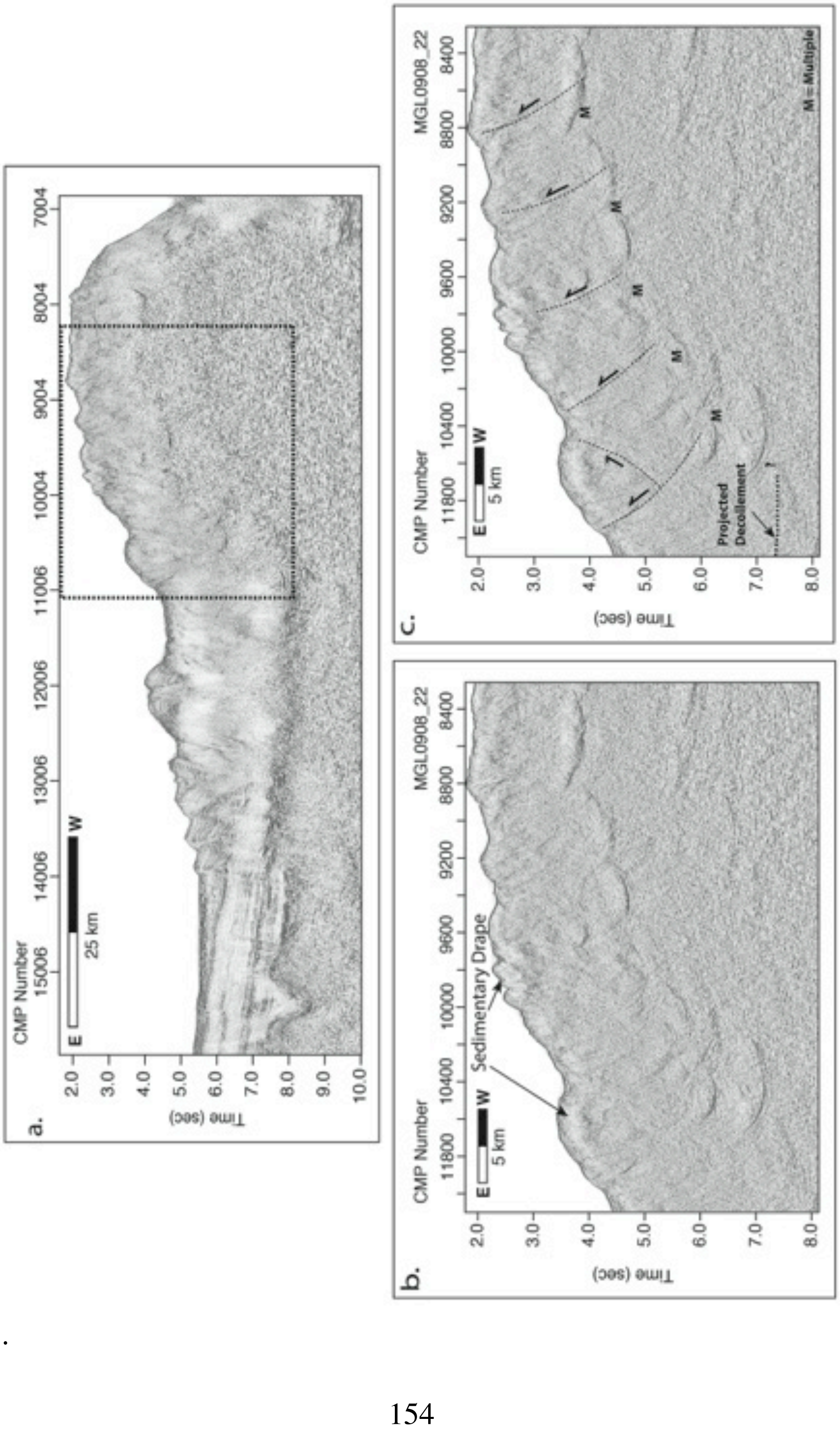
a.
CMP Number
15006
14006
13006
12006
11006
10004
9004
8004
7004
E
25 km
W
Time (sec)
2.0
3.0
4.0
5.0
6.0
7.0
8.0
9.0
10.0
b.
CMP Number
11800
10400
10000
9600
9200
8800
8400
MGL0908_22
E
5 km
W
Sedimentary Drape
Time (sec)
2.0
3.0
4.0
5.0
6.0
7.0
8.0
c.
CMP Number
11800
10400
10000
9600
9200
8800
8400
MGL0908_22
E
5 km
W
M
M
M
M
M
Projected Decollement
M = Multiple
Time (sec)
2.0
3.0
4.0
5.0
6.0
7.0
8.0

Figure 4-12.

Figure 4-12. a) Time-migrated seismic reflection section of Line 22 (a) with outline of zoomed uninterpreted (b) and interpreted (c). b-c) Uninterpreted and interpreted zooms of the central part of prism showing evidence for deep seeded thrusting associated with local topography at the seafloor. The thinly layered sedimentary section drapes much of the prism slope. Deeper interpretation of prism structure is obscured by strong multiple energy.

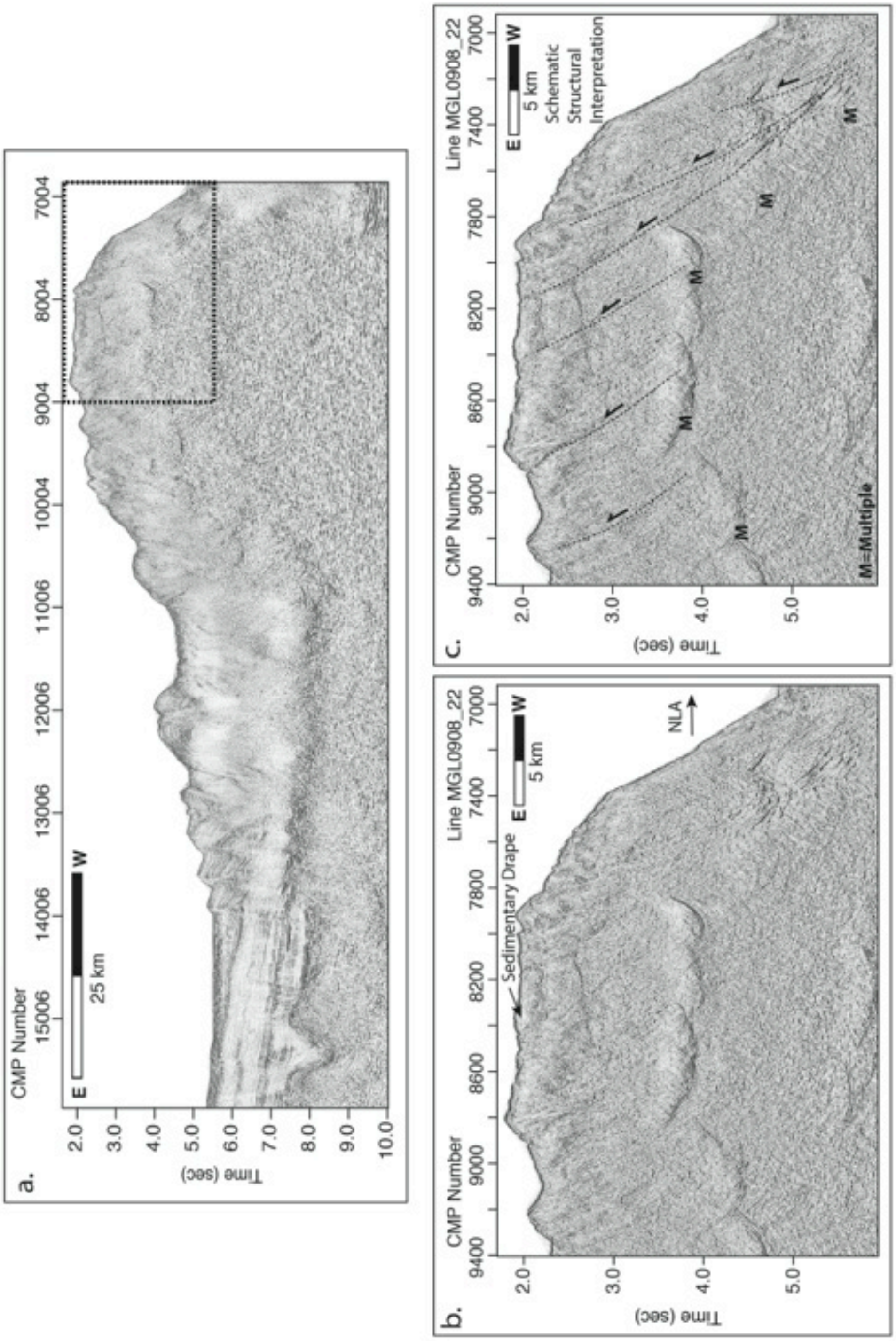
a.
CMP Number
15006
14006
13006
12006
11006
10004
9004
8004
7004
E
W
25 km
Time (sec)
2.0
3.0
4.0
5.0
6.0
7.0
8.0
9.0
10.0
b.
CMP Number
Line MGL0908_22
9400
9000
8600
8200
7800
7400
7000
Sedimentary Drape
E
W
5 km
NLA
Time (sec)
2.0
3.0
4.0
5.0
c.
CMP Number
Line MGL0908_22
9400
9000
8600
8200
7800
7400
7000
E
W
5 km
Schematic Structural Interpretation
M
M
M
M
M
M
M=Multiple
Time (sec)
2.0
3.0
4.0
5.0

Figure 4-13.

Figure 4-13. a) Time-migrated seismic reflection section of Line 22 (a) with outline of zoomed uninterpreted (b) and interpreted (c). b-c) Uninterpreted and interpreted zooms of the rear of the prism showing evidence for large, steeply dipping faults. Deeper interpretation of the faulting is obscured by residual multiple energy at ~4.0 and 6.0 sec TWTT. The layered forearc basin strata are missing and the seaward flank of the NLA abuts the prismward slope of the prism.

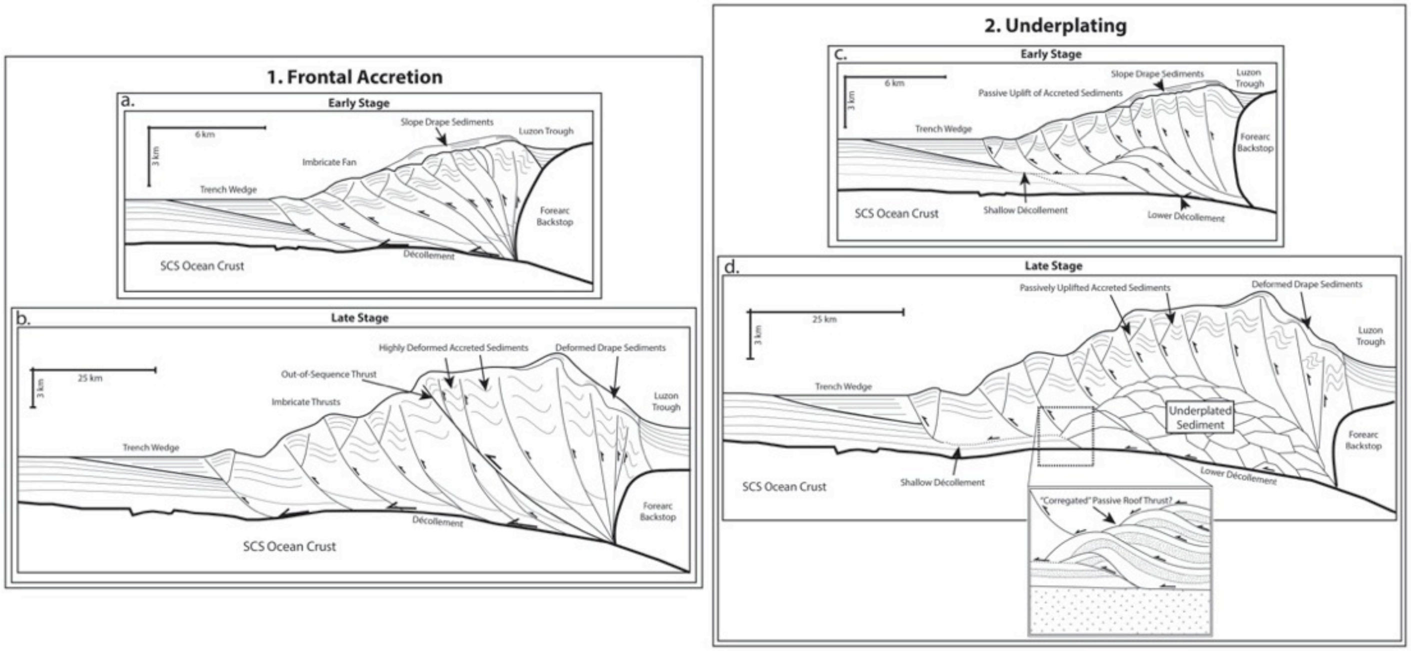
1. Frontal Accretion
a.
Early Stage
6 km
3 km
Slope Drape Sediments
Luzon Trough
Imbricate Fan
Trench Wedge
Forearc Backstop
SCS Ocean Crust
Décollement
b.
Late Stage
25 km
3 km
Highly Deformed Accreted Sediments
Deformed Drape Sediments
Out-of-Sequence Thrust
Imbricate Thrusts
Luzon Trough
Trench Wedge
Forearc Backstop
Décollement
SCS Ocean Crust
2. Underplating
c.
Early Stage
6 km
3 km
Slope Drape Sediments
Luzon Trough
Passive Uplift of Accreted Sediments
Trench Wedge
Forearc Backstop
SCS Ocean Crust
Shallow Décollement
Lower Décollement
d.
Late Stage
Passively Uplifted Accreted Sediments
Deformed Drape Sediments
25 km
3 km
Luzon Trough
Trench Wedge
Underplated Sediment
Forearc Backstop
SCS Ocean Crust
Shallow Décollement
Lower Décollement
"Corregated" Passive Roof Thrust?

Figure 4-14.

Figure 4-14. Summary of potential accretionary prism evolution scenarios as inferred from geophysical observations offshore northern Luzon. a-b). Prism growth driven by frontal accretion. c-d) Prism growth driven by accretion and underplating via passive duplex.

APPENDIX A: SEISMIC REFLECTION IMAGES

This appendix contains seismic reflection images used to inform the interpretations throughout the main body of the dissertation, but not presented in their entirety in the submitted manuscripts. The seismic images were produced using the processing flow discussed in chapters 2-4.

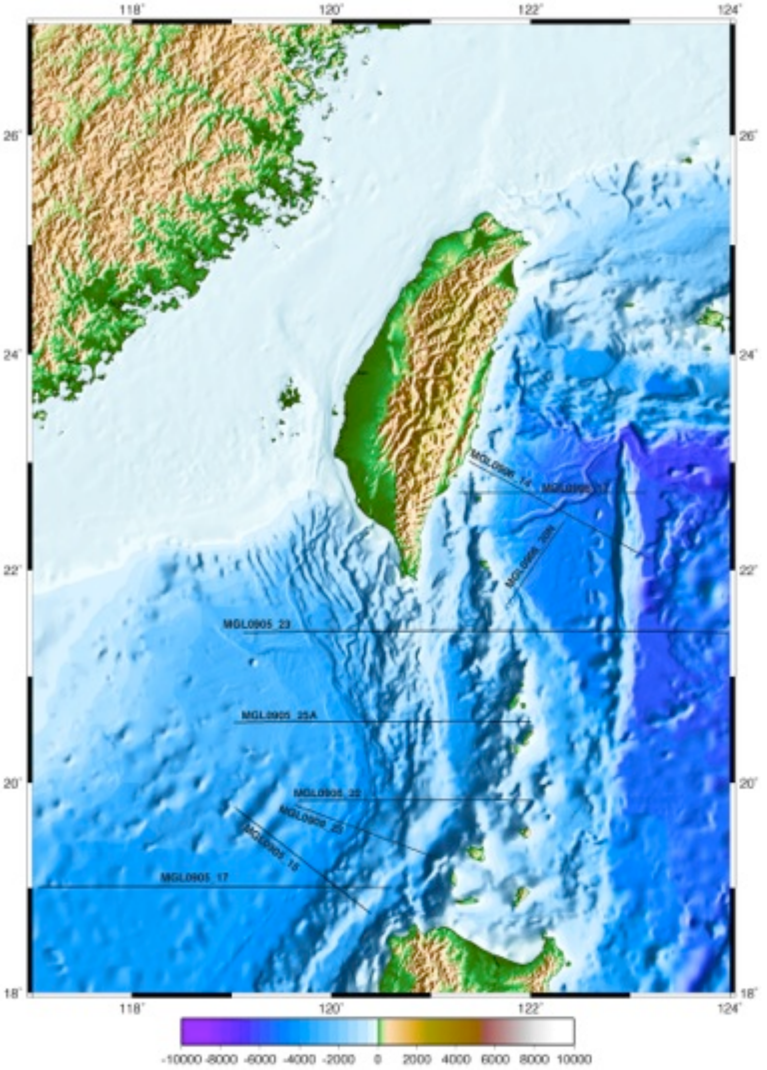

Figure A-1: Location of seismic profiles in Appendix A.

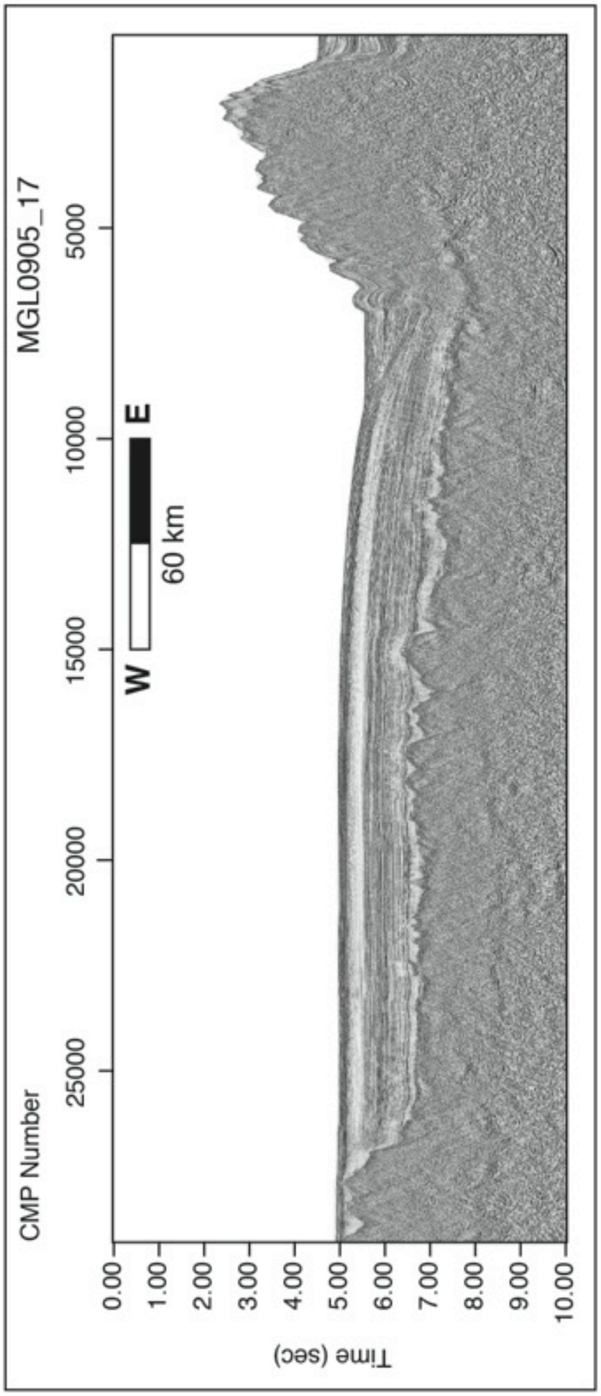

Figure A-2. Reflection profile MGL0905_17.

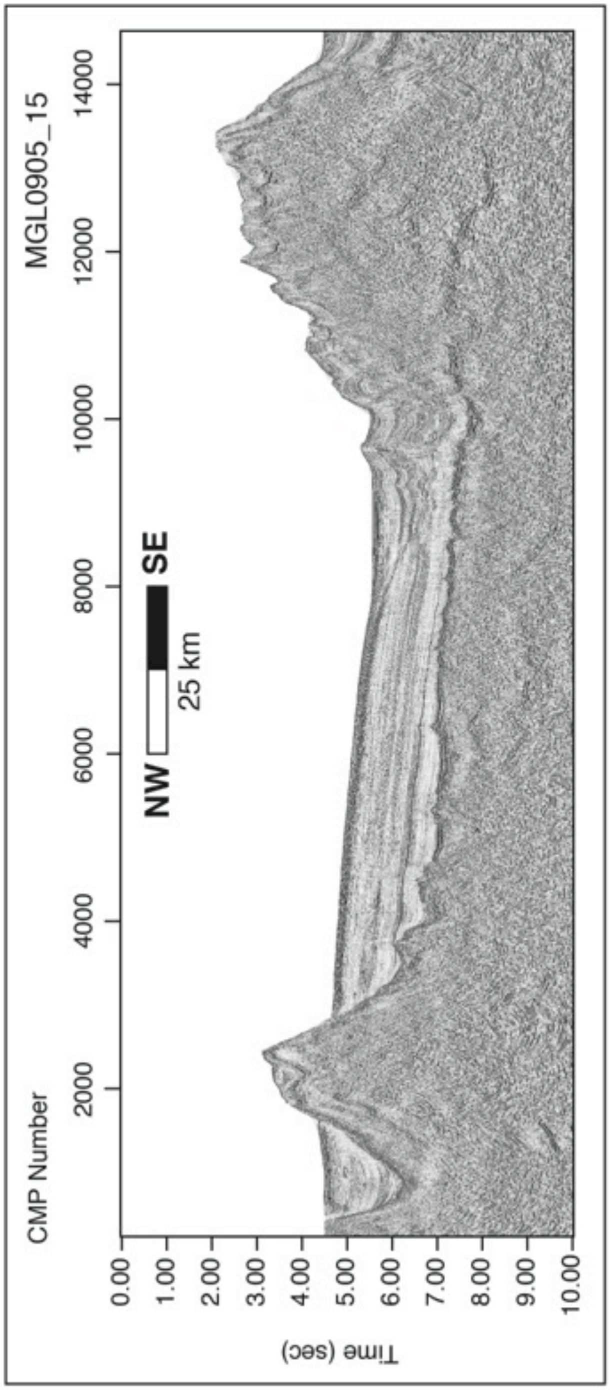

Figure A-3. Reflection profile MGL0905_15.

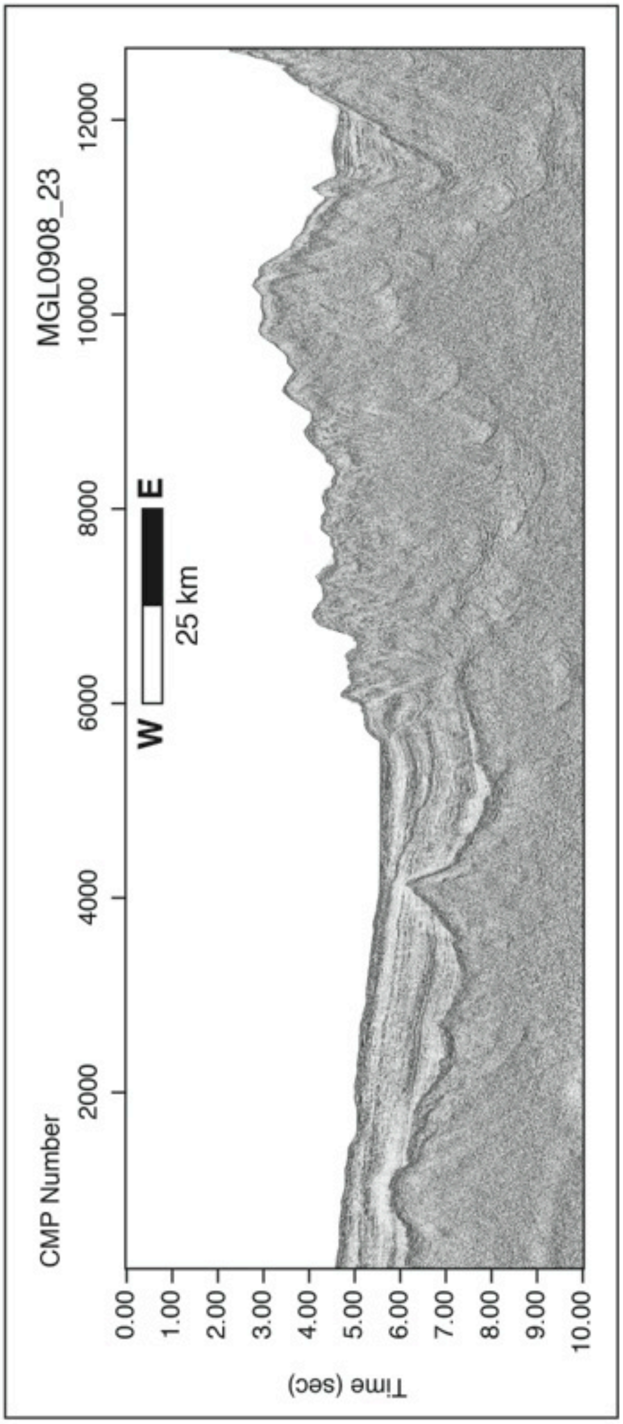

Figure A-4. Reflection profile MGL0908_23.

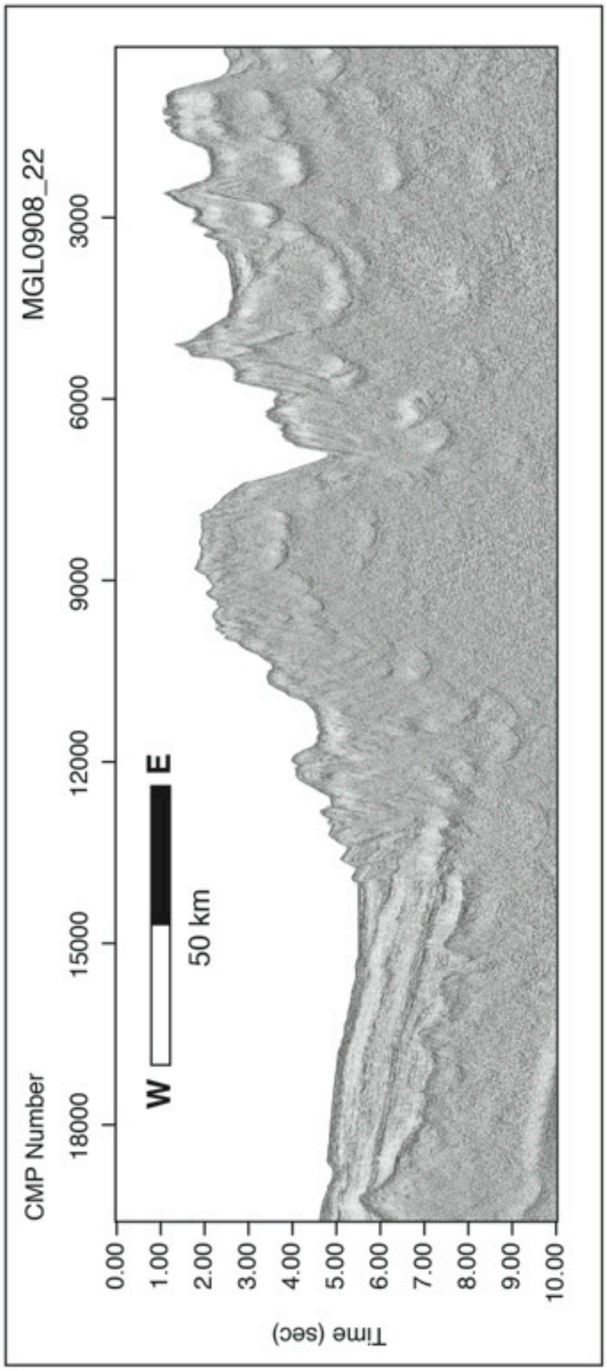

Figure A-5. Reflection profile MGL0908_22.

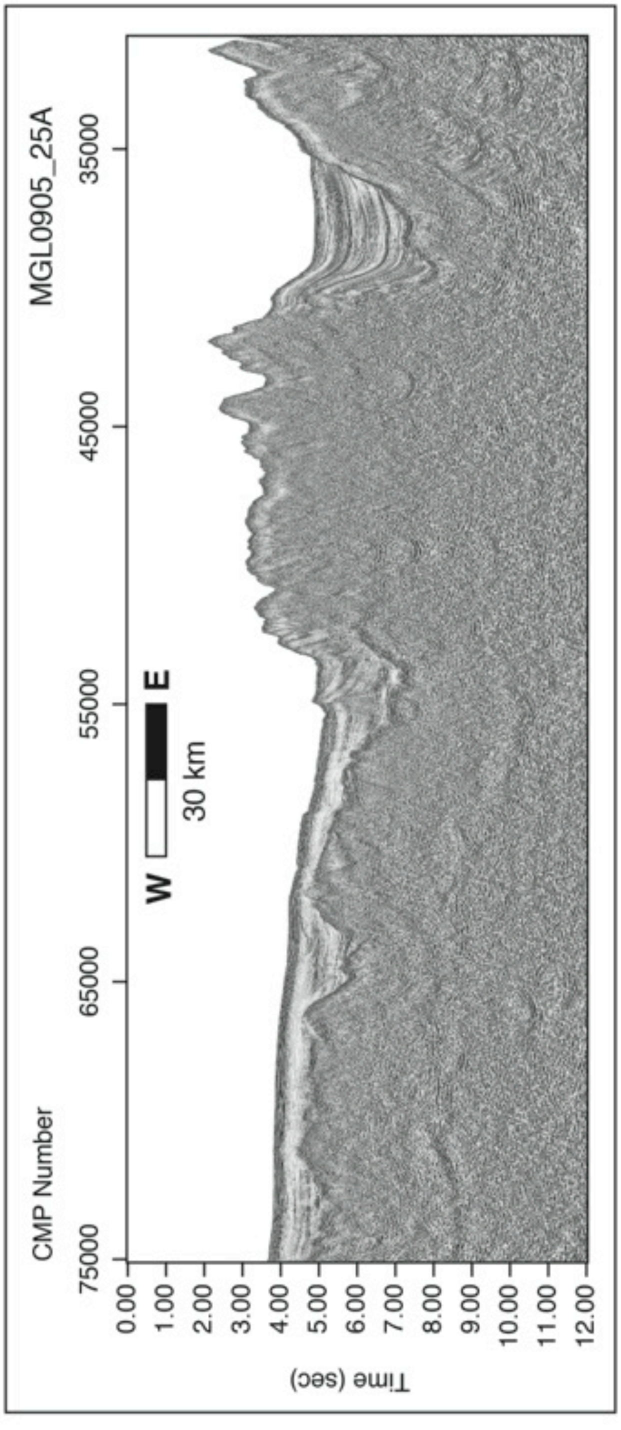

Figure A-6. Reflection profile MGL0905_25A.

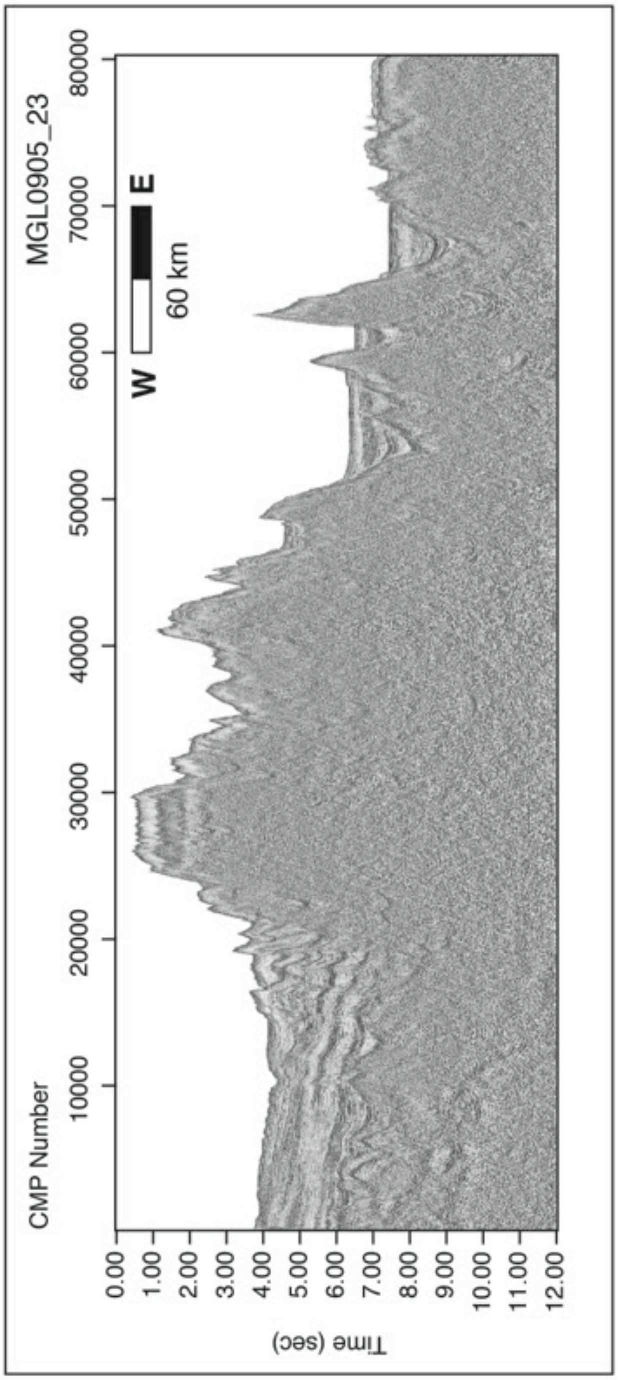

Figure A-7. Reflection profile MGL0905_23.

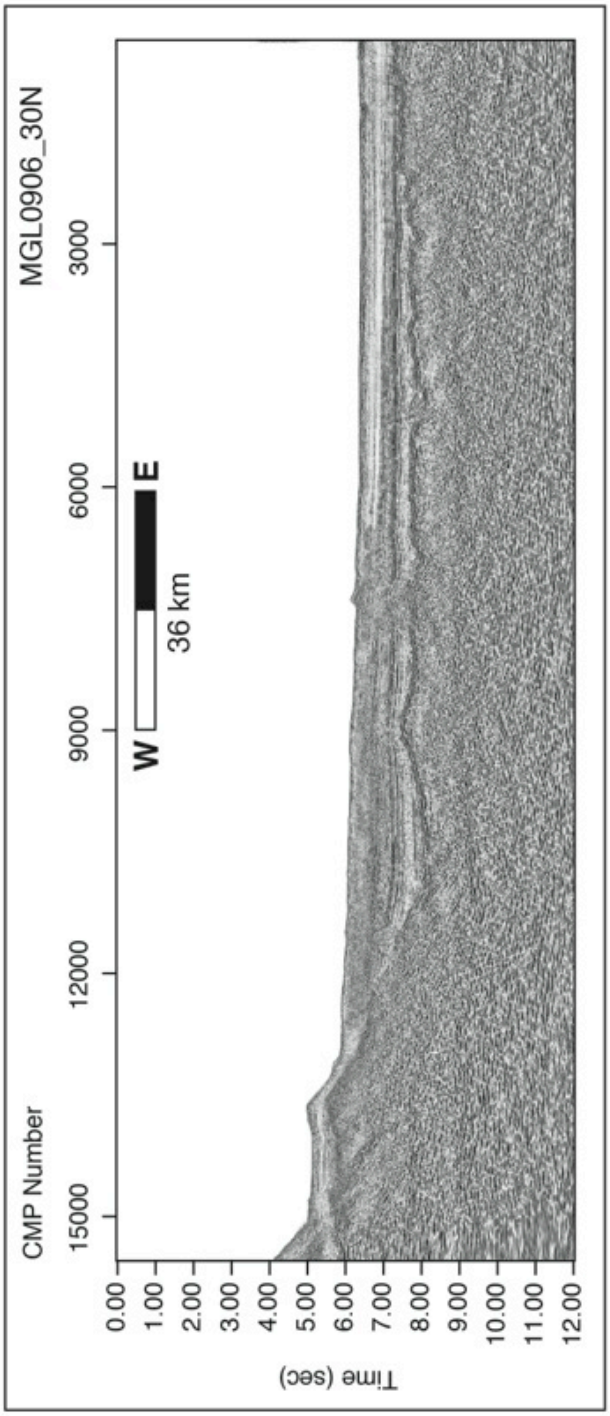

Figure A-8. Reflection profile MGL0906_30N.

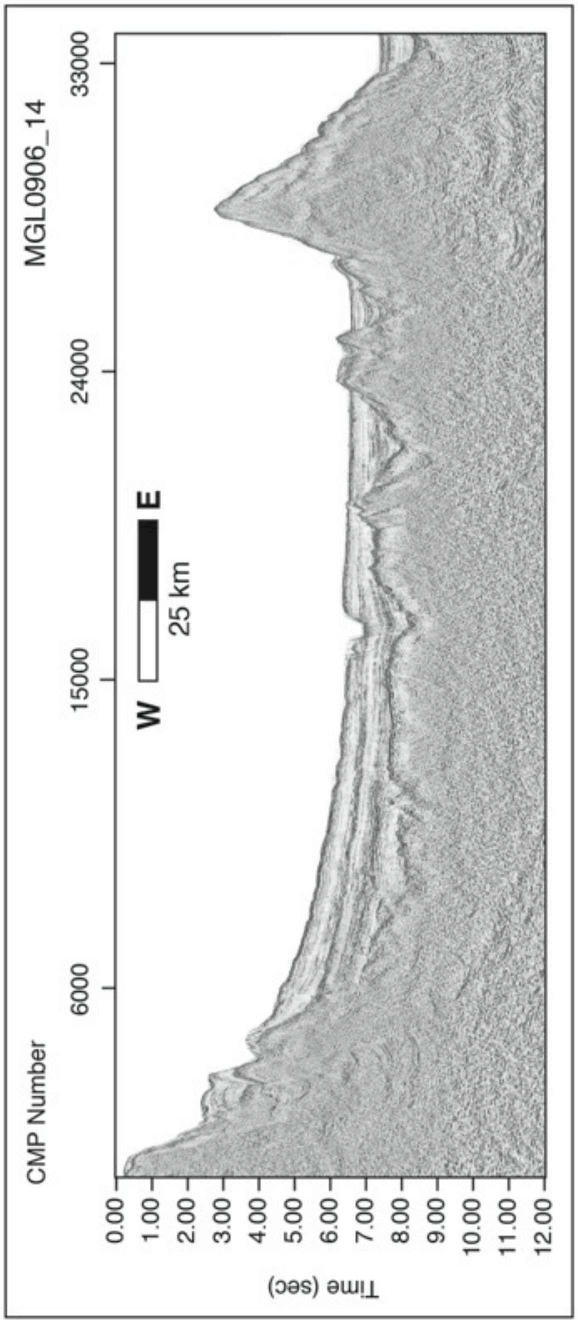

Figure A-9. Reflection profile MGL0906_14.

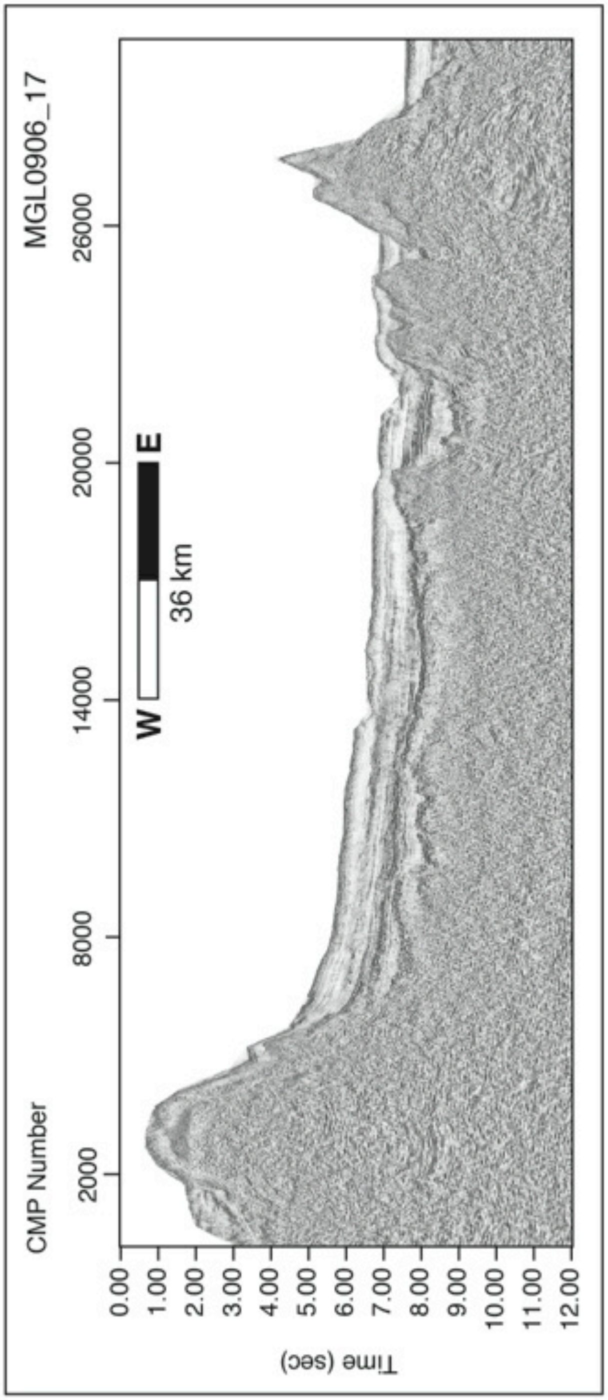

Figure A-10. Reflection profile MGL0906_17.

APPENDIX B: LINE T1 OBS

This section of the appendix contains the ocean bottom seismometer (OBS) records acquired along line T1 not included in chapter 2. OBS 04, OBS09, and OBS 16 are presented in chapter 2. Each includes the unprocessed record and a fully processed record with similar processing as described in chapter 2.

OBS	Long	Lat
OBS-02	119.375	20.5732
OBS-03	119.566	20.5745
OBS-04	119.753	20.5653
OBS-05	119.864	20.5707
OBS-06	119.953	20.5676
OBS-08	120.141	20.5703
OBS-09	120.236	20.5649
OBS-10	120.331	20.5703
OBS-11	120.433	20.5678
OBS-12	120.522	20.568
OBS-13	120.627	20.5732
OBS-14	120.714	20.5706
OBS-15	120.807	20.569
OBS-16	120.904	20.5666
OBS-17	121. 20	5653
OBS-18	121.098	20.5697
OBS-19	121.19	20.5705

Table B-1. Line T1 OBS locations.

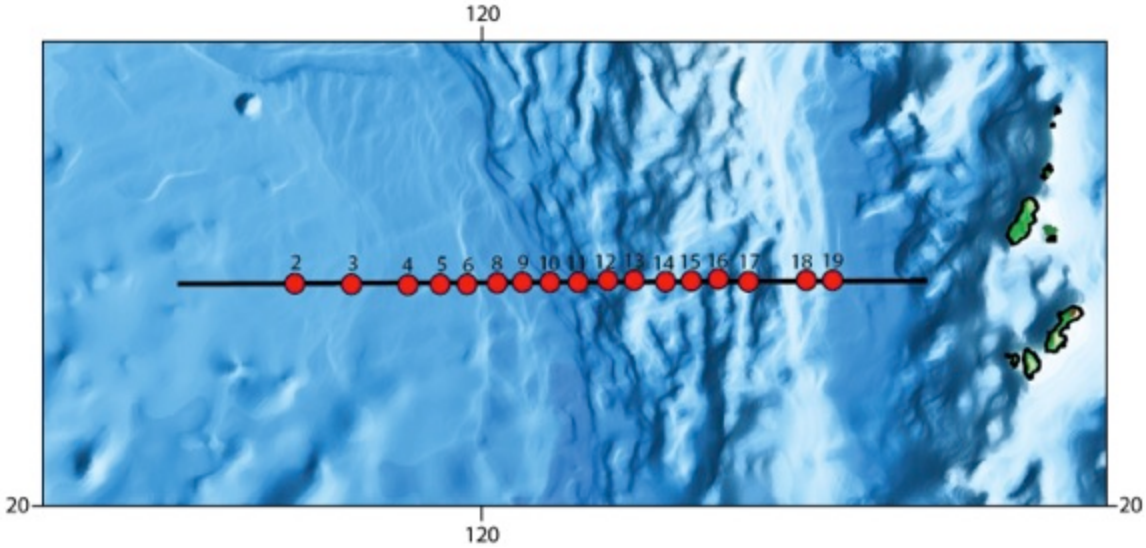

Figure B-1. Location map of line T1 coincident reflection and wide-angle refraction profile.

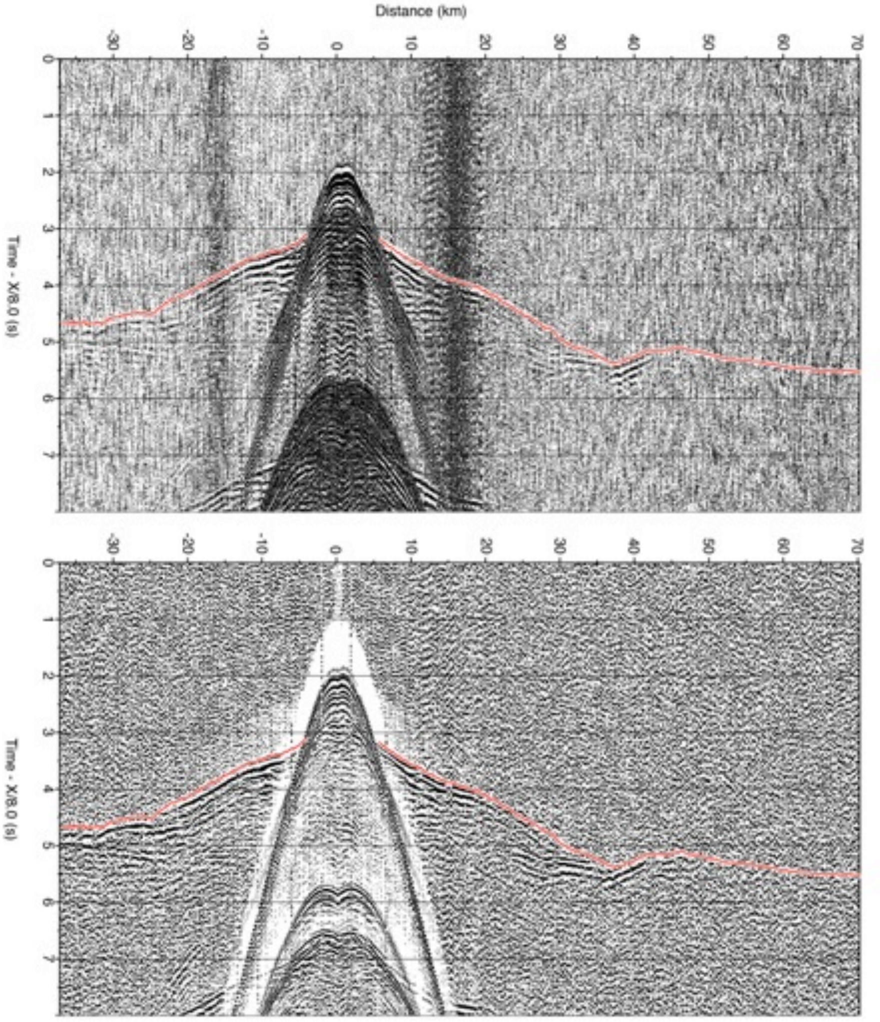

Figure B-2. OBS 02 hydrophone component with first-arrival travel-time picks. Top is unprocessed; bottom is processed to suppress previous shot noise using gapped deconvolution, bandpass filtering, AGC and gaining with offset.

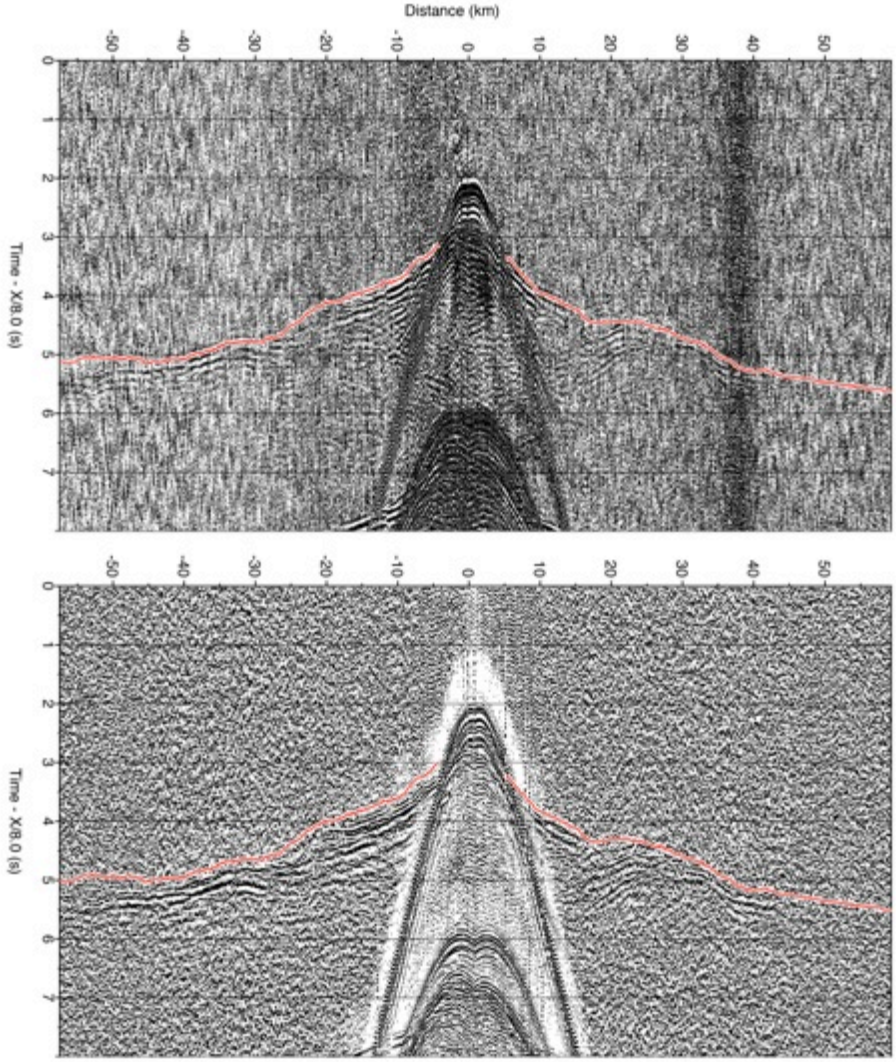

Figure B-3. OBS 03 hydrophone component with first-arrival travel-time picks. Top is unprocessed; bottom is processed to suppress previous shot noise using gapped deconvolution, bandpass filtering, AGC and gaining with offset.

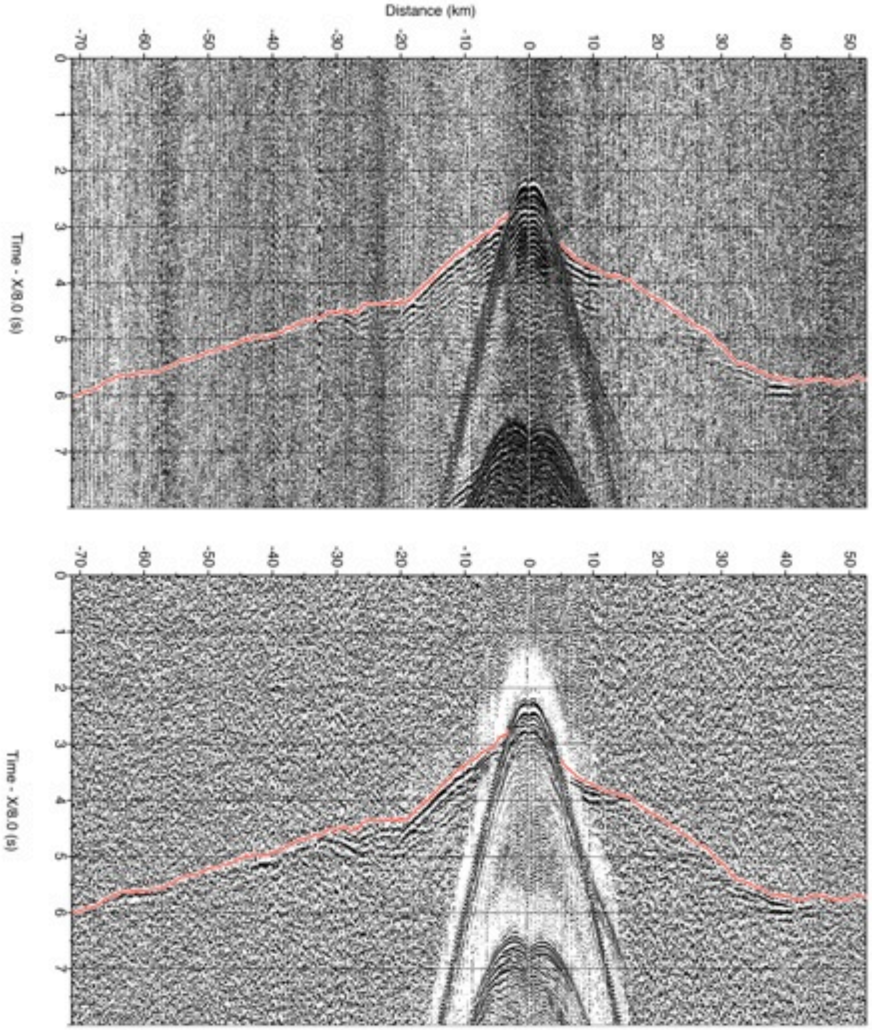

Figure B-4. OBS 05 hydrophone component with first-arrival travel-time picks. Top is unprocessed; bottom is processed to suppress previous shot noise using gapped deconvolution, bandpass filtering, AGC and gaining with offset.

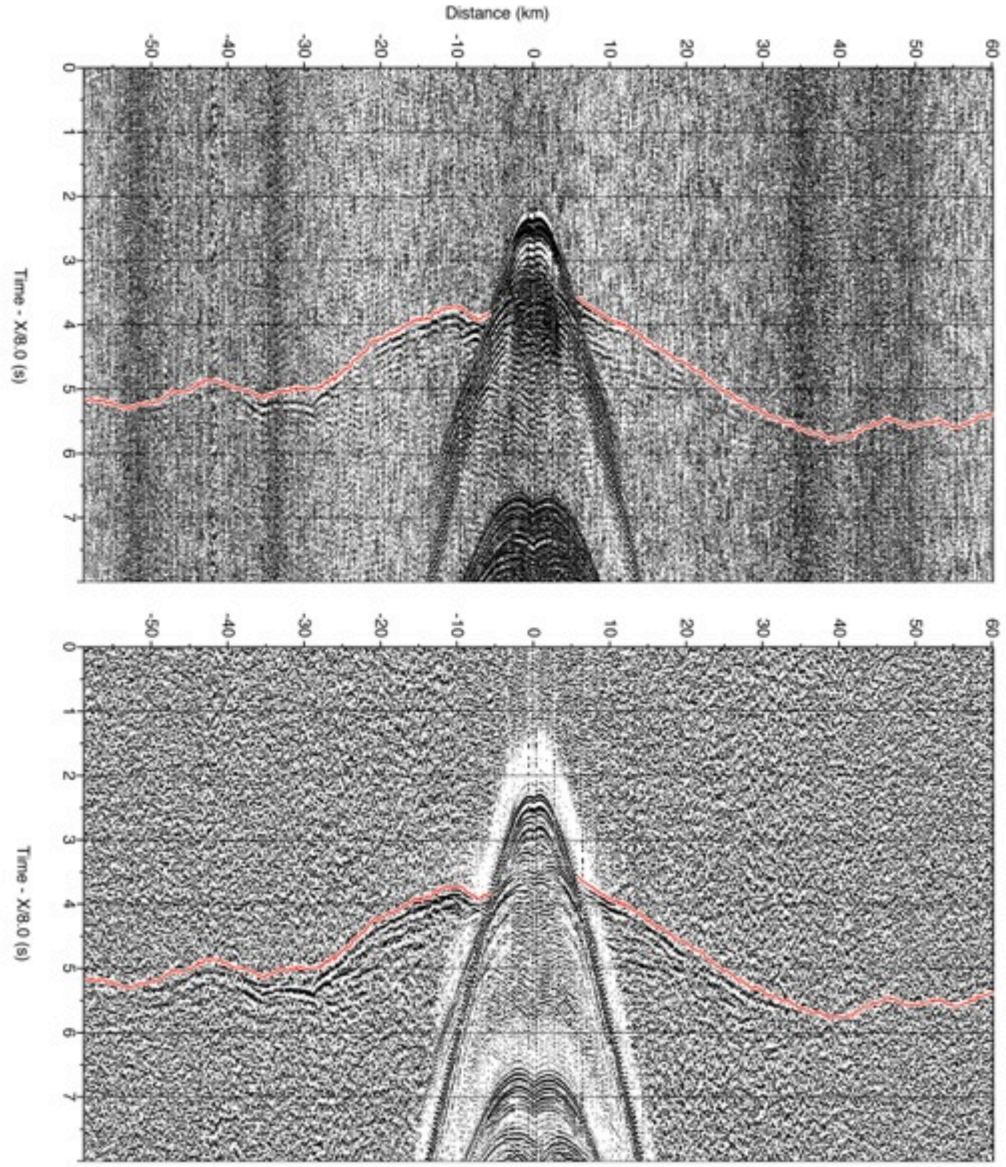

Figure B-5. OBS 06 hydrophone component with first-arrival travel-time picks. Top is unprocessed; bottom is processed to suppress previous shot noise using gapped deconvolution, bandpass filtering, AGC and gaining with offset.

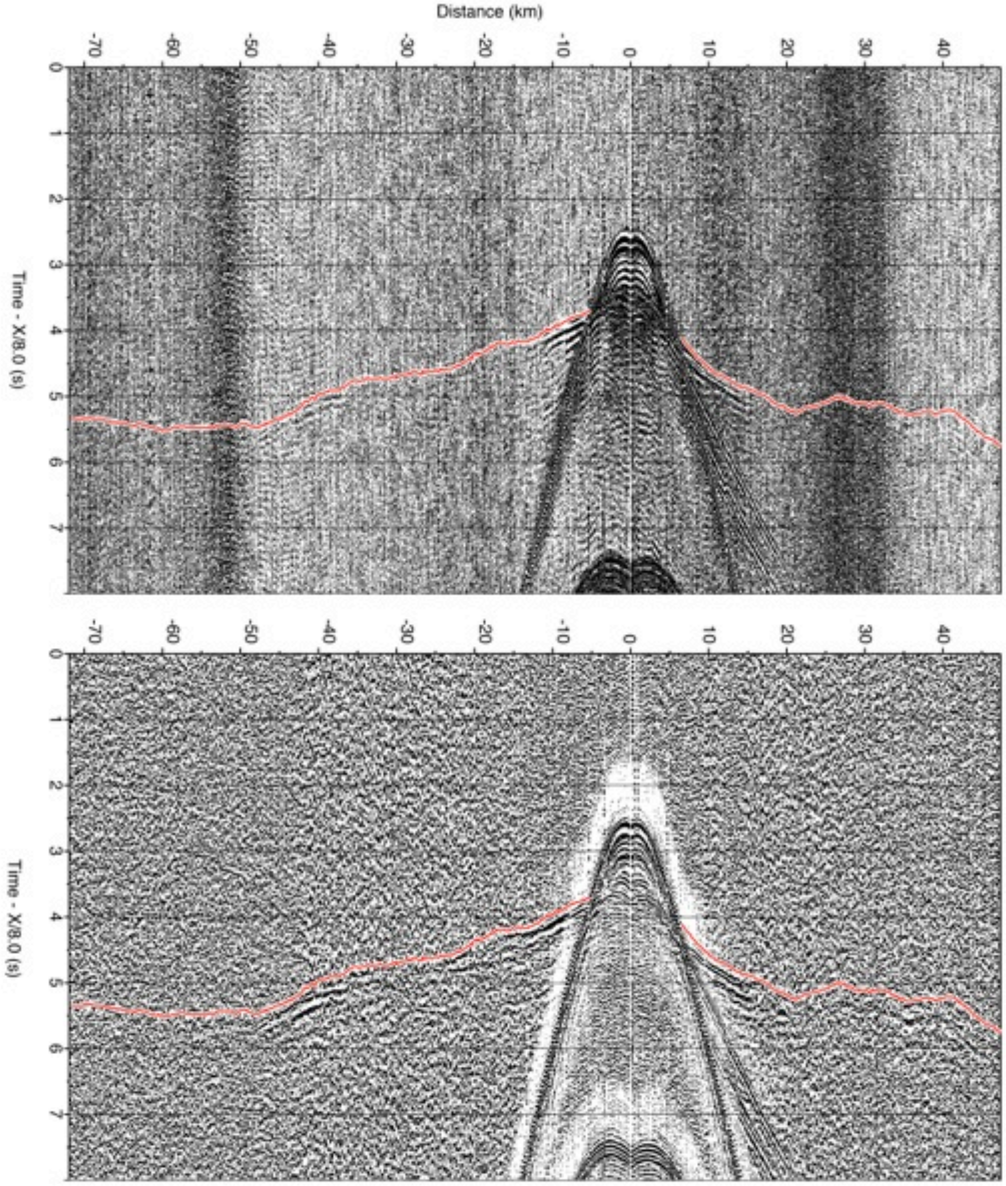

Figure B-6. OBS 08 hydrophone component with first-arrival travel-time picks. Top is unprocessed; bottom is processed to suppress previous shot noise using gapped deconvolution, bandpass filtering, AGC and gaining with offset.

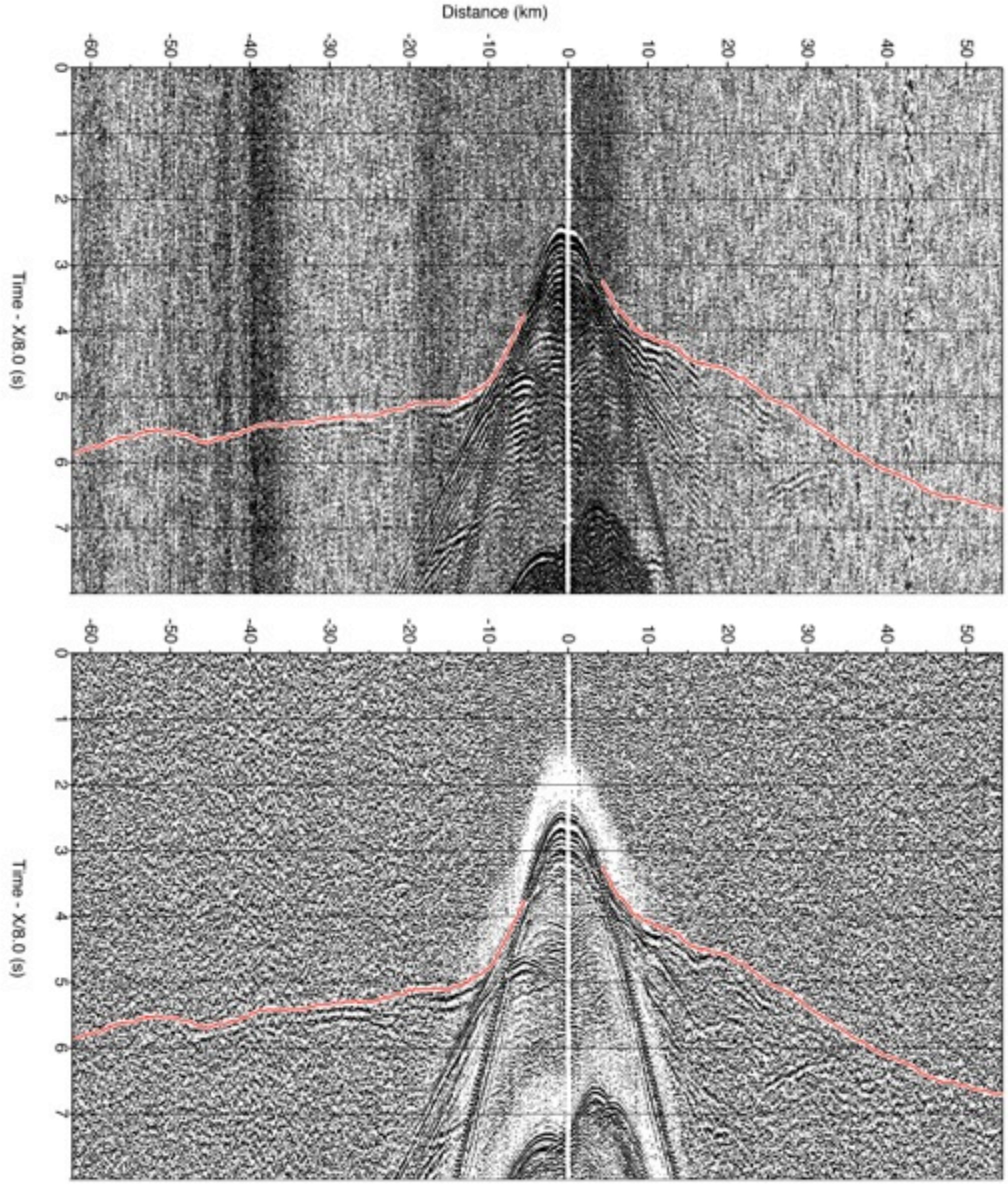

Figure B-7. OBS 10 hydrophone component with first-arrival travel-time picks. Top is unprocessed; bottom is processed to suppress previous shot noise using gapped deconvolution, bandpass filtering, AGC and gaining with offset.

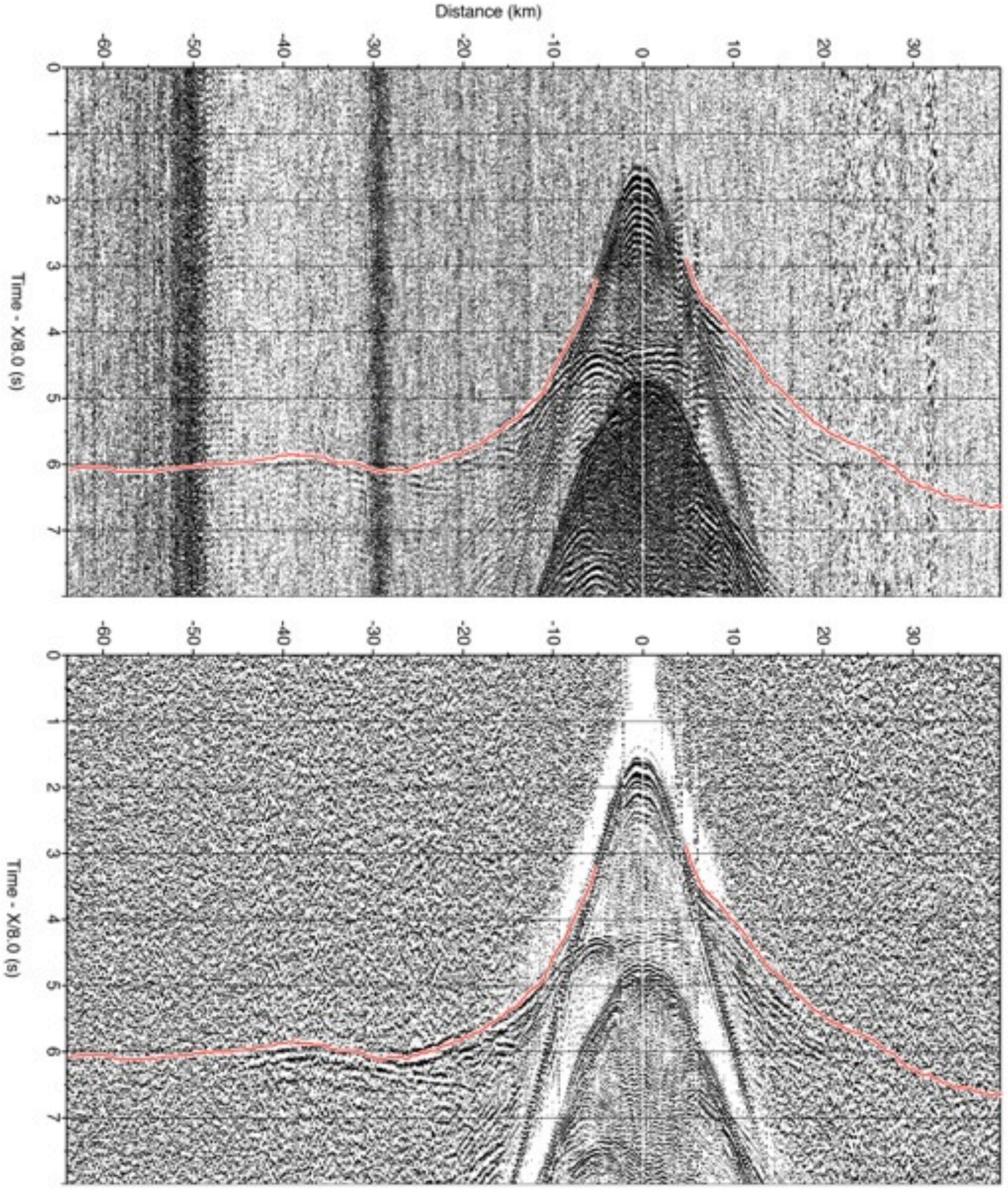

Figure B-8. OBS 11 hydrophone component with first-arrival travel-time picks. Top is unprocessed; bottom is processed to suppress previous shot noise using gapped deconvolution, bandpass filtering, AGC and gaining with offset.

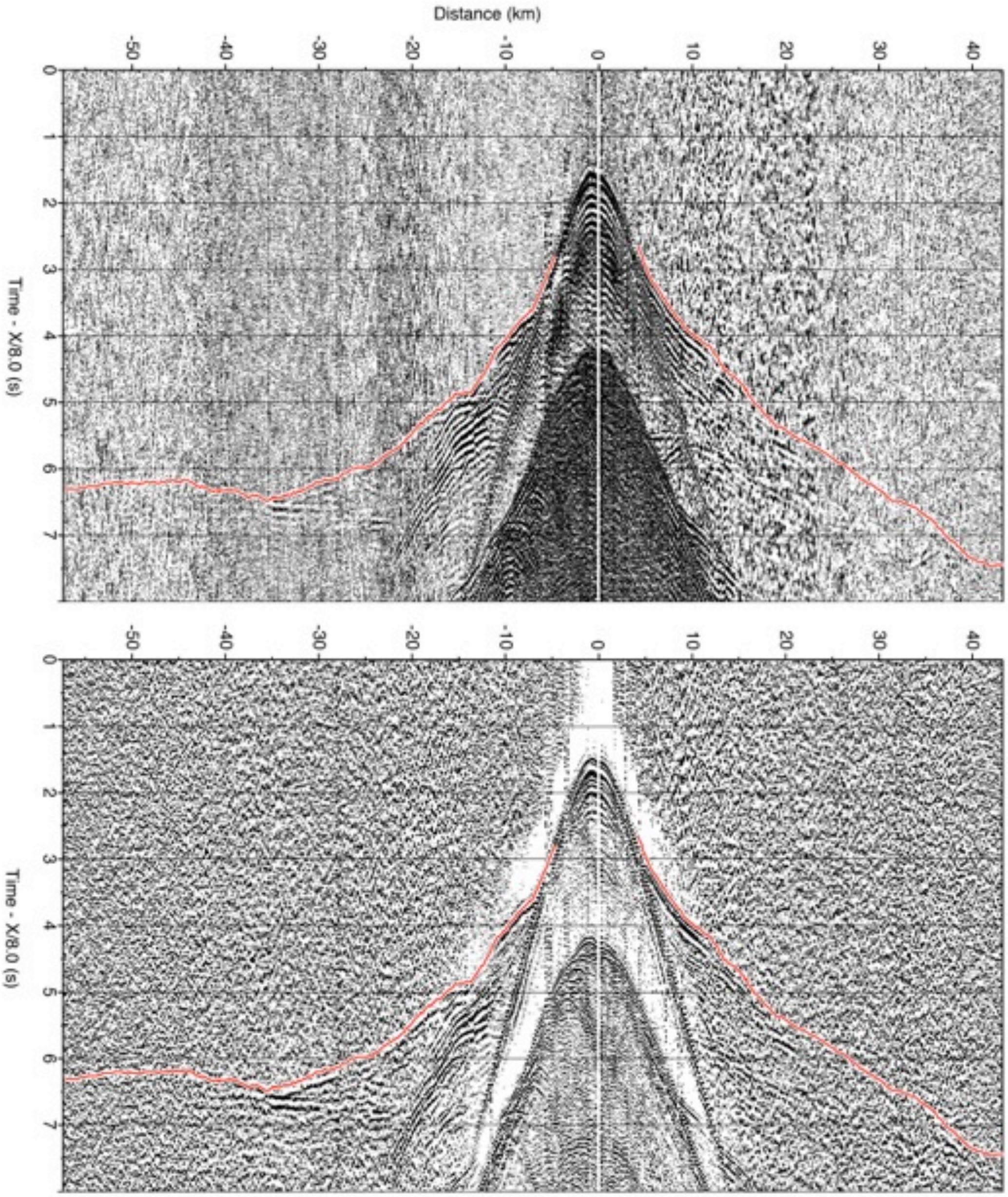

Figure B-9. OBS 12 hydrophone component with first-arrival travel-time picks. Top is unprocessed; bottom is processed to suppress previous shot noise using gapped deconvolution, bandpass filtering, AGC and gaining with offset.

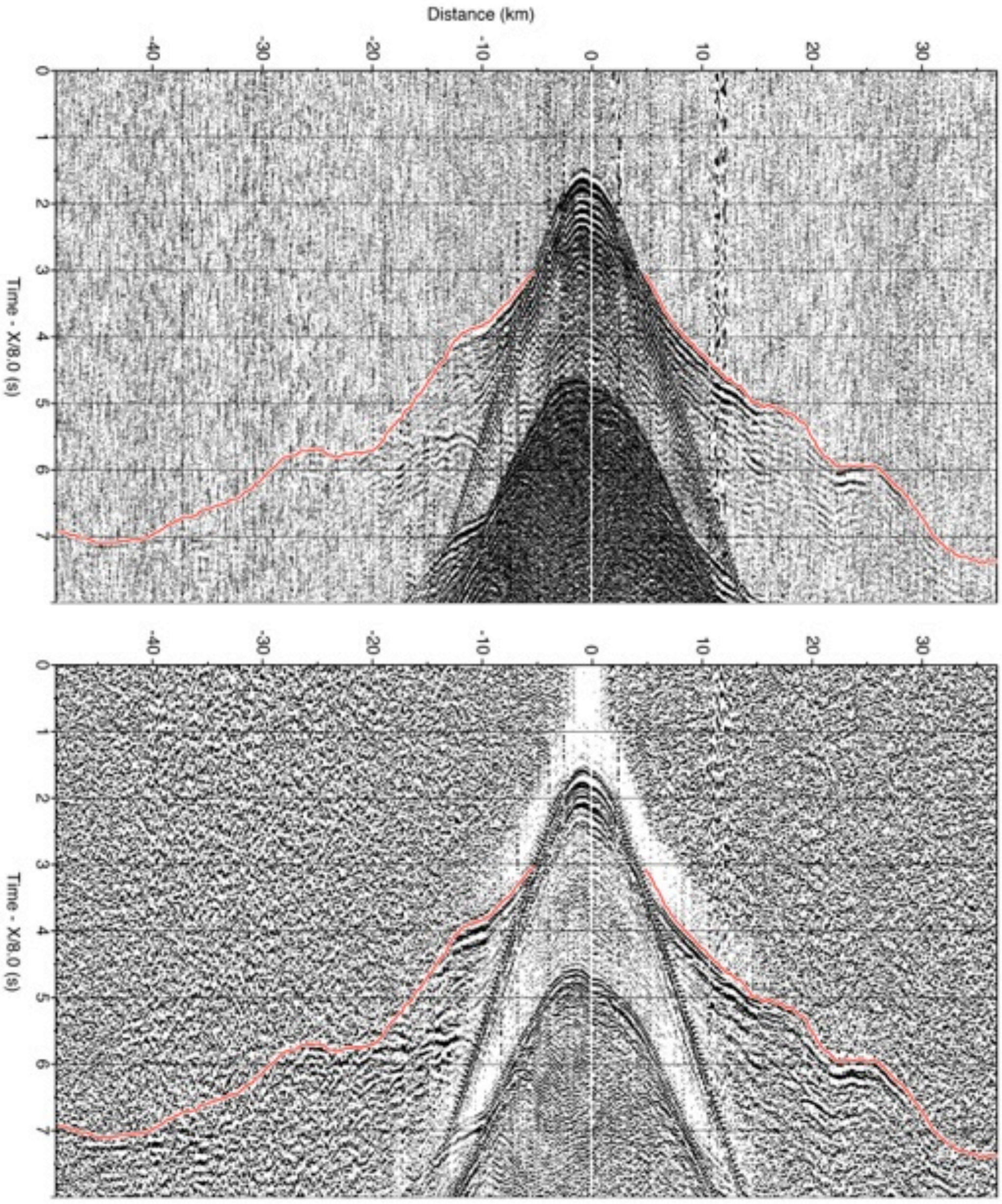

Figure B-10. OBS 13 hydrophone component with first-arrival travel-time picks. Top is unprocessed; bottom is processed to suppress previous shot noise using gapped deconvolution, bandpass filtering, AGC and gaining with offset.

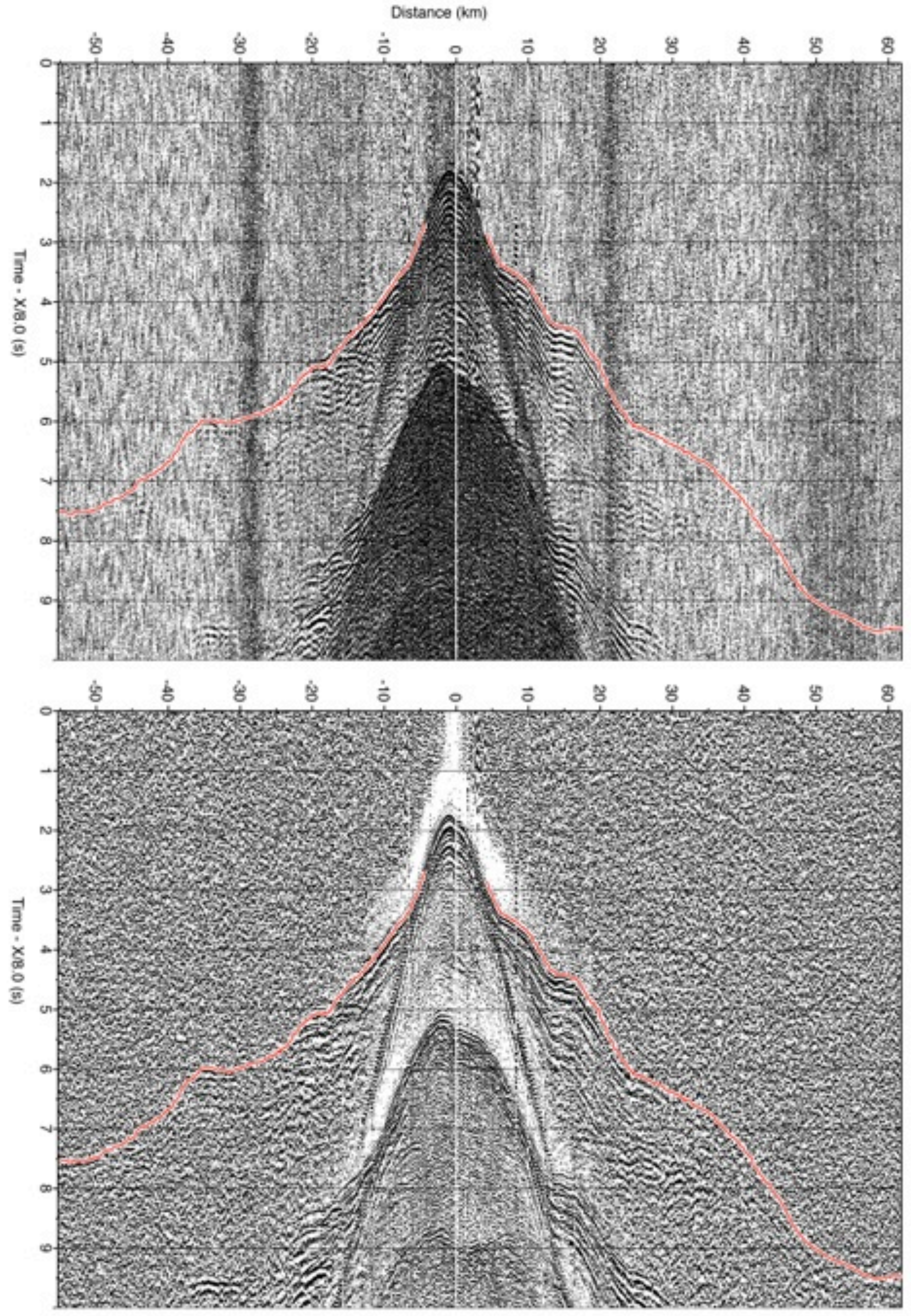

Figure B-11. OBS 14 hydrophone component with first-arrival travel-time picks. Top is unprocessed; bottom is processed to suppress previous shot noise using gapped deconvolution, bandpass filtering, AGC and gaining with offset.

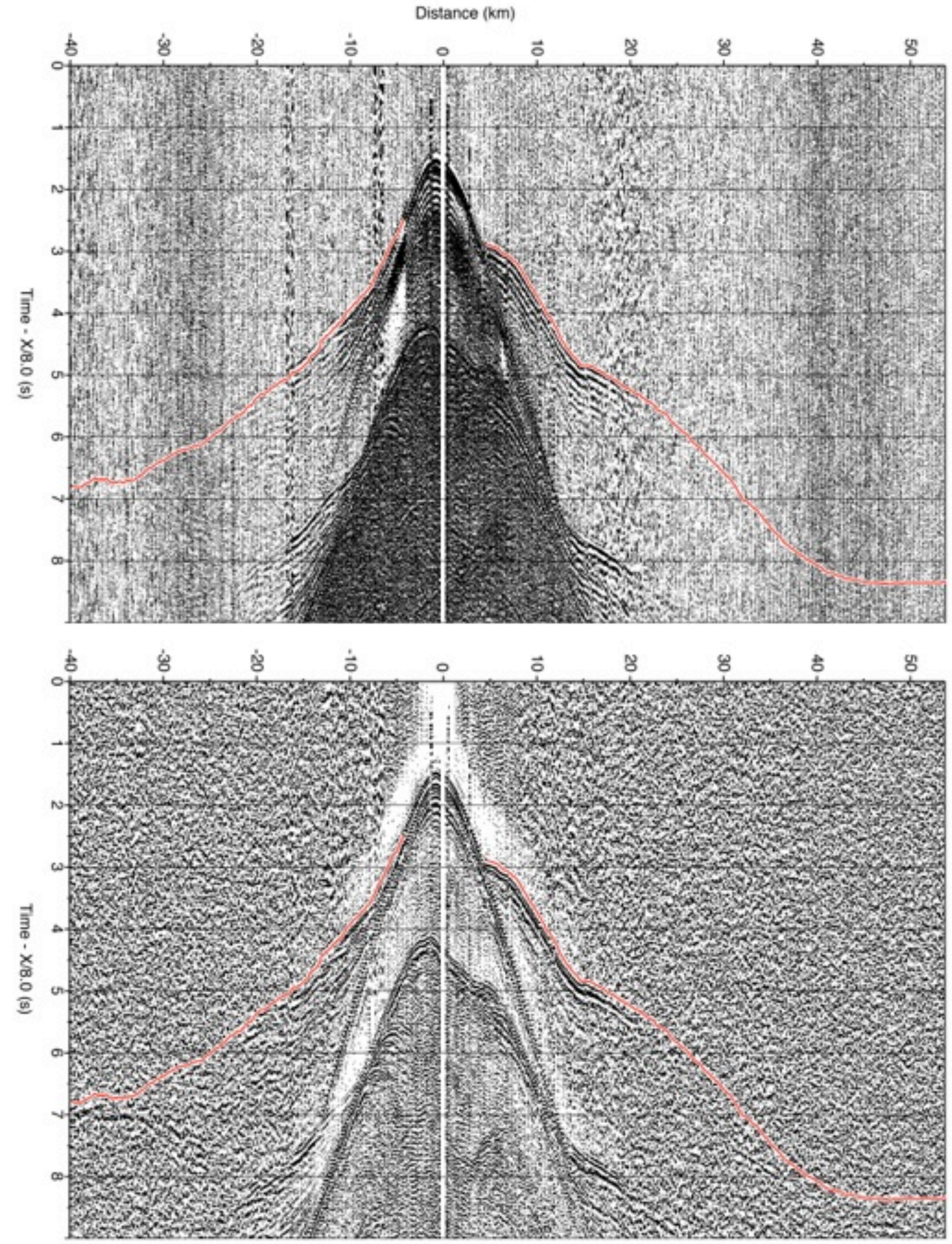

Figure B-12. OBS 15 hydrophone component with first-arrival travel-time picks. Top is unprocessed; bottom is processed to suppress previous shot noise using gapped deconvolution, bandpass filtering, AGC and gaining with offset.

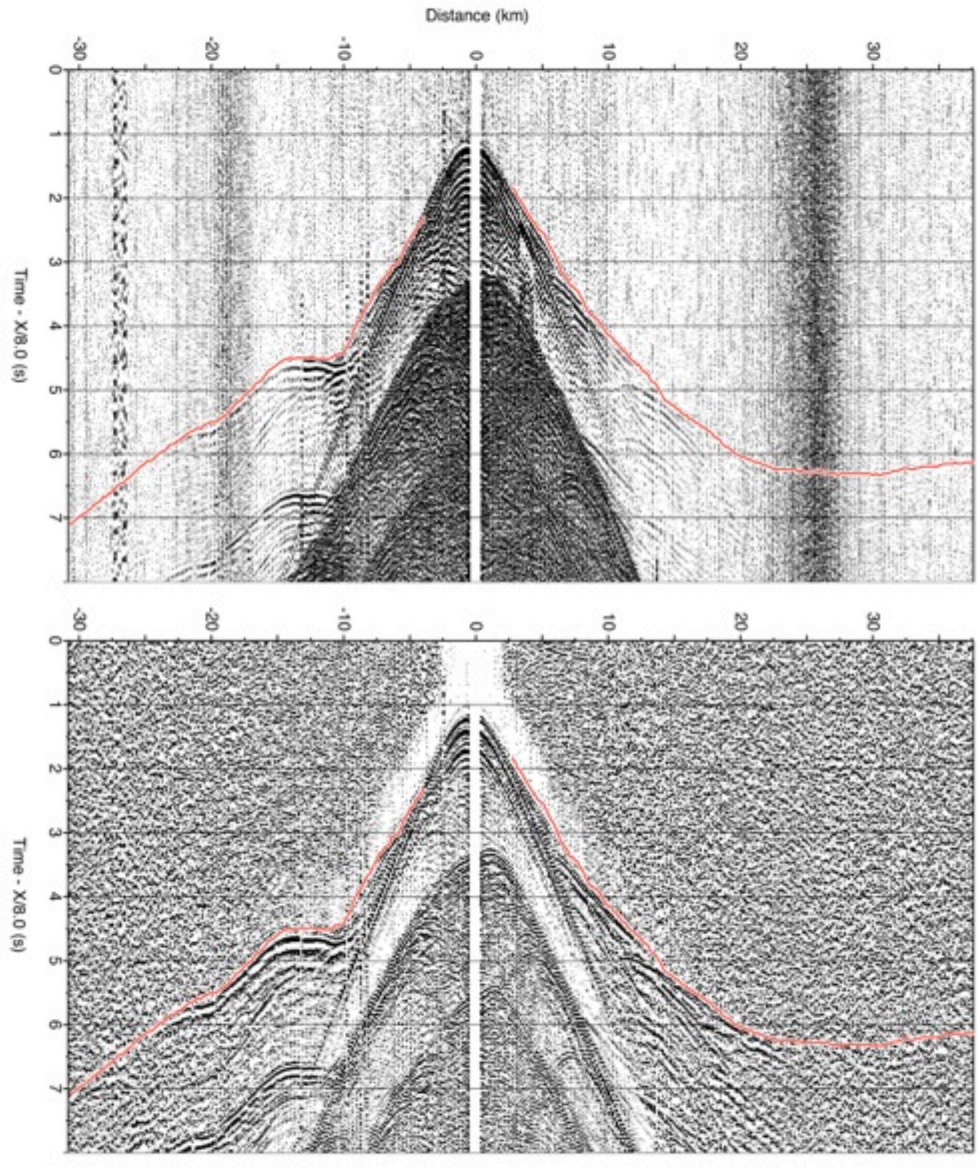

Figure B-13. OBS 17 hydrophone component with first-arrival travel-time picks. Top is unprocessed; bottom is processed to suppress previous shot noise using gapped deconvolution, bandpass filtering, AGC and gaining with offset.

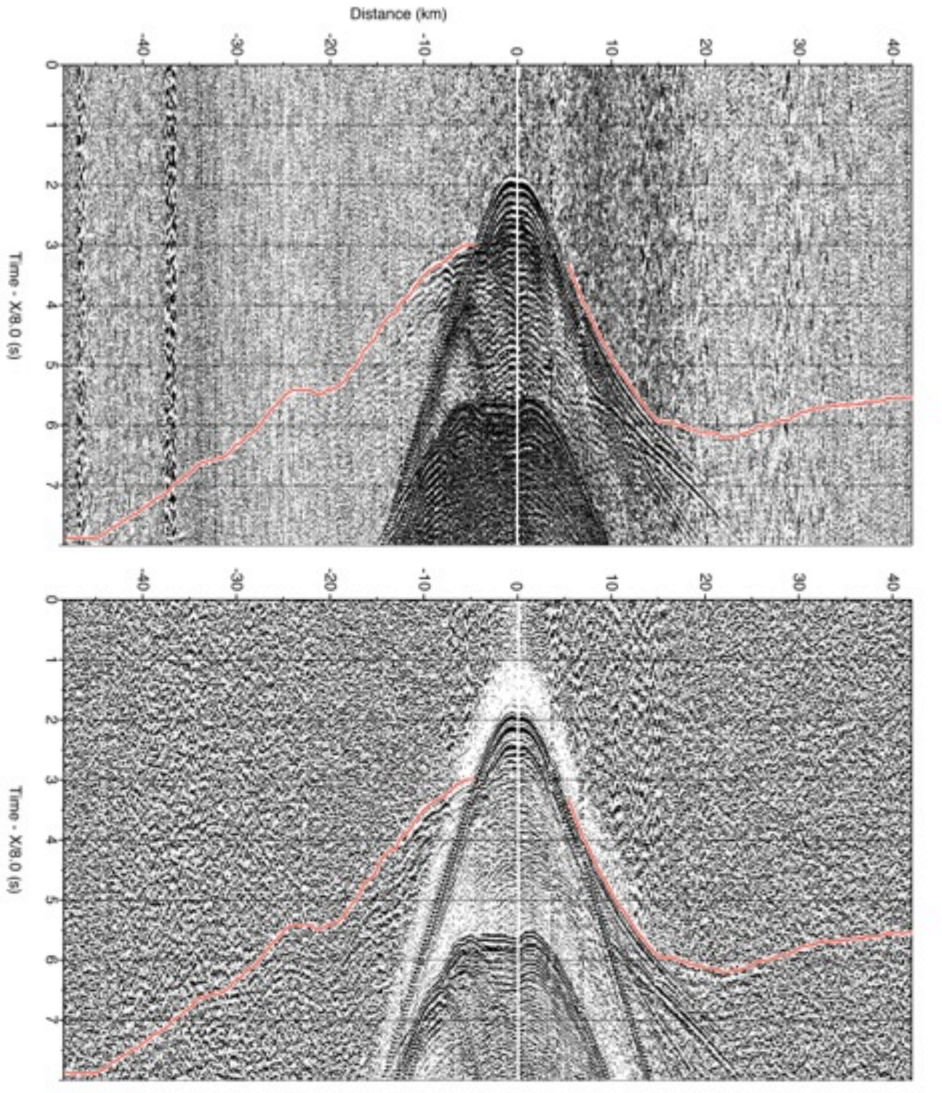

Figure B-14. OBS 18 hydrophone component with first-arrival travel-time picks. Top is unprocessed; bottom is processed to suppress previous shot noise using gapped deconvolution, bandpass filtering, AGC and gaining with offset.

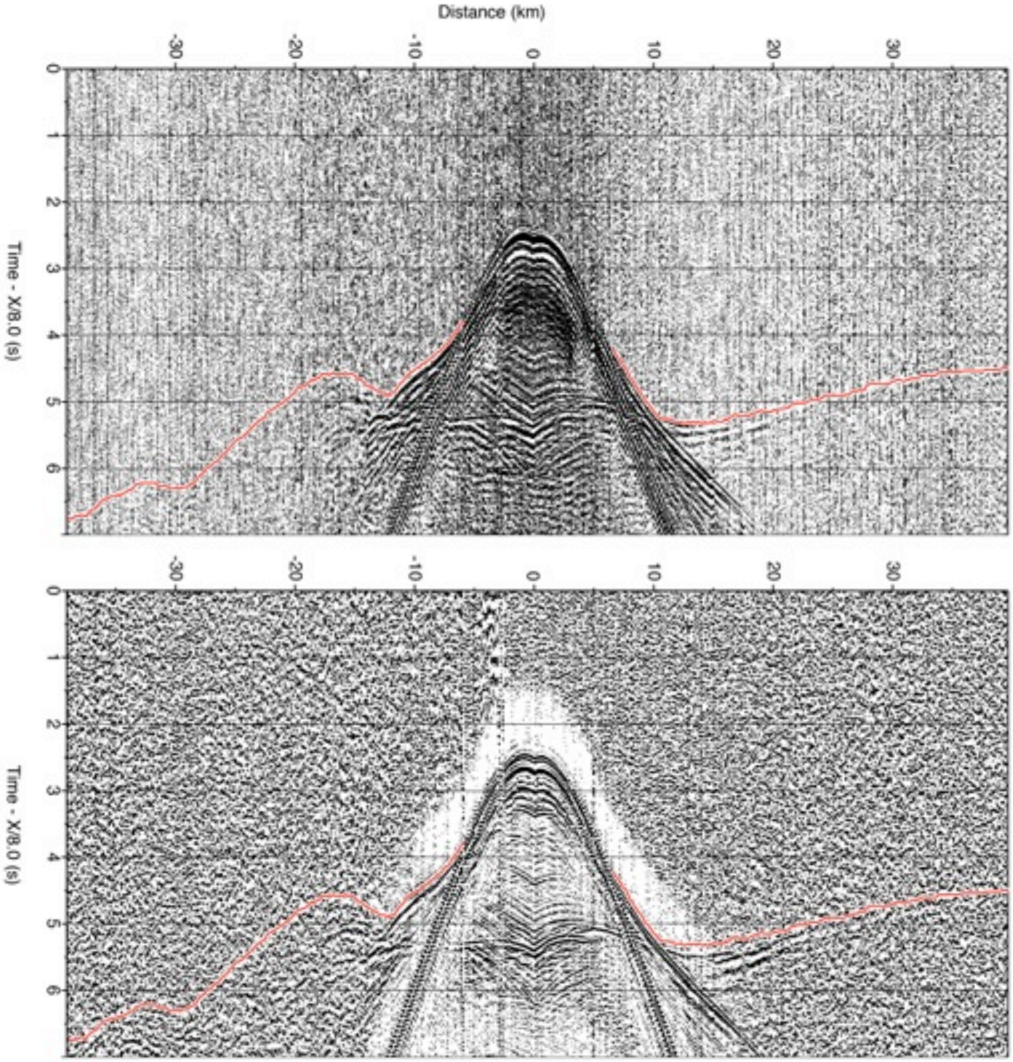

Figure B-15. OBS 19 hydrophone component with first-arrival travel-time picks. Top is unprocessed; bottom is processed to suppress previous shot noise using gapped deconvolution, bandpass filtering, AGC and gaining with offset.

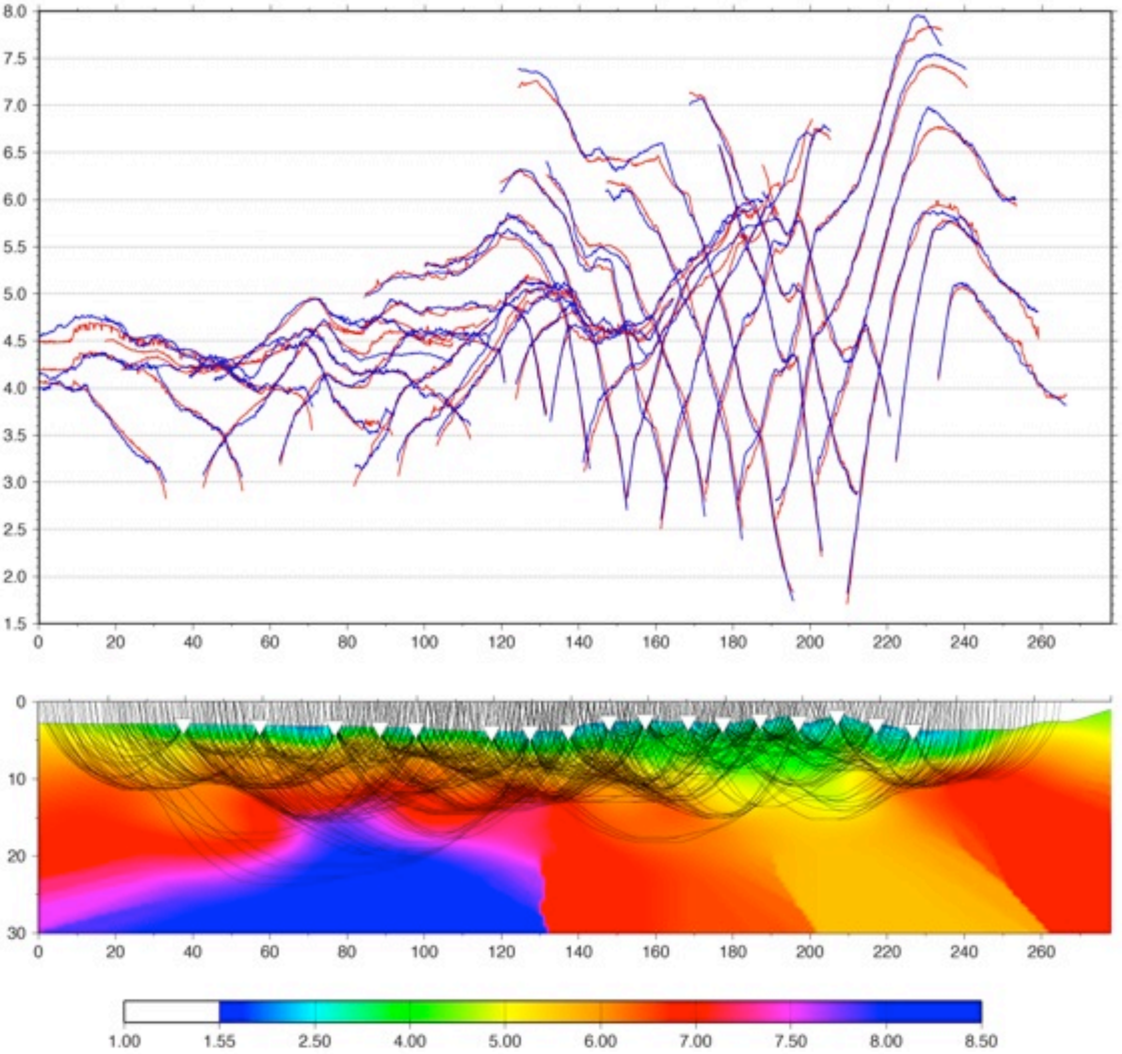

Figure B-16. Ray coverage of line T1 velocity model.

APPENDIX C: LINE T1B OBS

This section of the appendix contains the ocean bottom seismometer (OBS) records acquired along line T1B not included in chapter 3. OBS 20 and OBS 23 are presented in chapter 3.

OBS	Long	Lat
OBS-20	122.527	20.5675
OBS-21	122.628	20.5672
OBS-22	122.723	20.5676
OBS-23	122.819	20.5677
OBS-24	123.003	20.5679
OBS-25	123.105	20.5652
OBS-26	123.197	20.5619

Table C-1: Line T1B OBS locations.

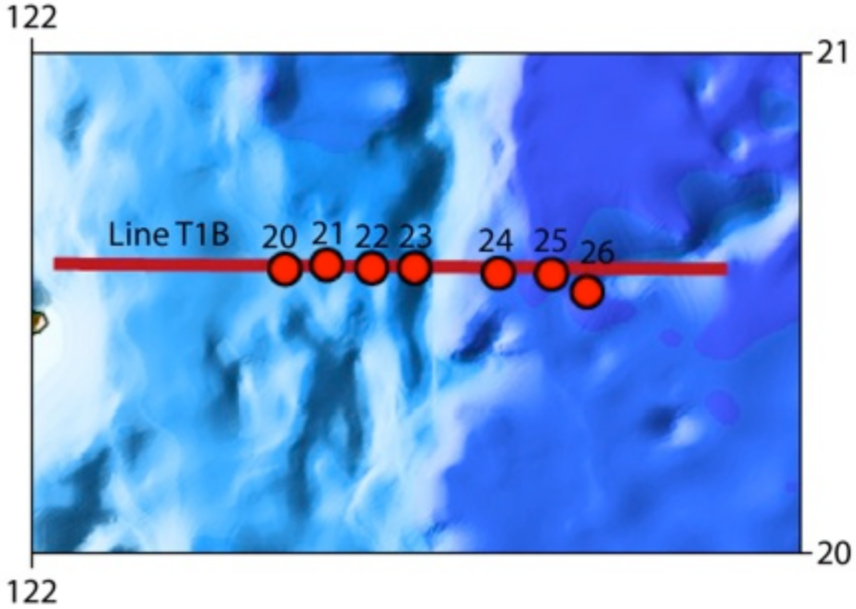

Figure C-1. Location map of line T1B wide-angle refraction profile.

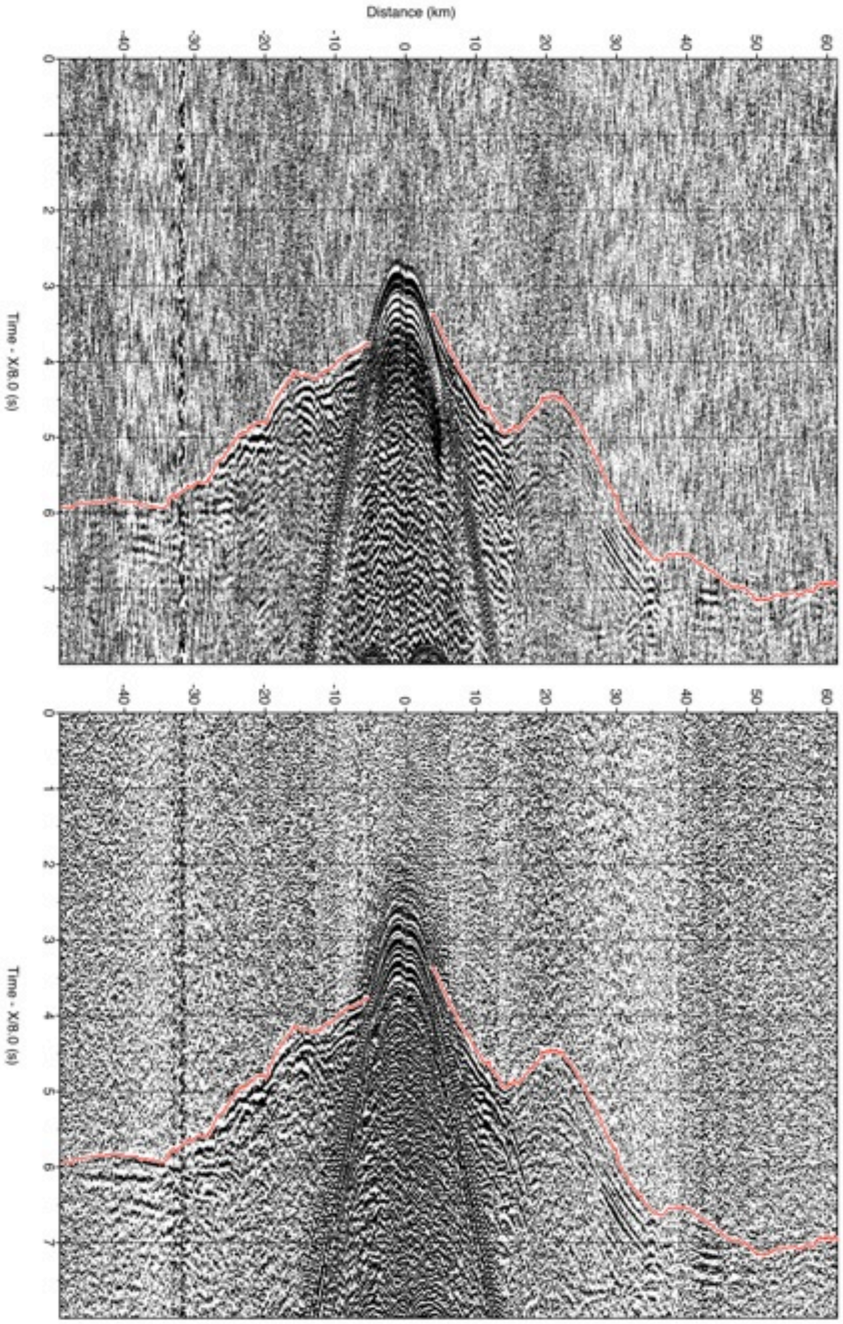

Figure C-2. OBS 21 hydrophone component with first-arrival travel-time picks. Top is un-processed; bottom is processed to suppress the previous shot noise using gapped deconvolution, bandpass filtering, AGC and gaining with offset.

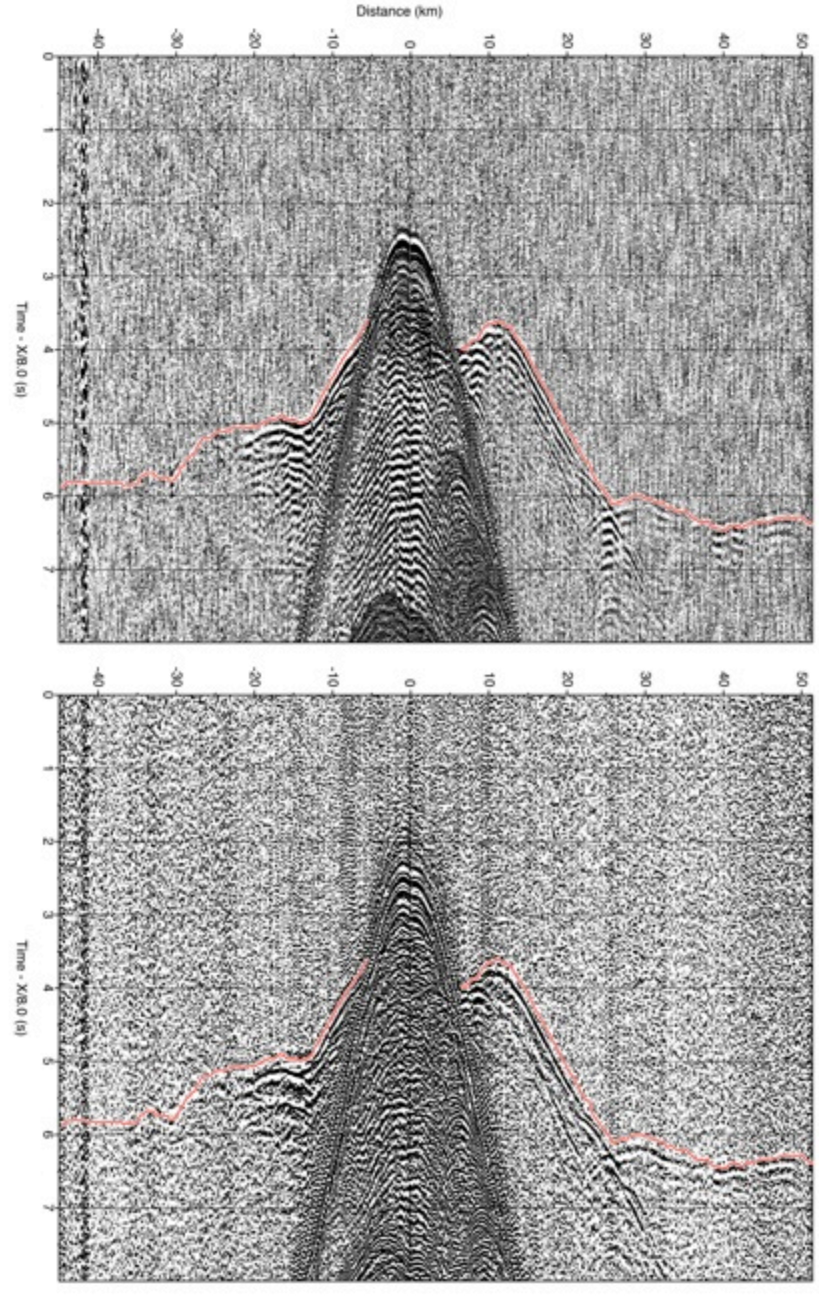

Figure C-3. OBS 22 hydrophone component with first-arrival travel-time picks. Top is un-processed; bottom is processed to suppress the previous shot noise using gapped deconvolution, bandpass filtering, AGC and gaining with offset.

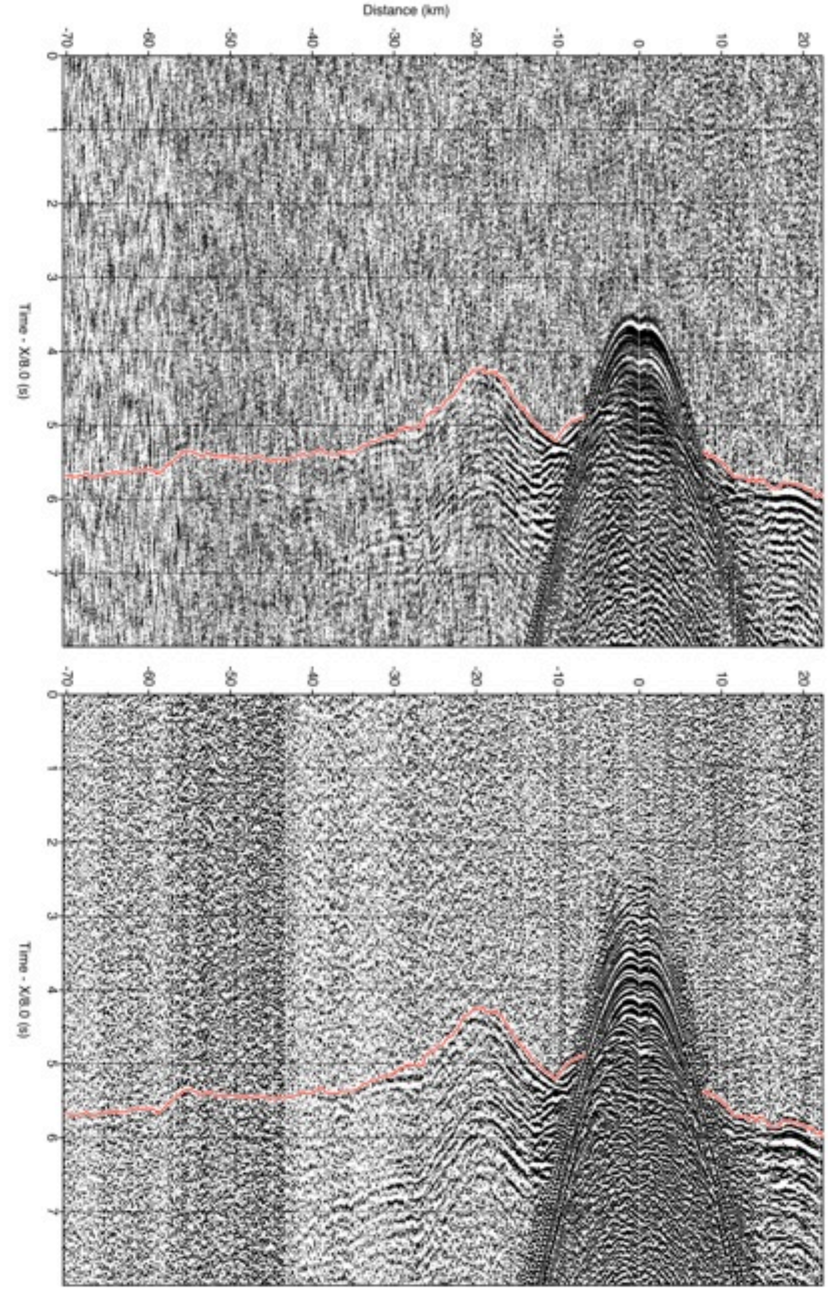

Figure C-4. OBS 24 hydrophone component with first-arrival travel-time picks. Top is un-processed; bottom is processed to suppress the previous shot noise using gapped deconvolution, bandpass filtering, AGC and gaining with offset.

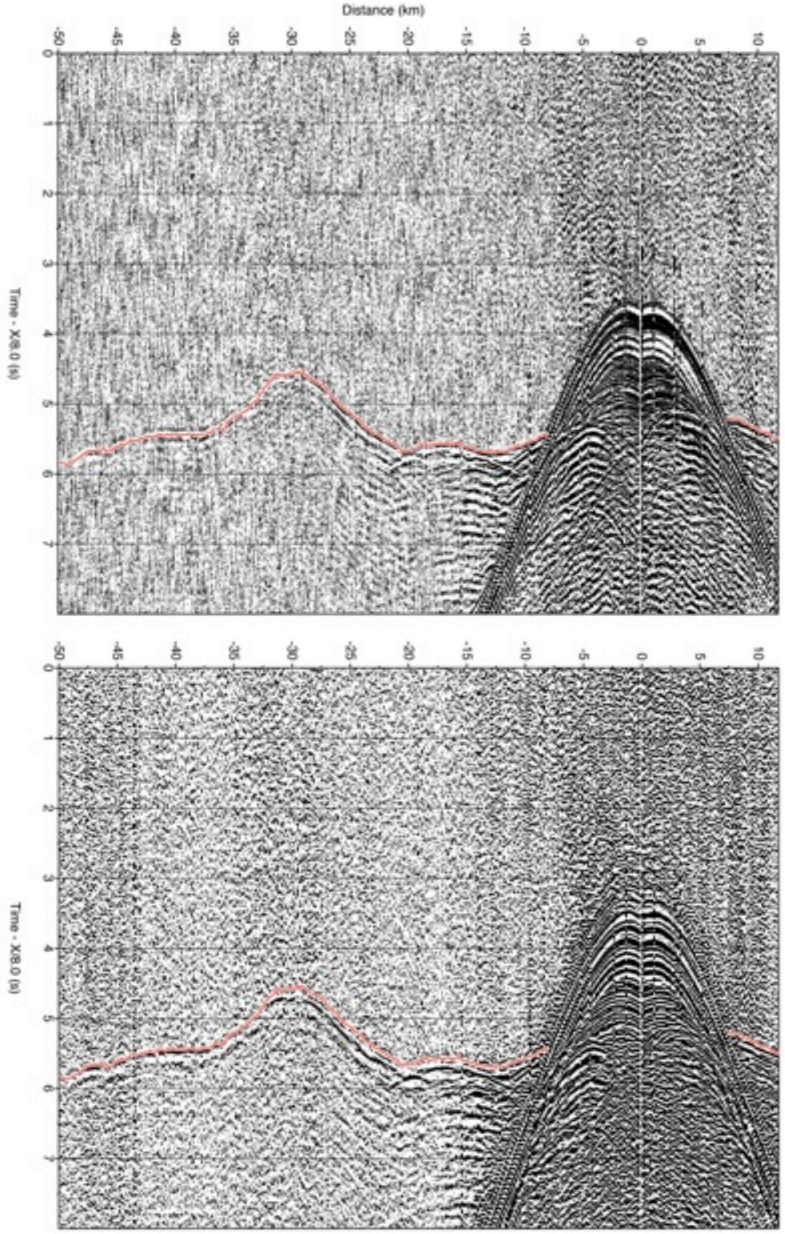

Figure C-5. OBS 25 hydrophone component with first-arrival travel-time picks. Top is un-processed; bottom is processed to suppress the previous shot noise using gapped deconvolution, bandpass filtering, AGC and gaining with offset.

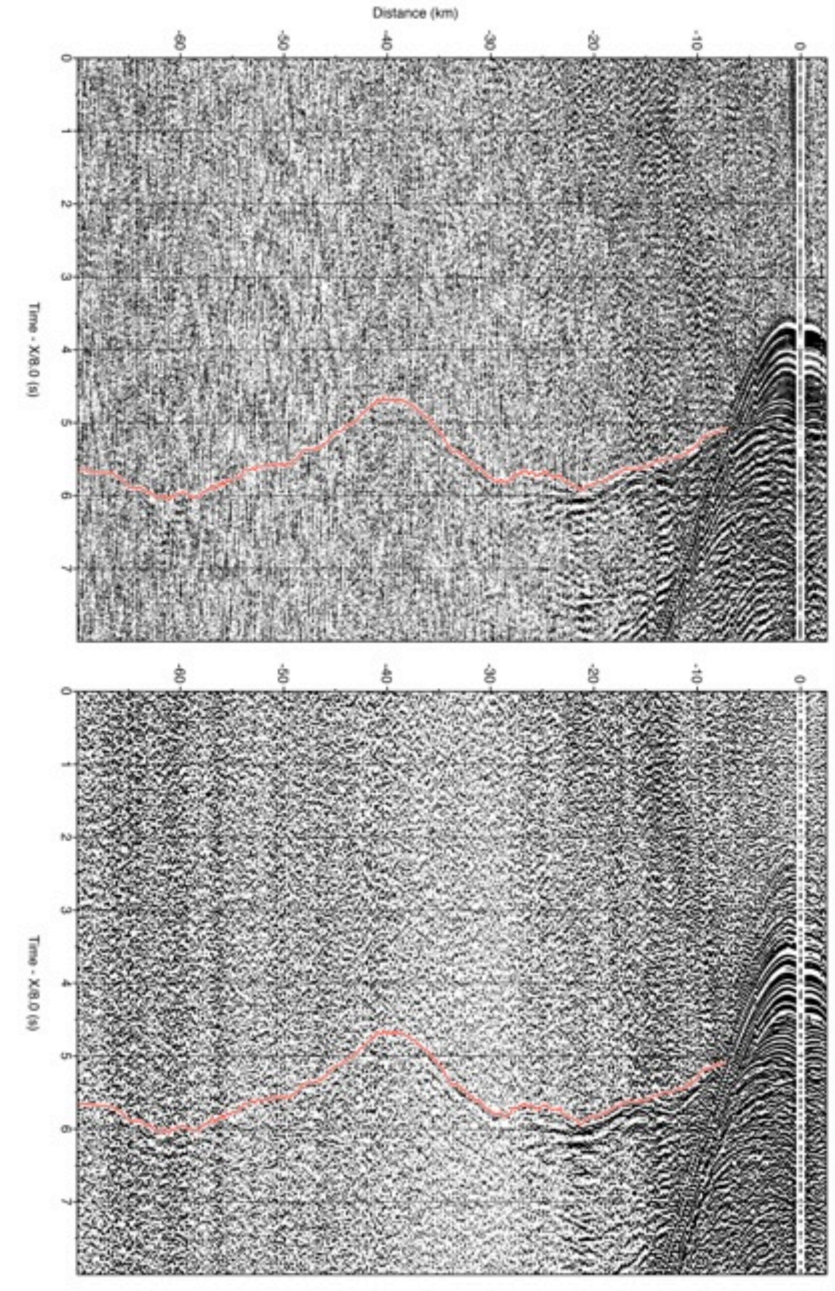

Figure C-6. OBS 26 hydrophone component with first-arrival travel-time picks. Top is un-processed; bottom is processed to suppress the previous shot noise using gapped deconvolution, bandpass filtering, AGC and gaining with offset.

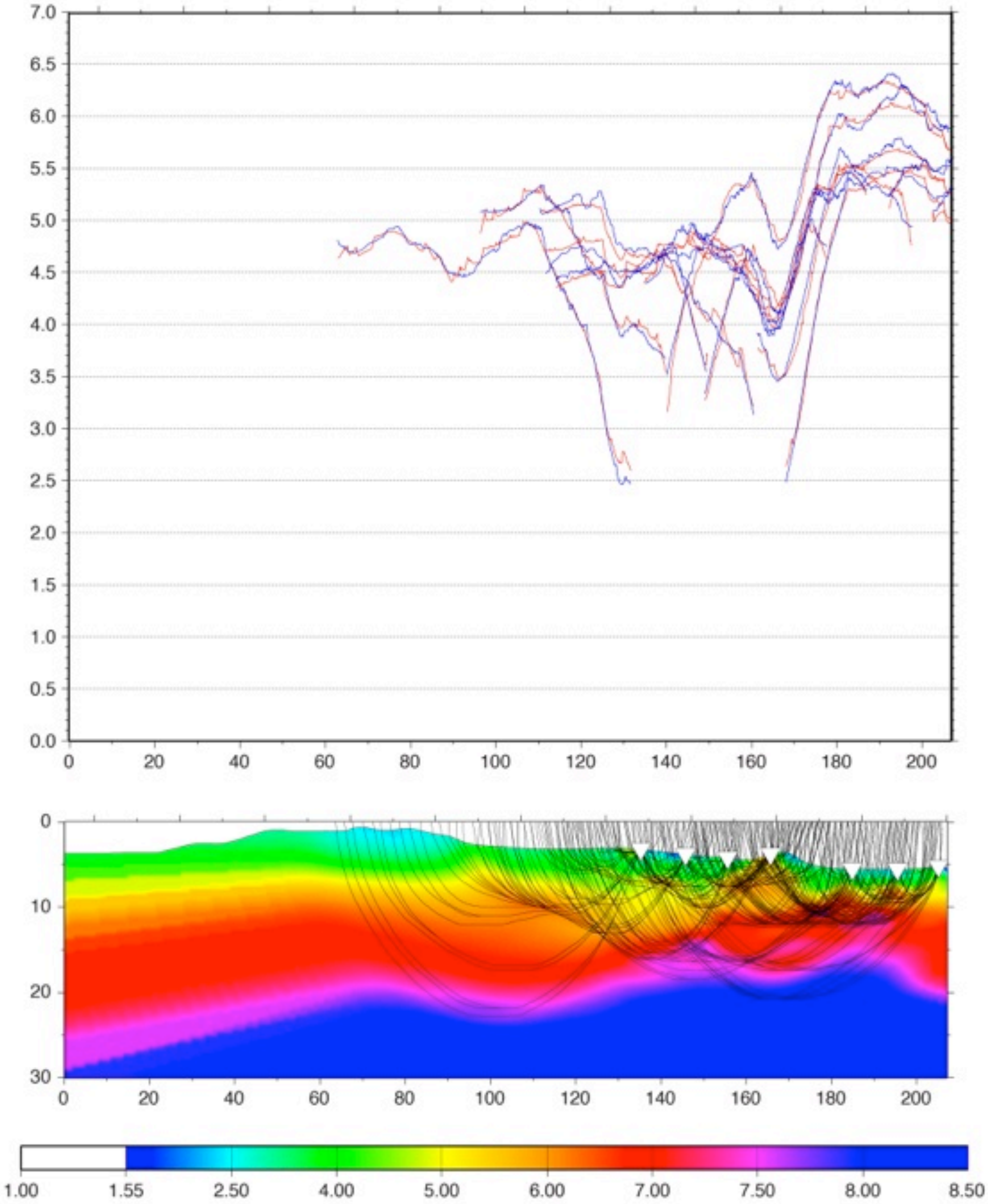

Figure C-7. Ray coverage of line T1B velocity model.

APPENDIX D: LINE T2 OBS

Appendix D contains the ocean bottom seismometer (OBS) records acquired along line T2. Three instruments (OBS 04, OBS 09, and OBS 16) are presented in the chapter 2 manuscript, and the other records are presented here. Each contains the unprocessed record and fully processes with similar parameters described in chapter 2 including gapped deconvolution and bandpass filtering.

OBS	Long	Lat
OBS-01	123.08371	21.41701
OBS-02	122.78369	21.41666
OBS-03	122.69003	21.41624
OBS-04	122.58936	21.41821
OBS-06	122.35509	21.42046
OBS-07	122.20772	21.42153
OBS-08	122.06498	21.4206
OBS-09	121.90083	21.42004
OBS-10	121.77063	21.42413
OBS-11	121.62478	21.42367
OBS-12	121.47881	21.42567
OBS-13	121.38452	21.42513
OBS-14	121.29148	21.42635
OBS-15	121.19689	21.42737
OBS-16	121.00285	21.42663
OBS-17	120.90568	21.42767
OBS-18	120.80978	21.42607
OBS-19	120.7136	21.42587
OBS-20	120.616	21.4261
OBS-21	120.471	21.4254
OBS-22	120.326	21.4256
OBS-23	120.181	21.4257
OBS-24	120.037	21.425
OBS-25	119.892	21.424

OBS-26	119.747	21.4231
OBS-27	119.602	21.4219
OBS-28	119.457	21.4209
OBS-29	119.312	21.4195
OBS-30	119.167	21.4181
OBS-31	119.022	21.4151

Table D-1. T2 OBS locations.

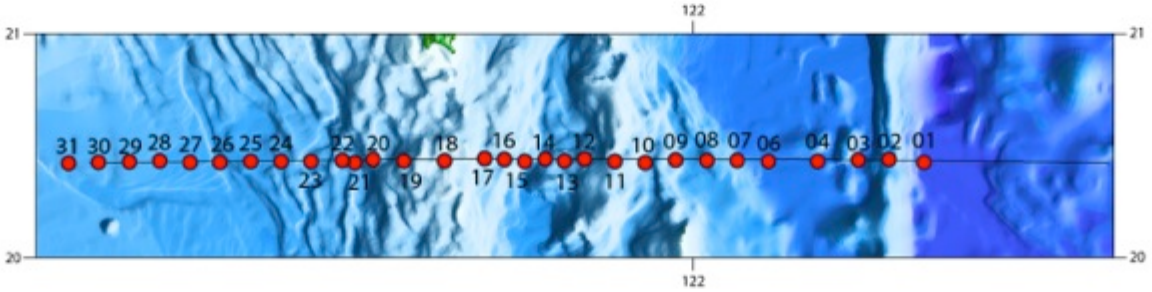

Figure D-1. T2 coincident reflection and wide angle refraction profile and OBS locations.

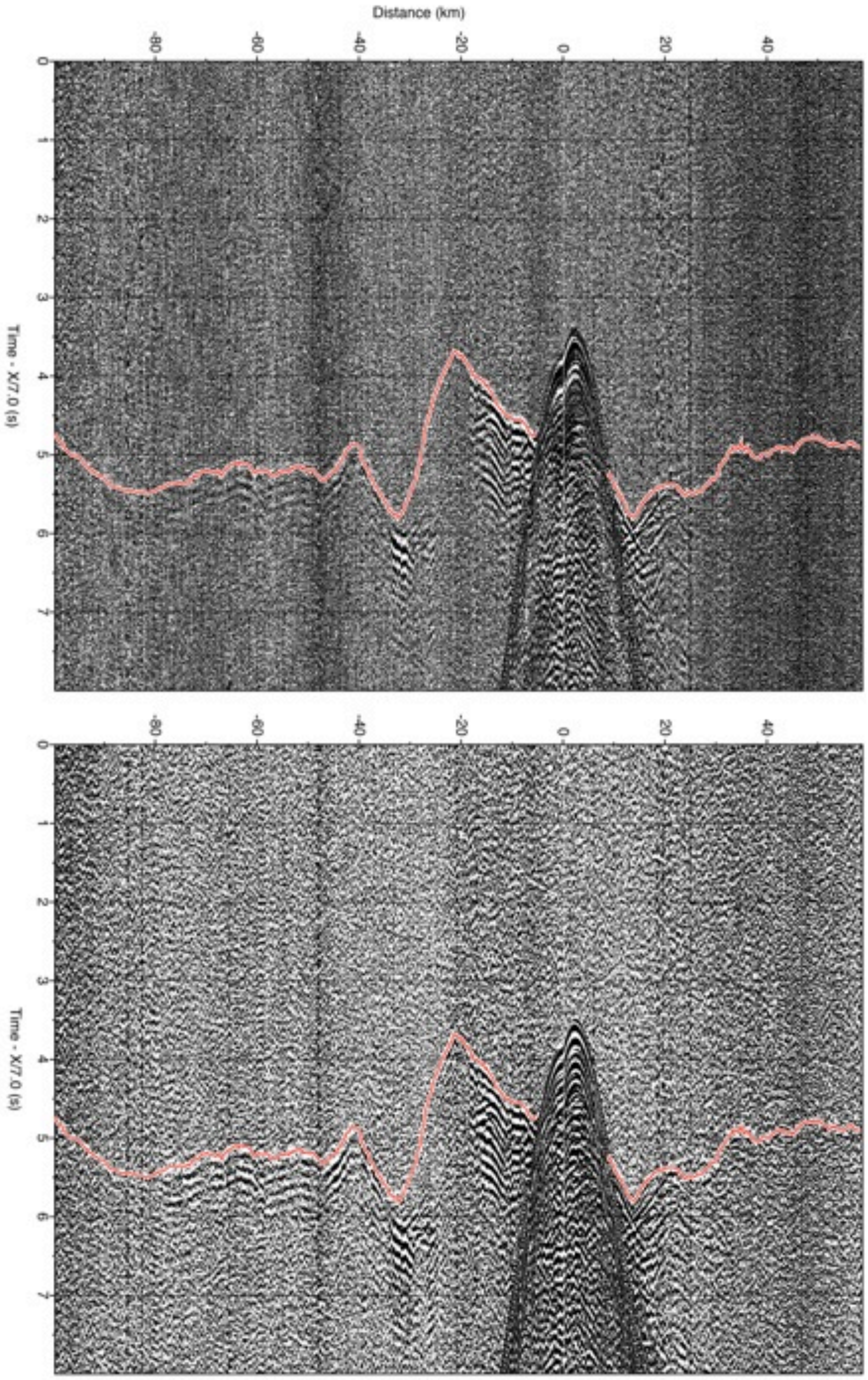

Figure D-2. OBS 01 hydrophone component with first-arrival travel-time picks. Top is unprocessed; bottom is processed to suppress the previous shot noise using gapped deconvolution, bandpass filtering, ACG and gaining with offset.

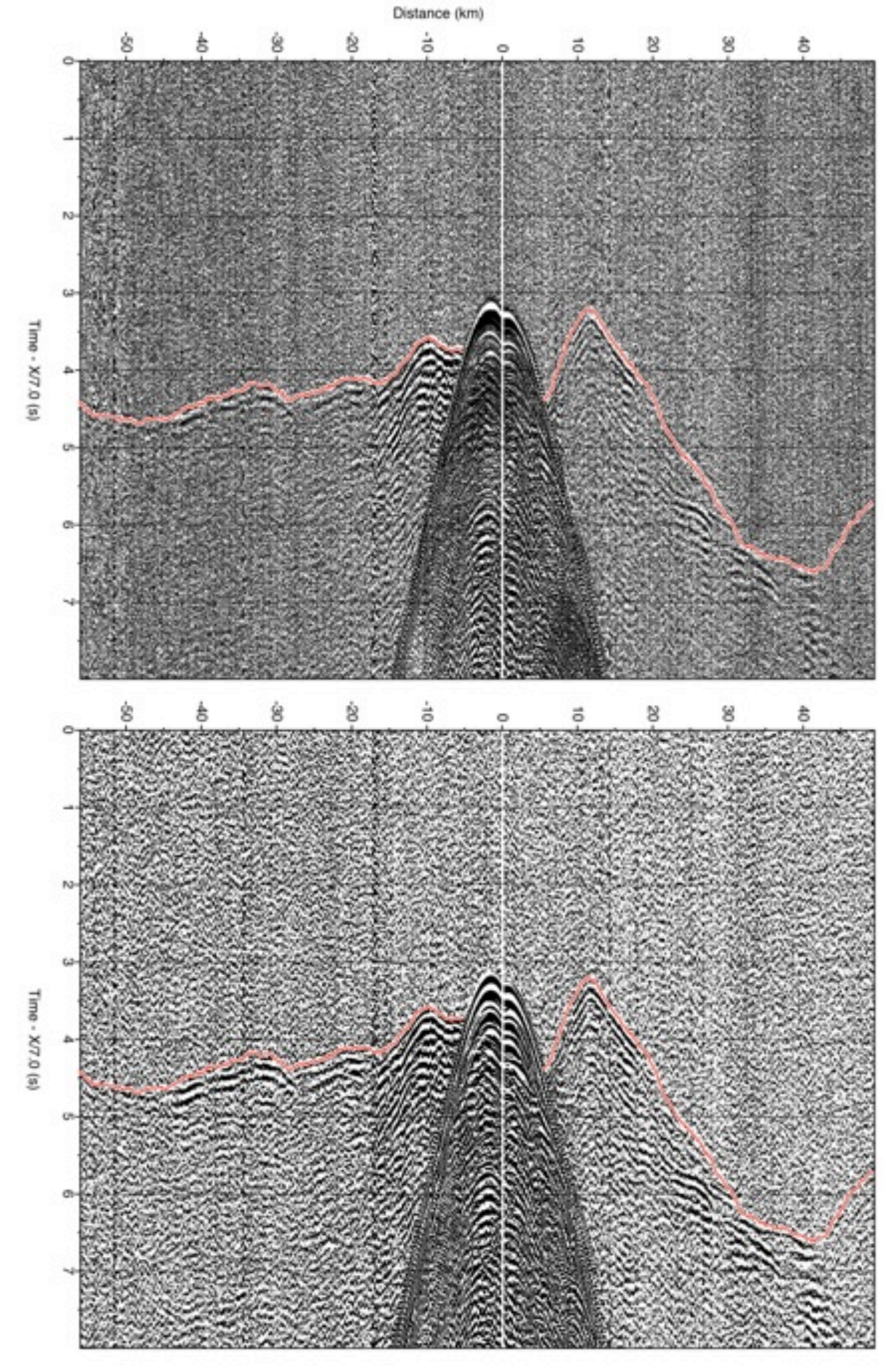

Figure D-3. OBS 02 hydrophone component with first-arrival travel-time picks. Top is unprocessed; bottom is processed to suppress the previous shot noise using gapped deconvolution, bandpass filtering, ACG and gaining with offset.

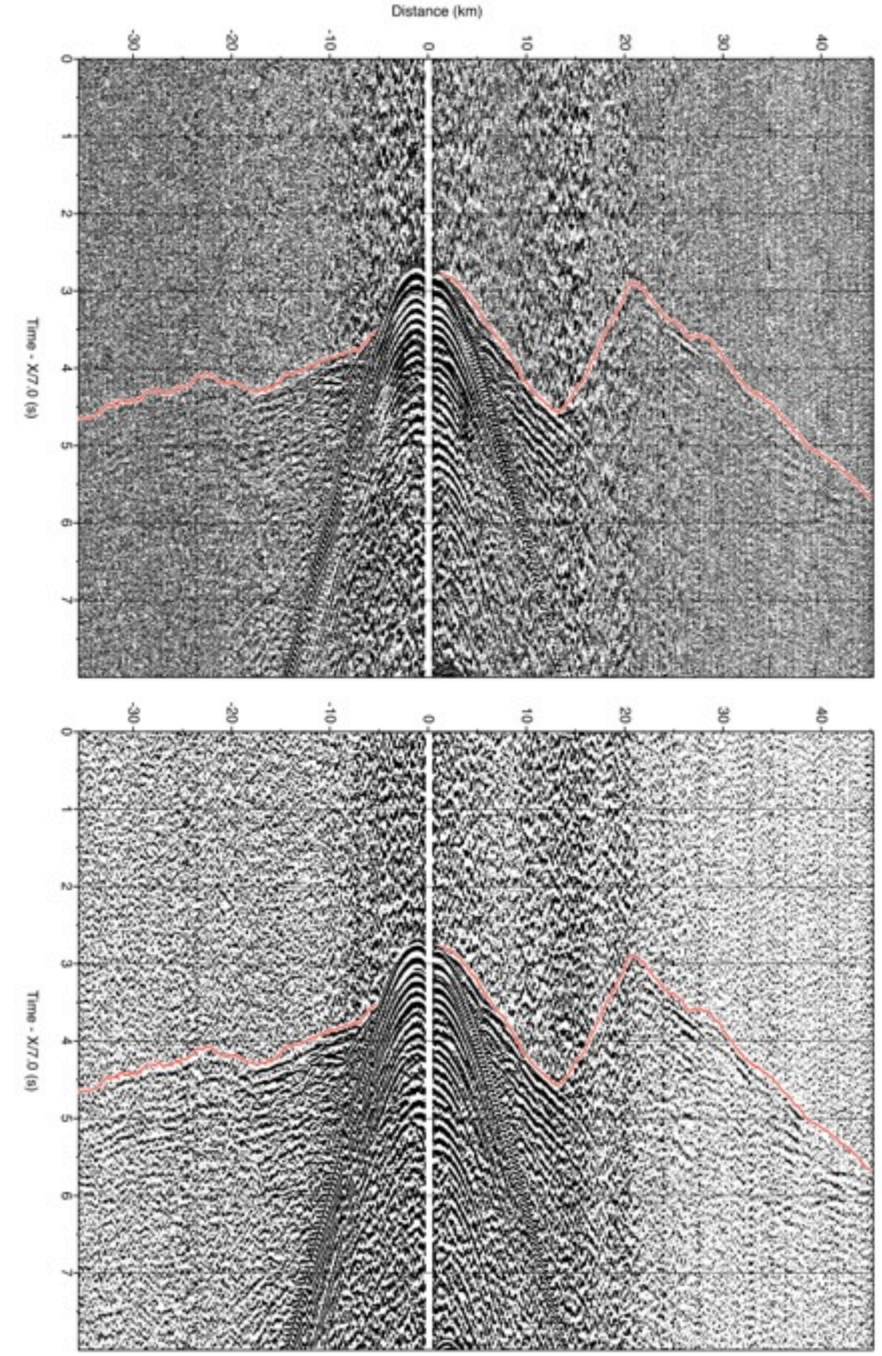

Figure D-4. OBS 03 hydrophone component with first-arrival travel-time picks. Top is unprocessed; bottom is processed to suppress the previous shot noise using gapped deconvolution, bandpass filtering, ACG and gaining with offset.

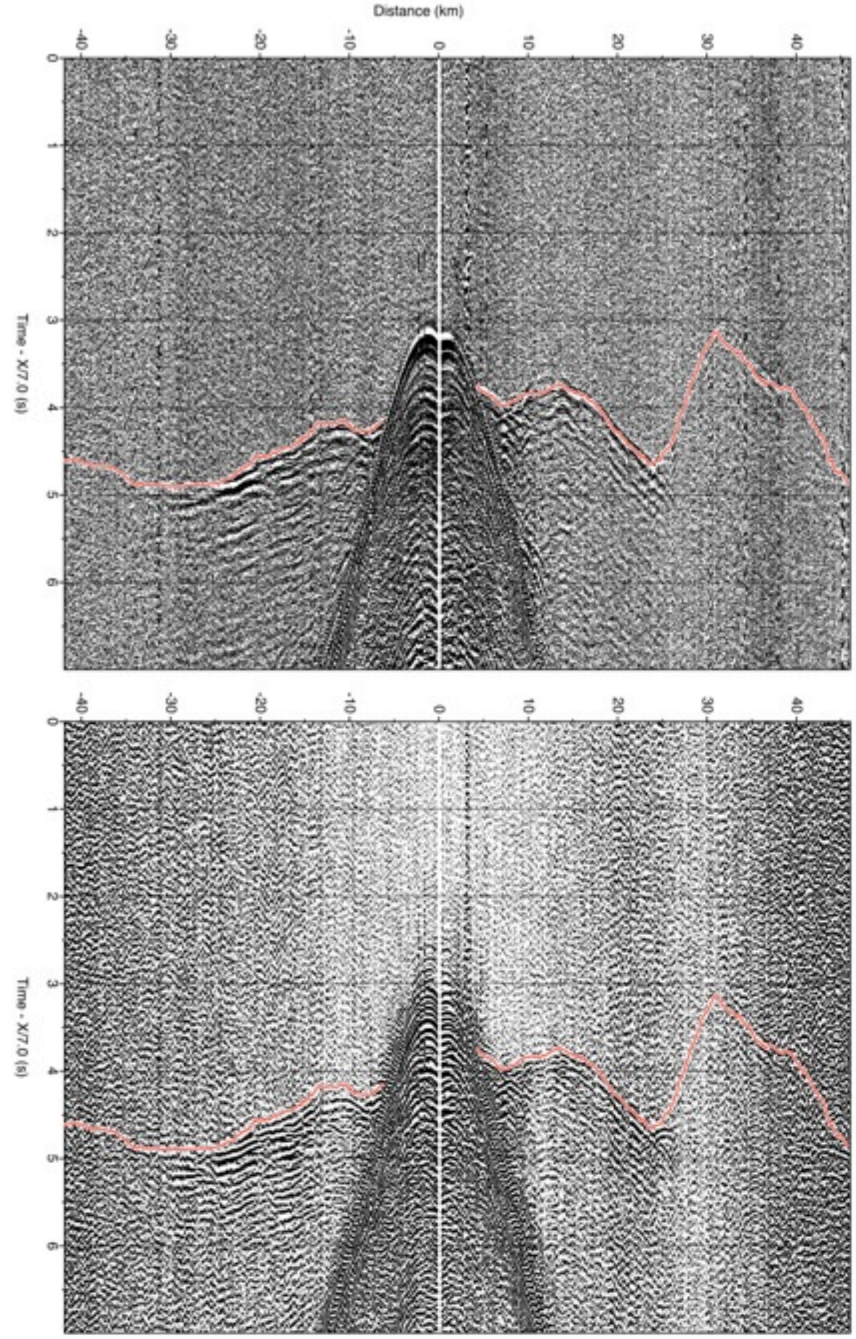

Figure D-5. OBS 04 hydrophone component with first-arrival travel-time picks. Top is unprocessed; bottom is processed to suppress the previous shot noise using gapped deconvolution, bandpass filtering, ACG and gaining with offset.

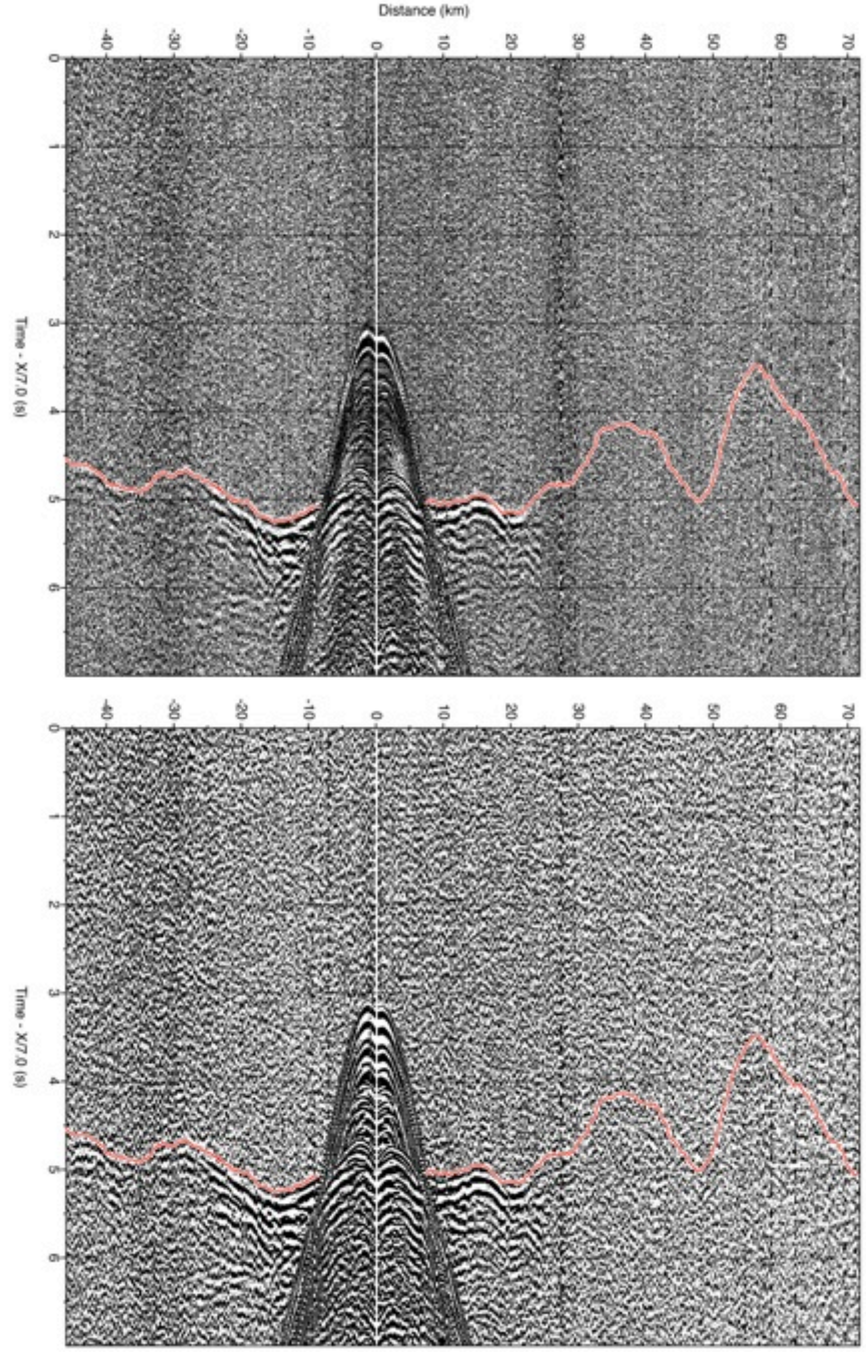

Figure D-6. OBS 06 hydrophone component with first-arrival travel-time picks. Top is unprocessed; bottom is processed to suppress the previous shot noise using gapped deconvolution, bandpass filtering, ACG and gaining with offset.

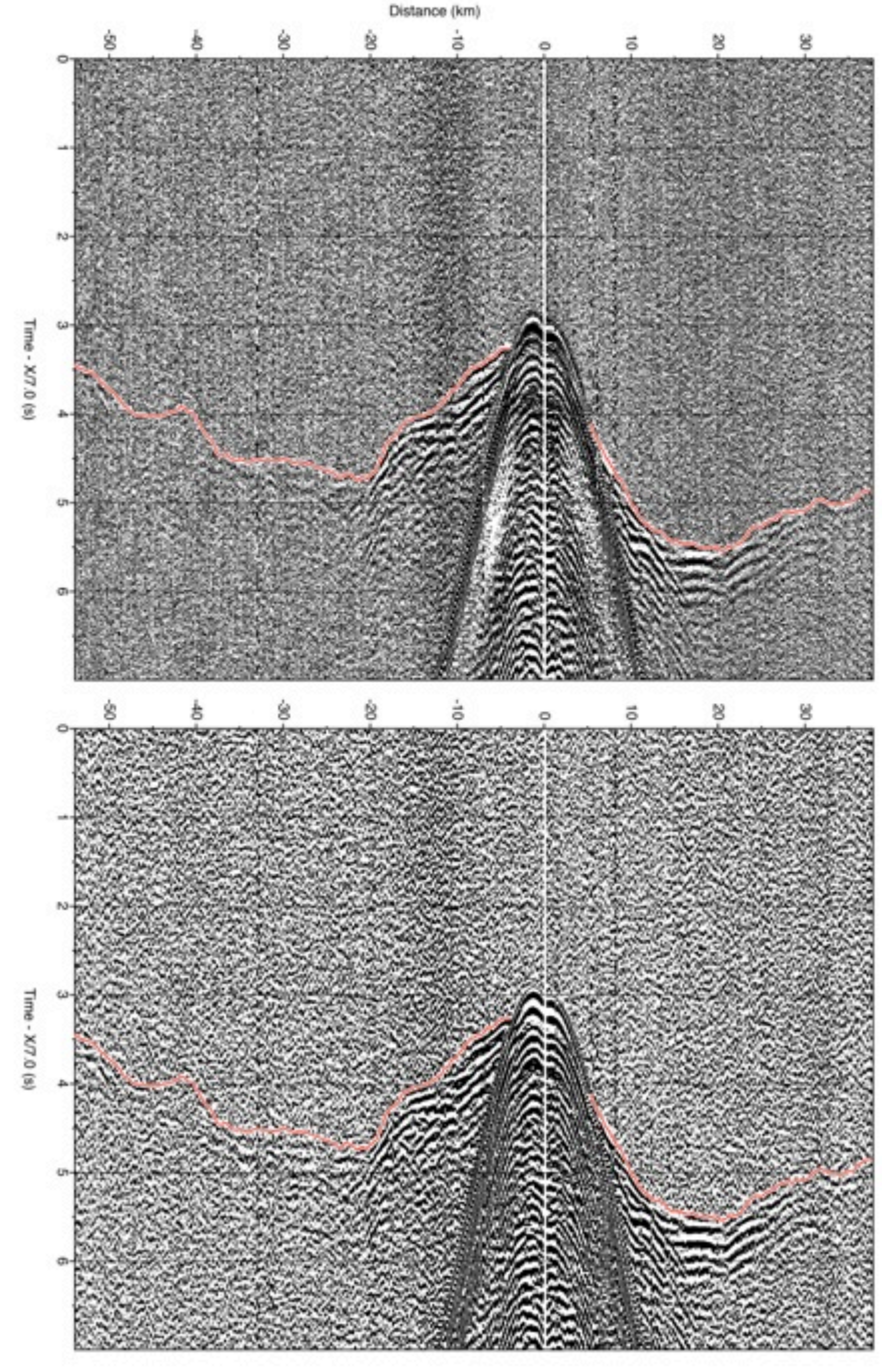

Figure D-7. OBS 07 hydrophone component with first-arrival travel-time picks. Top is unprocessed; bottom is processed to suppress the previous shot noise using gapped deconvolution, bandpass filtering, ACG and gaining with offset.

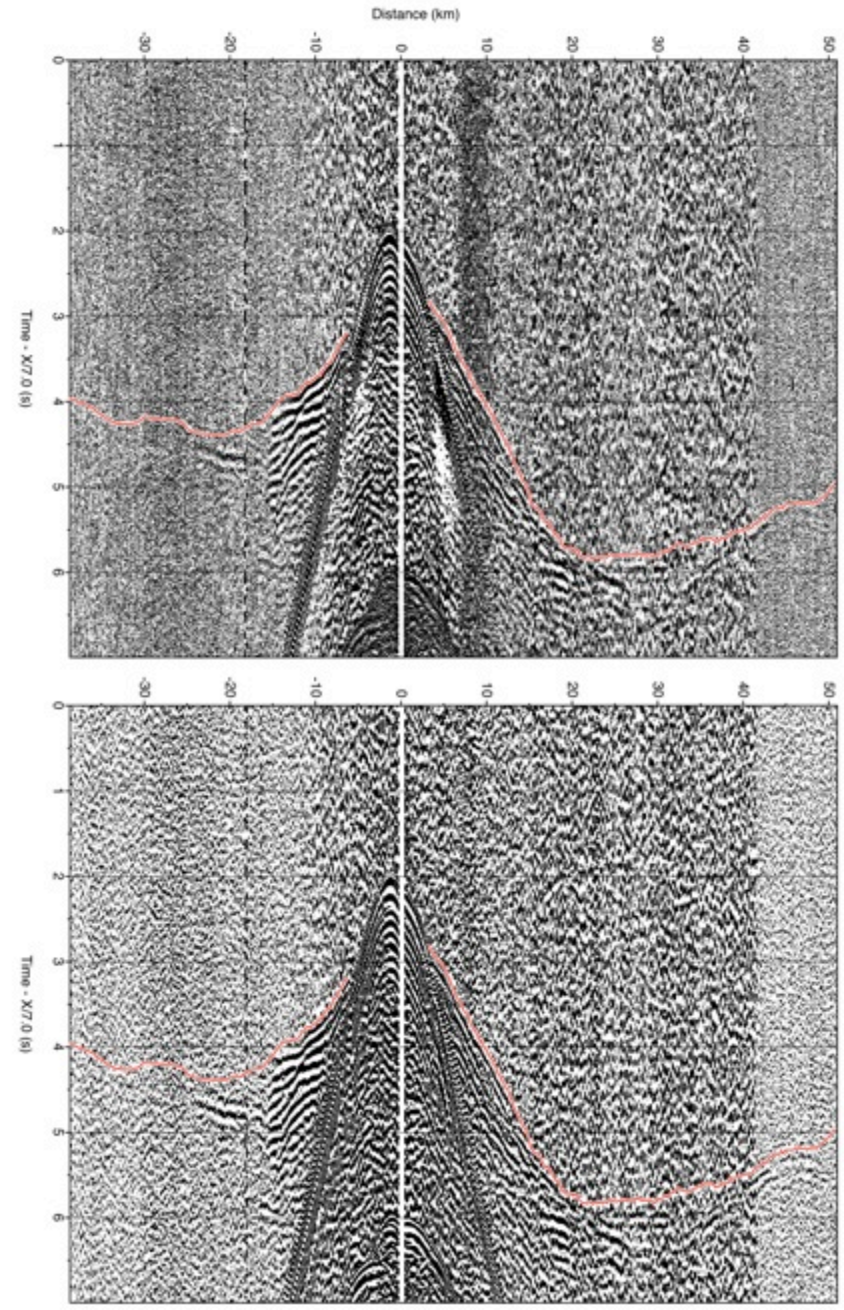

Figure D-8. OBS 08 hydrophone component with first-arrival travel-time picks. Top is unprocessed; bottom is processed to suppress the previous shot noise using gapped deconvolution, bandpass filtering, ACG and gaining with offset.

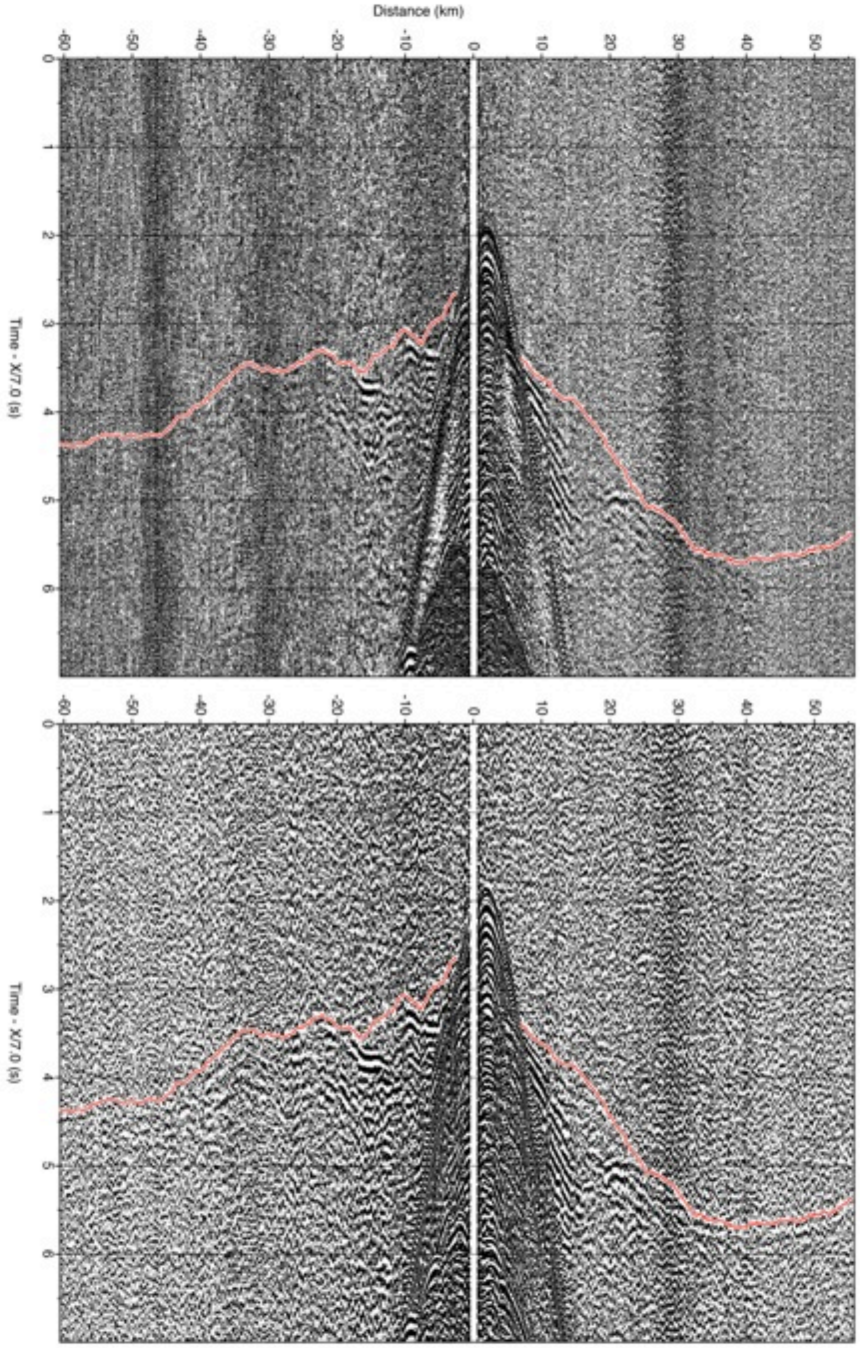

Figure D-9. OBS 09 hydrophone component with first-arrival travel-time picks. Top is unprocessed; bottom is processed to suppress the previous shot noise using gapped deconvolution, bandpass filtering, ACG and gaining with offset.

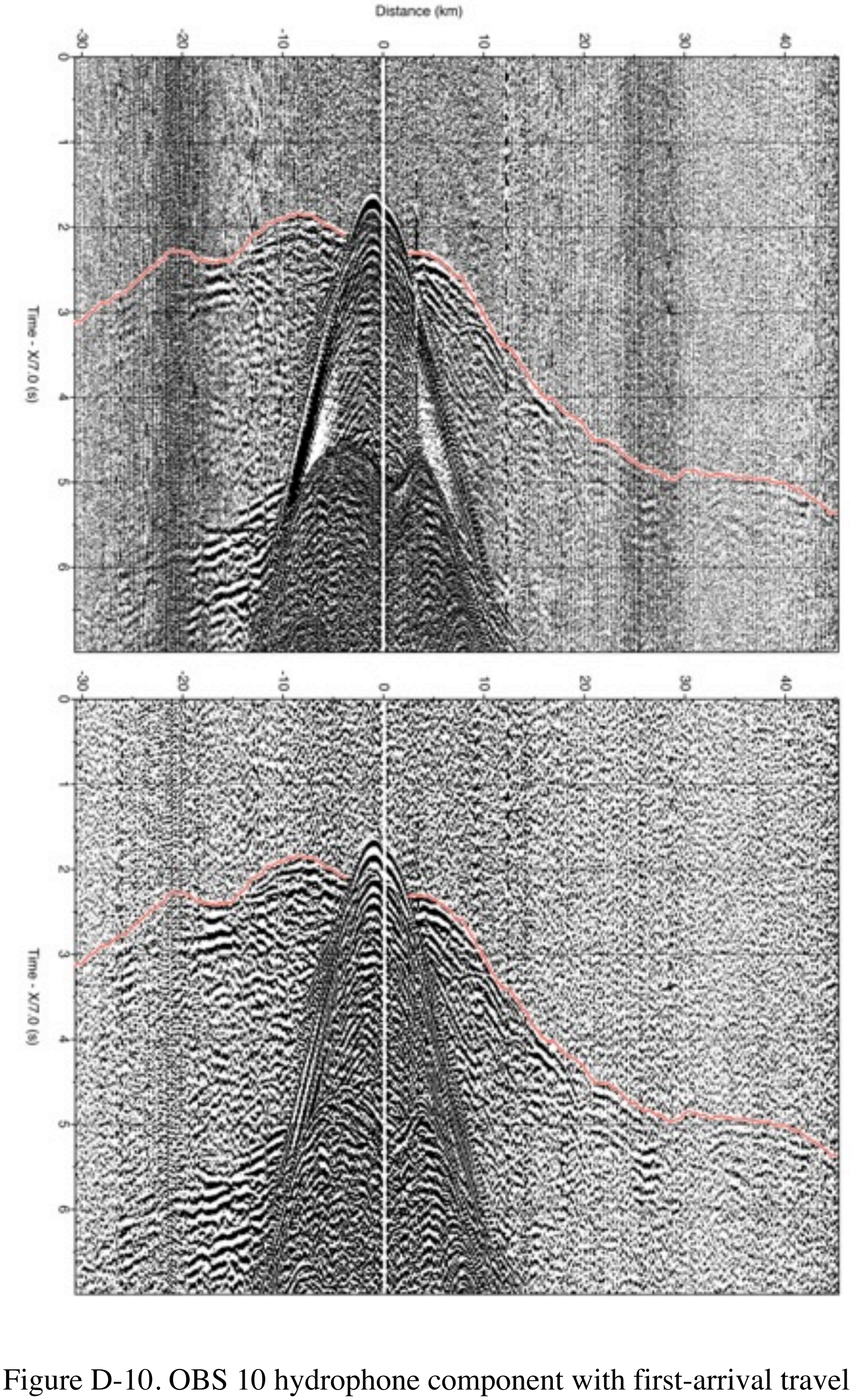

Figure D-10. OBS 10 hydrophone component with first-arrival travel-time picks. Top is unprocessed; bottom is processed to suppress the previous shot noise using gapped deconvolution, bandpass filtering, ACG and gaining with offset.

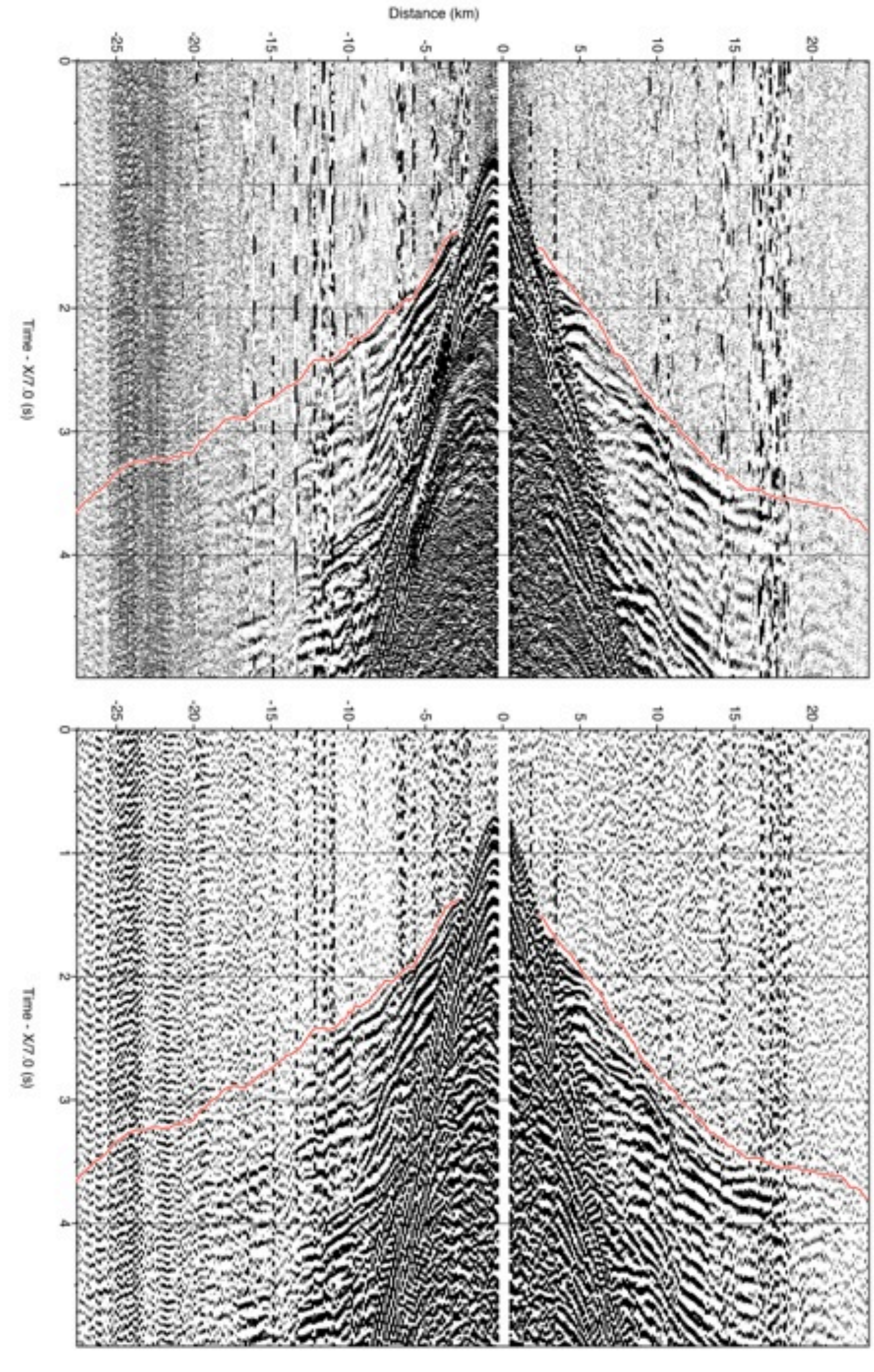

Figure D-11. OBS 11 hydrophone component with first-arrival travel-time picks. Top is unprocessed; bottom is processed to suppress the previous shot noise using gapped deconvolution, bandpass filtering, ACG and gaining with offset.

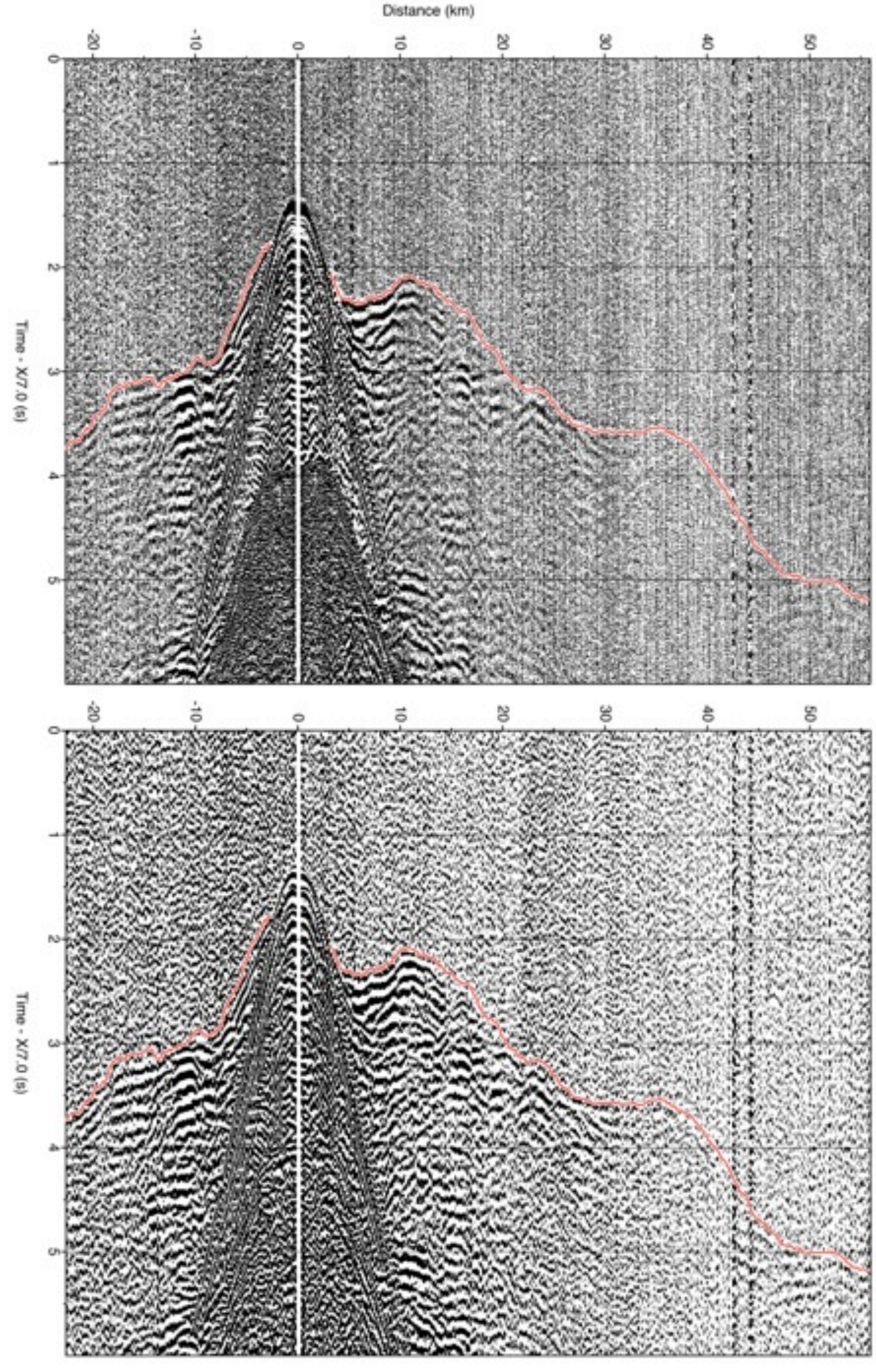

Figure D-12. OBS 12 hydrophone component with first-arrival travel-time picks. Top is unprocessed; bottom is processed to suppress the previous shot noise using gapped deconvolution, bandpass filtering, ACG and gaining with offset.

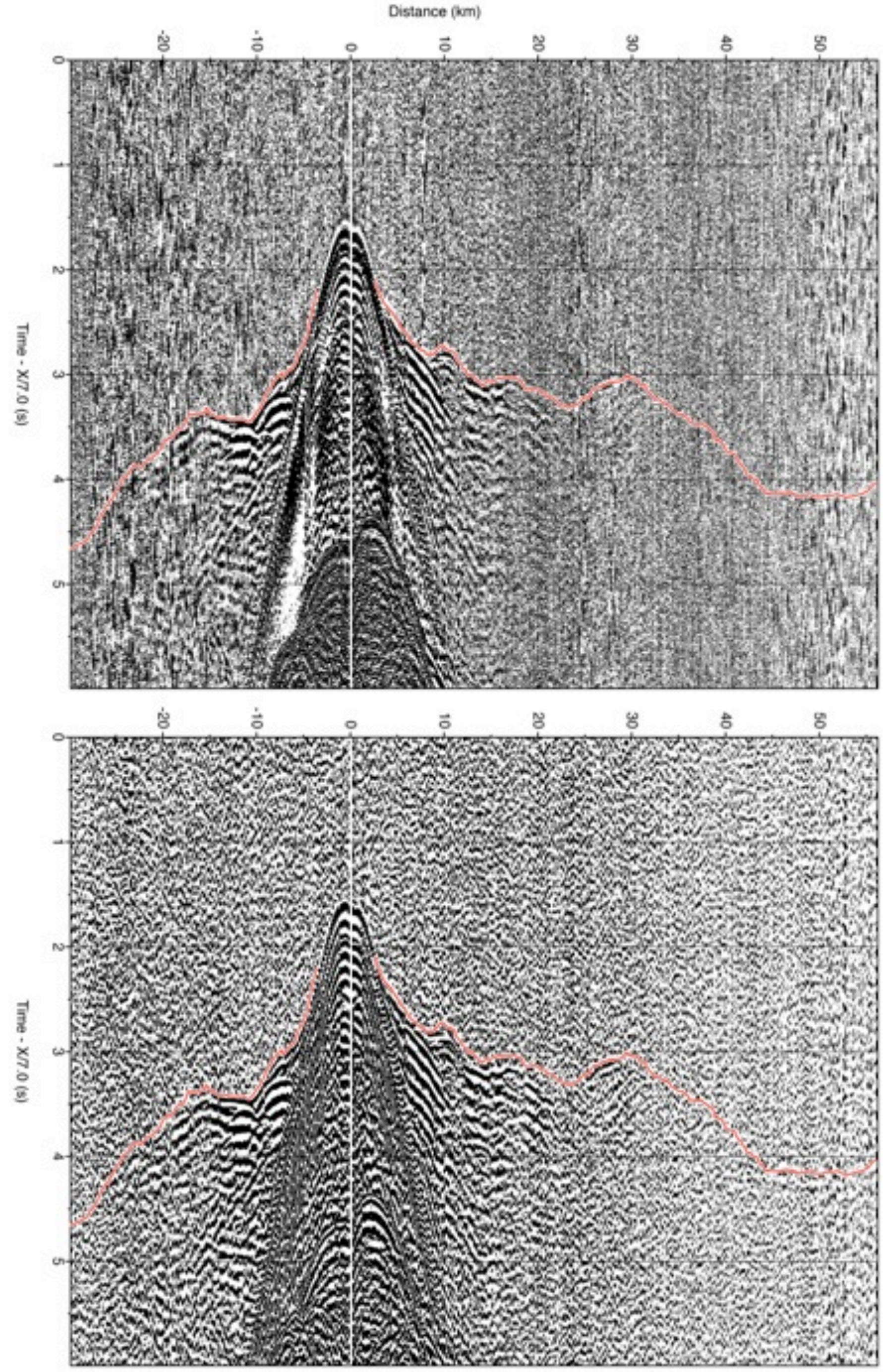

Figure D-13. OBS 14 hydrophone component with first-arrival travel-time picks. Top is unprocessed; bottom is processed to suppress the previous shot noise using gapped deconvolution, bandpass filtering, ACG and gaining with offset.

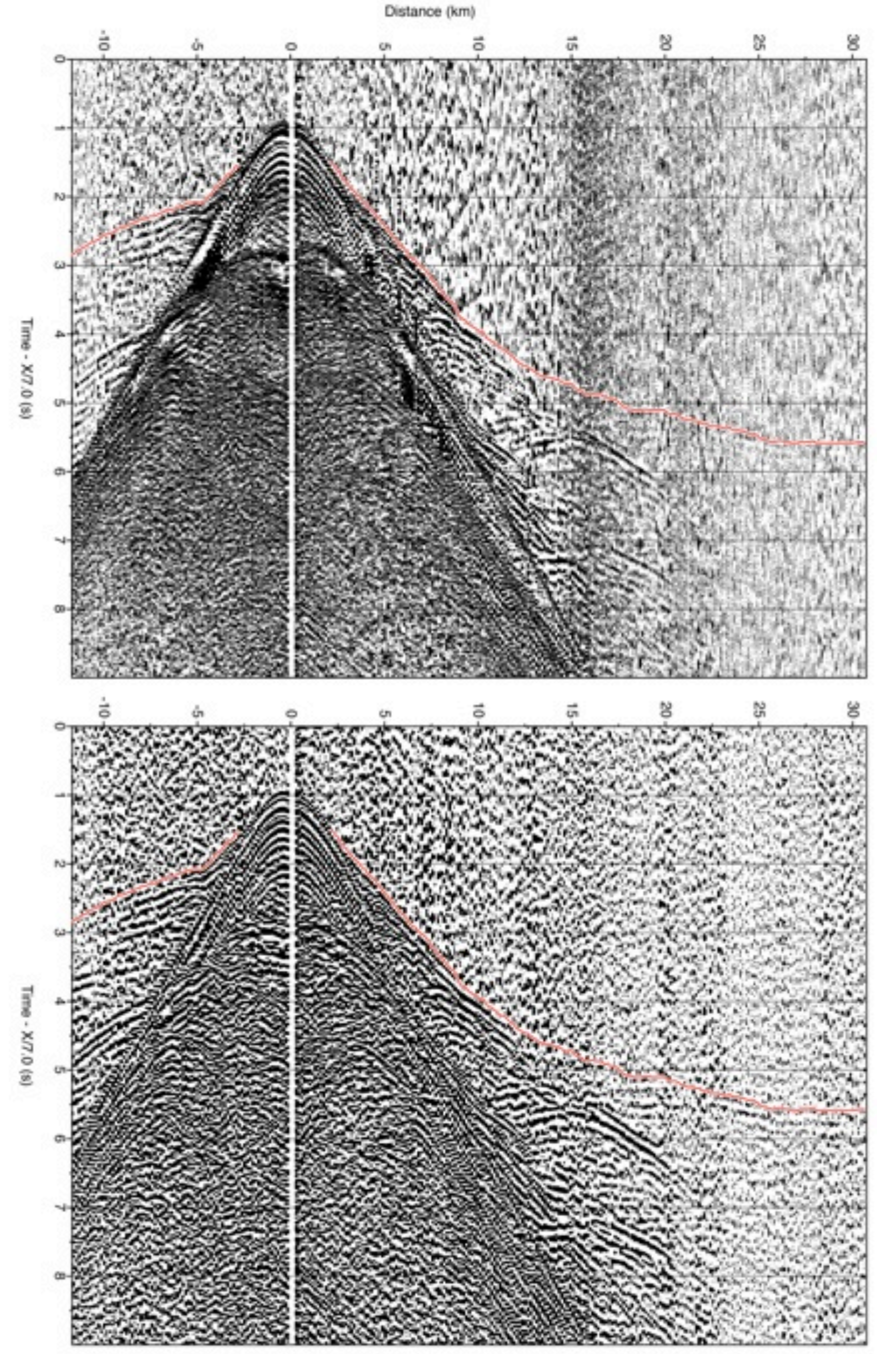

Figure D-14. OBS 15 hydrophone component with first-arrival travel-time picks. Top is unprocessed; bottom is processed to suppress the previous shot noise using gapped deconvolution, bandpass filtering, ACG and gaining with offset.

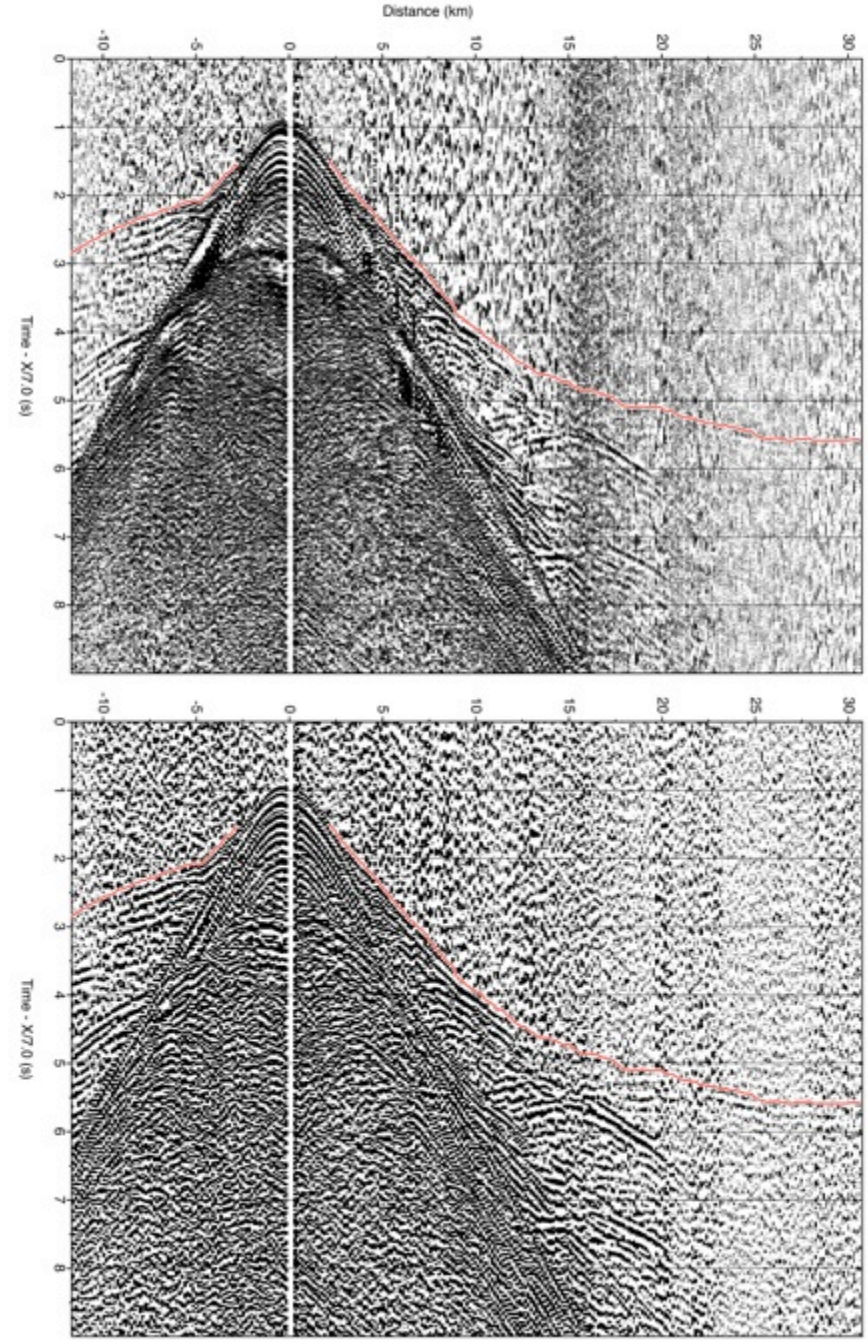

Figure D-15. OBS 16 hydrophone component with first-arrival travel-time picks. Top is unprocessed; bottom is processed to suppress the previous shot noise using gapped deconvolution, bandpass filtering, ACG and gaining with offset.

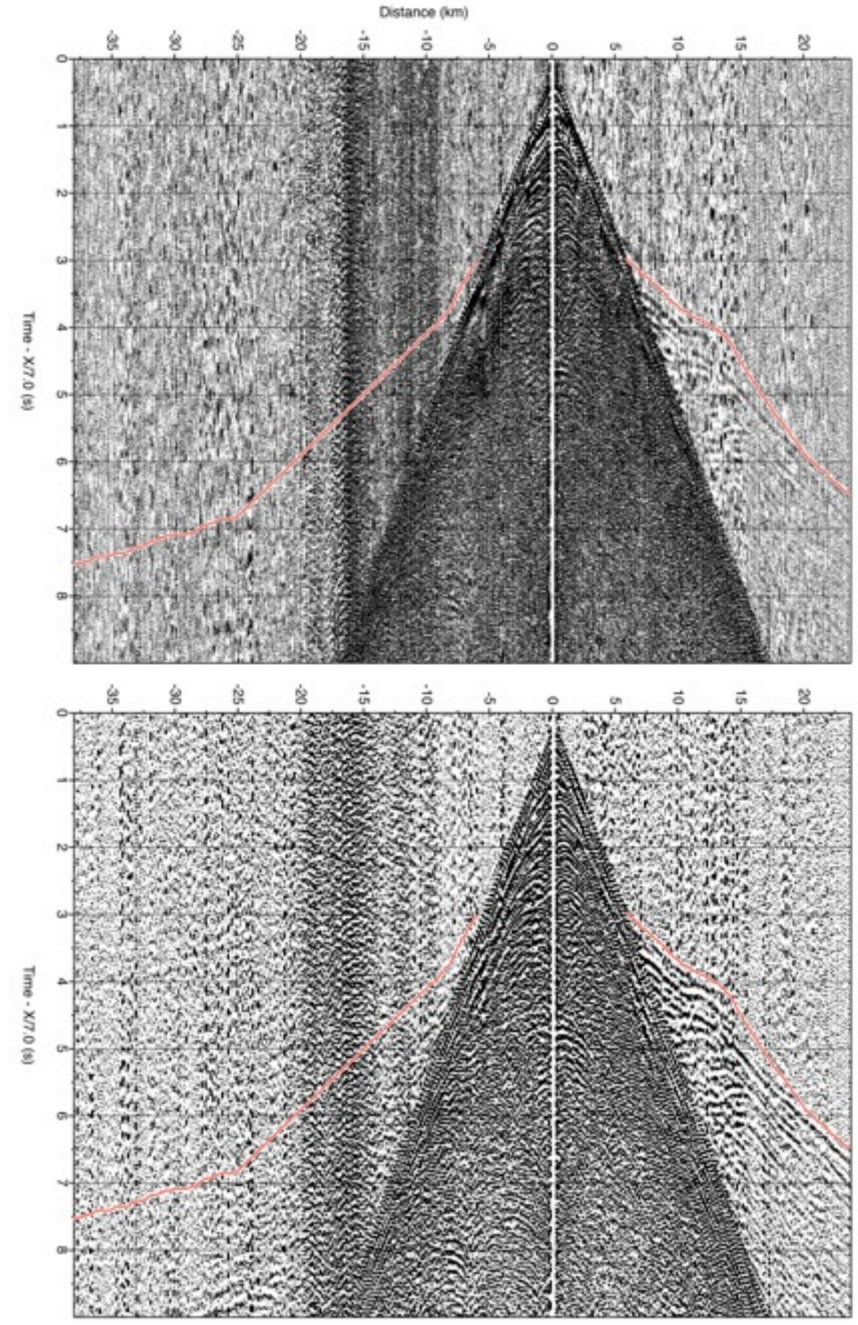

Figure D-16. OBS 17 hydrophone component with first-arrival travel-time picks. Top is unprocessed; bottom is processed to suppress the previous shot noise using gapped deconvolution, bandpass filtering, ACG and gaining with offset.

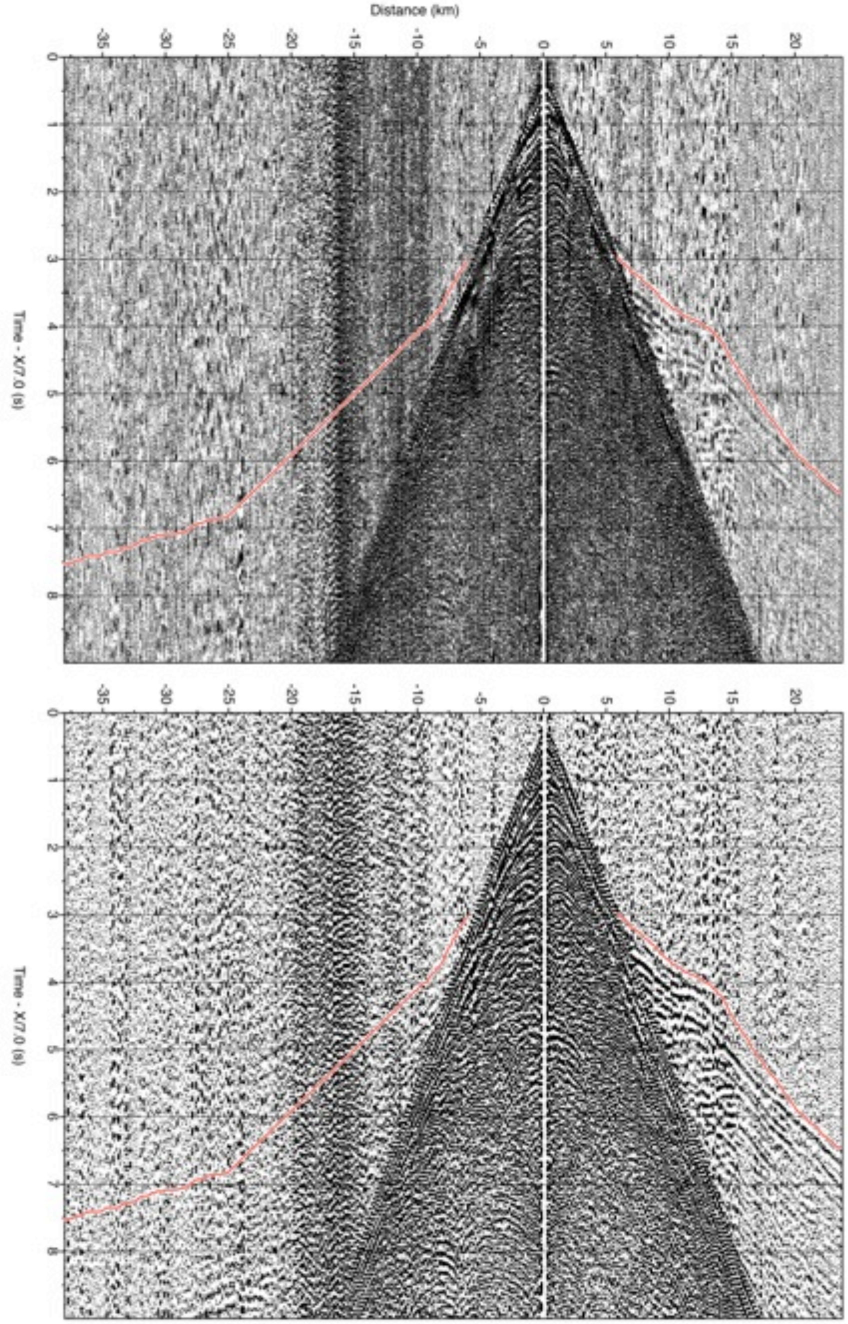

Figure D-17. OBS 18 hydrophone component with first-arrival travel-time picks. Top is unprocessed; bottom is processed to suppress the previous shot noise using gapped deconvolution, bandpass filtering, ACG and gaining with offset.

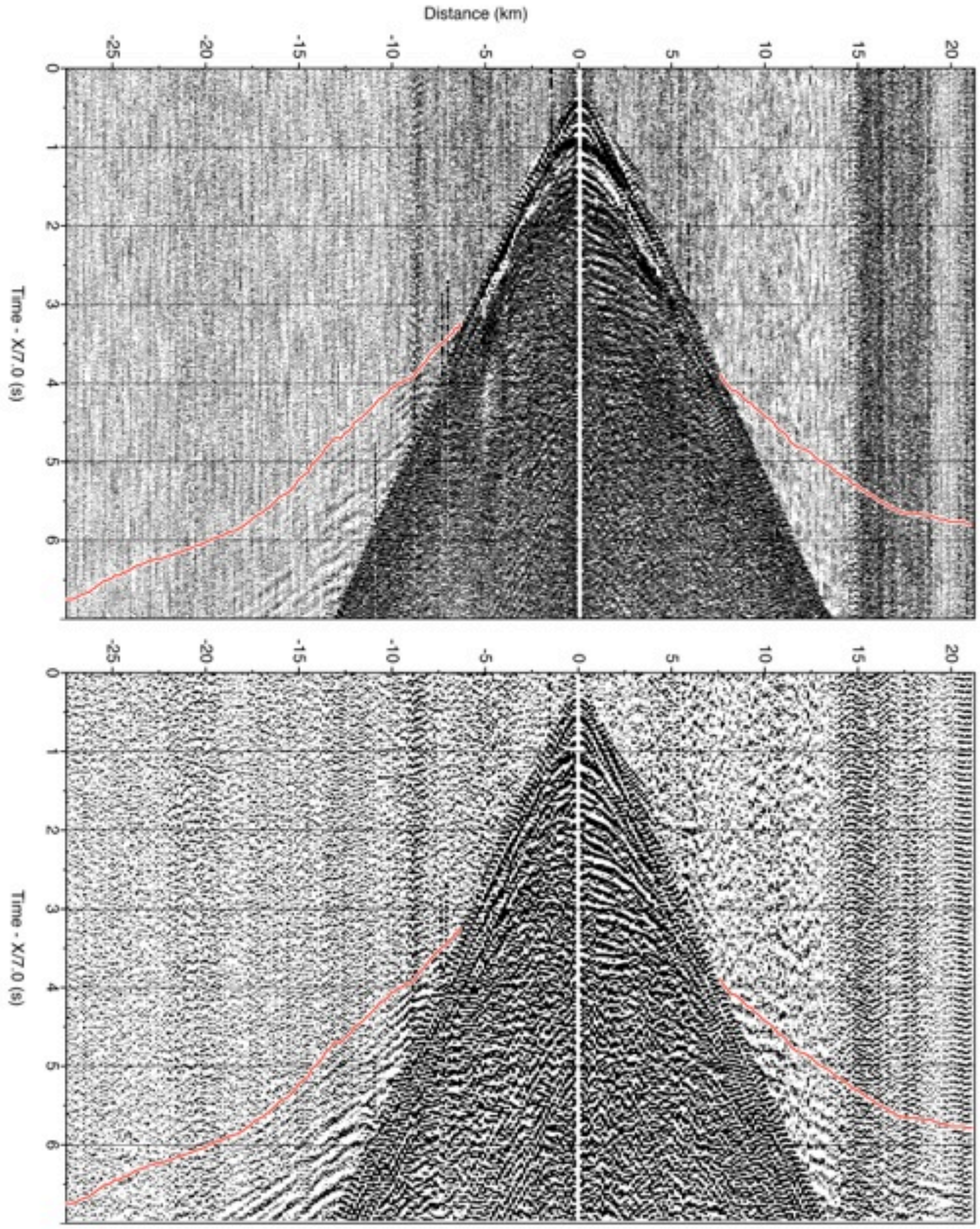

Figure D-18. OBS 19 hydrophone component with first-arrival travel-time picks. Top is unprocessed; bottom is processed to suppress the previous shot noise using gapped deconvolution, bandpass filtering, ACG and gaining with offset.

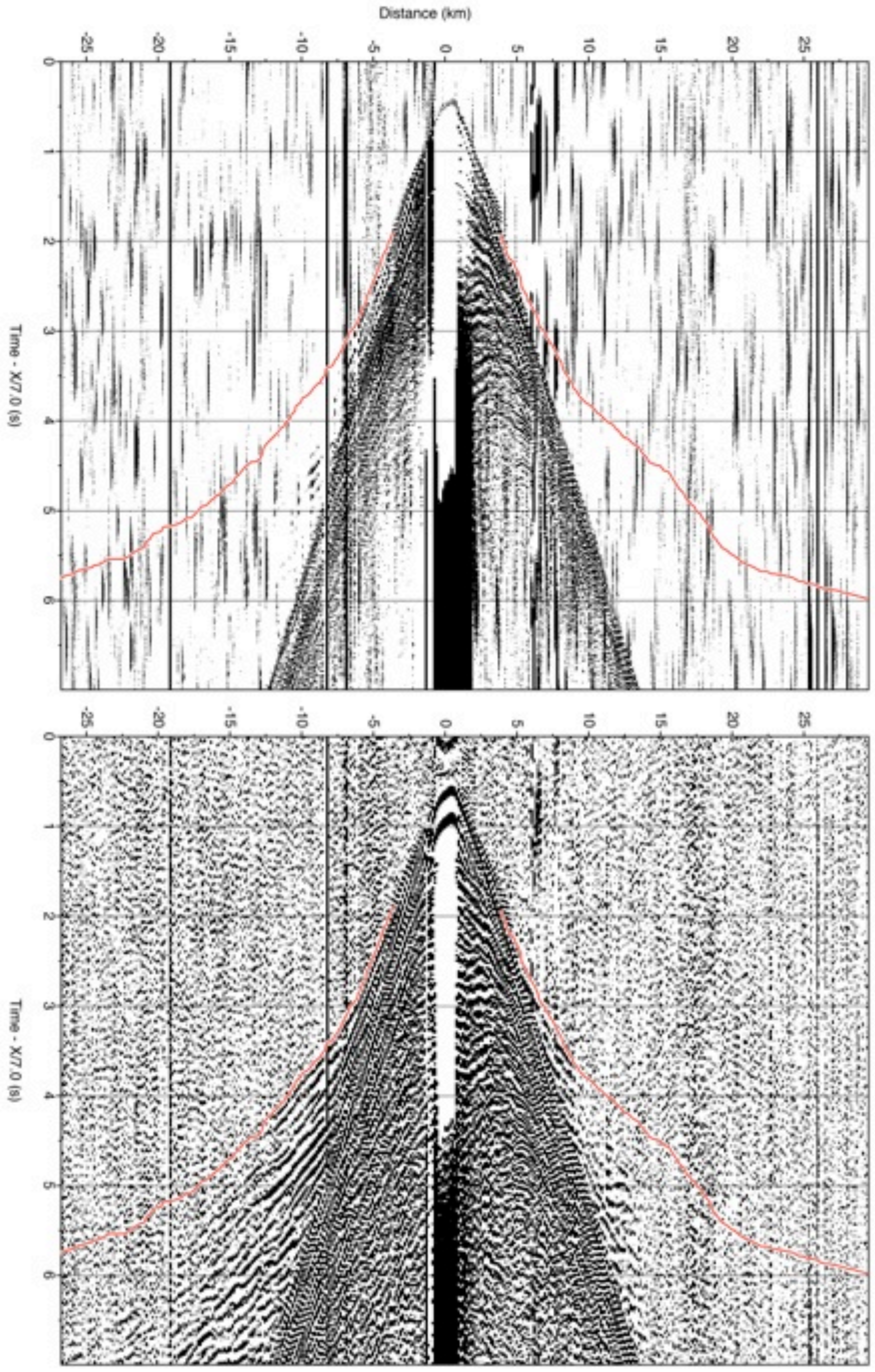

Figure D-19. OBS 20 hydrophone component with first-arrival travel-time picks. Top is unprocessed; bottom is processed to suppress the previous shot noise using gapped deconvolution, bandpass filtering, ACG and gaining with offset.

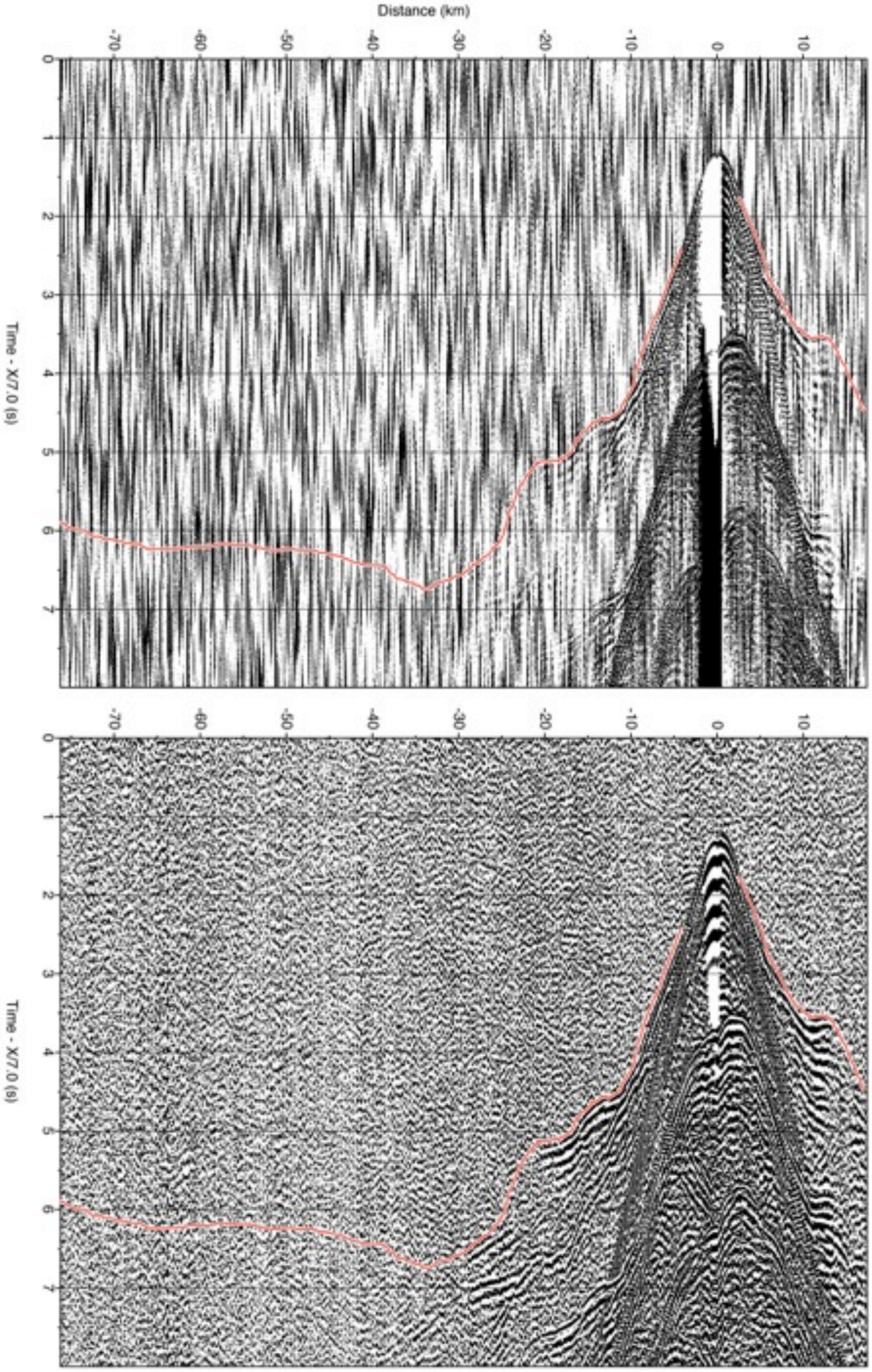

Figure D-20. OBS 21 hydrophone component with first-arrival travel-time picks. Top is unprocessed; bottom is processed to suppress the previous shot noise using gapped deconvolution, bandpass filtering, ACG and gaining with offset.

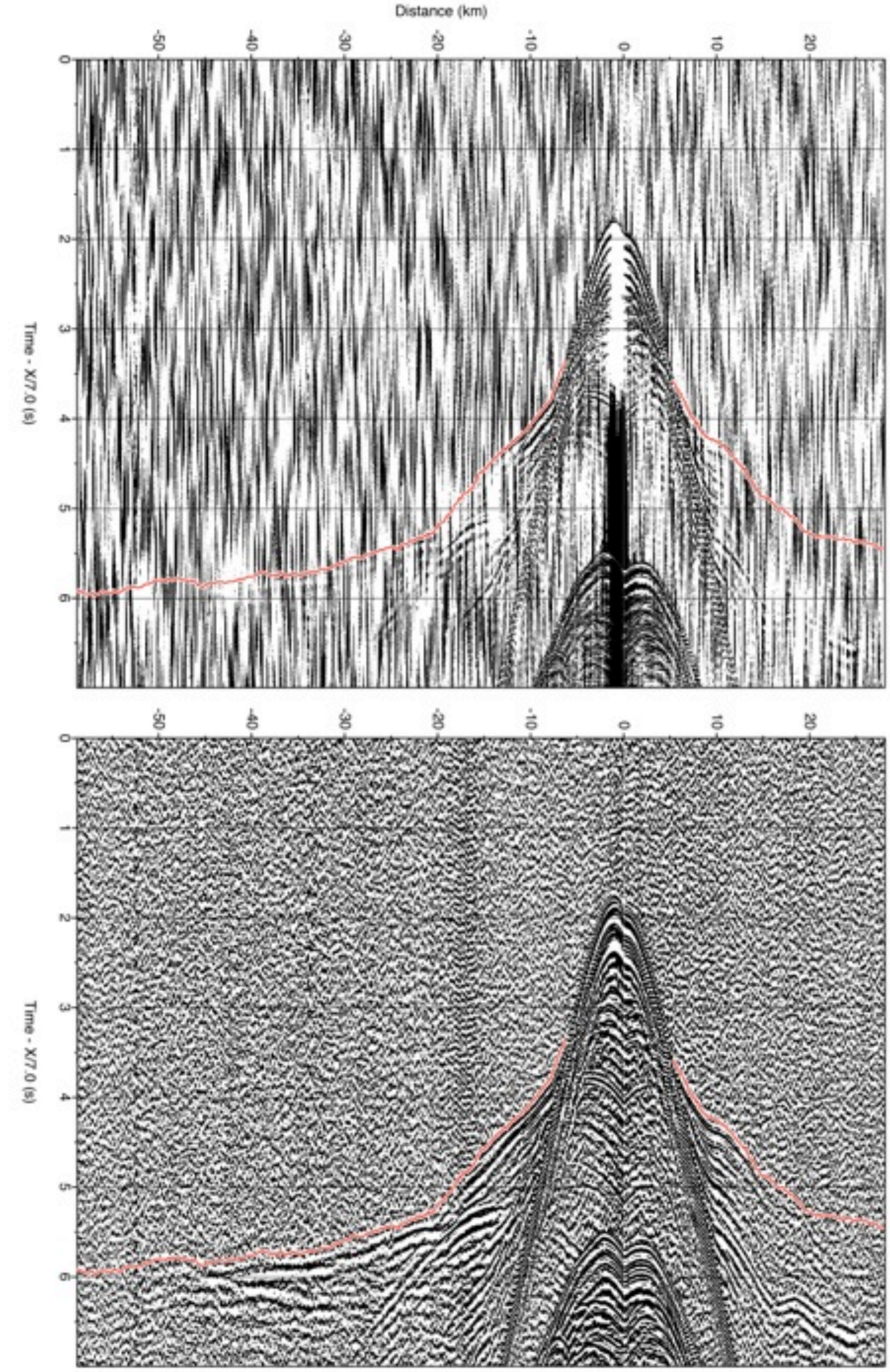

Figure D-21. OBS 23 hydrophone component with first-arrival travel-time picks. Top is unprocessed; bottom is processed to suppress the previous shot noise using gapped deconvolution, bandpass filtering, ACG and gaining with offset.

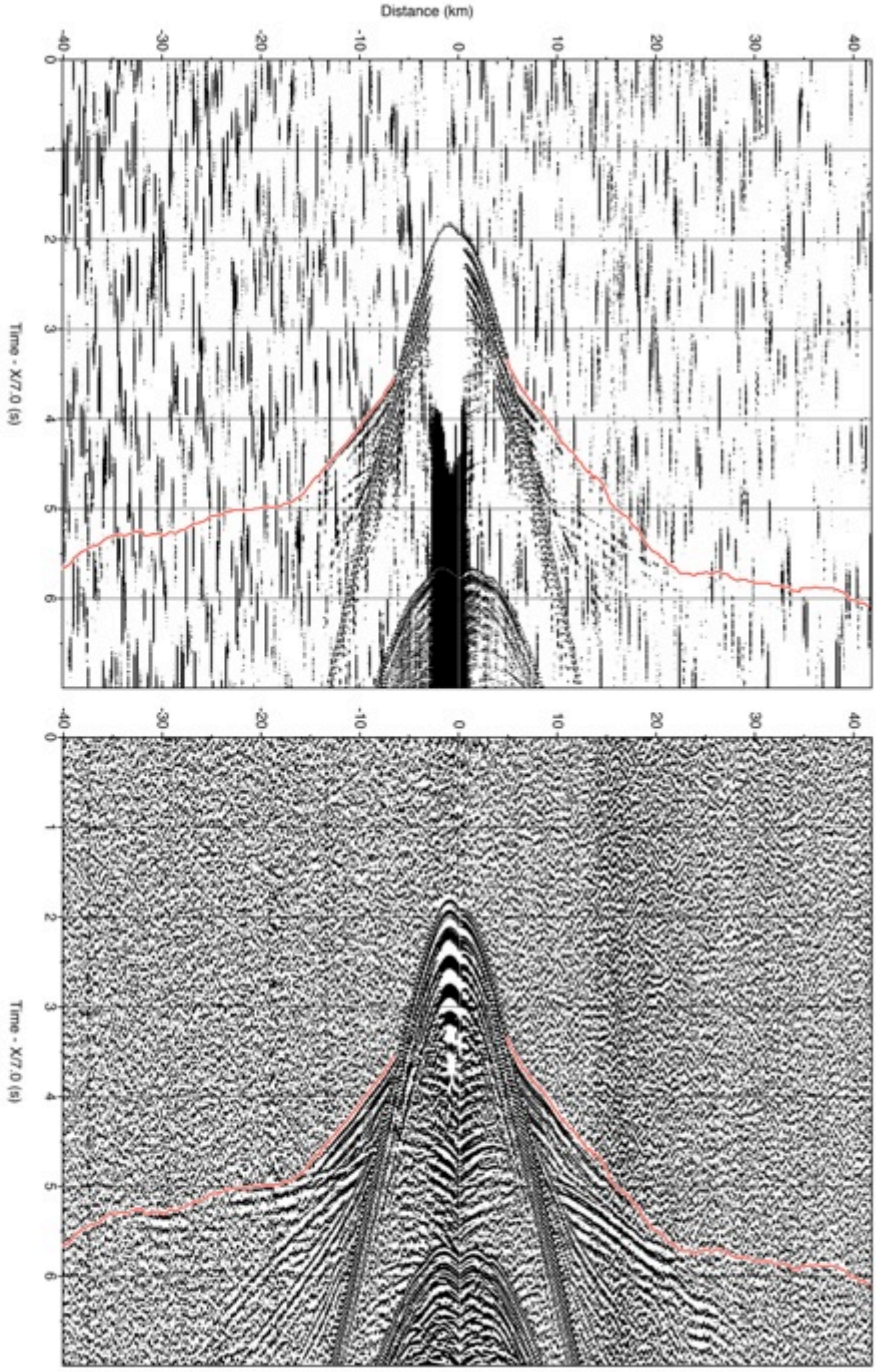

Figure D-22. OBS 24 hydrophone component with first-arrival travel-time picks. Top is unprocessed; bottom is processed to suppress the previous shot noise using gapped deconvolution, bandpass filtering, ACG and gaining with offset.

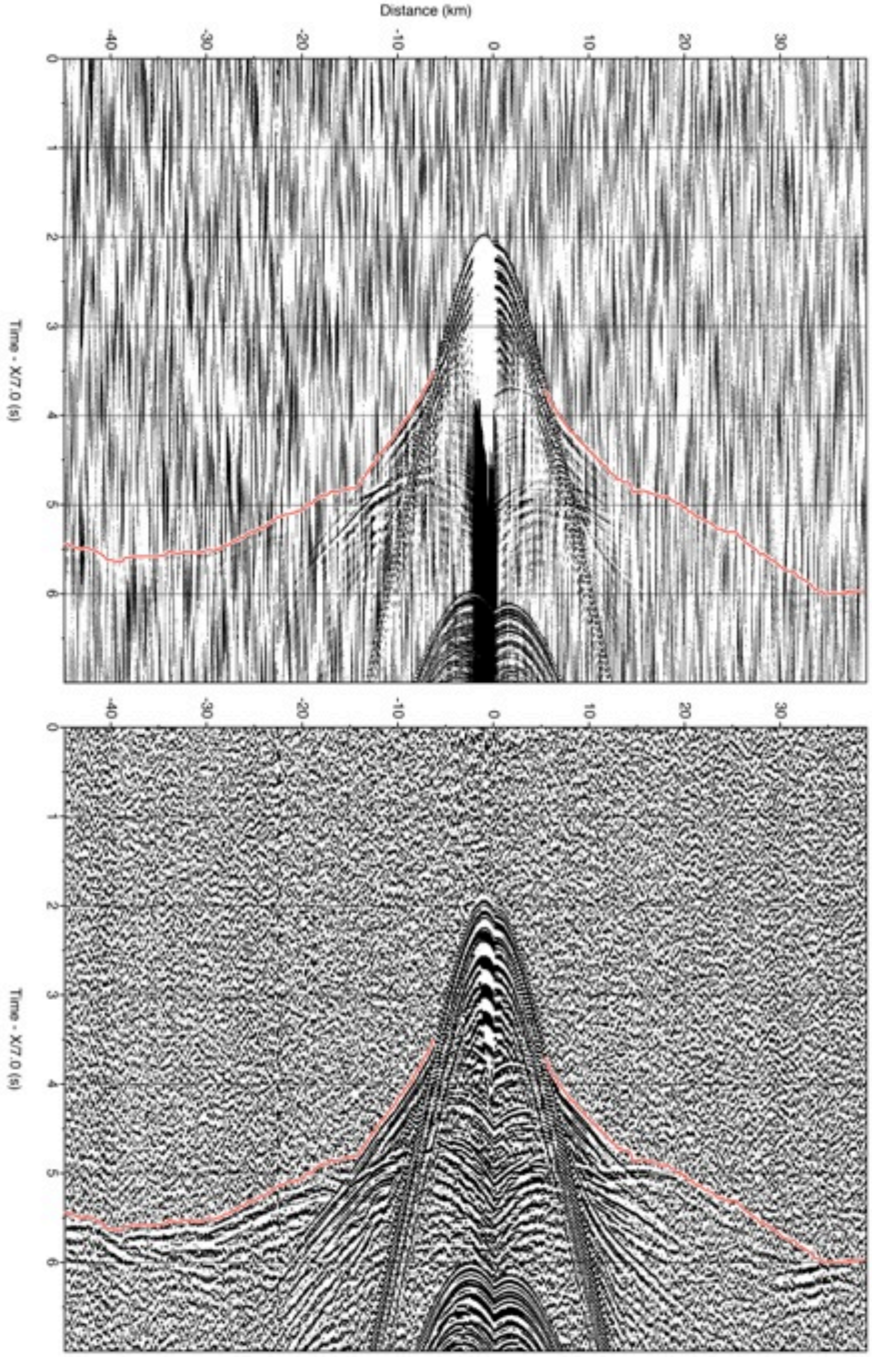

Figure D-23. OBS 25 hydrophone component with first-arrival travel-time picks. Top is unprocessed; bottom is processed to suppress the previous shot noise using gapped deconvolution, bandpass filtering, ACG and gaining with offset.

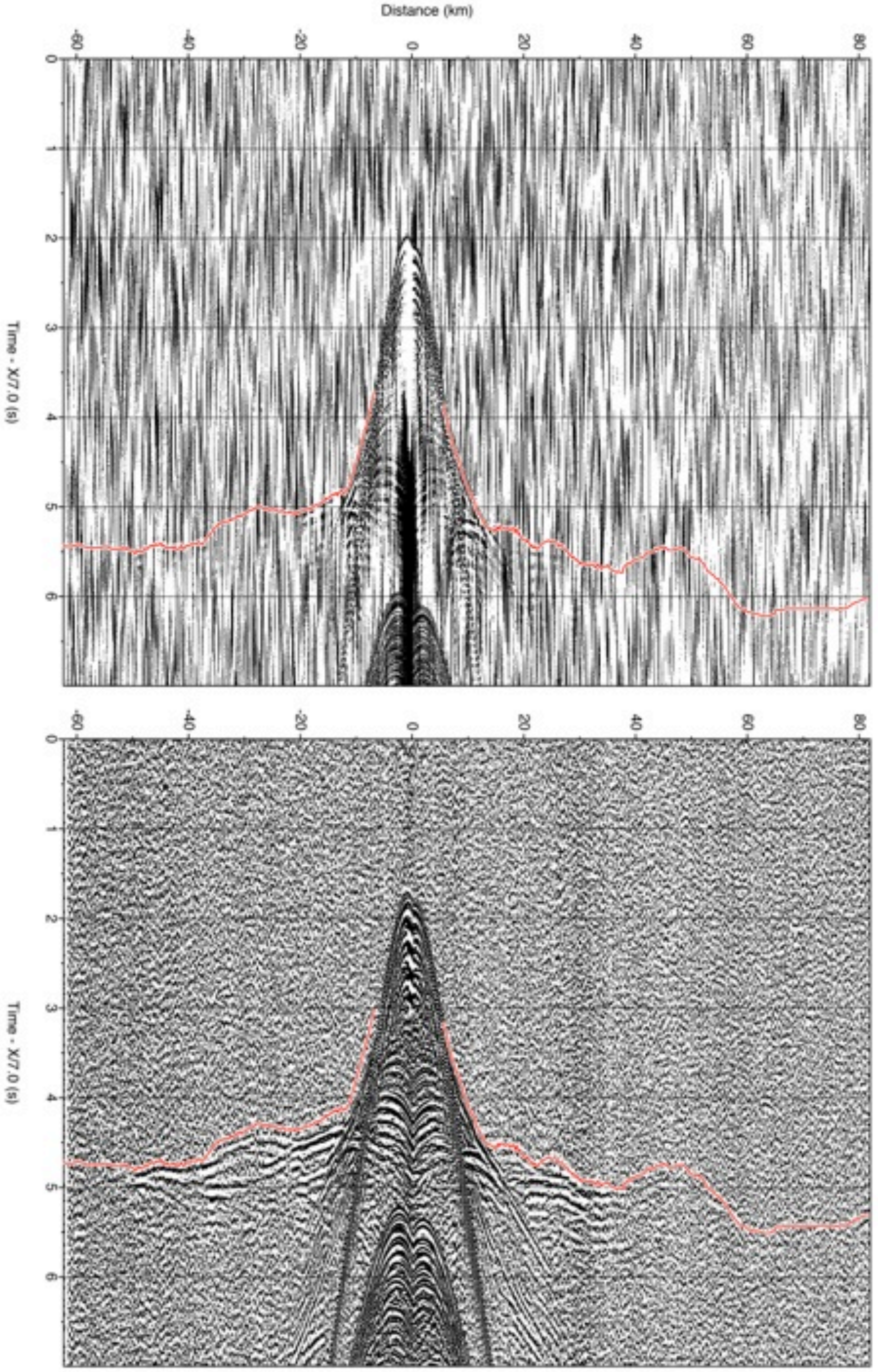

Figure D-24. OBS 27 hydrophone component with first-arrival travel-time picks. Top is unprocessed; bottom is processed to suppress the previous shot noise using gapped deconvolution, bandpass filtering, ACG and gaining with offset.

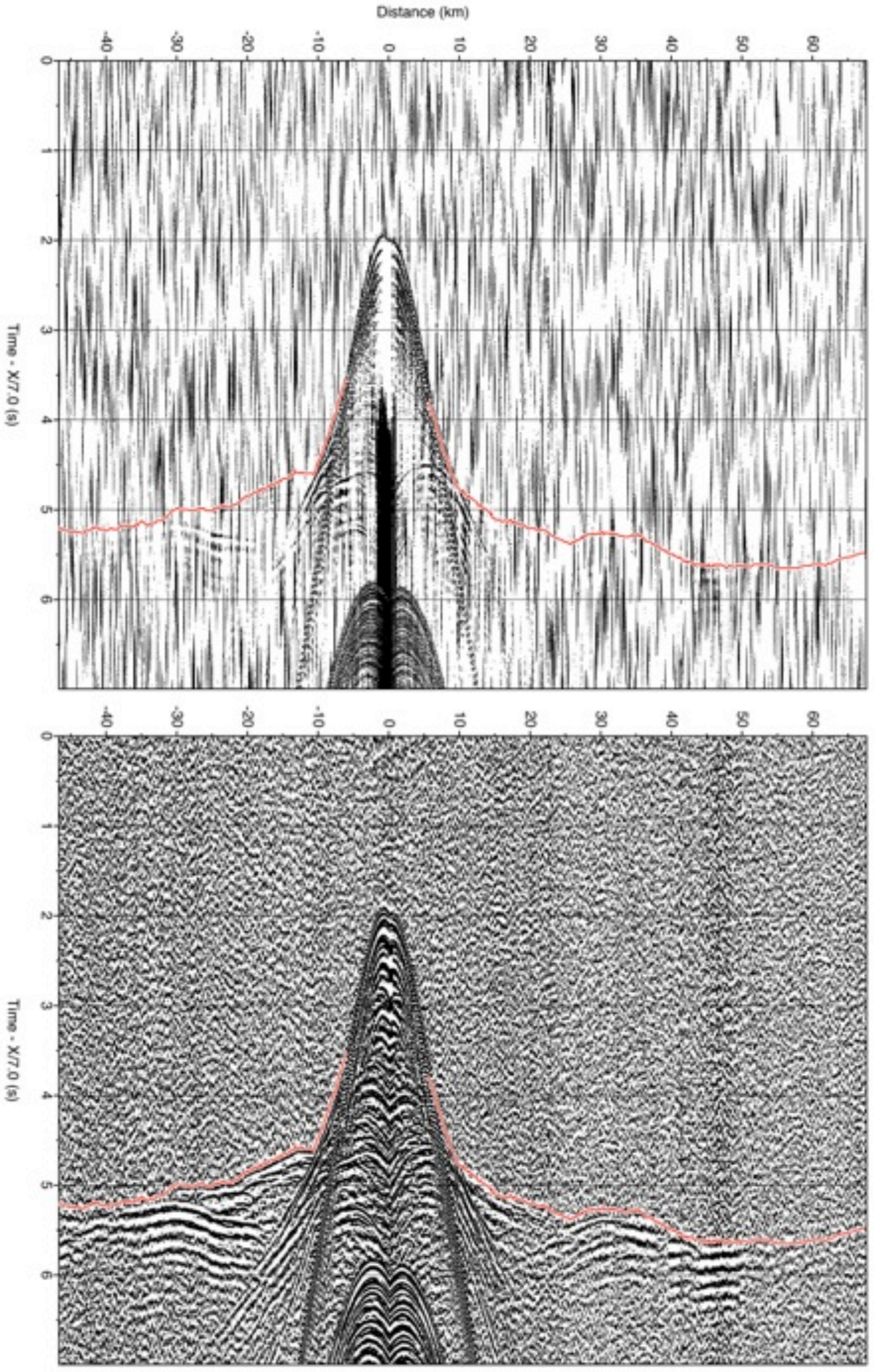

Figure D-25. OBS 28 hydrophone component with first-arrival travel-time picks. Top is unprocessed; bottom is processed to suppress the previous shot noise using gapped deconvolution, bandpass filtering, ACG and gaining with offset.

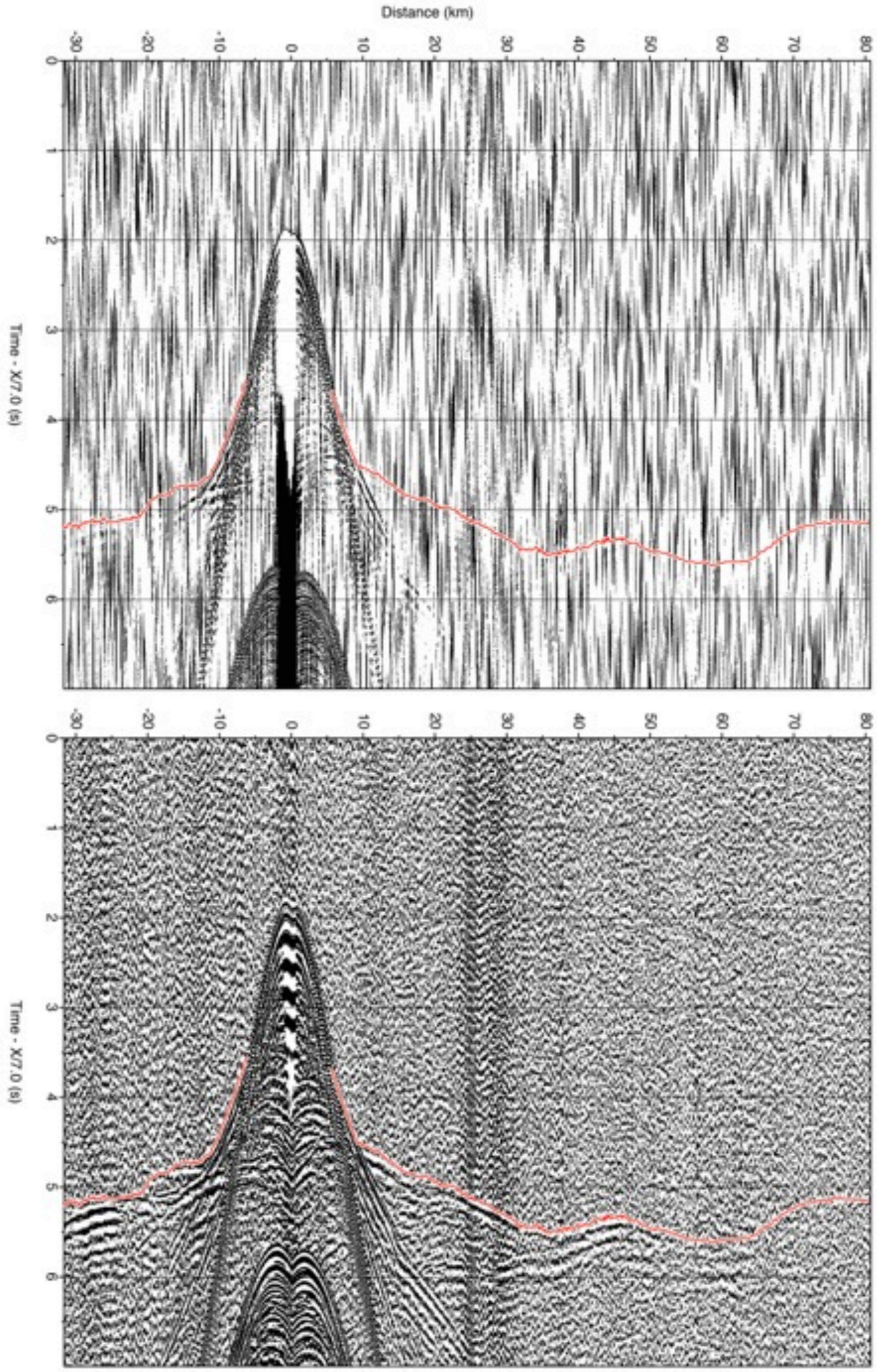

Figure D-26. OBS 29 hydrophone component with first-arrival travel-time picks. Top is unprocessed; bottom is processed to suppress the previous shot noise using gapped deconvolution, bandpass filtering, ACG and gaining with offset.

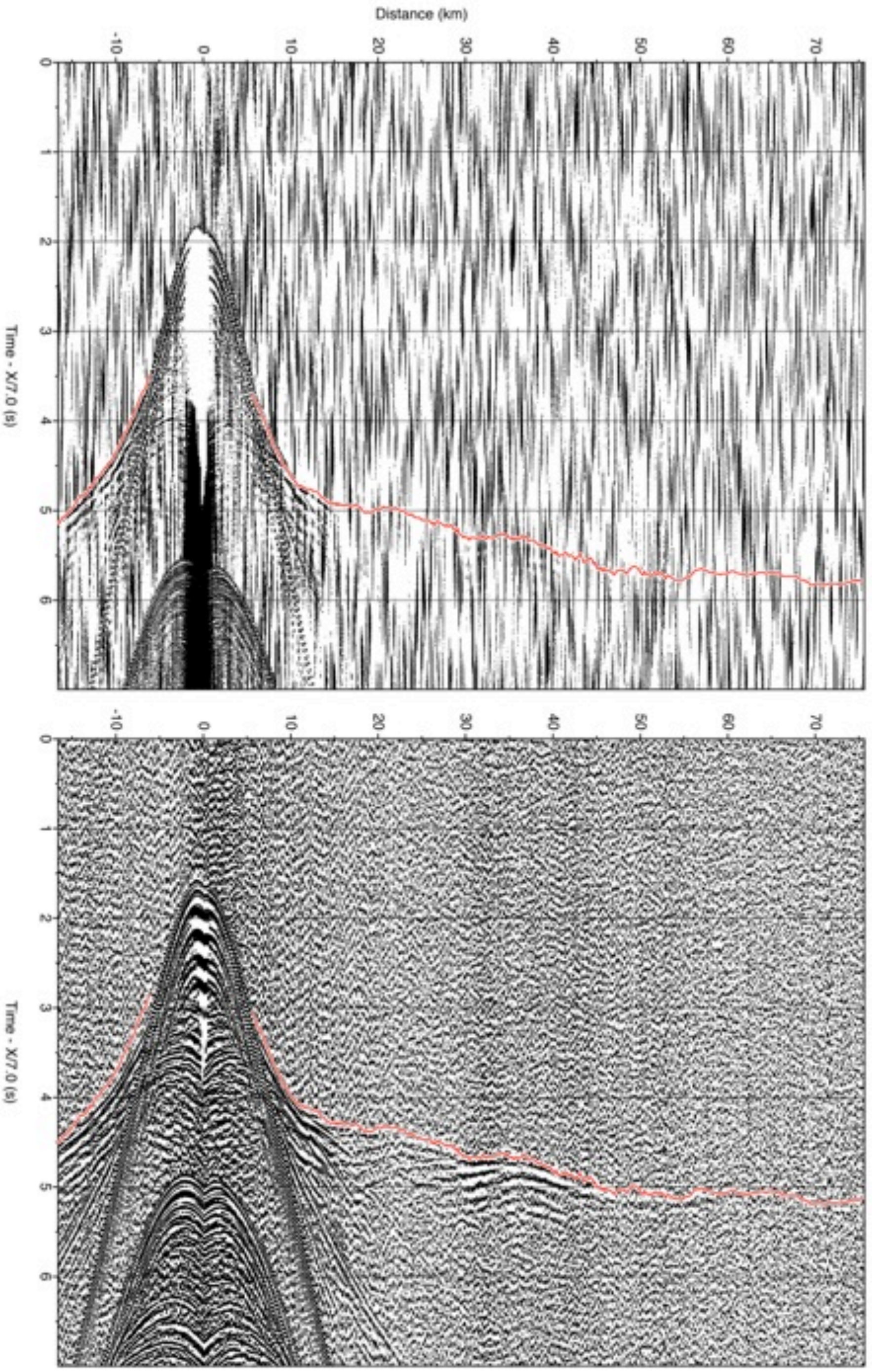

Figure D-27. OBS 30 hydrophone component with first-arrival travel-time picks. Top is unprocessed; bottom is processed to suppress the previous shot noise using gapped deconvolution, bandpass filtering, ACG and gaining with offset.

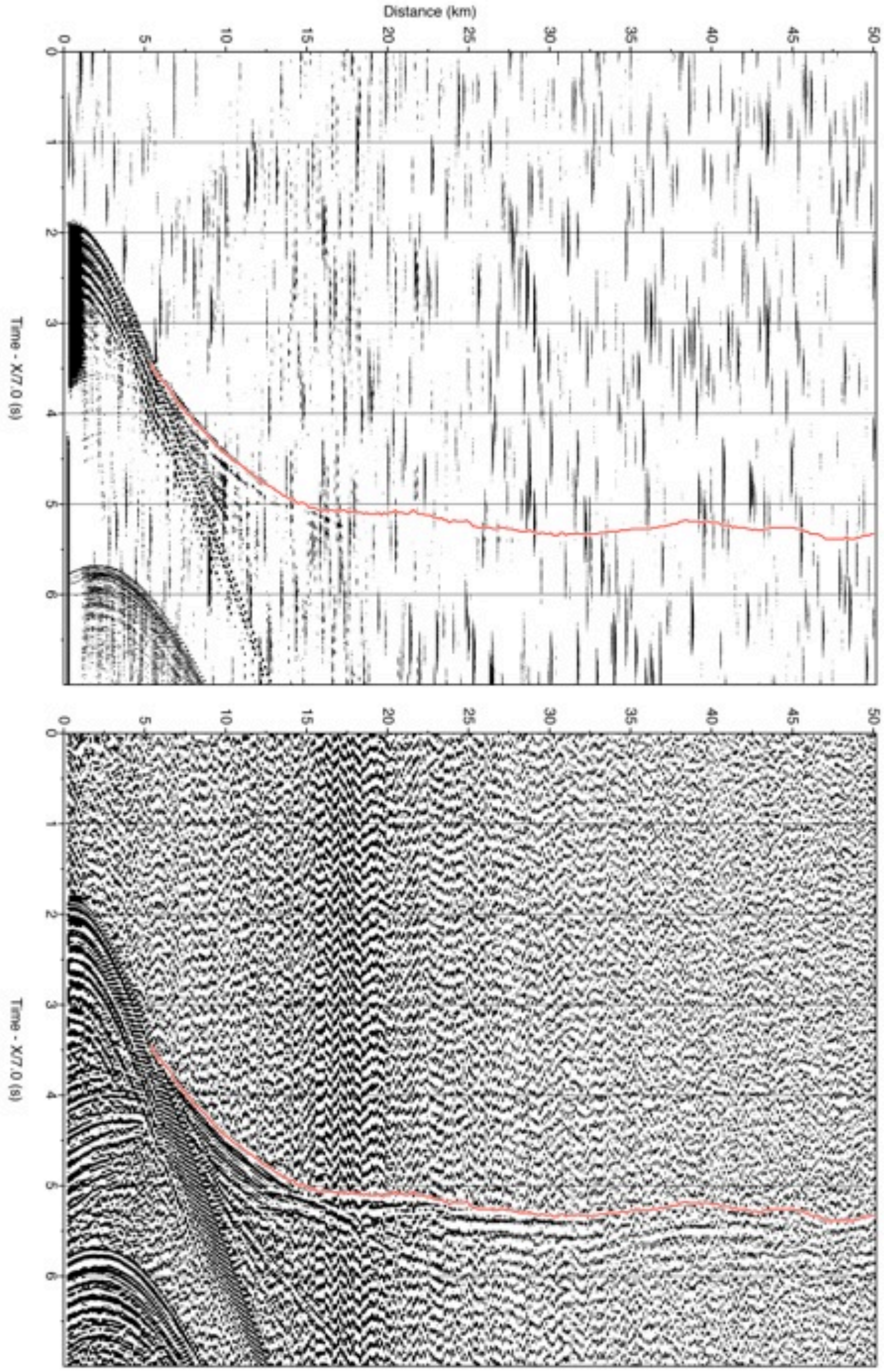

Figure D-28. OBS 31 hydrophone component with first-arrival travel-time picks. Top is unprocessed; bottom is processed to suppress the previous shot noise using gapped deconvolution, bandpass filtering, ACG and gaining with offset.

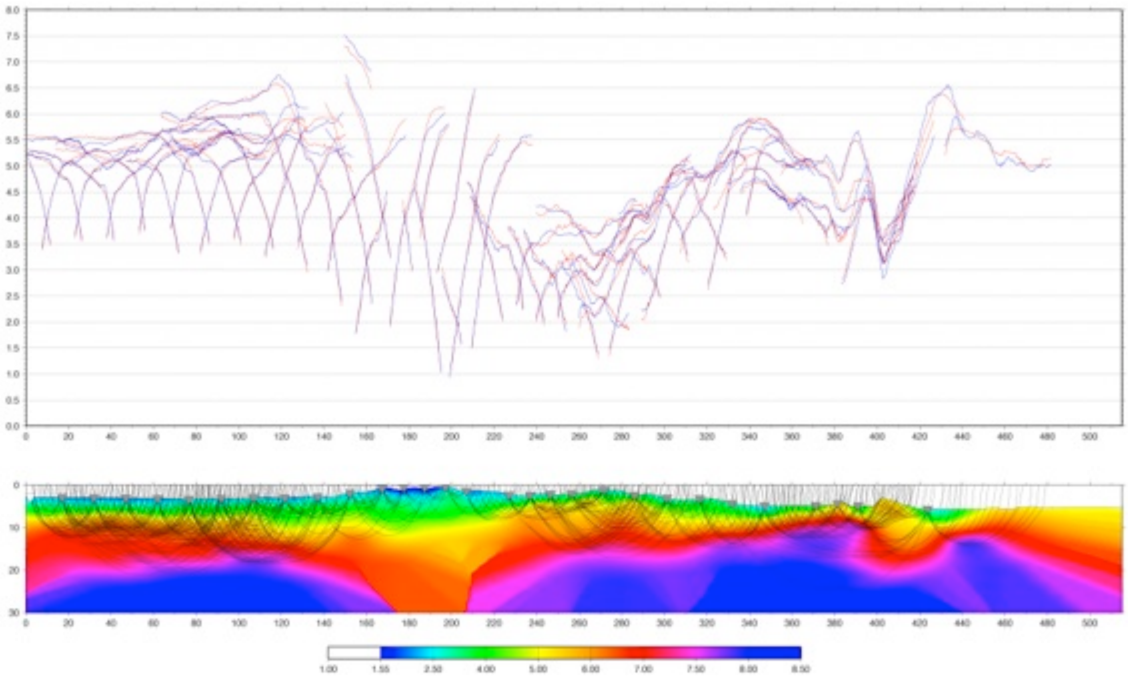

Figure D-29. Ray coverage of line T2 velocity model.

REFERENCES

Angelier, J., Chu, H.-T., Lee, J.-C. (1997). Shear concentration in a collision zone: kinematics of the Chihshang Fault as revealed by outcrop-scale quantification of active fautling. Longitudinal Valley, eastern Taiwan. Tectonophysics 274: 117-143.

Bahlburg, H., and K. P. Furlong (1996), Lithospheric modeling of the Ordovician foreland basin in the Puna of northwestern Argentina, Tectonophysics 259, 245-258.

Ballance, P. F., Scholl, D. W., Vallier, T. L., Stevenson, A. J., Ryan, H., Herzer, R. H., (1989). Subduction of the late Cretaceous seamount of the Louisville Ridge at the Tonga Trench: A model of normal and accelerated tectonic erosion. Tectonics, 8, 953-962.

Bangs, N. L. B., G. K. Westbrook, J. W. Ladd, and P. Buhl (1990), Seismic Velocities From the Barbados Ridge Complex: Indicators of High Pore Fluid Pressures in an Accretionary Complex, J. Geophys. Res., 95(B6), 8767–8782, doi:10.1029/JB095iB06p08767.

Barckhausen, U., Engels, M., Franke, D., Ladage, S., & Pubellier, M. (2014). Evolution of the South China Sea: revised ages for breakup and seafloor spreading. Marine and Petroleum Geology.

Barrier, E., (1985). Un grand accident actif: la faille de la vallée longitudinale de Taiwan. Rev. Géol. Geogr. Phys. 26(1): 43-58.

Barrier, E., Angelier, J. (1986) Active collision in eastern Taiwan: the Coastal Range. Tectonophysics 125: 39-72.

Bautista, B. C., M. L. P. Bautista, K. Oike, F. T. Wu, and R. S. Punongbayan (2001), A new insight on the geometry of subducting slabs in northern Luzon, Philippines, Tectonophysics, 339, 279-310.

Bertrand, E., M. Unsworth, C.-W. Chiang, C.-S. Chen, C.-C. Chen, F. Wu, E. Turkoglu, H.-L. Hsu, and G. Hill (2009), Magnetotelluric evidence for thick-skinned tectonics in central Taiwan, Geology, 37(8), 711-714.

Beyssac, O., Simoes, M., Avouac, J. P., Farley, K. A., Chen, Y-G., Chan, Y-C., Goffe, B. (2007). Late Cenezoic metamorphic evolution and exhumation of Taiwan. Tectonics 26: 1-32.

Beyssac, O., Negro, F., Simoes, M., Chan, Y. C., Chen, Y.G., (2008). High-pressure metamorphism in Taiwan: from oceanic subduction to arc-continent collision? Terra Nova 20, 118-125.

Boillot, G., and Froitzheim, N., (2001). Non-volcanic rifted margins, continental up and the onset of sea-floor spreading: some outstanding questions. Geological Society, London, Special Publications 187, 9-30.

Bowin, C., R. S. Lu, C.-S. Lee, and H. Schouten (1978), Plate convergence and accretion in the Taiwan-Luzon region. Am. Assoc. Pet. Geol. Bull., 62, 1645- 1672.

Briais, A., P. Patriat, et al. (1993). Updated Interpretation of Magnetic Anomalies and

Seafloor Spreading Stages in the South China Sea: Implications for the Tertiary Tectonics of Southeast Asia. J. Geophys. Res. 98(B4): 6299-6328.

Byerlee, J. (1978). Friction of rocks. Pure and Applied Geophysics 116(4): 615-626.

Byrne, D. E., W.-h. Wang, et al. (1993). Mechanical role of backstops in the growth of forearcs. Tectonics 12(1): 123-144.

Byrne, T. B., Liu, C.-S., (2002). Introduction to the geology and geophysics of Taiwan. in Byrne, T. B., and Liu, C.-S., eds, Geology and Geophysics of an Arc-Continent Collision, Taiwan: Boulder, Colorado. Geological Society of America Special Paper 358, 31-54.

Calvert, A. J., Fisher, M., Ramachandran, K., Tréhu, A. M., (2003). Possible emplacement of crustal rocks into the forearc mantle of the Cascadia Subduction Zone. Geophysical Research Letters 30, 1-3.

Carena, S., J. Suppe, et al. (2002). Active detachment of Taiwan illuminated by small earthquakes and its control of first-order topography. Geology 30(10): 935-938.

Casey, J. F., and J. F. Dewey (1984), Initiation of subduction zones along transform and accreting plate boundaries, triple-junction evolution, and forearc spreading centers—implications for ophiolitic geology and obduction, Geological Society, London, Special Publications, 13, 269-290.

Chai, B. H. T. (1972). Structure and Tectonic Evolution of Taiwan. American Journal of Science 272: 389-422.

Chang, P.-C., J. Angelier, C-Y, Lu (2009). Polyphase deformation in a newly emerged accretionary prism: Folding, faulting and rotation in the southern Taiwan mountain belt. Tectonophysics 466: 395-408.

Chapple, W. M. (1978). Mechanics of thin-skinned fold-and-thrust belts. Geological Society of America Bulletin 89(8): 1189-1198.

Chemenda, A., Yang, R., Hsieh, C. H., Groholsky, A., (1997). Evolutionary model for the Taiwan collision based on physical modeling. Tectonophysics, 361, 61-82.

Chemenda, A. I., Yang, R. K. (2001). New results from physical modelling of arc-continent collision in Taiwan: evolutionary model." Tectonophysics 333(1- 2): 159-178.

Cheng, W.-B. (2009). Tomographic imaging of the convergent zone in Eastern Taiwan - A subducting forearc sliver revealed?" Tectonophysics 466(3-4): 170-183.

Chen, A. T., Nakamura, Y. (1998). Velocity structure beneath the eastern offshore region of southern Taiwn based on OBS data. Terrestrial, Atmospheric, and Ocean Sciences (TAO) 9(3): 425-452.

Chi, W.-C. D. L. R., G. Moore, T. Nguyen, C-S. Liu, and N. Lundberg (2003). Tectonic wedging along the rear of the offshore Taiwan accretionary prism. Tectonophysics 374: 199-217.

Chi, W. R., Namson, J., Suppe, J. (1981). Stratigraphic record of the plate interactions of the Coastal Range of eastern Taiwan. Memoir of the Geological Society of China 4: 155-194.

Christeson , G. L., McIntosh, K. D., Shipley, T. H., Flueh, E. R., Goedde, H., (1999). Structure of the Coasta Rica convergent margin, offshore Nicoya Peninsula. J.

Geophys. Res. 104, 25443-25468.

Clift, P. D., Lin, J., (2001). Patterns of extension and magmatism along the continent-ocean boundary, South China margin. In Wilson, R. C. L.,Whitmarsh, R. B., Taylor, B., Froitzheim, N., (Eds), Non-Volcanic Rifting of Continental Margins: A Comparison of Evidence from Land and Sea. Geological Society of London Special Publications, pp. 489-509.

Cloetingh, S., R. Wortel, and N. J. Vlaar (1989). Passive Margin Evolution, initiation of subduction and the Wilson cycle, Tectonophysics, 109, 147-163.

Cloos, M.(1993). Lithospheric buoancy and collisional orogenisis: Subduction of oceanic plateaus, continental margins, island arcs, spreading ridges, and seamounts. Geological Society of Americal Bulletin 105: 715-737.

Collot, J.-Y., G. Lamerche, R. A. Wood, J. Delteil, M. Sosson, J.-F. Lebrun, and M. F. Coffin (1995), Morphostructure of an incipient subduction zone along a transform plate boundary: Puysegur ridge and trench, Geology, 23, 519-522.

Couzens-Schultz, B. A., & Wiltschko, D. V. (2000). The control of the smectite–illite transition on passive-roof duplex formation: Canadian Rockies Foothills, Alberta. Journal of Structural Geology, 22(2), 207-230.

Dahlen, F. A. and T. D. Barr (1989). Brittle Frictional Mountain Building 1. Deformation and Mechanical Energy Budget. J. Geophys. Res. 94(B4): 3906- 3922.

Dahlen, F. A., Suppe, J. (1984). Mechanics of Fold-and-Thrust Belts and Accretionary Wedges: Cohesive Coulomb Theory. J. Geophys. Res. 89(B12): 10087-10101.

Davis, D., Suppe, J. (1980). Critical taper in mechanics of fold-and-thrust belts. Geological Society of America Abstracts w/Programs 12(410).

Davis, D., Suppe, J., Dahlen, J.A. (1983). Mechanics of Fold-and-Thrust Belts and Accretionary Wedges. Journal of Geophysical Research 88: 1153-1172.

Davis, D. M., & von Huene, R. (1987). Inferences on sediment strength and fault friction from structures at the Aleutian Trench. Geology, 15(6), 517-522.

Davies, J. H., von Blanckenburg, F., (1995). Slab breakoff: a model of lithosphere detachment and its test in the magmatism and deformation of collisional orogens. Earth Planet. Sci. Lett. 129, 85-102.

Deschamps, A. E., Lallemand, S. E., Collot, Y.-J. (1998). A detailed study of the Gagua Ridge: A fracture zone uplifted during a plate reorganization in the Mid-Eocene. Marine Geophysical Researches 20: 403-423.

Deschamps, A. E., P. Monié, S. E. Lallemand, S.-K. Hsu, K. Y. Yeh (2000), Evidence for Early Cretaceous oceanic crust trapped in the Philippine Sea Plate, Earth. Planet. Sci. Lett., 179, 503-516.

Dewey, J. F. and J. M. Bird (1970). Mountain Belts and the New Global Tectonics. J. Geophys. Res. 75(14): 2625-2647.

Dominguez, S., S. E. Lallemand, J. Malavielle, and P. Schnürle (1998), Oblique subduction of the Gagua Ridge beneath the Ryukyu accretionary wedge system: insights from marine observations and sandbox experiments, Mar. Geophys. Res., 20, 383-402.

Eakin, D. H., K. D. McIntosh, H. J. A. Van Avendonk, L. Lavier, R. Lester, C.-S., and

C.-S. Lee (2014), Crustal-scale seismic profiles across the Manila subduction zone: The transition from intraoceanic subduction to incipient collision, Journal of Geophysical Research: Solid Earth, 119, 1-17.

Ernst, W. G., Ho, C.-S., Liou, J.-G. (1985). Rifting, drifting, and crustal accretion in the Taiwan sector of the Asiatic continental margin. Tectonostratigraphic terranes of the Circum-Pacific region: 375-389.

Fisher, R. V. (1984), Submarine volcaniclastic rocks. Geo. Soc. London, 16, 5-27.

Fisher, D. M., Liu, C.-Y., Chu, H.-T. (2002). Taiwan Slate Belt: Insights into the ductile interior of an arc-continent collision. Geology and Geophysics of an Arc-Continent Collision, Taiwan Special Paper 358, Geological Society of America.

Font, Y., Liu, C.-S., Schnurle, P., Lallemand, S., (2001). Constraints on the backstop geometry of the southwest Ryukyu subduction based on reflection seismic data. Tectonophysics 333, 135-158.

Fowler, S. R., White, R. S., Louden, K. E., (1998). Sediment dewatering in the Makran accretionary prism. Earth Planet Sci. Lett. 75, 427-438.

Franke, D., Barckhausen, U., Baristeas, N., Engles, M., Ladage, S., Lutz, R., Montano, J., Pellejera, N., Ramos, E. G., Schnabel, M., (2011). The continent-oceantransition at the southeastern margin of the South China Sea. Marine and Petroleum Geology 28, 1187-1204.

Franke, D., (2012). Rifting, lithosphere breakup and volcanism: Comparison of magma-poor and volcanic rifted margins. Marine and Petroleum Geology (in press), 1-25.

Fuller, C. W., Willett, S. D., Fisher, D., Lu, C. Y., (2006). A thermomechanical wedge model of Taiwan constrained by fission-track thermochronometry. Tectonophysics, 1-24.

Gurnis, M., C. Hall, and L. L. Lavier (2004), Evolving force balance during incipient subduction, Geochemistry, Geophysics, Geosystems, 5, 1-31.

Hall, R., J. R. Ali, C. D. Anderson, and S. J. Baker (1995), Origin and motion history of the Philippine Sea Plate, Tectonophysics, 251, 229-250.

Hall, R. (2002), Cenozoic geological and plate tectonic evolution of SE Asia and the SW Pacific: computer-based reconstructions, model and animations, J. Asian. Earth. Sci., 20, 353-431.

Hayes, D. E., R. E. Houtz, R. D. Jarrard, C. L. Mrozowski, and T. Watanbe (1978), Crustal Structure. In D. E. Hayes (Editor). A Geophysical Atlas of the East and Southeast Asian Seas. Geo. Soc. Am., Map and Chart Ser., MC-25.

Hayes, D. E. and S. D. Lewis (1984). A Geophysical Study of the Manila Trench, Luzon, Philippines 1. Crustal Structure, Gravity, and Regional Tectonic Evolution. J. Geophys. Res. 89(B11): 9171-9195.

Hegarty, K. A., J. K. Weissel, and D. E. Hayes (1982), Convergence at the Caroline-Pacific Plate boundary: Collision and subduction. In The Tectonic and Geological Evolution of Southeast Asian Seas and Islands, Part 2. Geophys. Monogr. Ser., vol. 27, edited by D. E. Hayes, pp. 326-348, AGU, Washington, D.C.

Henry, M., D. E. Karig, and G. G. Shor Jr. (1975), Two seismic refraction profiles in the West Philippine Sea. In D. E., Karig, J. C. Ingle Jr. et al. Initial Reports of the

Deep Sea Drilling Project. U. S. government Printing Office, Washington, D. C. 31, 611-614.

Hilde, T. W. C., and C.-S. Lee (1984), Origin and Evolution of the West Philippine Basin: A new interpretation, Tectonophysics, 102, 85-104.

Hirtzel, J., Chi, W.-C., Reed, D., Chen, L., Liu, C.-S., Lundberg, N. (2009). Destruction of Luzon forearc basin from subduction to Taiwan arc-continent collision. Tectonophysics 479(1-2): 43-51.

Ho, C. S. (1986). A synthesis of the geologic evolution of Taiwan. Tectonophysics 125(1-3): 1-16.

Hobro, J. W. D., Singh, S. C., Minshull, T. A. (2003). Three-dimensional tomographic inversion of combined reflection and refraction seismic traveltime data. Geophysical Journal International 152(1): 79-93.

Hole, J. A. (1992). Nonlinear High-Resolution Three-Dimensional Seismic Travel Time Tomography. J. Geophys. Res. 97(B5): 6553-6562.

Hsu, S.-K., Y.-c. Yeh, et al. (2004). New Bathymetry and Magnetic Lineations Identifications in the Northernmost South China Sea and their Tectonic Implications. Marine Geophysical Research 25(1): 29-44.

Hu, D., Zhou, D., Wu, X., He, M., Pang, X., Wang, Y., (2009). Crustal structure and extension from slope to deepsea basin in the northern South China Sea. Journal of Earth Science 20, 27-37.

Huang, C.-Y., Yuan, P. B., Tsao, S.-J. (2006). Temporal and spatial records of active arc-continent collision in Taiwan: A synthesis. Geological Society of America Bulletin 118: 274-288.

Huang, C.-Y., Wu, W.-Y. (1997). Tectonic evolution of accretionary prism in the arc-continent collision terrane of Taiwan. Tectonophysics 281(1-2): 31-51.

Huang, C.-Y., Yuan, P. B. (2000). Geodynamic processes of Taiwan arc-continent collision and comparison with analogs in Timor, Papua New Guinea, Urals and Corsica. Tectonophysics 325(1-2): 1-21.

Hussong, D., and S. Uyeda (1981), Tectonic processes and the history of the Mariana arc: a synthesis of the results of Deep Sea Drilling Project Leg 60. In M. Lee and R. Powell (eds), Int. Repts. DSDP 60, Vol. 60, National Sciences Foundation, Washington, D. C., pp. 909-929.

Johnson, K. M., P. Segall, and S. B. Yu (2005), A viscoelastic earthquake cycle model for Taiwan, Journal of Geophysical Research, 110(B10).

Karig, D. E., and J. M. Wageman (1975), Structure and sediment distribution in the northwest corner of the West Philippine Basin. In D. E. Karig, J. C. Ingle Jr. et al. (eds), Initial Reports of the Deep Sea Drilling Project, U. S. Government Printing Office, Washington, D. C., Vol. 31, pp. 615-620.

Karig, D. E., and Sharman, G. F. (1975). Subduction and accretion in trenches. Geological Society of America Bulletin, 86(3), 377-389.

D. E. Karig (1983), Accreted terranes in the northern part of the Philippine archipelago, Tectonics, 2, 211-236.

Karig, D.E., Barber, A.J., Charlton, T.R., Klemperer, S., Hussong, D.M., (1987). Nature and distribution of deformation across the Banda arc-Australian collision zone at Timor. Geol. Soc. Am. Bull. 98, 18-32.

Konstantinovskaia, E., Malavieille, J. (2005). Erosion and exhumation in accretionary orogens: Experimental and geological approaches. Geochemistry Geophysics Geosystems 6(2): 1-25.

Kopp, H., Flueh, E. R., Papenberg, C., Klaeschen, D., and SPOC-Scientists, (2004). Seismic investigations of the O'Higgins Seamount Group and Juan Fernandez Ridge: aseismic ridge emplacement and lithosphere hydration. Tectonics 23. doi 10.1029/2003TC001590.

Ku, C.-Y. and S.-K. Hsu (2009). Crustal structure and deformation at the northern Manila Trench between Taiwan and Luzon islands. Tectonophysics 466(3-4): 229-240.

Kuo, B.-Y., W.-C. Chi, C.-R. Lin, E.-T.-Y. Chang, J. Collins, and C.-S. Liu (2009), Two-station measurement of Rayleigh-wave phase velocities for the HB, the westernmost Philippine Sea, with OBS implications for regional tectonics, Geophys. J. Int., 179, 1859-1869.

Lallemand, S. E., Schnürle, P., Malavieille, J., (1994). Coulomb theory applied to accretionary and nonaccretionary wedges: Possible causes for tectonic erosion and/or frontal accretion. Journal of Geophysical Research, 99, 12033-12055.

Lallemand, S., and C.-S. Liu (1997), Swath Bathymetry Mapping Reveals Details of the Acrive Arc-Continent Collision Offshore Taiwan, EOS Transactions, AGU, 78, 173-175.

Lallemand, S., Font, Y., Bijwaard, H., Kao, H. (2001). New insights on 3-D plates interaction near Taiwan from tomography and tectonic implications. Tectonophysics 339: 229-253.

Lallemand, S., T. Theunissen, P. Schnürle, C.-S. Lee, C.-S. Liu, Y. Font (2013), Indentation of the Philippine Sea plate by the Eurasia plate in Taiwan: Details from recent marine seismological experiments, Tectonophysics, 594, 60-79.

Lan, C.-Y., Chen, C-H., Chung, S-L., Lee, T., Lee, C-M-W., Yu, T-F. (1996). The crustal evolution of continental Taiwan. Journal of the Geological Society of China39: 337-353.

Langseth, M. G., and C. L. Mrozowski (1980), Geophysical surveys for Leg 59 sites. Deep Sea Drilling Project. In L. Kroenke, R. Scott et al., Initial Reports of the Deep Sea Drilling Project. U. S. Government Printing Office, Washington, D. C. 59, 487-502.

Lavier, L. L., Manatschal, G. (2006). A mechanism to thin the continental lithosphere at magma-poor margins. Letters to Nature 440: 324-328.

Lee, J.-C., Angelier, J. (1993). Localisation des deformations actives et traitment des données géodésiques:]' exemple de la faille de la Vallée Longitudinale, Taiwan. Bull. Soc. Géol. Fr. 164(4): 533-570.

Lee, T.-Y. Lawver, L. A. (1995). Cenezoic plate reconstruction of Southeast Asia. Tectonophysics 251: 85-138.

Lee, C.-S., S.-K. Hsu, K. Okino, and K. Tamaki (1999), Deep drag ocean bottom magnetometer and its application on the Tertiary magnetic isochrones.

Geophysical Meeting, Keelung, October 28-29, Abstract.

Lee, C.-I., Y.-L. Chang, and M. P. Coward (2002), Inversion tectonics of the fold-and-thrust belt, western Taiwan, in Geology and Geophysics of an Arc-Continent Collision, Taiwan, edited by T. B. Byrne and C.-S. Liu, pp. 13-30, Geological Society of America.

Lee, Y.-H., Chen, C.-C., Liu, T.-K., Ho, H.-C., Lu, H.-Y., Lo, W. (2006). Mountain building mechanisms in the Southern Central Range of the Taiwan Orogenic Belt - From accretionary wedge deformation to arc-continent collision. Earth and Planetary Science Letters 252: 413-422.

Lester, R., McIntosh, K., (2012). Multiple attenuation in crustal-scale imaging: examples from the TAIGER marine reflection data set. Marine Geophys. Res. doi: 10.1007/s11001-012-9149-1

Lester, R., McIntosh, K., Van Avendonk, H. J. A., Lavier., (2013). Crustal Accretion in the Manila Trench Accretionary Wedge at the Transition from Subduction to Mountain-Building in Taiwan. Geology.

Lewis, S. D. and D. E. Hayes (1984). A Geophysical Study of the Manila Trench, Luzon, Philippines 2. Fore Arc Basin Structural and Stratigraphic Evolution. J. Geophys. Res. 89(B11): 9196-9214.

Li, C.-F., Z.-Y. Zhou, J.-B. Li, H.-J. Chen, J.-H. Geng, and H Li (2007), Pre-collisional tectonics and terrain amalgamation offshore southern Taiwan: Characterizations from reflection seismic and potential field data, Sci, China Ser. D-Earth Sci., 50, 897-908.

Lin, C.-H. (2000). Thermal modeling of continental subduction and exhumation constrained by heat flow and seismicity in Taiwan. Tectonophysics 324: 189-201.

Lin, J.-Y., Sibuet, J.-C., Lee, C.-S., Hsu, S.-K., Klingelhoefer, F. (2007). Origin of the 196 southern Okinawa Trough volcanism from detailed seismic tomography. Journal of Geophysical Research 112: 1-20.

Lin, A. T., Yao, B., Hsu S.-K., Liu, C.-S., Huang, C.-Y. (2009). Tectonic features of the incipient arc-continent collision zone of Taiwan: Implications for seismicity. Tectonophysics(479): 28-42.

Liu, C.-S., Deffontaines, B. (2004). Deformation Patterns of an Accretionary Wedge in the Transition Zone from Subduction to Collision Offshore Southwestern Taiwan. Marine Geophysical Researches 25(1): 123-137.

Lin, A. T., Liu, C.-S., Lin, C.-C., Schnurle, P., Chen, G.-Y., Liao, W.-Z., Teng, L. S., Chuang, H.-J., Wu, M.-S., (2008). Tectonic features associated with the overriding of an accretionary wedge on top of a rifted continental margin: An example from Taiwan. Marine Geology 255, 186-203.

Liu, C.-S., Huang, I. L. (1997). Structural features off southwestern Taiwan. Marine Geology 137(3-4): 305-319.

Liu, M., X. Cui, and F. Liu. (2004). Cenozoic rifting and volcanism in eastern China: a mantle dynamic link to the Indo-Asian collision?, Tectonophysics, 393(1), 29- 42.

Louden, K. E. (1980), The crustal and lithospheric thickness of the Philippine Sea as compared to the Pacific, Earth. Planet. Sci. Lett., 50, 275-288.

Ludwig, W. J., (1969). The Manila Trench and West Luzon Trough – III. Seismic refraction measurements. Deep Sea Research and Oceanographic Abstracts 17, 553-562.

Ludwig, K., W. J., N. (1979). Profiler-sonobuoy measurements in the South China Sea basin. J. Geophys. Res. 84(B7): 3505-3518.

Lundberg, N., D. L. Reed, C-S. Liu, J. Lieske (1997). Forearc-basin closure and arc accretion in the submarine suture zone south of Taiwan. Tectonophysics 274: 5-23.

Malavieille, J., Lallemand, S. E., Dominguez, S., Deschamps, A., Lu, C.-Y., Liu, C.-S., Schnürl, P., (2002). Arc-continent collision in Taiwan: New marine observations and tectonic evolution. Geol. Soc. Amer. Special Paper 358.

Malavieille, J. and G. Trullenque (2007). Consequences of continental subduction on forearc basin and accretionary wedge deformation in SE Taiwan: Insights from analogue modeling. Tectonophysics 466(3-4): 377-394.

Malavieille, J. (2010). Impact of erosion, sedimentation, and structural heritage on the structure and kinematics of orogenic wedges: Analog models and case studies. GSA Today 20(1): 4-10.

Massell, C., M. F. Coffin, P. Mann, S. Mosher, C. Frohlich, C. S. Duncan, G. Karner, D. Ramsay, and J.-F. Lebrun (1999), Neotectonics of the Marquarie Ridge complex, Australia-Pacific plate boundary, J. Geophys. Res., 105, 13,457-413,480.

McIntosh, K. D., Y and Nakamura (1998), Crustal structure beneath the Nanao forearc basin from TAICRUST MCS/OBS line 14, TAO 9, 345-362.

McIntosh, K., Y. Nakamura, Wang, T.-K., Shih, R.-C., Chen, A., Liu, C.-S. (2005). Crustal-scale seismic profiles across Taiwan and the western Philippine Sea. Tectonophysics 401(1-2): 23-54.

McIntosh, K., Van Avendonk, H. J., Wu, F. T., Okaya, D. A., Wang, C. (2010), Results from an onshore/offshore transect of southern Taiwan, Abstract xxxxx-xxxx presented at 2010 Fall Meeting, AGU, San Francisco, Calif., 13-17 Dec.

McIntosh, K. D., H. J A. Van Avendonk, L. Lavier, R. M. Lester, D. Eakin, F. Wu, C.-S. Liu, and C.-S. Lee (2013), Inversion of a hyper-extended rifted margin in the southern Central Range of Taiwan, Geology, 41, 871-874.

McKenzie, D. P. (1977), The initiation of trenches: A finite amplitude instability. In Island Arcs, Deep Sea Trenches and Back-Arc Basins, Maurice Ewing Ser, vol. 1, edited by M. Talwani and W. C. Pitman, pp. 57-61, AGU, Washington, D. C.

Meneghini, F., Marroni, M., Moore, J. C., Pandolfi, L., and C. D. Rowe. (2009). The process of underthrusting and underplating in the geologic record: structural diversity between the Franciscan Complex (California), the Kodiak Complex (Alaska) and the Internal Ligurian Units (Italy). Geological Journal, doi:10.1002/gi.1144.

Minshull, T., & White, R. (1989). Sediment compaction and fluid migration in the Makran accretionary prism. Journal of Geophysical Research: Solid Earth (1978–2012), 94(B6), 7387-7402.

Mitra, G., and Boyer, S. E., (1986). Energy balance and deformation mechanisms of duplexes. Journal of Structural Geology, 8, 291-304.

Molnar, P. and D. Gray (1979). Subduction of continental lithosphere: Some 198 constraints and uncertainties. Geology 7(1): 58-62.

Morzowski, C. L., S. D. Lewis, and D. E. Hayes (1982), Complexities in the tectonic evolution of the West Philippine Basin, Tectonophysics, 82, 1-24.

Mouthereau, F., O. Lacombe, B. Deffontaines, J. Angelier, and S. Brusset (2001), Deformation history of the southwestern Taiwan foreland thrust belt: insights from tectono-sedimentary analyses and balanced cross-sections, Tectonophysics, 333(1), 293-318.

Mouthereau, F., B. Deffontaines, O. Lacombe, J. Angelier (2002). Variations along the strike of the Taiwan thrust belt: Basement control on structural style, wedge geometry, and kinematics. Geological Society of America Special Paper 358: 31-54.

Mouthereau, F., and O. Lacombe (2006), Inversion of the Paleogene Chinese continental margin and thick-skinned deformation in the Western Foreland of Taiwan, Journal of Structural Geology, 28, 1977-1993.

Mueller, S., and R. J. Phillips (1991), On the initiation of subduction, J. Geophys. Res., 96, 651-665.

Murauchi, S., M. Den, S. Asano, H. Hotta, T. Yoshii, T. Asanuma, K. Hagiwara, K. Ichikawa, R. Sato, W. J. Ludwig, J. I. Ewing, N. T. Edgar, and R. E. Houtz (1968), Crustal structure of the Philippine Sea, J. Geophys. Res., 73, 3143-3171.

Mutter, C. Z., Mutter, J. C., (1993). Variations in thickness of layer 3 dominate oceanic crustal structure. Earth and Planetary Science Letters 117, 295-317.

Nakamura, Y., McIntosh, K., Chen, A. T., (1998). Preliminary results of a large offset seismic survey west of Hengchun Peninsula, southern Taiwan. Terr. Atmos. Oceanol. 9, 395-408.

Nakamura, M., Yasuhiro, Y., Zhao, D., Katao, H., Nishimura, S. (2003). Three-dimensional P – and S-wave velocity structures beneath the Ryukyu arc. Tectonophysics 369: 121-143.

Nikolaeva, K., Gerya, T. V., & Marques, F. O. (2010). Subduction initiation at passive margins: numerical modeling. Journal of Geophysical Research: Solid Earth (1978–2012), 115(B3).

Nissen, S. S., D. E. Hayes, Bochu, Y., Weijun, Z., Yongqin, C., Xiaupin, N. (1995). Gravity, heat flow, and seismic constraints on the processes of crustal extension: Northern margin of the South China Sea. J. Geophys. Res. 100(B11): 22447-22483.

Nissen, S. S., Hayes, D. E., Buhl, P., Diebold, J., Bochu, Y., Weijun, Z., Yongqin, C., (1995). Deep penetration seismic soundings across the northern margin of the South China Sea. J. Geophys, Res. 100, 22, 422-447.

Ozima, M., I. Kaneoka, and H. Ujiie (1977), $^{40Ar/39Ar}$ age of rocks, and development mode of the Philippine Sea, Nature, 267, 816-818.

Park, J.-O., Tsuru, T., Kaneda, Y., Kono, Y., (1999). A subducting seamount beneath the

Nankai accretionary prism off Shikoku, southwestern Japan. Geophysical Research Letters, 26, 931-934.

Paterson, M. S. (1978). Experimental Rock Deformation: The Brittle Field. New York, Springer-Verlag.

Ranero, C. R., Morgan, J. P., McIntosh, K., Reichert, C., (2003). Bending-related faulting and mantle serpentinization at the Middle American trench. Nature 425, 367-373.

Rangin, C., and M. Pubellier (1990), Subduction and accretion of Philippine Sea Plate fragments along the Eurasian margin, In J. Aubouin and J. Boutgois (eds), Tectonics of Circum-Pacific Continental Margins, VSP, Utrecht, pp. 139-164.

Ranken, B., R. K. Cardwell., D. E. Karig. (1984). Kinematics of the Philippine Sea Plate. Tectonics 3(5): 555-575.

Rau, J.-R., Wu., F. T. (1995). Tomographic imaging of lithospheric structures under Taiwan. Earth and Planetary Science Letters 133: 517-532.

Reed, D., Lundberg, N., Liu, C-S., Kuo, B-Y. (1992). Structural relations along the margins of the offshore Taiwan accretionary wedge; implication for accretion and crustal kinematics. Acta Geologica Taiwanica 30: 105-122.

Rossetti, F., Faccenna, C., Ranalli, G., (2002). The influence of backstop dip and convergence velocity in the growth of viscous doubly-vergent orogenicwedges: insights from thermomechanical laboratory experiments. J. Struc. Geol. 24, 953-962.

Ru, K., Pigott, J.D., (1986). Episodic rifting and subsidence in the South China Sea. AAPG Bulletin 70, 1136-1155.

Sandwell, D. T., E. Garcia, K. Soofi, P. Wessel, and W. H. F. Smith (2013), Towards 1 mGal Global Marine Gravity from CryoSat-2, Envisat, and Jason-1, The Leading Edge, vol. 32, issue 8, pp. 892-899.

Schillington, D. J., Holbrook, W. S., Van Avendonk, H. J. A., Tucholke, B. E., Hopper, J. R., Louden, K. E., Larsen, H. C., (2006). Evidence for asymmetric nonvolcanic rifting and slow incipient oceanic accretion from seismic reflection data onthe Newfoundland margin. Journal of Geophysical Research: Solid Earth 111.

Schnürle, P., C.-S. Liu, S. Lallemand, and D. Reed (1998), Structural insight into the south Ryukyu margin: Effects of the subducting Gagua Ridge, Tectonophysics, 288, 237-250.

Schouten, H., K. D. Klitgord, and J. A. Whitehead (1985), Segmentation of mid-ocean ridges, Nature, 317, 225-229.

Seno, T. (1977). The instantaneous rotation vector of the Philippine sea plate relative to the Eurasian plate. Tectonophysics 42(2-4): 209-226.

Seno, T., S. Stein., A. E. Gripp (1993). A Model for the Motion of the Philippine Sea Plate Consistent with NUVEL-1 and Geological Data. Journal of Geophysical Research 98: 17941-17948.

Shyu, J. B. H., Sieh, K., Chen, Y.-G., Liu, C.-S. (2005). Neotectonic architecture of Taiwan and its implications for future large earthquakes. J. Geophys. Res. 110(B8): B08402.

Sibuet, J.-C., S.-K. Hsu, X. Le Pichon, J.-P. Le Formal, D. Reed, G. Moore, and C.-S. Liu

(2002), East Asia plate tectonics since 15 Ma: constraints from the Taiwanregion, Tectonophysics, 344, 103-134.

Silver, E.A., M.J. Ellis, N.A. Breen, and T.H. Shipley., (1985). Comments on the growth of accretionary wedges, Geology, 13, 6-9.

Simoes, M., & Avouac, J. P. (2006), Investigating the kinematics of mountain building in Taiwan from the spatiotemporal evolution of the foreland basin andwestern foothills. Journal of Geophysical Research: Solid Earth (1978–2012), 111(B10).

Simoes, M., J. P. Avouac, O. Beyssac, B. Goffe, K. A. Farley, and Y.-G. Chen (2007), Mountain building in Taiwan: A thermokinematic model, Journal of Geophysical Research, 112(B11405).

Simpson, D. H. (2010). Formation of accretionary prisms influenced by sediment subduction and supplied by sediments from adjacent continents. Geological Society of America 38: 131-134.

Singh, S.C., Carton, H., Tapponnier, P., Hananto, N. D., Chauhan, A. P. S., Hartoyo, D., Bayly, M., Moeljopranoto, S., Bunting, T., Christie, P., Lubis, H., Martin, J., (2008). Seismic evidence for broken oceanic crust in the 2004 Sumatra earthquake epicentral region. Letters to Nature, doi:10.1038, 777-781.

Sleep, N. H. (1990), Hotspots and mantle plumes, some phenomenology, Journal of Geophysical Research, 98, 6715-6736.

Smith, G. A., J. D. Moore, and W. C. McIntosh (2002), Assessing roles of volcanism and basin subsidence in causing Oligocene-Lower Miocene sedimentation in the northern Rio Grande Rift, New Mexico, USA, Journal of Sedimentary Research, 72, 836-848.

Song, T.-R. A. Ma, K.-F. (2002). Estimation of the thermal structure of a young orogenic belt according to a model of whole-crust thickening. Geological Society of America Special Paper 358: 121-136.

Stanley, R. S., Hill, L. B., Chang, H. C., Hu, H. N. (1981). A cross-section through the southern central mountains of Taiwan. Memoir of the Geological Society of China 4: 443-474.

Stern, R. J., and S. H. Bloomer (1992), Subduction zone infancy: Examples from the Eocene Izu-Bonin-Mariana and Jurassic California arcs, Geol. Soc. Am. Bull., 104, 1621-1636.

Storti, F., McCay, K. (1995). Influence of syntectonic sedimentation on thrust wedges in analogue models. Geology 25: 999-1002.

Suppe, J. (1981). Mechanics of Mountain Building and Metamorphism in Taiwan. Memoir of the Geological Society of China(4): 67-89.

Suppe, J. (1984). Kinematics of arc-continent collision, flipping of subduction, and back-arc spreading near Taiwan, Memoir of the Geological Society of China, 6, 21-33.

Suppe, J., (1987). The active Taiwan mountain belt. In: Shaer, J. P., Rodgers, J. (Eds.), Anatomy of Mountain Chains. Princeton University Press, pp. 277-293.

Sutra, E., Manatschal, G., (2012). How does the continental crust thin in a hyperextended rifted margin? Insights from the Iberia margin. Geology 40, 139-142.

Tang, J. C., Chemenda, A. I., Chery, J., Lallemand, S. E., Hassani, R. (2002).

Compressional subduction regime and initial arc-continent collision: Numerical modeling. Geological Society of America Special Papers 358: 177-186.

Taylor, B., Hayes, D. E., Ed. (1980). The tectonic evolution of the South China Sea Basin. The Tectonic and Geologic Evolution of Southeast Asian Seas and Islands, 1. Washington, DC, Am. Geophys. Union.

Taylor, B., Hayes, D. E. (1983). Origin and history of the South China Sea Basin. The Tectonic and Geologic Evolution of Southeast Asian Seas and Islands, Geophys. Monogr. Ser. 27: 23-56.

Teng, L.S., (1990). Geotectonic evolution of late Cenozoic arc continent collision in Taiwan. Tectonophysics 183, 57-76.

Teng, L. S., (1996). Extensional collapse of the northern Taiwan mountain belt. Geology 24, 949-952.

Teng, L. S., Lee, C. T., Tsai, Y. B., Hsiao, L. Y., (2000). Slab break off as a mechanism for flipping subduction polarity in Taiwan. Geology 28, 155-158.

Thurber, C., Eberhart-Phillips, D., (1999). Local earthquake tomography with flexible gridding. Computers and Geosciences 25, 809-818.

Toth, J., and M. Gurnis (1998), Dynamics of subduction initiation at preexisting fault zones, J. Geophys. Res., 103, 18-053-18,067.

Tsai, C.-H., Hsu, S.-K., Yeh, Y.-C., Lee, C.-S., Xia, K. (2004). Crustal thinning of the northern continental margin of the South China Sea. Marine Geophysical Researches 25: 63-78.

Uyeda, S., and Z. Ben-Avraham (1972), Origin and development of the Philippine Sea, Nature, 240, 176-178.

Van Avendonk, H. J. A., D. J. Shillington, W. S. Holbrook, M. J. Hornbach (2004). Inferring crustal structure in the Aleutian island arc from a sparse wide-angle seismic data set. Geochemistry Geophysics Geosystems 5: 24.

Van Avendonk, H. J. A., Lester, W., McIntosh, K. D., Lee, C., Wang, T. K., Wu, F. T., Liu, C. (2009). Seismic velocity strucutre of the Eurasian margin of the southern Taiwan Strait. Eos Trans. AGU Fall Meet. Suppl., Abstract xxxxx-xx 90(52).

Waltham, D., R. Hall, H. R. Smyth, and C. J. Ebinger (2008), Basin formation by volcanic arc loading, Geophysical Society of America Speical Paper, 436, 11- 26.

Wang, T. K., Chen, M.-K., Lee, C.-S., Xia, K., (2006). Seismic imaging of the transitional crust across the northeastern margin of the South China Sea. Tectonophysics 412, 237-254.

Wang, Z., Huang, R., Huang, J., He, Z. (2008). P-wave velocity and gradient images beneath the Okinawa Trough. Tectonophysics 455: 1-13.

Warneke, L. A., W. G. Ernst. (1984). Progressive Cenezoic metamorphism of rocks cropping out along the southern east-west cross-inland highway. Memoir of the Geological Society of China 6: 159-183.

Watts, A. B., U. S. ten Brink, P. Buhl, T. Brocher (1985), A multichannel seismic study of lithospheric flexure across the Hawaiian-Emperor seamount chain, Nature, 315, 105-111.

Westbrook, G. K., Ladd, J. W., Buhl, P., Bangs, N., Tiley, G. J., (1988). Cross section of an accretionary wedge: Barbados Ridge complex. Geology 16, 631-635.

White, R. S., McKenzie, D., O'Nions, R. K., (1992). Oceanic Crustal Thickness from Seismic Measurements and Rare Earth Element Inversions. J. Geophys. Res. 97, 19683-19715.

Whitmarsh, R. B., Manatschal, G., Minshull, T. A., (2001). Evolution of magma-poor continental margins from rifting to seafloor spreading. Nature 413, 150-154.

Willett, S., Beaumont, C., Fullsack, P. (1993). Mechanical model for the tectonics of doubly vergent compressional orogens. Geology 21(4): 371-374.

Willett, S. D. (1999a), Rheological dependence of extension in wedge models of convergent orogens, Tectonophysics, 305(4), 419-435.

Willett, S. D., D. Fisher, C. Fuller, Y. En-Chao, and L. Chia-Yu (2003), Erosion rates and orogenic-wedge kinematics in Taiwan inferred from fission-track thermochronometry, Geology, 31(11), 945-948.

Wu, F. T., Rau, R.-J., Salzberg, D. (1997). Taiwan orogeny: thin-skinned or lithospheric collision? Tectonophysics 274: 191-220.

Wu, F. T., C. S., Chang., and Y. M. Wu. (2004). Precisely relocated hypocenters, focal mechanisms and active orogeny in Central Taiwan. Geological Society of London Special Publication 226: 333-353.

Wu, Y.-M., Zhao, L., Chang, C.-H., Hsiao, N.-C., Chen, Y.-G., Hsu, S.-K., (2009). Relocation of the 2006 Pingtung Earthquake sequence and seismotectonics in Southern Taiwan. Tectonophysics 479, 19-27.

Yamato, P., F. Mouthereau, and E. Burov (2009), Taiwan mountain building: insights from 2-D thermomechanical modelling of a rheologically stratified lithosphere, Geophysical Journal International, 176(1), 307-326.

Yan, P., Zhou, D., Liu, Z., (2001). A Crustal Structure Profile Across the Northern Continental Margin of the South China Sea. Tectonophysics 338, 1-21.

Yang, T. F., J. L. Tien, C. H. Chen, T. Lee, and R. S. Punongbayan (1995), Fission-track dating of volcanics in the northern part of the Taiwan-Luzon arc: eruption ages and evidence for crustal contamination, J. SE Asian Earth Sci., 11, 81-93.

Yang, T. F., T. Lee, T, C.-H., Chen, S.-N. Cheng, U., Knittel, R. S. Punongbayan, and A. R. Rasdas (1996), A double island arc between Taiwan and Luzon:consequence of ridge subduction, Tectonophysics, 258, 85-101.

Yang, Y.-S., and T.-K.Wang (1998), Crustal Velocity Variation of the Western Philippine Sea Plate From TAICRUST OBS/MCS Line 23, TAO 9, 379-393.

Yu, S.-B., Kuo, L-S., Punongbayan, R.S., Ramos, E. G. (1999). GPS observation of crustal deformation in the Taiwan and Luzon Region. Geophys. Res. Lett. 26(7): 923-926.

Yu, S.-B., and L.-C. Kuo. (2001) Present-day crustal motion along the longitudinal Valley Fault, eastern Taiwan. Tectonophysics 333: 199-217.

Zelt, C. A. and R. B. Smith (1992). Seismic traveltime inversion for 2-D crustal velocity structure." Geophysical Journal International 108(1): 16-34.

Zelt, C. A., K. Sain, J. V. Naumenko, and D. S. Sawyer (2003), Assessment of crustal velocity models using seismic refraction and reflection tomography, Geophysical

Journal International, 153, 609-626.

Zhu, J., Qiu, X., Kopp, H., Xu, H., Sun, Z., Ruan, A., Sun, J., Wei, X., (2012). Shallow anatomy of a continent-ocean transition zone in the northern South China Sea from multichannel seismic data. Tectonophysics 554, 18-29.